FATIGUE OF COMPOSITE MATERIALS AND SUBSTRUCTURES FOR WIND TURBINE BLADES

John F. Mandall, Daniel D. Samborsky, Douglas S. Cairns

Sandia National Laboratories

Fatigue of Composite Materials and Substructures for Wind Turbine Blades

John F. Mandell, Daniel D. Samborsky and Douglas S. Cairns
Montana State University
Bozeman, MT 59717

Abstract

This report presents the major findings of the Montana State University Composite Materials Fatigue Program from 1997 to 2001, and is intended to be used in conjunction with the DOE/MSU Composite Materials Fatigue Database. Additions of greatest interest to the database in this time period include environmental and time under load effects for various resin systems; large tow carbon fiber laminates and glass/carbon hybrids; new reinforcement architectures varying from large strands to prepreg with well-dispersed fibers; spectrum loading and cumulative damage laws; giga-cycle testing of strands; tough resins for improved structural integrity; static and fatigue data for interply delamination; and design knockdown factors due to flaws and structural details as well as time under load and environmental conditions. The origins of a transition to increased tensile fatigue sensitivity with increasing fiber content are explored in detail for typical stranded reinforcing fabrics. The second focus of the report is on structural details which are prone to delamination failure, including ply terminations, skin-stiffener intersections, and sandwich panel terminations. Finite element based methodologies for predicting delamination initiation and growth in structural details are developed and validated, and simplified design recommendations are presented.

Acknowledgments

Table of Contents

List of Tables

List of Figures

13

15

16

17

19

EXECUTIVE SUMMARY

This report brings together the findings of a broad range of individual studies related to the strength and fatigue resistance of composite materials and substructural elements intended for application in wind turbine blades. Previous contractor reports have provided extensive data and analysis for the effects of major materials parameters on strength and constant amplitude fatigue properties for commonly used blade materials, as well as validation of the application of the materials database to a beam substructural element representative of blade structure. Previous findings are summarized in the Background chapter of this report.

The focus of individual chapters of the first part of this report is new data, including: new fatigue results for carbon fiber composites and glass/carbon hybrids, as well as other new reinforcing fabrics; the effects of tougher resins on structural integrity; the effects of moisture and temperature on static and fatigue strengths for different resin systems; the first fatigue data to 10^{10} cycles; knockdown factors for a variety of flaws, structural details, time scales, and hot/wet conditions, which relate to partial safety factors in design; the first data for the delamination resistance of blade materials under static and fatigue loading; and a systematic study of the effects of spectrum fatigue loading on material lifetime, including an assessment of different cumulative damage laws.

The second part of the report considers generic types of structural details which are typically prone to delamination failure, including skin-stiffener intersections and sandwich panel closeouts, in addition to ply drops which are addressed earlier. Structural detail test geometries have been designed, fabricated, and tested. The test geometries serve two main purposes: first, to establish and validate design methodologies based on finite element analysis and using database properties, particularly delamination resistance; and, second, for use as a standard specimen for evaluation of different fabrics, resins, and manufacturing methods in a structural context.

Design recommendations are provided at the end of the substructure chapters, as well as for chapters on materials studies, where appropriate. The following provides a summary of individual chapters, in order of appearance.

PART A: MATERIALS STUDIES

The chapters in this part of the report provide data and analysis primarily from coupon-type materials tests. The data are available in the current installment of the DOE/MSU Composite Materials Fatigue Database available on the SNL website at www.sandia.gov/Renewable_Energy/wind_energy/.

Chapters 3 and 4 Resins, Fabrics, and Environmental Effects

Chapters 3 and 4 explore issues in the selection of resins and reinforcing fabrics, the former with a focus on environmental resistance and structural integrity. The DOE/MSU Fatigue Database has been expanded to include a number of matrix resins of potential interest in wind turbine blades. The

main considerations in resin selection have been to increase the structural integrity (such as delamination resistance) in blades while maintaining or improving other mechanical properties, particularly under hot, wet conditions. The resins included in this phase of the study are also appropriate for the wind turbine blade application in terms of cost and processing characteristics (all materials were prepared by resin transfer molding). Resins included unsaturated polyesters, vinyl esters, epoxies, and a urethane. Mechanical properties have been obtained for wet and dry specimens tested at temperatures from -25 to 70°C. Fatigue, delamination resistance (Mode I and II crack growth), and performance in stiffener substructure sections have been evaluated for selected cases. Significantly improved performance relative to baseline polyester is shown for several resins; the baseline ortho-polyester is found to have inadequate resistance to hot/wet conditions for blade applications.

The static and fatigue properties of typical wind turbine blade composite materials depend strongly on the architecture of the reinforcing fabric (woven, stitched, etc.) as well as the overall fiber type (glass versus carbon), content and orientation. Fabric architecture also has a strong influence on resin flow characteristics during manufacturing and on the sensitivity of the properties to structural detail geometry. The DOE/MSU Fatigue Database contains data on many commercially available reinforcing fabrics tested in a variety of laminate configurations under several loading conditions. Two factors of concern are the low compressive strength of woven fabrics, and a transition to poor tensile fatigue resistance at high fiber content, which can plague all stranded fabrics under some conditions. Furthermore, the unidirectional stitched fabrics, which have shown the best overall performance, are not generally available in the long, or warp direction of the fabric roll except when stitched to additional layers such as mat, which significantly reduces the tensile fatigue resistance. Thus, the best performing stranded fabric cannot be used for the main lengthwise reinforcement in the blade. This chapter presents a summary of the merits of several widely used fabrics as well as results for several new fabric types including bonded fabrics which show potential for improved performance. The results include an assessment of manufacturability and performance in structural details. The final section deals with European fabrics having large 0° tows stitched to a woven fabric, with disappointing tensile fatigue resistance as well. Tests on evolving large tow carbon reinforcements are reported in Chapter 10. The effects of fabric on simulated flaws and structural details are addressed in a Chapters 8 and 10.

Chapter 5 Spectrum Loading

This chapter addresses the effects of spectrum loading on lifetime and residual strength. Over 1100 tests have been run on a typical fiberglass laminate configuration under a variety of load sequences. Repeated block loading at two or more load levels as well as a modified standard spectrum have been studied. Data have been obtained for residual strength at various stages of the lifetime. Several lifetime prediction theories have been applied to the results.

The repeated block loading data show lifetimes that are usually shorter than predicted by the most widely used linear damage accumulation theory, Miner's sum. Actual lifetimes are in the range of 10 to 20 percent of predicted lifetime in many cases. Linear and nonlinear residual strength models tend to fit the data better than Miner's sum, with the nonlinear providing the better fit of the two.

Direct tests of residual strength at various fractions of the lifetime are consistent with the residual strength damage models for several cases. Load sequencing effects are not found to be significant. The more a spectrum deviates from constant amplitude, the more sensitive predictions are to the damage law used. The nonlinear model provided improved correlation with test data for a modified standard wind turbine spectrum. When a single, relatively high load cycle was removed, all models provided adequate correlation with the experimental results.

Additional results for compression, reversed loading, and the unmodified WISPERX spectrum may be found in a forthcoming SNL report or Wahl's doctorial dissertation. The effects of constant amplitude data extrapolation models are also explored in these references, and found to be significant.

The residual strength models may provide a more accurate estimate of blade lifetime than Miner's rule for some loads spectra. They have the added advantage of providing an estimate of current blade strength throughout the service life. A simplified approach suggested in the literature is also found to provide a conservative prediction of lifetime in this study: use Miner's Sum, but consider failures to occur when the sum is 0.1 instead of 1.0.

Chapters 6 and 7 High Cycle Testing and Time Under Load Effects

Chapters 6 and 7 provide results for very high (giga) cycle tensile fatigue testing of small strands, as well as data for the effects of static load duration and strain rate. Chapter 6 describes the development and application of a novel, low-cost, high-frequency fatigue testing apparatus, and its application in obtaining very high cycle data for small impregnated glass strands. The first known tensile fatigue data out to 10^9 to 10^{10} cycles have been obtained using two matrix systems. The results can be represented by a power law S-N trend or an exponential trend with a fatigue limit around 10^8 cycles, or a combination of the two. Both these results and related tests to 10^9 cycles using larger strands support the use of a power law extrapolation of S-N data trends to very low stresses and long lifetimes. This is critical in the application of cumulative damage laws to spectrum loading. Interpretation of the results for larger volumes of material is difficult due to the high static strength and less steep S-N curve for the very small strands. A tougher resin system, 8084 vinyl ester, showed only slight improvements in fatigue resistance at high cycles.

Chapter 7 considers the effects of strain rate and time under load on strength. Static tensile and compressive strength data are presented in the database for a wide range of materials, including different environmental conditions. These data are obtained from standard size test coupons loaded at a high strain rate to be consistent with fatigue strain rates. The high strain rate produces higher strength values than would low strain rates. The use of these strength data in blade design requires consideration of the timescale of loading under extreme wind conditions. If the maximum stress conditions for the blade involve significant time at high stress, such as more than one second, then the timescale of the event should be considered before using strength values in the database.

This chapter provides a detailed consideration of time under load effects for various laminates. The effects of time under load and strain rate are more significant than expected from earlier investigations. Load transfer between ±45° and 0° plies is sensitive to time under load, and

contributes significantly to time effects in addition to the expected static fatigue effects for the glass fibers. Rate effects are significant in compression as well as tension. Knockdown in strength required for longer time durations are additive with factors such as strand waviness in woven fabrics, which reduce compressive strength, and environmental effects.

Chapter 8 Design Knockdowns

Chapter 8 considers design knockdowns for flaws, structural details, time and environment. Material partial safety factors are an important part of blade design. They are intended to account, in part, for the effects of flaws and geometries not present in normal material test coupons, as well as environmental conditions and time effects. Safety factors can be rendered more rational by exploring specific contributing factors, which is the subject of this chapter.

Laminates fabricated from stranded glass fiber fabrics commonly used in wind turbine blades have been found to exhibit a strong sensitivity to fiber content. The tensile fatigue resistance decreases rapidly over a narrow range of fiber volume fraction as the fiber content is increased. Many manufacturing processes produce fiber contents in this range, and local variations in fiber content around details such as stiffeners are often not well controlled. Thus, the fatigue resistance around structural details may drop precipitously if the fibers are locally pinched during manufacturing.

A second problem associated with structural details is delamination between plies of fabric due to out-of-plane stresses. Delamination can lead to breakdown of a structure directly, often with subsequent buckling, or indirectly, by accelerating fatigue breakdown of the fiber strands. Another, independent type of flaw, fiber waviness, affects compression strength in many types of composites. This is inherent in woven fabrics, and is often introduced by manufacturing processes in otherwise straight-fiber reinforcements. It is particularity difficult to avoid in thick sections.

This chapter explores the static and fatigue strength of a number of real and simulated flaws and structural details which may be associated with local increases in fiber content as well as delamination and waviness. The flaws and structural details investigated include ply drops, skin-stiffener intersections in I-beams, local matrix rich and transverse fiber areas, surface indentation, sandwich panel closeouts and waviness. These are compared to unflawed laminates and laminates containing severe flaws such as through-thickness holes. The results are represented in two ways. First, the stress or strain required to produce a 25 mm delamination in static or fatigue tests in 10^5 cycles is documented for cases which delaminate; and second, as knockdown factors on the ultimate static strain and maximum strain to produce total laminate failure in 10^6 cycles. Two types of 0° fabric are included in most cases. The knockdown factors on static properties ranged up to 4.0, with the worst case being a sandwich panel closeout. In fatigue, knockdown factors also ranged up to 4.0, with the worst case being a double ply drop in compression, with a sandwich panel closeout a close second. Extended time under load showed a knockdown of about 1.3, while 50°C/wet conditions produced a knockdown of 1.9 for the ortho-polyester resin in compressive fatigue. Materials with poor initial properties, such as woven fabrics in compression and high fiber contents in tension fatigue, require lower knockdowns than did materials with the best performance.

Chapter 9 Delamination

Chapter 9 provides the first significant look at delamination problems in this program. Delamination between plies is widely viewed as the "Achilles heel" of composite material structures. Failures in blades due to delamination have been observed in both service and full-scale blade tests. Delaminations occur in areas of complex, three-dimensional stress states which are rarely analyzed in detail during design. The resistance to failure due to thickness-direction shear and normal stresses is very low relative to the fiber dominated properties along the primary load paths. Lower cost thermoset resins are brittle, and their composites have low delamination resistance, as shown in the matrix resin chapter. Manufacturing problems such as resin-rich areas and porosity can provide sites for delamination initiation. Environmental factors and fatigue loading can lead to the spread of delaminations at low load levels. In aerospace applications, the delamination problem has been addressed primarily through increased resin toughness (which is costly), conservative designs in structural detail areas, and a variety of rules-of-thumb.

Relative to aerospace composites, where delamination problems have been addressed in detail, wind turbine blades tend to be more heterogeneous (thicker plies and stranded fabrics), which may raise both the stresses causing delamination and the material's resistance to delamination growth. The more brittle, low cost resins which are commonly used in blades produce lower delamination resistance, while glass fibers tend to reduce delamination stresses due to the reduced anisotropy relative to carbon fiber composites.

Methodologies for dealing with delamination are described in this chapter, and in later substructure chapters. Test methods which are applicable to blade materials are identified, and test procedures are described which produce conservative measures of delamination resistance. Methods of analysis for both standard delamination tests and complex substructures are described, with applications of the latter in the substructures chapters. Test data are limited to a few cases at this time; these cases relate to the matrix study discussed earlier, and the substructure studies which follow. To use delamination data in the design of structural details, it is necessary to have data for basic opening and shearing modes of delamination growth for the ply interfaces of concern, with the appropriate fabrics, resins, and fiber contents. To date, only limited data have been obtained for static delamination and fatigue crack growth. A simplified procedure of using only initiation values in design is recommended.

Chapter 10 Other Database Additions

This chapter contains results for several types of materials not previously available in the database. Data are presented in separate subsections for carbon fiber and carbon/glass hybrid laminates; glass fiber composites with well-dispersed fibers (compared with stranded fabric reinforcement); sandwich panels; injection molded carbon fiber/thermoplastic matrix composites; and useful relationships between molding pressure, ply thickness, and fiber content for most materials in the database.

The carbon fiber results focus primarily on the large tow, low cost carbon fabrics. Most of the

results are for hybrid laminates with carbon 0° plies and glass ±45°plies. There were difficulties with fabrication and testing in some cases and tests are on-going. Results to date indicate good performance in tension for static and fatigue properties. Fatigue stress and strain levels in tension are better than those for all glass laminates, as is the elastic modulus, as expected. The compression data are disappointing when viewed in terms of strain levels for static and fatigue properties. While prepreg materials, with relatively well dispersed and well aligned fibers, show longitudinal compressive ultimate strains above 1.0 percent, woven fabrics with large tows are in the 0.6 to 0.7 percent range, and stitched fabric is in the 0.7 to 0.8 percent range. Million-cycle compression fatigue strains are in the range of 0.35 to 0.45 percent for the woven fabrics and 0.55 to 0.60 percent for the stitched fabrics. The fabrics were tested with a vinyl ester matrix. The carbon fabric compression strains fall well below values for glass fabrics, and may be sufficiently low to be a limiting factor in blade design.

New data for impregnated strands and prepreg laminates with well dispersed glass strands support the earlier view that the transition to poor tensile fatigue resistance with increasing fiber content (reviewed in the background section) is related to the stranded architecture of the fabrics. While this transition occurs around 40 percent fiber by volume in stranded glass fiber laminates, it is shifted to the 60 percent fiber by volume range when the fibers are well dispersed, as in prepreg laminates. This is explored further in Chapter 11.

Sandwich panel construction is used to raise the bending and buckling resistance of thin airfoil skin areas in most blades. If this construction is used in high stress areas of blades, it must withstand the same strain levels as do adjacent primary structures. A typical sandwich panel with glass fiber laminate skins and balsa core was subjected to static and fatigue testing. The results show very similar tensile ultimate and fatigue strengths when compared to the base laminate without the core. Chapter 14 deals with the greater problem of transitions between the sandwich panel and plain laminate.

Static and fatigue testing was also done on an injected molded carbon fiber/thermoplastic matrix material. Test specimens were cut from small turbine blades. The results show relatively good stiffness, strength and fatigue properties compared with typical database glass fiber laminates. However, these materials are probably not appropriate for large blades due to relative brittleness and probable molding related problems in thick sections.

A final part of this chapter provides data for most database materials, relating molding pressure and ply thickness to fiber content. These data can be useful in initial mold and process design, to obtain desired fiber contents (associated with weight and mechanical properties).

Chapter 11 Tensile Fatigue Effects

This chapter provides a detailed interpretation of database trends in the area of fiber content effects on tensile fatigue. The transitions to poor tensile fatigue performance with increasing fiber content have been discussed in earlier sections. Materials with well dispersed fibers (strands and prepreg) have been found to provide good tensile fatigue resistance up to 60 percent or more fiber by volume. The stranded fabric architectures, which constitute most of the database materials, show

26

such a transition in the 40 percent fiber volume content range, with the transition occurring at about two percent lower fiber content for multidirectional laminates than for unidirectional materials with the same 0° reinforcing fabric. Chapter 10 clarifies the later trend, since the actual fiber content and ply thickness is higher in the 0° plies when laminates contain ±45° plies with most fabrics, since the ±45° absorb more resin.

This chapter explores the origins of the difference between stranded fabrics and materials with well dispersed fibers, in terms of the fiber content where the transition in tensile fatigue resistance occurs. Detailed microscopy analysis has been carried out for laminates with different fiber contents. As expected, the fiber content within strands is much higher than the average fiber content of the laminate. Furthermore, as the average fiber content increases, the local fiber content within the strands also increases significantly, particularly near stitch or weave crossover points. The strands also distort significantly at higher fiber contents.

The results of this study, and data presented earlier, clearly show that the transition in tensile fatigue resistance is related to increases in the local fiber content within the strands of the 0° plies. While some fabrics, such as A130, are less severe in this respect than others, such as D155, all stranded fabrics have problems at high fiber contents, particulary near stitch or weave points. To obtain good tensile fatigue resistance in glass fiber laminates at average fiber contents in the 50 to 60 percent by volume range, it is necessary to use materials, like prepreg, with well dispersed fibers.

PART B : SUBSTRUCTURE STUDIES

Substructure studies were designed to explore four areas: (1) validation of use of the DOE/MSU database in design and analysis of blade substructures, (2) identification of critical materials issues to be addressed in the database, (3) development and validation of methodologies for designing complex structural detail areas where delamination is the dominant failure mode and (4) to provide standard test specimen geometries for structural integrity, which could be used for comparison of different resins, reinforcement, and processing methods. The choice of structural details was influenced strongly by the design/manufacturing effort centered on the AOC 15/50 blade as part of the Montana DOE EPSCoR program, but the geometries are generic to most blades constructed from composite materials.

Chapter 12 Skin/Stiffener Intersection (Strength)

Chapter 12 considers the skin/stiffener intersection under static loading. Most composite blades contain some type of internal stiffener spar. The goals for this study were to combine experimental testing with finite element analysis (FEA) to establish design guidelines and develop accurate FEA methods for predicting skin-stiffener fracture loads and locations. A follow-on study reported in the next chapter explored the fatigue response. An additional goal of the study was to establish a structural integrity test geometry for materials and manufacturing evaluation.

A strength-based failure prediction with FEA results was adequate to predict damage onset in the stiffener samples in regions without high stress gradients. However, a fracture mechanics

approach was necessary to analyze the flange tip region. Good agreement with experimental delamination initial growth loads was obtained by using the one-step virtual crack closure technique (VCCT-1) to calculate strain energy release rate values. These values were used with the linear interaction criterion for crack growth to predict propagation loads. An initial crack length of less than 0.2 mm and a crack length to crack extension ratio (a/da) of greater than 20 provided good results for the modeling of damage onset at the flange tip. The use of R-curve data for predicting the extension of large delaminations produced generally conservative results.

Experimental fracture toughness tests showed that delamination growth resistance was higher for cracks propagating at a ±45 degree ply interface than for cracks between two 0° plies. Increasing the skin bending stiffness and matrix material toughness produced large increases in pull-off loads. Increasing the flange thickness and the adhesive bond-line thickness caused the damage location to change from the web/flange bend region to the flange tip. This was due to the increasing geometric discontinuity at the flange tip, which created high interlaminar stresses. Detailed design recommendations are presented.

Chapter 13 Skin/Stiffener Intersection (Fatigue)

This chapter considers the same skin-stiffener intersection geometry under fatigue loading. Experiments have been run to measure damage initiation conditions and geometries as well as delamination growth rates. Using finite element analysis and data for strength, delamination resistance, and delamination fatigue crack growth, damage initiation and growth under static and fatigue loading is predicted following a prescribed methodology, and compared to experimental data. Delamination growth is by a mixture of Modes I and II, and a mixed-mode criterion has been assumed in the absence of definitive data. Overall fatigue lifetime trends with varying maximum load are also established, and the sensitivity to matrix variations is explored.

The results in this section serve to define and validate a methodology for predicting delamination failures at structural details using finite element analysis and database delamination fatigue crack growth and fracture data. While the correlations of predictions with experimental data are generally good, they indicate a need for a definitive fracture mode interaction criterion for static and fatigue delamination for a range of reinforcing fabrics, matrices, and particular ply interfaces. A simplified method for predicting fatigue performance in the design of delamination-prone substructures is also presented.

Chapter 14 Sandwich Panel Terminations

Chapter 14 addresses the complex substructure geometry where sandwich panels are closed-out against normal laminate. Typically, sandwich panel construction is used in the trailing edge side of most blades to increase resistance to panel buckling of thin airfoil skins. Sandwich panels are composed of thin structural skins and a very lightweight core material, such as balsa, polymer foam, or honeycomb. The thickness added by the core raises the moment of inertia of thin panels, increasing the bending stiffness and buckling resistance at little expense in terms of weight or cost. Achieving the same buckling resistance with a thicker laminate would greatly add to weight and cost. Other

stiffening methods such as multiple webs and "hat" shaped ribs are also effective.

The results show very poor tensile performance for the standard 30° longitudinal closeout geometry. Delamination and failure occur at much lower strains than can be withstood for the laminate or sandwich panel without terminations. Decreasing the termination angle to 10° or 5° significantly increases the structural performance, with the 5° case approaching the control laminate performance with no closeout. Finite element predictions based on point-stress failure criteria are in good agreement with the experimental data, using input material properties for the fiberglass and balsa which were developed in this study. In tensile fatigue, the sandwich panel lifetime without closeouts approached that of the baseline laminate. Specimens with a 30° closeout showed a similar fatigue sensitivity to other delamination results, but a steeper S-N curve to failure than for the base laminate. On an absolute basis, the strain levels for delamination and failure at 10^6 cycles were low, in the range of 0.3 percent, compared with the baseline laminate value above 1.0 percent. Design recommendations are given at the end of the chapter.

Chapter 15 Concluding Remarks

The overall findings with regard to different material parameters expressed in this and previous reports lead in two directions. The use of materials with well dispersed fibers, like prepreg, should provide near optimum properties, assuming that severe fiber waviness problems could be avoided. Furthermore, adequate carbon fiber compression strain levels could probably be obtained if the fibers were straight. A toughened resin system could provide improved resistance to delamination in structural details, but would probably prove costly.

A second direction involves the use of hand layup, RTM, and similar processes, using various stitched and woven reinforcing fabrics. Here, there is a question of whether the materials which produce the highest strength and fatigue properties are worth additional materials and manufacturing costs, since their performance would be subject to high knockdown factors due to the effects of common flaws and structural details. Lower performing materials in simple coupon tests are often subject to greatly reduced knockdown factors. Higher fiber contents, with improvements in most properties except tensile fatigue resistance, makes sense if the good tensile fatigue resistance at low fiber contents is unavoidably lost due to local strand packing near details.

Regardless of material and process choices, several other factors must be addressed. The time duration of high-load events could significantly reduce strength properties. In spectrum loading, the use of Miner's Sum of 1.0 is nonconservative by up to an order of magnitude. An improved model or a reduced sum like 0.1 is recommended. Finally, the efficient and reliable design of structural detail areas is essential; the fracture mechanics based methods explored here are promising, but require further refinement, validation, and simplification. The response of structural details under more severe environments and spectrum loading has not yet been addressed.

1. INTRODUCTION

The study of composite materials for wind turbine blade applications at Montana State University (MSU) was initiated in 1989 with support from Sandia National Laboratories (SNL). The program has continued since that time with continuous support from SNL as well as additional support at various times from the National Renewable Energy Laboratory (NREL) and the Department of Energy (DOE) EPSCoR program, the latter with matching state funds.* Two earlier SNL contractor reports in 1992 [1] and 1997 [2] detailed fatigue studies on material coupons, while an NREL report [3] gave the results of a study of sub-structural beams representative of blade structures, and effects of ply drops used in tapering the thickness. Additional results have been available in literature publications [4 - 23] and graduate student theses [24 - 44]. The application of these results to the fatigue design of wind turbine blade structures has been reported by Sutherland [45]. This report presents results generated since the 1997 report [2] from both basic materials tests and tests on representative structural details; funding in this period was provided by SNL,** as well as the DOE EPSCoR program.

Individual test results from nearly all of the basic materials tests may also be found in the DOE/MSU Composite Materials Fatigue Database, with the most current version available through SNL's website at www.sandia.gov/Renewable_Energy/wind_energy/. The database, which is updated regularly, contains summaries of the static and fatigue properties with detailed materials descriptions, as well as raw test results. The current database contains results from over 7000 tests on 130 different materials. Detailed descriptions of the test methods were given, for basic materials, in the 1997 SNL contractor report [2], and, for sub-structural beam elements, in the 1998 NREL contractor report [3]. Greater details in both of these areas, as well as special small strand testing may be found in the masters thesis by Samborsky [38]. This report only describes test methods which differ from those published in the sources just cited.

Additions to the database since the 1997 report are mostly in the following areas: high cycle strand tests, which address questions such as fatigue limits and S-N (maximum stress versus cycles to failure) curve trend shapes at high cycles; effects of matrix variations on delamination and environmental (hot-wet) resistance; new reinforcing fabric styles and prepreg materials with uniformly distributed fibers (rather than strand segregation); carbon fibers and glass/carbon hybrids; and the effects of spectrum loading, including simple spectra and spectra representative of actual blade loading.

Substructure studies are not generally included in the database, and details may be found in the student theses cited. The main focus of the substructure studies is on the behavior of structural details under static and fatigue loading. Details studied include ply drops, skin-stiffener intersections, sandwich panel (balsa wood core) closeouts at the edges of stiffened areas, and stud - root connections. The substructures and details were selected from the design and manufacturing of an 8 meter blade from an AOC 15/50 turbine as part of the DOE EPSCoR program, although the studies are generic and apply to most blade designs. Most of the substructure studies involve delamination failures (separation of plies of the composite or secondary bonded areas). A common feature of the

studies is the development of methodology to predict delamination failures, including fracture mechanics based static and fatigue crack growth generic data generation, applied to the specific complex geometries through finite element analysis.

2. BACKGROUND

The 1997 SNL contractors report [2] provided a detailed analysis of the static and fatigue properties of a wide range of materials, tested under a variety of loading conditions. Test development is often required to obtain desired gage-section failures in test coupons for each significantly new material. Variations in the fraction of axial (0°) fibers (in the load direction), fiber content, thickness, fiber properties (glass versus carbon) and reinforcement architecture (woven versus unidirectional layers, for example) all require modifications to test geometry. Test conditions such as the frequency of fatigue loading must be chosen to avoid excessive hysteretic heating. Higher frequencies are possible with thinner specimens due to improved heat transfer. Reference 2 describes the development of thin test sections for higher frequency testing, in the 50 to 100 Hz (cycles per second) range. These tests were used to generate fatigue data to 10^8 cycles at various tension and compression loading conditions, which yield Goodman diagrams that can be used for design. The present study extends the high frequency test approach using small strands and frequencies to 300 Hz, for study of very high cycle frequency trends, out to 10^{10} cycles.

Fatigue trends were analyzed in Reference 2 for over 4000 test results, including materials supplied by industry as well as materials fabricated at MSU. The materials fabricated at MSU by resin transfer molding included systematic variations in fiber content, fraction of 0° and ±45° material, reinforcement architecture, and loading conditions (tension-tension, compression-compression, and reversed tension-compression). The following is a summary of the findings reported in Reference 2. All results are for E-glass fiber reinforcements, primarily with an orthophthalic unsaturated polyester matrix. All fatigue tests were run with sine-wave loading at a constant stress amplitude. An S-N curve was generated for a constant ratio of R (minimum stress over maximum stress).

The S-N fatigue trends have been fit to an exponential relationship which is linear on a maximum stress versus log cycles to fail basis, yielding, for a static strength So,

$$\frac{S}{S_O} = 1 - b \ Log \ N, \tag{1}$$

where S is the maximum cyclic stress, N is the cycles to failure, and b is the fatigue coefficient, the slope of the normalized S-N curve. In this form, the fit is forced through the static strength at a single cycle. An alternative representation would be as a power law,

$$\frac{S}{S_O} = C \ N^{-\frac{1}{m}}, \tag{2}$$

where C is the value of S/So at one cycle, which may be forced through 1.0, m is the fatigue

32

exponent, and -1/m is the slope of the S-N curve on a log stress versus log N plot.

The findings of the earlier studies are summarized in the following:

1. Tensile fatigue resistance. The fatigue coefficient, b, varied significantly in tension. The best glass fiber composites have a value of b close to 0.10, while the worst have a value close to 0.14. As shown in Figure 1, this difference in b can represent a difference in cycles to failure of about a factor of 100, depending on the stress. Figure 1 also illustrates that composites with high fiber content have reduced fatigue resistance, with b approximately 0.14. Figures 2 and 3 express similar results in terms of the value of b versus fiber content, and the maximum strain which can be withstood for 10^6 cycles, respectively. The value of b goes through a transition from around 0.10 to 0.14 in the fiber content range of 40 percent for fabrics with discrete strands. The 10^6 cyclic strain-to-failure drops markedly in the same range. Thus, by either measure, the high fiber content laminates are significantly more fatigue sensitive, so that strains must be kept much lower to avoid fatigue failures. These results also show that the transition occurs at slightly higher fiber contents for unidirectional 0° materials than for materials containing some ±45° fibers; triax fabrics, with ±45° fibers stitched to ±0° fibers, show poor fatigue resistance down to very low fiber contents. The origins of these effects are explored later in this report. It should be noted that the fiber content where the transition is observed, in the range of 40 percent fiber by volume, is in the upper range of simple hand layup processes, and the lower range of many resin transfer and bag molding processes. For reasons to be discussed later, the transition for typical prepreg materials, with more uniform fiber dispersions, occurs at much higher fiber contents. Materials with less than 50 percent 0° material show somewhat lower 10^6 cycle strains.
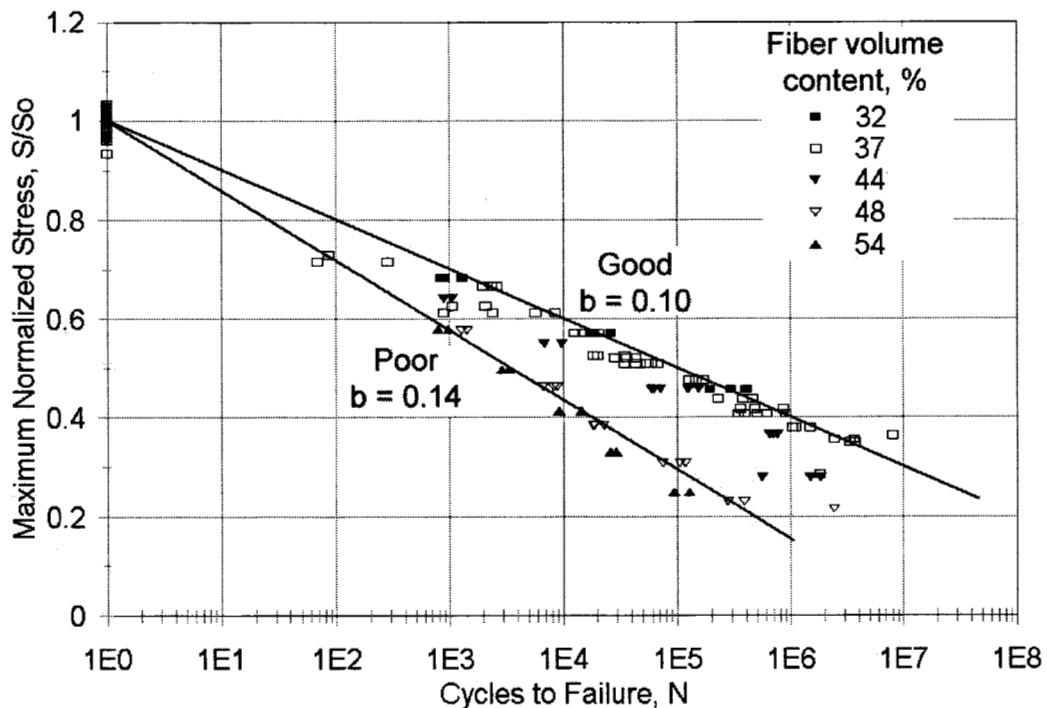
Figure 1. Normalized Tensile Fatigue Data for DD Materials $(0/\pm45/0)_s$, R = 0.1
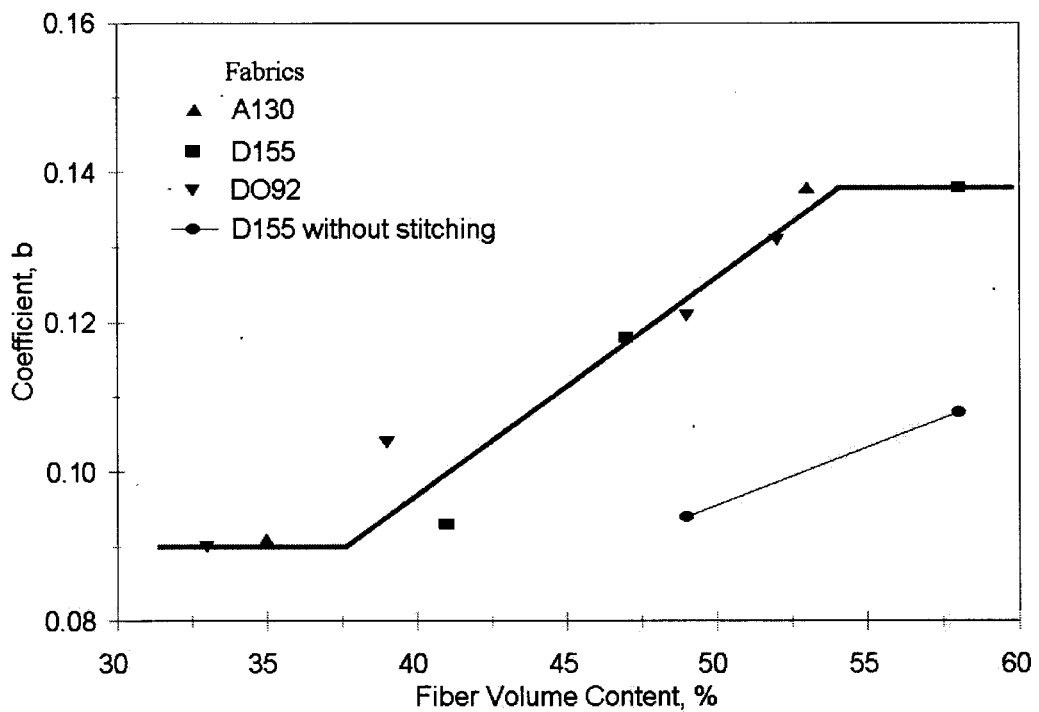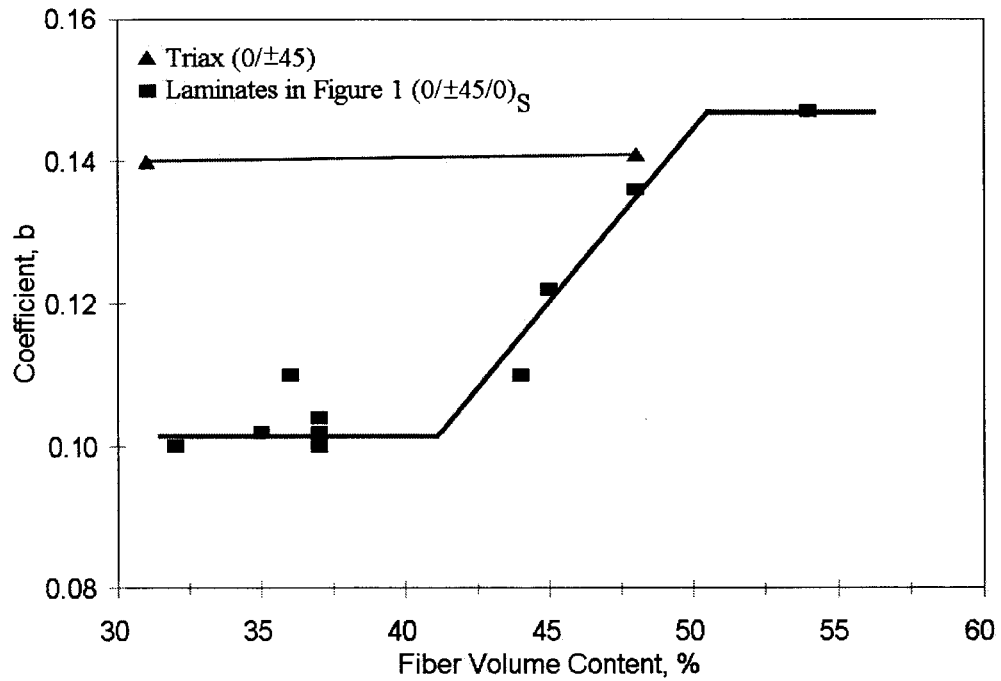
Figure 2. Fiber Content versus Tensile Fatigue Sensitivity Coefficient, b, for Laminates with 0° and ±45° Fibers (top), and for Unidirectional 0° Composites Based on Various Fabrics (bottom), R = 0.1.
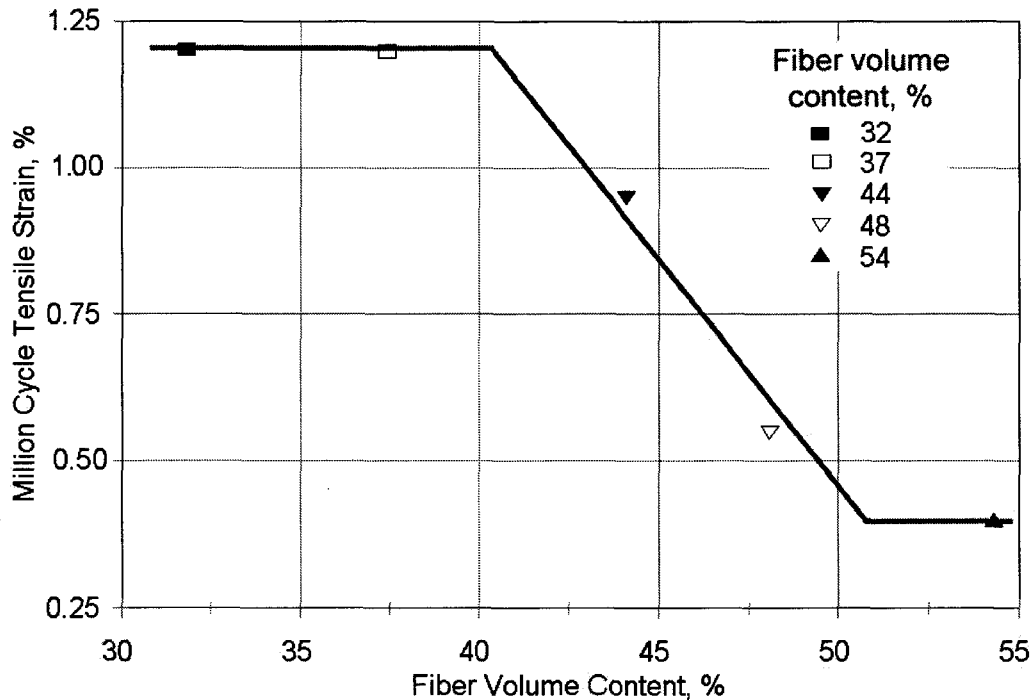
Figure 3. Fiber Content versus Million Cycle Tensile Strain for Various
Materials From Figure 1, R = 0.1

2. Compression fatigue is significantly less sensitive to fiber content and fabric style in terms
of the coefficient, b, and the 10^6 cyclic strain-to-failure. Initial strengths are usually lower than in
tension, but S-N curves are less steep. Although the value of b does not change significantly with
most parameters, the initial static strength is much more sensitive to reinforcement style than is the
tensile strength. Woven fabrics, which cause an out-of-plane waviness to the fiber strands, have a
much lower static compressive strength than do materials with straight fibers. Woven fabrics often
produce a compressive strength reduction to about half the value found with straight fibers, but with
the value of b not significantly affected.

3. Reversed tension-compression fatigue trends fall below the lowest of the tension and
compression curves, considering absolute values of stress. Thus, reversed loading produces the
greatest fatigue sensitivity, when considered in terms of absolute maximum stress as opposed to cyclic
amplitude.

4. Tensile S-N data sets for conditions which produce the best fatigue resistance, b = 0.10,
show no tendency to reach a fatigue limit out to 10^7 cycles when plotted as linear stress versus log
cycles; the data for tests with gage-section failures fit well to Equation 1, as shown in Figure 4 for
a laminate with relatively small scatter. Tensile fatigue S-N trends for laminates with steeper S-N
curves, such as those at higher fiber contents in Figure 1, tend to flatten at stresses in the range of 15
to 20 percent of the static strength. However, these curves may appear linear if plotted as log
stress versus log cycles. The proper fatigue trend to use in extrapolating beyond the cycle range
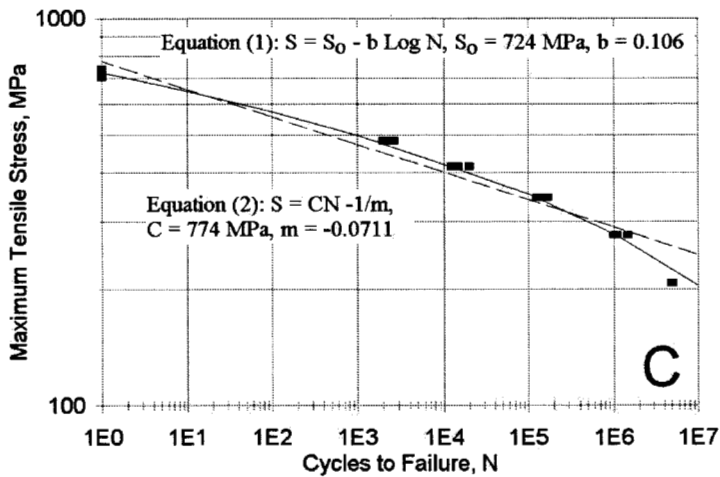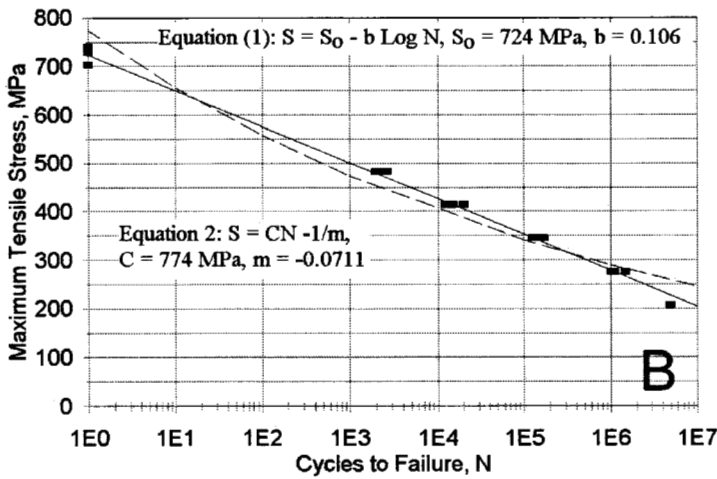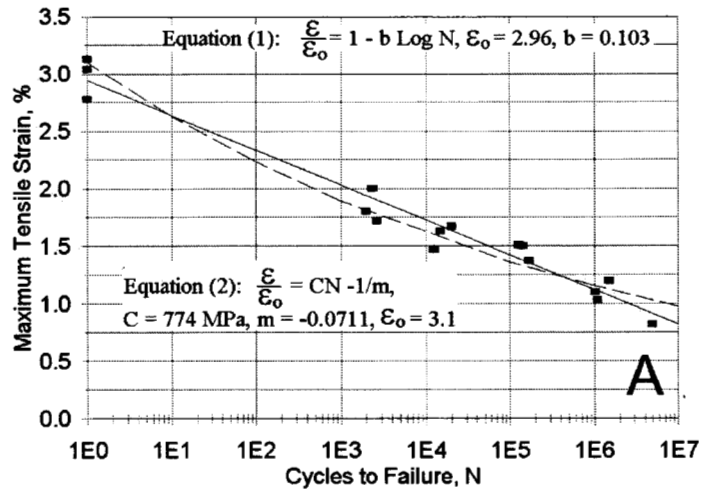
Figure 4. Tensile Fatigue (R=0.1) S-N curve for Material DD5, $(0/\pm 45/0)_S$, (a) Linear Strain versus Log N, (b) Linear Stress versus Log N and (c) Log Stress versus Log N.

where data are available has been uncertain. The best fit to those data for extrapolation purposes is explored in this report.

5. The choice of resin has not been found to influence the strength or fatigue resistance for laminates with a significant 0° fiber content. Polyesters, vinyl esters, and epoxies gave similar S-N results out to 10^6 cycles. The important role of the matrix in providing delamination and environmental resistance is explored in this report.

6. Goodman Diagrams (plots of alternating stress or strain versus mean values for particular number of cycles) for unidirectional material loaded in the longitudinal (0°) and transverse (90°) directions were generally nonsymmetrical about zero mean stress or strain. Longitudinal direction diagrams showed higher static and fatigue strength in tension than in compression. The transverse direction diagram was the opposite, much stronger in compression. Diagrams for both directions were provided out to 10^8 cycles without extrapolation, using specialized (small) high frequency test coupons. Additional Goodman diagrams are provided in this report.

The materials database represents a major step in the efficient design of blades. However, full scale tests conducted on blades usually show failure at static and fatigue strains far below database values. One source of error is that many structural failures involve buckling, which has also been addressed in detail at MSU as part of the DOE EPSCoR program [37, 46]. Other factors which result in structural failure below database values may include structural details, material flaws, and size effects. Many failures of composite material structures involve delamination failures due to thickness-direction stresses, particularly in load transfer areas in structural details such as ply drops, skin-stiffener intersections, root connections, etc.

A first attempt at addressing these concerns involved using selected database materials in substructural elements representative of blades. An I-beam test specimen was developed for static and fatigue testing under four-point bending. The beam was developed with detailed finite element analysis (FEA) in several iterations, until fatigue failures in load transfer areas were diminished, and most failures occurred in the flange and web areas. The methodology of using FEA with database properties was validated in the beam performance. Failure strains were in agreement with predictions from test coupons used in generating the database values. In all, tests of 52 beams were reported in Reference 3. As predicted, the mode of failure in fatigue switched from compression at low cycles/high stresses, to tension at higher cycles/lower stresses. Stiffnesses and strains were well-predicted by FEA using database properties. However, accurate prediction of web-flange delamination was not achieved for cases with poor load-transfer design, and the iterative design and testing process required in that study is prohibitive in full-scale blade design. Improved methodology for the prediction of delamination has been a focus of the substructure studies presented later in this report.

Other research reported in Reference 3 included a parametric study of ply-drop effects in regions of thickness tapering. Static and fatigue tests were run on a number of configurations involving position of plies dropped, number of plies dropped at a single point, and the optimum spacing of ply drops. Design recommendations were made for minimizing delamination at ply drops,

so that the potential strength of the laminate with tapered thickness could be realized.

A review of European experience in the area of fatigue of composites and structures for blade applications is provided in Reference 47.

PART A: MATERIALS STUDIES

3. SELECTION OF RESIN MATRIX FOR ENVIRONMENTAL RESISTANCE AND STRUCTURAL INTEGRITY

3.1. Summary

The DOE/MSU Fatigue Database has been expanded to include a number of matrix resins of potential interest in wind turbine blades. The main considerations in resin selection have been to increase the structural integrity (such as delamination resistance) in blades while maintaining or improving other mechanical properties, particularly under hot, wet conditions. The resins included in this phase of the study are also appropriate for the wind turbine blade application in terms of cost and processing characteristics (all materials were prepared by resin transfer molding). Resins included unsaturated polyesters, vinyl esters, epoxies, and a urethane. Mechanical properties have been obtained for wet and dry specimens tested at temperatures from -25 to 70°C. Fatigue, delamination resistance (Mode I and II crack growth), and performance in stiffened substructure sections have been evaluated for selected cases. Significantly improved performance relative to baseline polyester is shown for several resins and the baseline ortho-polyester is found to have inadequate resistance to hot/wet conditions for blade applications.

3.2. Introduction

Wind turbine blades should perform under a variety of loads and environmental conditions for a twenty to thirty year service life. Fiberglass blade materials derive much of their strength and stiffness from the fiber reinforcement. However, several key properties are dominated by the matrix resin, including compressive strength and resistance to delamination between plies. Delamination is a dominant failure mode in composite material structures, leading to the breakdown of structural integrity in areas such as the trailing edge, spars, and root connections. Experience in aerospace composites [48] indicates that the toughness of the matrix resin, as well as the design of details, controls interlaminar fracture resistance and structural performance, as well as facewise impact resistance. The low cost matrix resins (general purpose polyesters, vinyl esters, and epoxies) used in most turbine blades are relatively brittle, and so the delamination resistance of most blade materials is relatively low. Tougher versions of these and other resins are investigated in this study. A second type of resin, thermoplastics, also have high toughness, but their high viscosity limits their use in conventional blade manufacturing techniques. Tougher resins which bond well to the fiberglass also tend to give higher strengths in off-axis directions relative to the fiber reinforcement.

A second concern with matrix resins is that, if their elastic moduli are not high enough, they do not support the fibers adequately against compressive buckling. Thus, a softer matrix will produce a lower compression strength for loads along the fiber axis, usually the lengthwise direction of the blade. Compression strength and fatigue resistance are design drivers of primary importance. Typical

39

matrix resins used in blades, such as ortho polyesters, generally have adequate elastic modulus at moderate temperatures to provide good compressive strength. However, at elevated temperatures and with high moisture contents, these resins may not retain sufficient modulus (a neat resin modulus of around 3.0 GPa is usually adequate). Resins such as polyesters and epoxies will generally absorb several weight percent moisture, which swells and softens the polymer network (reversibly) and reduces the elastic modulus and glass transition temperature (T_g). Toughened resins can have reduced modulus relative to the base resin if toughness is achieved through the addition of low modulus materials like elastomers. Epoxies are usually the resin of choice for carbon fibers, with some use of vinyl esters; polyesters provide poor bonding to carbon fibers.

This phase of the study evaluated a number of base and toughened resin systems which are suitable for common blade manufacturing processes (including resin transfer molding (RTM), which requires a low resin viscosity). Resin cost was limited to about $6.50/kg to be competitive in blade applications, which eliminated many of the toughened aerospace resins. The main objective was to evaluate resins with improved toughness and temperature and moisture resistance as compared with common blade resins.

3.3. Experimental Methods

All materials were resin transfer molded in closed molds, including neat resin samples (without reinforcement), which were molded into their final dog-bone shape without machining. Types and sources of resins and reinforcement are listed in Table 1. Test methods for static and fatigue loading in tension and compression followed standard procedures described in detail in Reference 2.

Delamination resistance in Modes I and II used unidirectional 0° double cantilever beam (DCB) and end notched flexure test specimens [13, 49]. Test methods for delamination studies are described in a Chapter 9. These specimens used a teflon crack-starter strip embedded during fabrication as an initial crack. The Mode I fracture toughness, G_{IC}, was determined after a short increment of crack growth beyond the starter strip; this value is termed the initial G_{IC} to distinguish it from higher values, which result from fiber bridging as the crack grows longer. The Mode II value, G_{IIC}, was determined using the Mode I specimens after the crack was grown for several cm, with the specimen then loaded in three-point bending for Mode II. These methods are described in References 36 and 47. The structural integrity was evaluated with the T-section pull-off test shown in Figure 5 and described in detail in the substructures section of this report. The typical load-displacement curve in Figure 6 was used to determine the initial damage force, the maximum force, and the displacement at maximum force.

3.4. Results and Discussion

3.4.1. Matrix Resin Properties

Table 1 lists the resins studied, all of which are thermoset polymers. Further details of the resins and their processing can be found in Reference 36. Figure 7 gives prices quoted (spring 1999) for each resin in 208 liter drums for a total of 20,000 kilogram lots. Prices can vary significantly.

More costly resins with improved properties are also available, but were not included in this work.

Table 1. Materials Investigated.

MATRIX MATERIALS			
Resin	Description	Product Description	Supplier
Ortho-polyester	orthophthalic	63-AX-051	Interplastics Corporation
Iso-polyester	isophthalic	75-AQ-010	
PET Polyester	PET modified orthophthalic	PET P460	Alpha Owens Corning
Vinyl ester	rubber toughened	Swancorp 980	TECTRA Incorporated
Vinyl ester	unmodified	Derakane 411C-50	Dow Chemical
Vinyl ester	rubber toughened	Derakane 8084	
Epoxy	unmodified	System 41	System Three
Epoxy	acrylate modified	SC-12	Applied Poleramic Inc.
Epoxy	acrylate modified	SC-14	
Urethane	unmodified	Poly 15-D65	Polyteck Development
FIBER REINFORCING FABRICS			
E- glass Fabric	Type		Supplier
D155	Stitched unidirectional 0°		Owens Corning Fabrics
A130	Woven unidirectional 0°		
DB120	Bias, stitched ±45° Fabric		Owens Corning Fabrics

Figure 8 compares tensile stress-strain curves for several of the neat resins, and Table 2 lists their properties. Due to difficulty in preparing neat resin specimens, such as the urethane matrix, some resin properties are not included in Table 2. The target modulus of 3.0 GPa is not achieved by the 980 vinyl ester, SC-14 epoxy, or the urethane. The stress-strain curves for the more brittle resins such as unmodified polyesters and epoxies can vary significantly depending on sample molding and machining procedures. The yield strength is taken as the 0.2 percent offset yield strength where this could be determined. Table 2 gives heat deflection temperatures measured for each resin. This may be taken as an upper use limit.

The moisture absorption characteristics of several resins are shown in Figure 9 as weight gain in distilled water at 50°C versus square root of time in hours, following typical Fickian diffusion representation. As expected, the vinyl esters and the iso-polyester absorb much less moisture than the ortho-polyester and the epoxy. The composites (Figure 10) absorb less moisture, since the entire composite is not resin, but the ordering of the materials according to weight gain is consistent with the neat resin data.
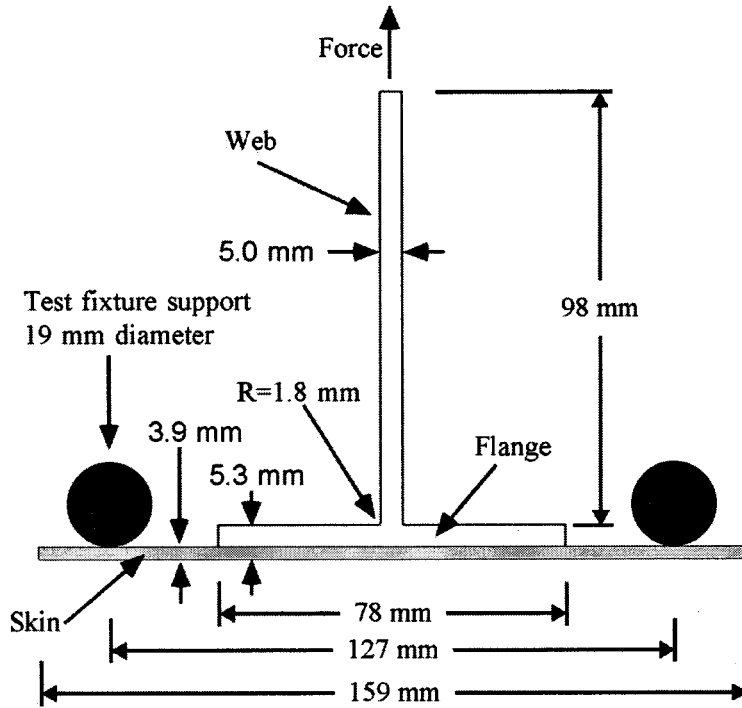
Figure 5. Loading and Approximate Dimensions for Skin-Stiffener T-Specimens.
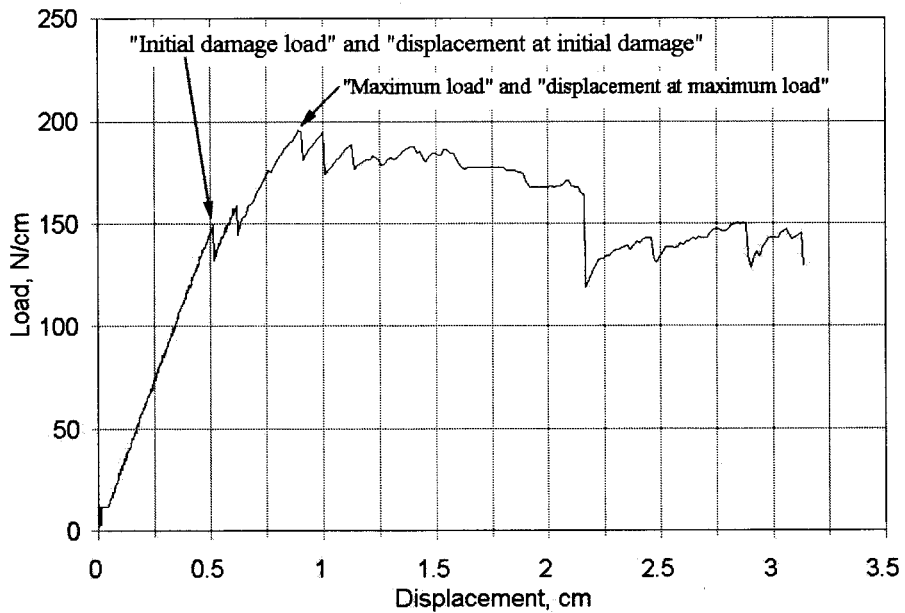
Figure 6. Typical Load-Displacement Curve for a Skin-Stiffener T-Specimen (Displacement is the position of the load point relative to the lower supports in Figure 5).
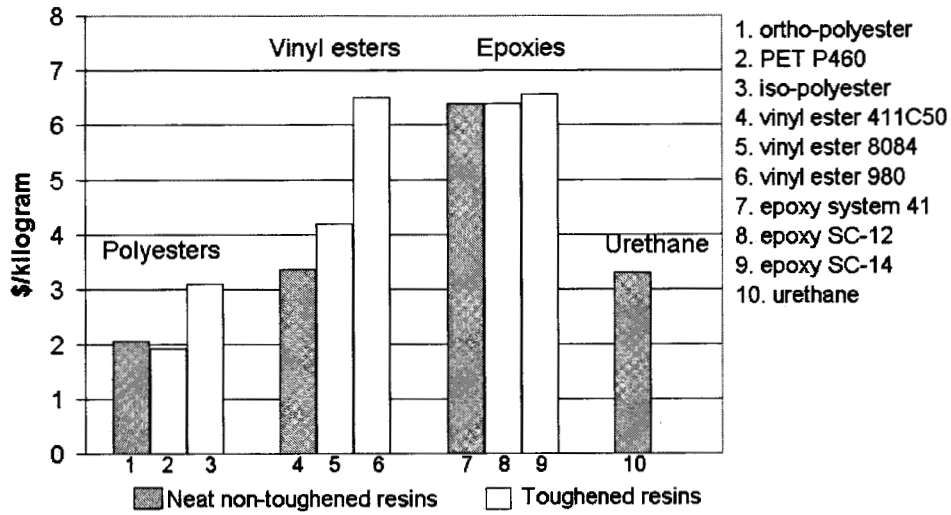
Figure 7. Price Comparison for Different Resins (20,000 kilogram base estimation).
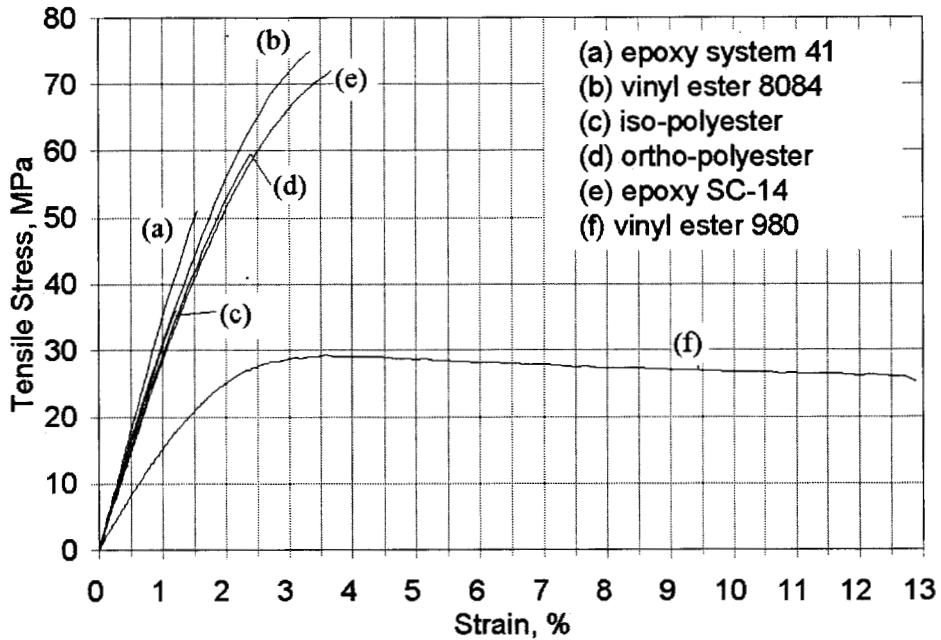
Figure 8. Typical Stress-Strain Curves for Neat Resins.

Table 2. Average Tensile and Thermal Properties of Neat Resins.

Resin	UTS, MPa	0.2% Offset Yield Strength, MPa	Modulus, GPa	Failure Strain, %	Heat Deflection Temperature, °C
Ortho-polyester	54.1 (4.6)[1]	45.2 (2.5)	3.18 (0.12)	2.0 (0.3)	55 (0.9)
Iso-polyester	34.6 (2.8)	----	3.32 (0.14)	1.2 (0.2)	69 (1.2)
Vinyl ester 980	25.7 (0.3)	20.6 (0.5)	1.63 (0.02)	30 (15)	60 (1.7)
Vinyl ester 411C50	57.7 (0.8)	50.4 (2.5)	3.21 (0.04)	2.1 (0.1)	78 (3.7)
Vinyl ester 8084	72.6 (2.7)	55.2 (2.4)	3.25 (0.15)	3.0 (0.3)	75 (1.4)
Epoxy System 41	52.6 (1.1)	52.6 (1.1)	3.56 (0.06)	1.6 (0.1)	56 (3.6)
Epoxy SC-12	44.3 (3.1)	----	3.48 (0.04)	1.4 (0.1)	95 (1.2)
Epoxy SC-14	68.3 (2.7)	48.5 (1.3)	2.80 (0.03)	3.3 (0.3)	83 (1.9)

[1] Numbers in parentheses indicate the sample standard deviation.
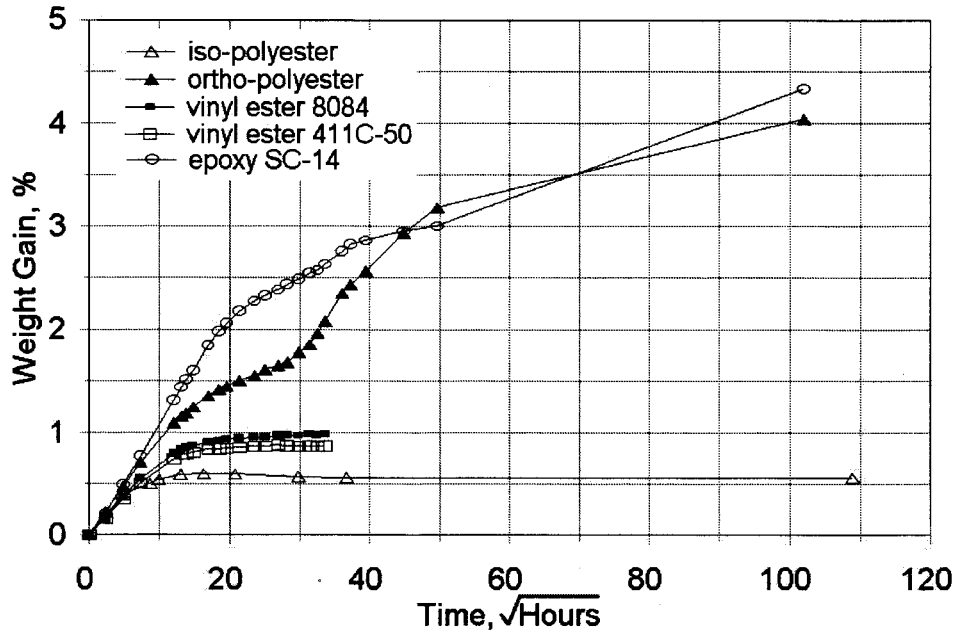
Figure 9. Water Absorption for Neat Resin in Distilled Water at 50°C.
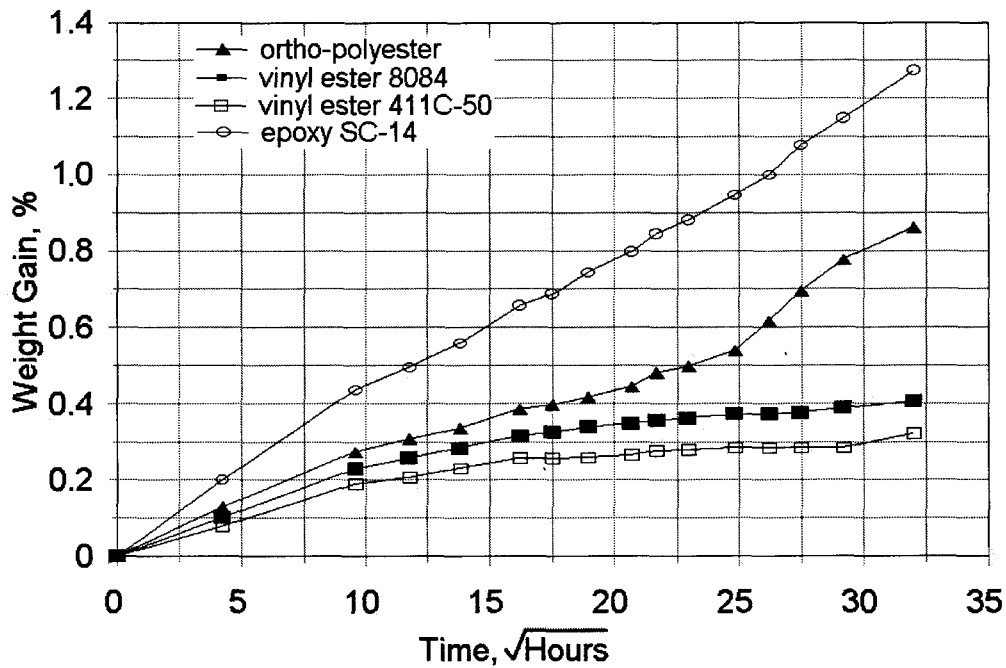
Figure 10. Water Absorption at 50°C in Distilled Water for $[0/\pm45/0]_S$
Composites with an Initial Fiber Volume Fraction of 0.37.

3.4.2. Interlaminar Fracture Toughness

Figures 11 and 12 summarize the Mode I and Mode II interlaminar fracture toughness, respectively, for selected resin systems. Additional data are given in Reference 36. The baseline ortho-polyester has a very low G_{IC}, typical of the lowest cost polyesters, vinyl esters and epoxies. The other matrices have significantly higher Mode I toughness. All systems have increased Mode I toughness at 50°C wet conditions due to increased fiber debonding and fiber bridging, as found in other composites [50]. The Mode II toughness in Figure 12 tends to correlate more closely with the T-stiffener test, described below. The toughened vinyl ester and epoxy SC14 show the highest G_{IIC} values at room temperature, dry, but the epoxy loses Mode II toughness at elevated temperature, particularly when conditioned and tested wet. The iso-polyester has higher G_{IIC} than the ortho-polyester, particularly at elevated temperatures. The two vinyl esters show very good toughness under all conditions. While the vinyl ester and epoxy toughness values are slightly lower at -20°C than at room temperature, the differences do not indicate any ductile-brittle transitions in this temperature range.

45
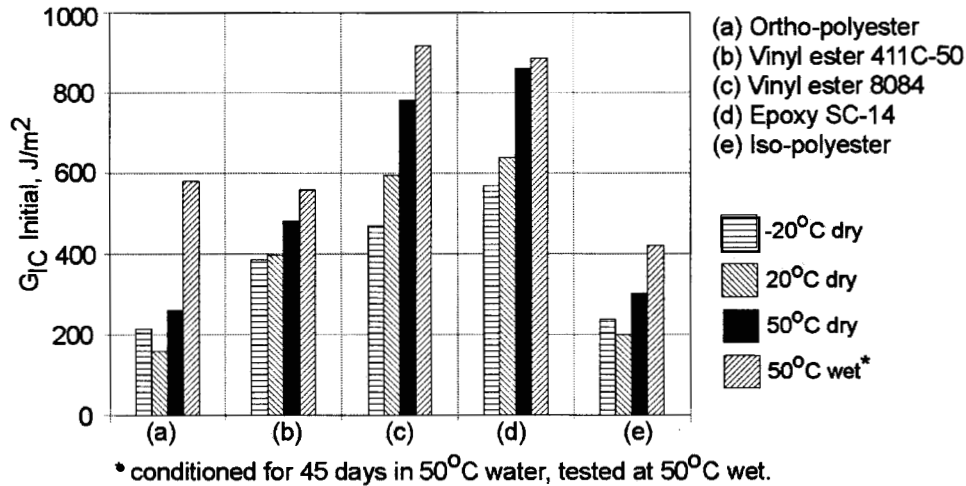
Figure 11. Effect of Matrix on the Initial Mode I Interlaminar Fracture Toughness (0 degree D155 fabric, $V_F = 0.36$).
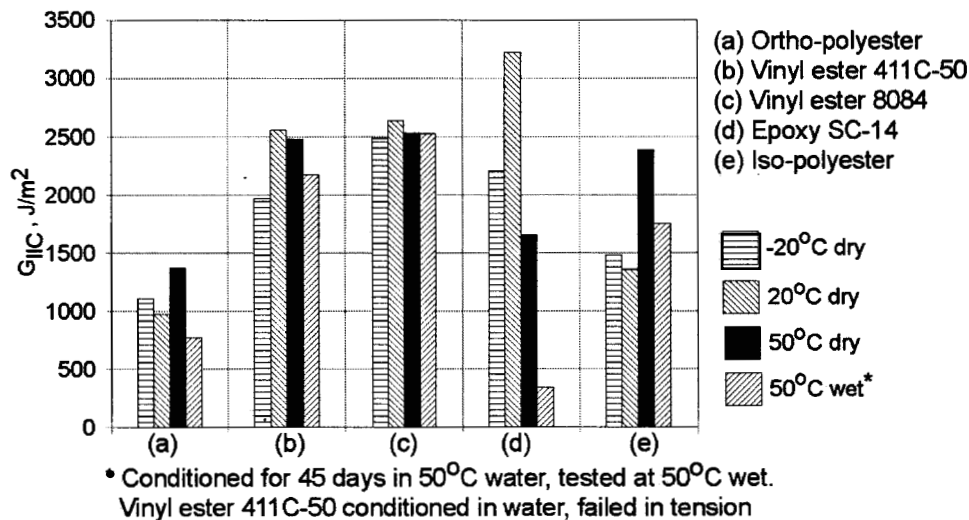
Figure 12. Effect of Matrix on the Mode II Interlaminar Fracture Toughness (0 degree D155 fabric, $V_F = 0.36$).

3.4.3. T-Stiffener Pull-off

Figure 13 shows typical T-stiffener pull-off specimens after testing; the test configuration is described in Chapter 12. These specimens show the usual delamination-dominated fracture mode, simulating separation of the skin-spar interface area of blades. The damage has been modeled in detail and associated with the basic G_{IC} and G_{IIC} results in Chapter 12. Figure 14 compares several load-displacement curves from the pull-off tests, and Table 3 lists results for seven resin systems. The tougher resin systems produce increased stiffener pull-off resistance, as expected. Since slight thickness differences can affect this test significantly [13], the results should be viewed in terms of

46
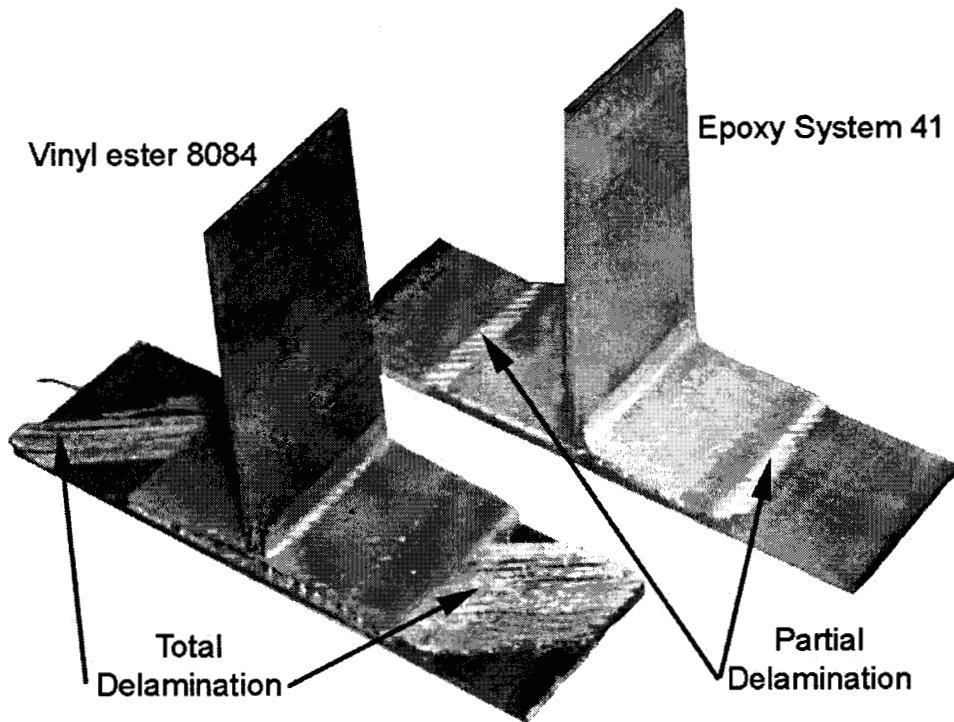
Figure 13. T-Stiffener Pull Off Specimens of Vinyl Ester 8084 and Epoxy System 41, Showing Delamination Damage.

1 - 63-AX-051 polyester
2 - System 41 epoxy
3 - SC-14 epoxy
4 - 8084 vinyl ester
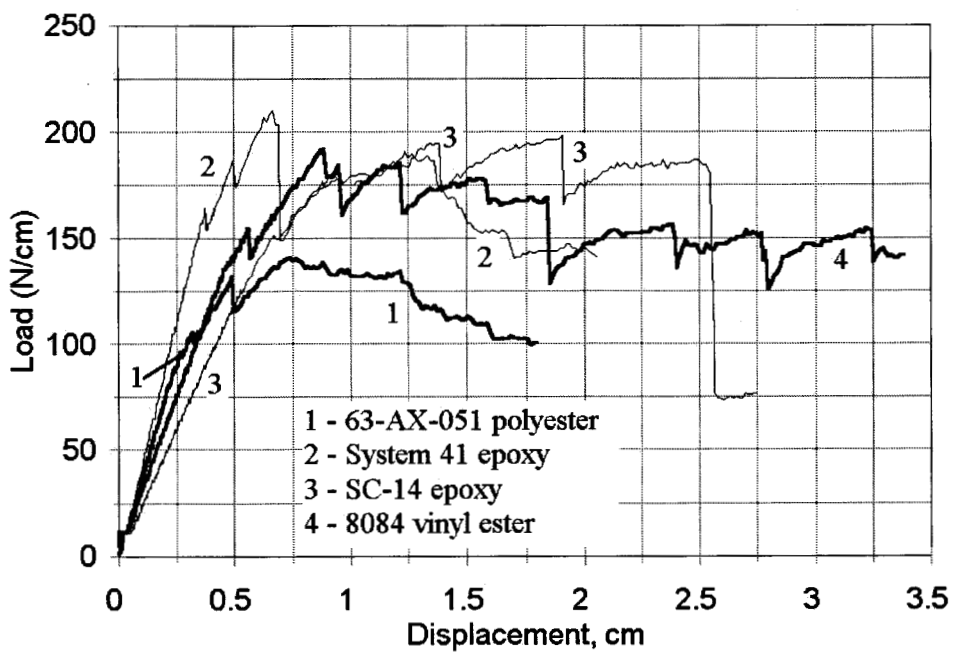
Figure 14. Typical Load-Displacement Curves for T-Specimens.

Table 3. Effects of Matrix on T-Stiffener Pull-off Resistance (average values).

Resin (See Table 1)	Initial Damage Load, N/cm[1]	Maximum Load, N/cm	Displacement at Maximum Load, mm	Specimens Tested
Ortho-polyester	87 (6)[2]	135 (6)	6.8 (0.6)	3
PET polyester	120	164	8.4	1
vinyl ester 980	119 (9)	182 (6)	13.5 (1.8)	4
vinyl ester 8084	144	194	9.0	2
epoxy System 41	168	209	6.7	2
epoxy SC-14	132	192	19.1	2
urethane	141	262	11.6	1

[1] N per cm of T-specimen width,

[2] Numbers in parentheses indicate the sample standard deviation.

both the force levels and the displacement, with higher values of both indicating greater structural integrity. The System 41 epoxy (untoughened) is particularly interesting, since it shows high T-stiffener pull-off resistance. The average G_{IC} value for this resin was 231 J/m^2, lower than most other resins (Figure 11), while the average G_{IIC} was 3776 J/m^2, among the highest measured at room temperature (Figure 12). The ortho-polyester system, low in both G_{IC} and G_{IIC} (Figures 11 and 12), produced the poorest pull-off resistance. Thus, the T-stiffener resistance appears to correlate better with G_{IIC} than with G_{IC}.

3.4.4. Composite Strength and Modulus versus Temperature and Moisture Condition

Figures 15 through 21 give basic composite mechanical properties for composites fabricated with five of the more interesting resins as a function of temperature, both for dry (ambient) conditioned specimens and for specimens conditioned for approximately 45 days in 50°C distilled water. The laminates were either $[0/\pm45/0]_s$ tested at 0° or 90° or $[(\pm45)_3]$ tested at 0° as indicated.

Figure 15 gives the most critical matrix sensitive property: compression strength in the 0° direction. The compression strength decreases moderately for dry specimens up to 70°C, with the greatest decrease shown in the ortho polyester. The wet conditioned and tested specimens show even greater decreases, particularly the ortho-polyester and the epoxy (which also absorbs the most moisture, Figure 9). The iso-polyester and both vinyl esters are much less sensitive to moisture. The sensitivity of the ortho polyester composite to moisture at elevated temperature for longer times is even more significant, as shown in Table 4, with reductions of 26 percent and 30 percent under hot-wet conditions for composites based on D155 and A130 0° fabrics, respectively. These are very

serious decreases, particularly for the A130 fabric, whose woven architecture gives a low baseline compressive strength. This demonstrates that the effects of weave and environment on compressive strength are additive.

Tension properties in the 0° direction are fiber dominated, and are not much affected by temperature and moisture (Figures 16 and 17). The same laminate tested in tension in the 90° direction is more matrix sensitive, showing decreases in modulus which parallel the compressive strength (Figure 18); 90° tensile strength (Figure 19) is surprisingly insensitive. The ±45° laminates tested in tension in the 0° direction are also matrix dominated, giving significant temperature and moisture sensitivity (Figures 20 and 21).

The fatigue sensitivity has been found to be matrix insensitive in earlier results [2]. Figures 22 and 23 compare the baseline ortho-polyester with the two Derakane vinyl esters under tensile, compressive, and reversed loading, $R = 0.1$, 10, and -1, where R is the ratio of minimum to maximum stress in each cycle. These tests were run under ambient conditions. Again, there is no significant improvement in room temperature fatigue resistance, even for the toughened vinyl ester 8084.
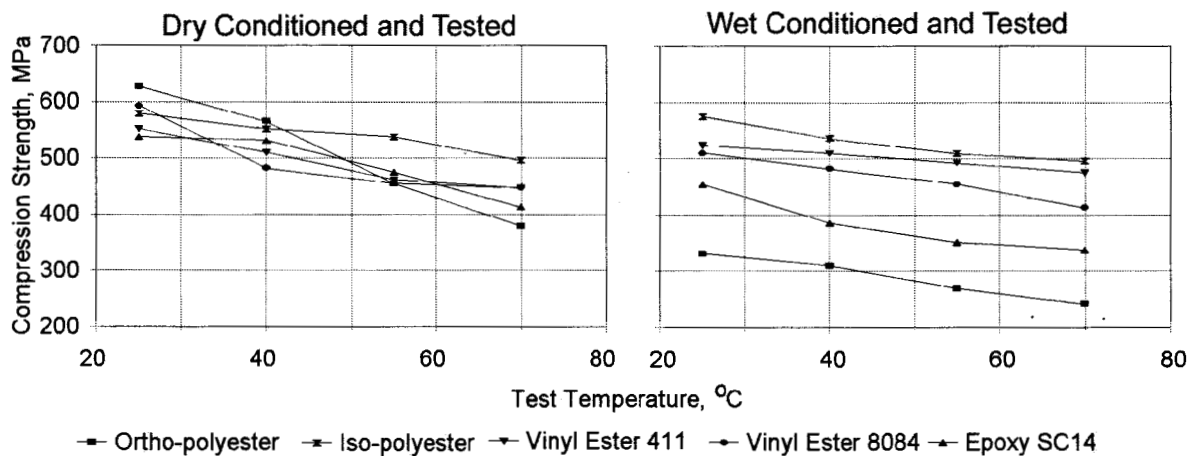
Figure 15. Compression Strength in the 0° Direction versus Test Temperature, Dry and Wet, $[0/\pm45/0]_S$ Laminates.
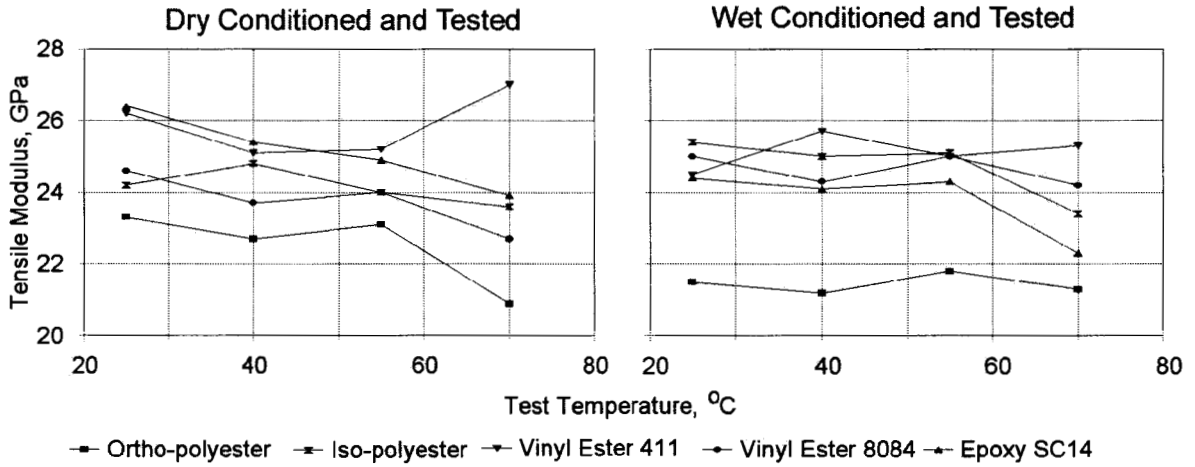
Figure 16. Tensile Modulus in the 0° Direction versus Test Temperature, Dry and Wet, [0/±45/0]$_S$ Laminates.
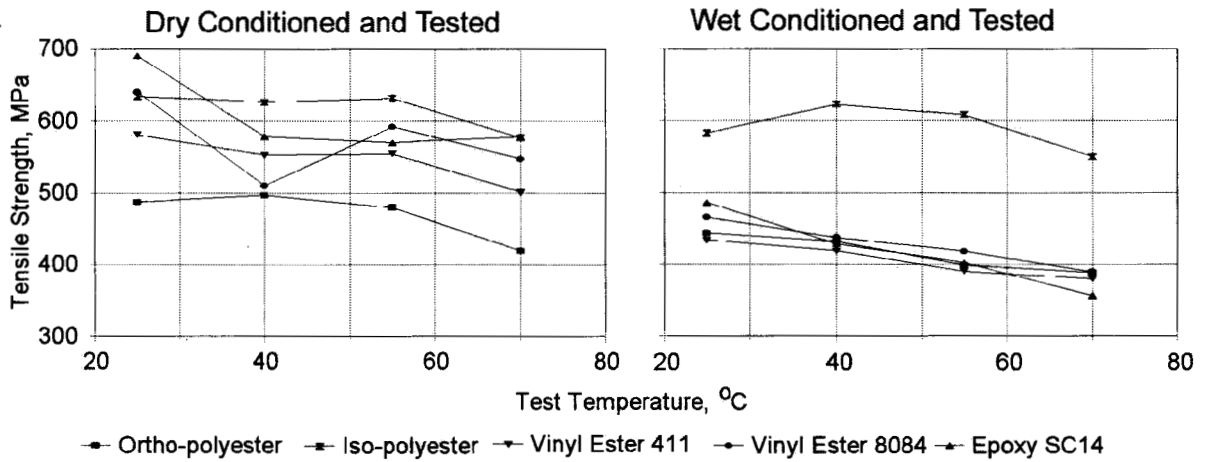
Figure 17. Tensile Strength in the 0° Direction versus Test Temperature, Dry and Wet, [0/±45/0]$_S$ Laminates.
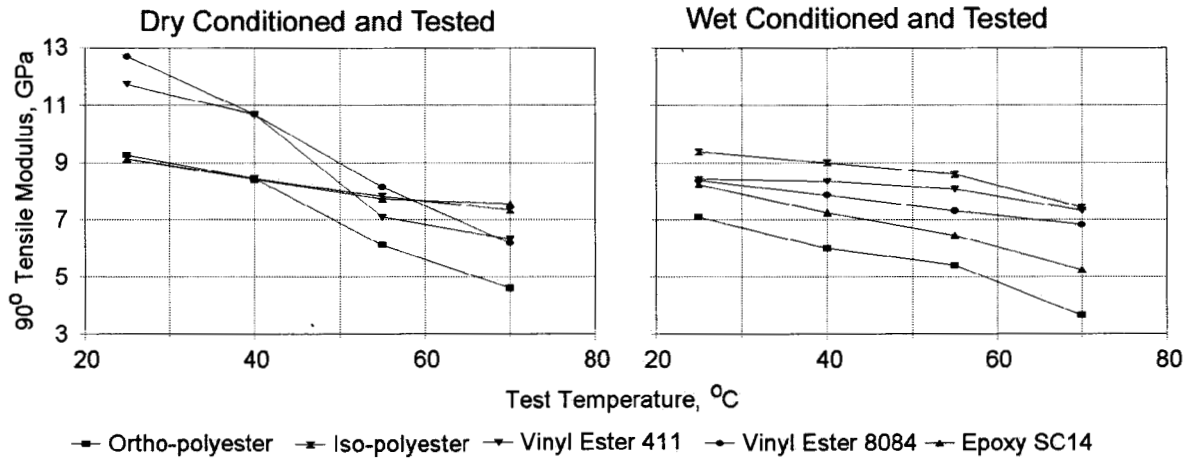
Figure 18. Tensile Modulus in the 90° Direction versus Test Temperature, Dry and Wet, $[0/\pm45/0]_S$ Laminates.
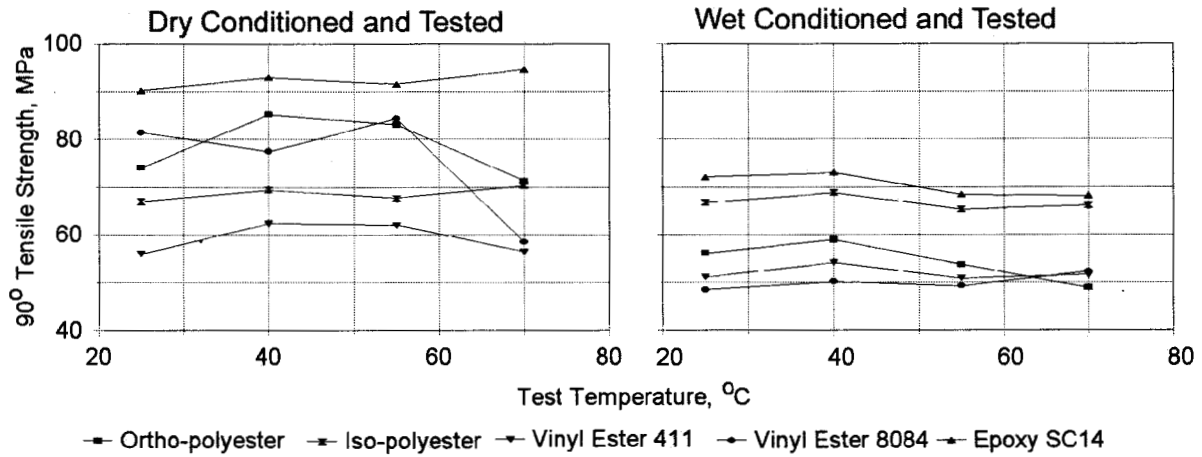
Figure 19. Tensile Strength in the 90° Direction versus Test Temperature, Dry and Wet, $[0/\pm45/0]_S$ Laminates.

Dry Conditioned and Tested

Wet Conditioned and Tested

‐•‐ Ortho-polyester   ‐✻‐ Iso-polyester   ‐▼‐ Vinyl Ester 411   ‐•‐ Vinyl Ester 8084 ‐▲‐ Epoxy SC14
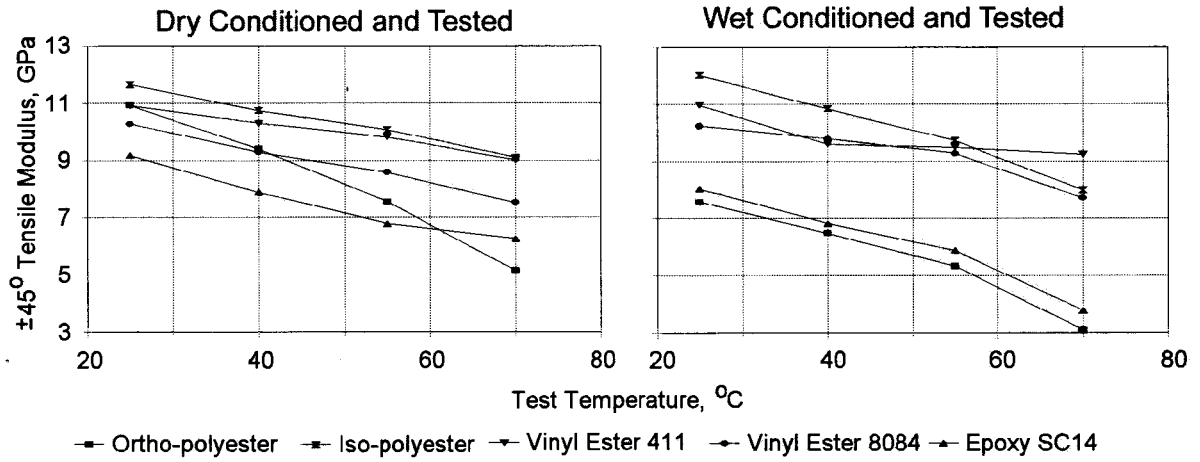
Figure 20. Tensile Modulus in the 0° Direction versus Test Temperature, Dry and Wet, [(±45°)₃] Laminates.

Dry Conditioned and Tested

Wet Conditioned and Tested

‐•‐ Ortho-polyester   ‐✻‐ Iso-polyester   ‐▼‐ Vinyl Ester 411   ‐•‐ Vinyl Ester 8084 ‐▲‐ Epoxy SC14
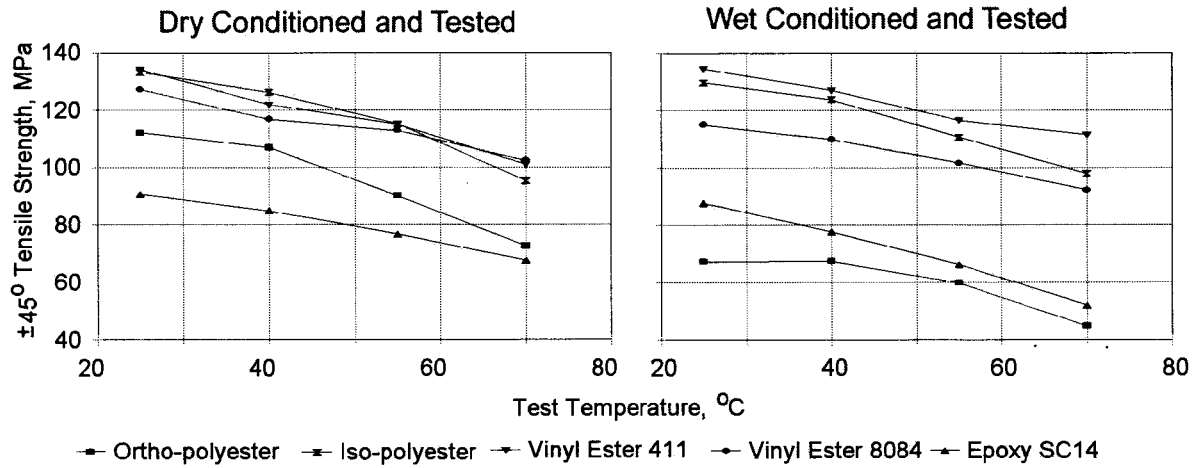
Figure 21. Tensile Strength in the 0° Direction versus Test Temperature, Dry and Wet, [(±45°)₃] Laminates.

Table 4. Effect of Moisture Exposure and Elevated temperature Testing on Compressive Strength of $(0/\pm45/0)_S$ Laminates. Distilled Water Conditioning at 40°C for the First 5000 Hours, Followed by 20°C Conditioning. (Ortho-polyester, D155 and A130 0° Fabrics, $V_F = 0.36$).

Exposure Time, hours	Test Temperature, °C	Average Weight Gain (S.D.), %		D155 Ave. strength (S.D.), MPa	% Change	A130 Ave. strength (S.D.), MPa	% Change
		D155	A130				
0	20	0	0	517 (39)	--	265 (39)	--
0	50	0	0	472 (57)	-9.5	250 (17)	-5.7
24	20	0.20 (0.01)	0.29 (0.03)	516 (19)	-0.3	262 (55)	-0.8
144	20	0.47 (0.01)	0.54 (0.02)	481 (30)	-6.9	287 (27)	8.4
1,315	20	0.61 (0.06)	0.73 (0.04)	471 (35)	-9.0	219 (26)	-17
4,650	20	0.62 (0.11)	0.64 (0.08)	421 (31)	-19	240 (17)	-9.3
4,650	50	0.62	0.64	403 (30)	-15	174 (32)	-30
15,355	20	0.94 (0.25)	1.02 (0.05)	404 (31)	-22	203 (28)	-23
15,355	50	0.99 (0.22)	0.99 (0.04)	348 (34)	-26	175 (40)	-30
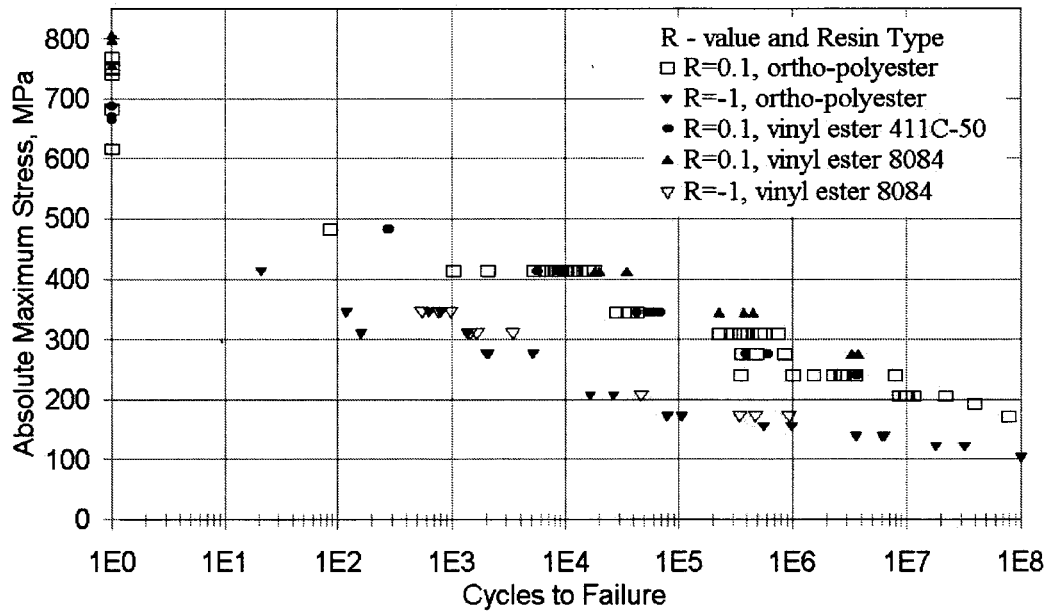
Figure 22. Effect of Matrix on 20°C Dry Fatigue Resistance in the 0° Direction Under Tensile (R=0.1) and Reversed Loading (R = -1); [0/±45/0]$_S$ Laminates, V$_F$ = 0.34 - 0.36.
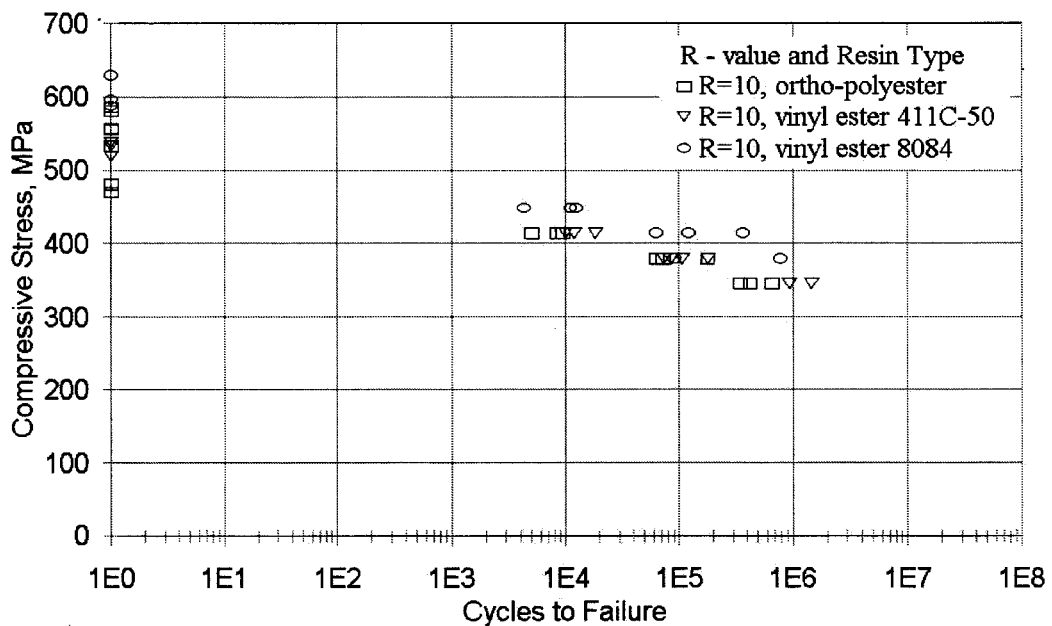
Figure 23. Effect of Matrix on 20°C Dry Fatigue Resistance in the 0° Direction Under Compression (R=10) [0/±45/0]$_S$ Laminates, V$_F$ = 0.34 - 0.36.

3.4.5. Fatigue Resistance Under Hot-Wet Conditions

<u>3.4.5.1. Materials and Testing</u>

Test coupons utilizing a $(0/\pm45/0)_S$ lay-up (D155 0's and DB120 45's) and $V_F = 0.36$ were manufactured using four different resin systems. The resin systems included CoRezyn 63-AX-051 orthothalic polyester, CoRezyn 75-AQ-010 isothalic polyester, Derakane 411C-50 vinyl ester and Derakane 8084 vinyl ester. Coupons were conditioned and placed in distilled water at 50 °C for 2200 hours and then at 20 °C until tested. The final fatigue test was completed approximately 7000 hours after first immersion. The temperature was lowered to 20°C after 2200 hours to equalize the through-thickness moisture content, while obtaining a high enough moisture content in a reasonable amount of time. The 50°C maximum soaking temperature was determined from prior tests, which at 60 °C showed extraction of material from the ortho polyester resin system.

Compression coupons were tested without any additional tab material, which is consistent with the other tests in the database. This also avoids environmental problems with tab adhesives. Tensile coupons were dogboned and tested with and without additional tab materials (ortho polyester only). No significant difference in properties or failure modes were seen in these tensile tests (with versus without tabs). Wet coupons were stored in water until tested to prevent drying. Wet and dry control coupons (four each per resin and condition) were routinely weighed to determine moisture absorption. The dry control coupons did not change weight significantly (±0.03 percent).

A temperature chamber was constructed inexpensively from plywood which encased the hydraulic grip assemblies and the coupon area. Two separate 1200 W elements with 5 m^3/minute blowers (100 percent regenerative) supplied the heat. This approach eliminated any grip thermal sinks and allowed for a large range of testing gage lengths. At 50 °C, the temperature control was ±1 °C. Temperature control was maintained by a thermocouple placed on or within 1 mm of the test coupon gage surface. With wet specimens the thermocouple was in contact with a plastic bag enclosing the specimen during the test. For the 50 °C tests, the coupons were placed in the oven for 10 - 15 minutes before testing was started.

Tensile (R = 0.1) and compressive (R = 10) constant amplitude fatigue tests were performed on the ortho-polyester coupons. The remaining resin systems were only tested in compression. Coupons were tested under an air temperature of 20 °C (lab air temperature ±3°C) and 50 ±1 °C in both a "dry" and "wet" condition. The wet coupons were sealed in a plastic bag containing a water soaked fabric to prevent drying. Since the compressive gage length was 13 mm, a thin sheet of plastic encased the water soaked fabric and was sealed/attached to the composite gage section with a thin rubber O-ring assembly and super glue. This reduced the amount of water contact with the hydraulic wedge gripping surfaces, which oxidized under these conditions.

<u>3.4.5.2. Results and Discussion</u>

Tables 5 through 8 and Figures 24 to 29 give the results of these tests. All systems showed some decrease in compressive static and fatigue strength at 50 °C both dry and wet. The fatigue data

were fit to Equation (1), where b is listed as b_c for compression. The decrease in fatigue resistance was very significant for the ortho-polyester system, but minor for the remaining matrix systems. Average moisture contents are given at the bottom of each table. Only the polyester, with the largest moisture gain and lowest heat distortion temperature (Table 2) showed a significant drop in static and fatigue strength when tested at 20 °C wet. Tensile fatigue resistance for this environmentally sensitive matrix system, ortho polyester, was not significantly affected by the 50 °C condition, dry or wet, and so tensile fatigue was not tested for the other matrix systems.

The results for this independent series of tests are consistent with the static strength results given earlier in this Chapter. Those materials were loaded in the 0° direction for the $[0/\pm45/0]_s$ laminates, so the tensile properties were fiber dominated and unaffected by the environment. Compressive properties are matrix dominated, and showed the expected level of sensitivity to hot/wet conditions, based on earlier data. The ortho-polyester system not only decreased in compressive static strength with higher moisture and/or temperature, but the slope of the S-N curve also increased significantly when normalized by the static strength. The strain for 10^6 cycles under 50 °C/wet conditions is 0.69 percent, compared with the dry 20 °C 10^6 cycle strain of 1.3 percent, a reduction of 47 percent in strain capability due to environmental effects.

Table 5. Summary of Compressive Fatigue Data for Material DD5P, $(0/\pm45/0)_s$, $V_F = 0.36$, CoRezyn 63-AX-051 Ortho Polyester Resin.

	UCS, MPa	b_c*	10^6 strain, %	E, GPa
20 °C Dry	-607	0.080	-1.30	23.6
50 °C Dry	-499	0.102	-0.90	21.8
20 °C Wet	-533	0.089	-1.17	21.3
50 °C Wet	-398	0.107	-0.69	20.9

* S/So = 1 - b_c Log N; Wet coupons had a moisture content of 1.0 percent.

Table 6. Summary of Compressive Fatigue Data for Material DD5P2, $(0/\pm45/0)_s$, $V_F = 0.36$, CoRezyn 75-AQ-010 Iso Polyester Resin.

	UCS, MPa	b_c*	10^6 strain, %	E, GPa
20 °C Dry	-611	0.067	1.56	
50 °C Dry	-526	----	----	23.5
20 °C Wet	-586	0.069	1.45	
50 °C Wet	-546	0.081	1.18	

*S/So = 1 - b_c Log N; Wet coupons had a moisture content of 0.55 percent.

Table 7 Summary of Compressive Fatigue Data for Material DD5V, $(0/\pm45/0)_S$, $V_F = 0.36$, Derakane 411C-50 Vinyl Ester Resin.

	UCS, MPa	b_C*	10^6 strain, %	E, GPa
20 °C Dry	-562	0.066	-1.44	
50 °C Dry	-500	----	----	23.5
20 °C Wet	-571	0.066	-1.47	
50 °C Wet	-507	0.067	-1.29	

*$S/So = 1 - b_C$ Log N; Wet coupons had a moisture content of 0.52 percent.

Table 8. Summary of Compressive Fatigue Data for Material DD5V2, $(0/\pm45/0)_S$, $V_F = 0.36$, Derakane 8084 Vinyl Ester Resin.

	UCS, MPa	b_C*	10^6 strain, %	E, GPa
20 °C Dry	-548	0.065	-1.41	
50 °C Dry	-502	----	----	23.5
20 °C Wet	-564	0.077	-1.28	
50 °C Wet	-506	0.077	-1.13	

*$S/So = 1 - b_C$ Log N; Wet coupons had a moisture content of 0.56 percent.
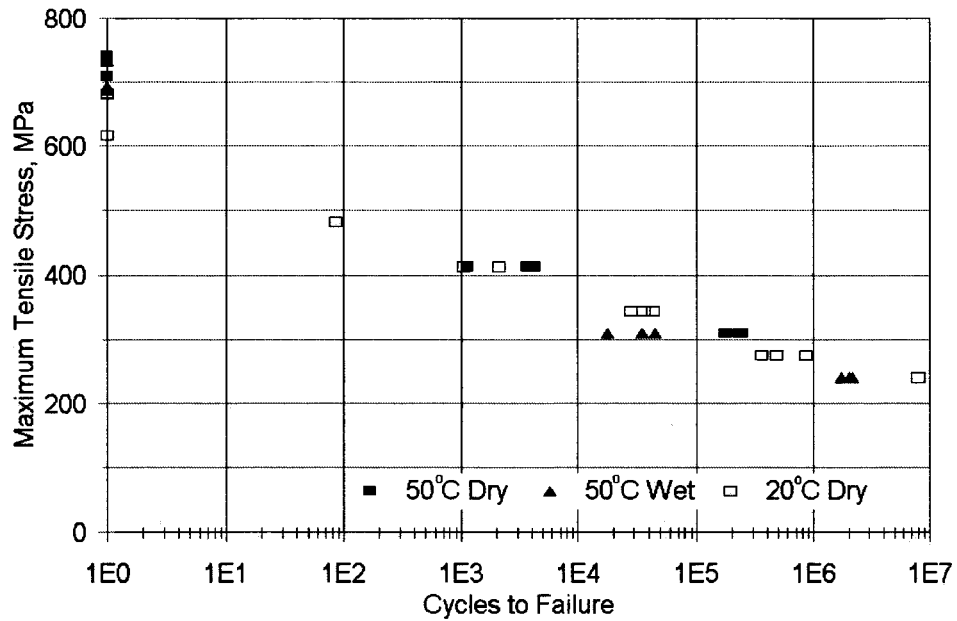
Figure 24. Ortho-polyester Resin, Tensile Fatigue Data for Dry and Moisture Conditioned (wet) Coupons at 20 and 50°C. Material DD5P, $(0/\pm45/0)_S, V_F = 0.36$, R = 0.1, wet coupons averaged 1.0 percent moisture content.
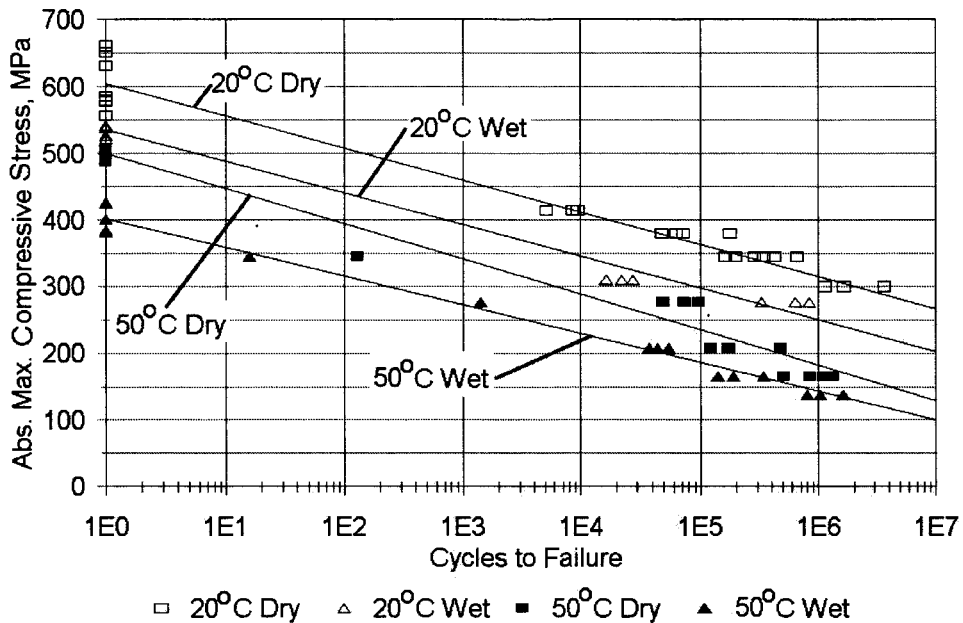
Figure 25. Ortho-polyester Resin, Compression Fatigue Data for Dry and Moisture Conditioned (wet) Coupons at 20 and 50°C. Material DD5P, $(0/\pm45/0)_S$, $V_F = 0.36$, R = 10, wet coupons averaged 1.0 percent moisture content.

58
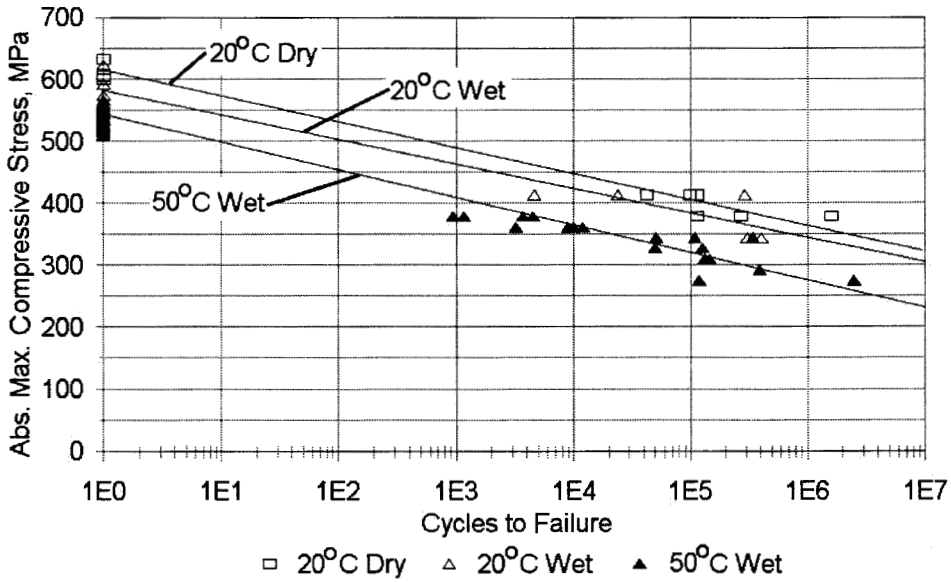
Figure 26. Iso-polyester Resin, Compression Fatigue Data for Dry and Moisture Conditioned (wet) Coupons at 20 and 50°C. Material DD5P2, $(0/\pm45/0)_S$, $V_F = 0.36$, $R = 10$, wet coupons averaged 0.55 percent moisture content.
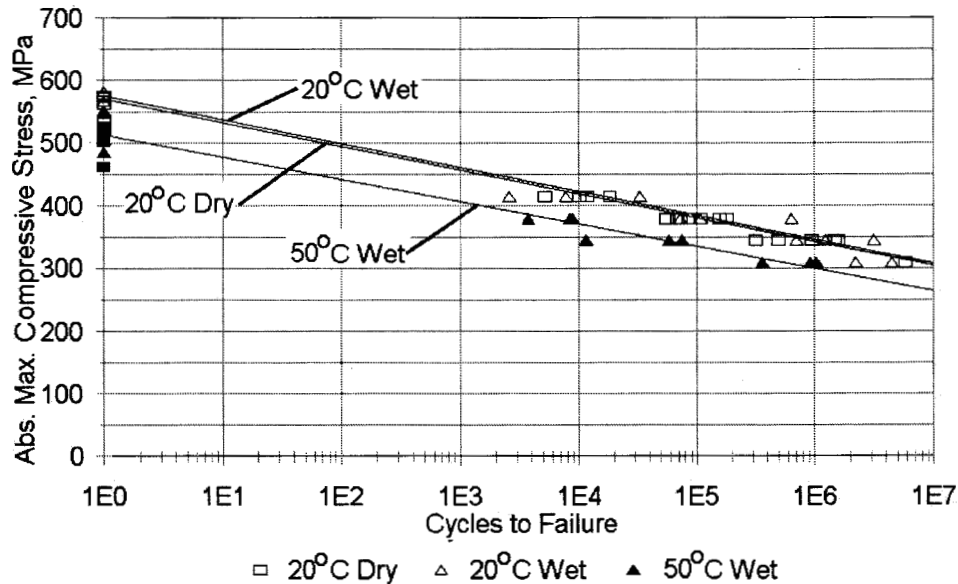
Figure 27. Derakane 411C-50 Vinyl Ester Resin, Compression Fatigue Data for Dry and Moisture Conditioned (wet) Coupons at 20 and 50°C. Material DD5V, $(0/\pm45/0)_S$, $V_F = 0.36$, $R = 10$, wet coupons averaged 0.52 percent moisture content.

59
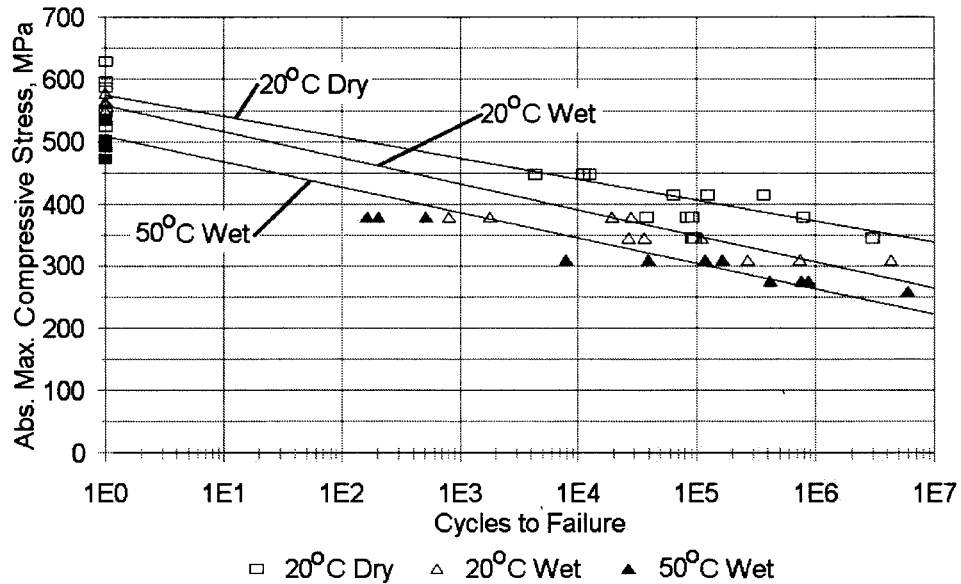
Figure 28. Derakane 8084 Vinyl Ester Resin, Compression Fatigue Data for Dry and Moisture Conditioned (wet) Coupons at 20 and 50°C. Material DD5V2, $(0/\pm45/0)_S$, $V_F = 0.36$, R = 10, wet coupons averaged 0.56 percent moisture content.
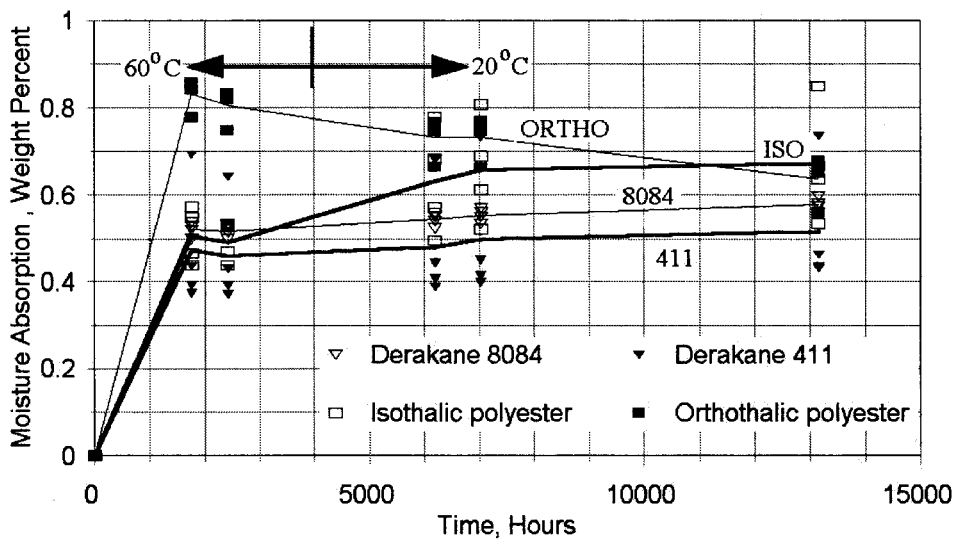
Figure 29. Moisture Absorption versus Coupon Soaking Time in Distilled Water at 60 and 20 °C.

60

3.5. Conclusions

More ductile resin systems produce improved structural integrity at moderate cost. The hot/wet properties are much better for the iso-polyester and vinyl ester systems than for the ortho-polyester or the epoxy SC14, again for moderate cost increases over the ortho-polyester. Thus, while the iso-polyester provides improved environmental resistance over the ortho-polyester for a small increase in cost, the 411 and 8084 vinyl esters additionally provide much greater toughness and structural integrity for a slightly greater cost increase. The independent series of tests for hot/wet fatigue showed static results which were consistent with the earlier series. Again, the ortho polyester matrix was very moisture/temperature sensitive, and, furthermore, the compressive fatigue S-N curve slope increased with hot/wet conditions. The overall knockdowns in properties for the ortho-polyester under realistic conditions indicate that it is not appropriate for most blade applications. The iso-polyester is suggested as the minimum acceptable resin matrix.

4. SELECTION OF E-GLASS REINFORCING FABRICS

4.1. Summary

The static and fatigue properties of typical wind turbine blade composite materials depend strongly on the architecture of the reinforcing fabric (woven, stitched, etc.) as well as the overall fiber type (glass versus carbon), content and orientation. Fabric architecture also has a strong influence on resin flow characteristics during manufacturing and on the sensitivity of the properties to structural detail geometry. The DOE/MSU Fatigue Database contains data on many commercially available reinforcing fabrics tested in a variety of laminate configurations under several loading conditions. Two factors of concern are the low compressive strength of woven fabrics, and a transition to poor tensile fatigue resistance at high fiber content, which can plague all stranded fabrics under some conditions. Furthermore, the unidirectional stitched fabrics, which have shown the best overall performance, are not generally available in the long, or warp direction of the fabric roll except when stitched to additional layers such as mat, which significantly reduces the tensile fatigue resistance. Thus, the best performing stranded fabric cannot be used for the main lengthwise reinforcement in the blade. This chapter presents a summary of the merits of several widely used fabrics as well as results for several new fabric types including bonded fabrics which show potential for improved performance. The results include an assessment of manufacturability and performance in structural details. The final section deals with European fabrics having large 0° tows stitched to a woven fabric, with disappointing tensile fatigue resistance as well. Tests on evolving large tow carbon reinforcements are reported in Chapter 10. The effects of fabric on simulated flaws and structural details is addressed in a Chapter 8.

4.2. Introduction

The selection of reinforcing fabrics for wind turbine blades has historically focused on the materials used in the marine industry. These have been chosen for ease in handling during hand layup fabrication as well as for cost considerations. Extensive testing of various materials as part of the DOE/MSU fatigue database [2] has led to recognition of the significance of fabric architecture to tensile fatigue properties. Convenient "triax" fabrics, with 0°and ±45° layers stitched together, perform poorly compared with laminates having separate 0° and ±45° layers [2].

Testing a broad range of laminates with separate 0° and ±45° layers has indicated additional problems. First, all of the fabrics with clearly delineated strands tend to show poor fatigue resistance if the overall fiber content is moderate to high, with transitions to poor fatigue resistance in the range of 40 to 50 percent fiber by volume (Figures 1, 2 and 3). The fiber content, V_f, where the transition occurs depends on the fabric architecture and the laminate construction, the latter primarily reflecting the percentage of fibers in the main load (0°) direction [2, 8]. A second problem is that most fabrics with unidirectional strands in the long, or warp direction (0°) of the fabric roll, use a woven architecture, causing strand distortion in the thickness direction. This significantly reduces the compressive strength for all known weave patterns when compared with fabrics which have straight strands, usually stitched together [2, 8]. The third problem, discussed in Chapter 8, is that those

stitched fabrics with straight, tight strands tend to lose their superior performance when structural details, such as ply drops, locally crowd the strands together. Thus, a blade fabricated by hand layup at a low fiber content, such as 35 to 40 percent fibers by volume, may show poor tensile fatigue resistance (high knock-down factors in design) if features such as ply drops or stiffeners are molded into the laminate [14].

Fabric selection must also involve manufacturability of the material. Hand layup manufacturing is relatively insensitive to the details of fabric architecture, with the main considerations being the thickness of material which can be added at each step, wet-out rate, and the handlability of the fabric. Resin transfer and resin infusion processes are enhanced by fabrics with high permeability, which is increased by tight strands with spaces for resin flow between strands. At high fiber contents, this leads to poor tensile fatigue resistance.

The foregoing observations indicate that none of the common reinforcing fabrics provides a good balance of properties and manufacturability. This paper provides a more useful comparison of different fabrics than has been available previously. Additionally, several new fabric types and variations suggested by vendors have been explored, and their performance, including manufacturability, is compared with that of commonly used fabrics. The best overall performance is observed for prepreg materials with well dispersed fibers, discussed in Chapter 10.3.

4.3. Experimental Methods

All materials were fabricated by resin transfer molding with the exception of manufacturability studies which also included hand layup. The reinforcing fabrics are noted with the results for each case. The matrix resin in all cases was a pre-promoted orthophthalic polyester (CoRezyn 63-AX-051) with 2 percent methyl ethyl ketone peroxide as a catalyst. Details of molding, test coupon preparation, and test methods can be found in References 1 and 2, and specimen preparation for coupons containing ply drops can be found in Reference 14. The ply delamination tests using specimens containing ply drops followed test procedures outlined in Reference 12 and are described in greater detail in Reference 34. The interlaminar fracture toughness data were obtained using double-cantilever-beam (DCB) test specimens with an artificial starter crack following test standard ASTM D5528, discussed in Chapter 9. All fabrics discussed in this section used E-glass fibers.

4.4. Results and Discussion

Table 9 describes various reinforcing fabrics studied, and Figure 30 shows photographs of several fabrics. As indicated earlier, a major problem with reinforcing fabrics lies in the lack of fabric with straight unidirectional fibers in the warp direction of the fabric roll, which can provide the primary load carrying structure in a blade. The widely used A130 class of woven fabric produces poor compressive strength, as will be shown later. Adaptations of the weft-direction D155 class of stitched unidirectional fabrics into the warp direction by stitching to ±45° fabric, producing a "triax" fabric, result in very poor tensile fatigue resistance for several stitching variations investigated (Figure 2) [2]. The work reported here gives more complete data for the baseline D155 and A130 fabrics than has been reported previously, and compares their properties. Results are also presented for the best of

the previously tested triax materials, CDB200. Three new fabric types have been studied including CM1701, with D155-like fabric stitched to a light veil mat; TV-3400, a very loosely stitched triax fabric; and UC1010V and UC1018V, both of which contain unidirectional strands bonded to a thin veil mat with no stitching. A European fabric similar to CM1701, but with larger strands, is reported in the last part of this chapter. The ±45° fabric used in all laminates except triax is DB120, with stitched ± 45° layers.

Table 9. Fiberglass Fabric Description.

Fabric	Manufacturer	Type	Weight (g/m²)
D155	Owens Corning	Weft Unidirectional, Stitched	527
A130		Warp Unidirectional, Woven	444
DB120		±45 Bias Ply, Stitched	393
CM1701		Warp Unidirectional, Stitched to mat	587
CDB200		Triax 0/±45, Stitched	759
UC1018V	Collins Craft	Warp Unidirectional, bonded to veil	632
UC1010V		Warp Unidirectional, Stitched	351
A1010		Warp Unidirectional, bonded to veil	351
TV3400	Brunswick	Triax 0/±45, Stitched	1150
42024L/M50	Ahlstrom	Warp Unidirectional, Stitched	1250
62002		±45 Bias Ply, Stitched	390

4.4.1. Tensile Fatigue Resistance

Table 10 compares the tensile fatigue resistance of laminates using the three new types of fabric with the baseline D155 weft unidirectional fabric and CDB200 Triax. Laminates with separate 0° and ±45° plies (Figure 31) contain 70 to 75 percent 0° fibers with the indicated fabrics in the ply configuration $[0/±45/0]_S$. The triax materials in Figure 32 each contain about 50 percent 0° fibers.

The DD14 laminate with CM1701 fabric, in Figure 31 and Table 10, shows a relatively low tensile fatigue resistance, with a maximum strain capability at 10^6 cycles of 0.60 percent, compared with the baseline DD5P value of 1.15 percent. This low tensile fatigue resistance, even at a low overall fiber volume content of 35 percent, is only slightly better than the usual range for triax fabrics (about 0.35 percent to 0.60 percent [2]), and is about half the tensile fatigue capability of the DD5P laminate based on D155 0° fabric. The A130 fabric produces slightly better tensile fatigue resistance compared to D155 at higher fiber contents (Table 10).
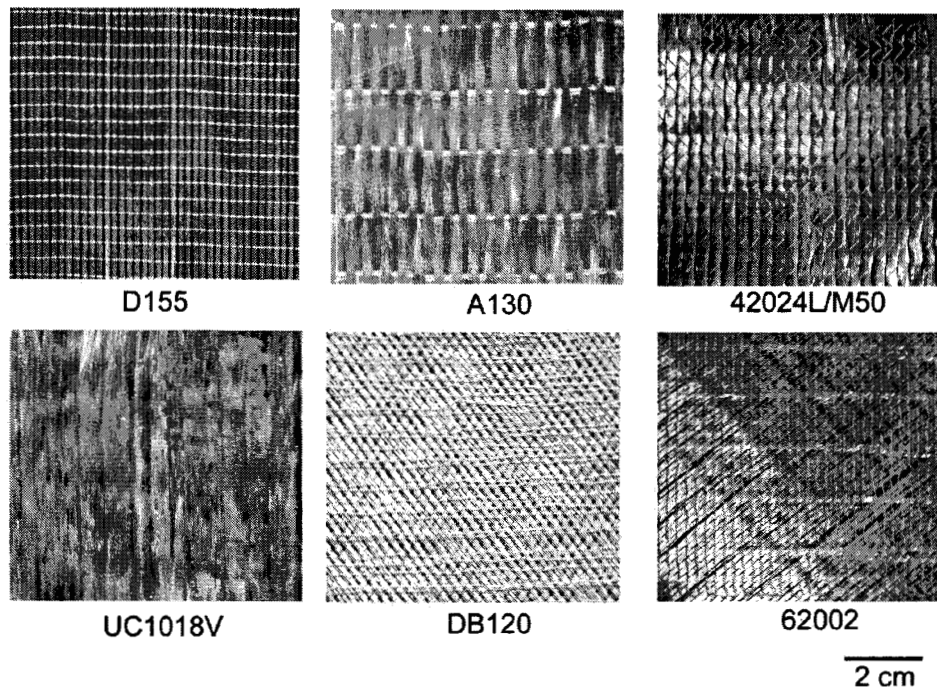
Figure 30. Dry Fabric Samples.

Tests of unidirectional laminates with no ±45° layers present (Table 11) show corresponding 10^6 cycle strain values of 0.64 percent for the CM1701 fabric and 1.12 percent for the D155 fabric. These values are consistent with the $[0/\pm45/0]_s$ laminate results. Another stitched warp unidirectional fabric, A1010, was briefly studied. The results for the corresponding laminate DD20 in Table 10 were very poor in tensile fatigue.

The bonded unidirectional warp fabrics, UC1010V and UC1018V, are the closest architecture to typical aerospace composites fabricated from prepreg. The 0° strands in the fabric are nested together with no stitching or weave crossover points to pinch the fibers together. It is anticipated that these fabrics might produce laminate properties at high fiber contents which are similar to the baseline D155 stitched fabric at lower fiber contents. As noted earlier, at higher fiber contents and in structural details which pinch the strands together, the D155 fabric laminates go through a transition to poor tensile fatigue resistance [1, 2]. Earlier data for the D155 fabrics with all stitching removed by hand showed good tensile fatigue resistance retained to higher fiber contents (Figure 2). The results in Table 11 and Figure 31 indicate that the bonded fabric laminate, DD24, with a fiber volume of 39 percent, performs in tension only slightly below the baseline DD5P laminate, with a 10^6 cycle maximum strain of 0.94 percent compared with 1.15 percent for the D155 fabric baseline DD5P laminate. Comparing the Table 10 laminates having higher, 46 to 49 percent fiber by volume, based on D155 fabric (DD4), A130 fabric (DD13), and the bonded UC1018V fabric (DD25A), the bonded fabric shows the highest compressive strength, slightly lower tensile strength, but the lowest fatigue coefficient, b.

65

4.4.2. Compressive Strength

The compressive strength of the DD24 laminate, 511 MPa, is also slightly below the 574 MPa for DD5P (another D155 fabric laminate with a V_f of 37 percent had a compressive strength of 534 MPa; this fiber content is closer to the 39 percent fiber content of DD24). The heavier bonded fabric, UC1018V, showed a laminate ultimate compressive strength of 629 MPa at a higher fiber content of 49 percent in material DD25A, which is comparable to values for D155 laminates at similar fiber content such as DD4, 48 percent fiber, 541 MPa strength; DD, 51 percent fiber, 788 MPa; and DD7, 54 percent fiber, 581 MPa [2]. Comparisons of the bonded fabric laminates with the woven fabric laminates in Table 10 show much higher values of compressive ultimate strength for the bonded fabric laminates, 511 and 629 MPa, compared with the woven fabric laminates, DD11 and DD13 with compressive strengths of 314 and 319 MPa for fiber contents of 31 and 50 percent.

Thus, the ultimate compressive strength of the bonded fabric laminates is similar to that of the stitched fabric laminates, which is expected based on the straight strands in each material. However, the stitched D155 unidirectional fabric is not available with the fibers parallel to the warp (long) direction of the fabric roll unless they are stitched to a backing material, such as the mat used with the CM1701 fabric. The latter fabric, CM1701, while producing a fair compressive strength ranging from 428 to 439 MPa in the database [2] for fiber contents ranging from 25 to 43 percent (laminates DD14, DD15, DD16) shows poor tensile fatigue resistance as noted earlier. It should be noted that the ultimate compressive strength is the parameter of interest in compression, since the fatigue sensitivity in compression is similar, relative to the ultimate strength, for all laminates [1,2].

Table 10. Comparison of Properties for Laminates Containing 0° and ±45° Layers,
Based on Different Fabrics.

Laminate*	0° Fabric	V_F, (%)	Ultimate Compressive Strength (MPa)	Ultimate Tensile Strength (MPa)	Fatigue R=0.1 strain for 10^6 cycles (%)	b, (R=0.1) Equation (1)	0° Elastic Modulus (GPa)
DD5P	D155	37	574	661	1.16	0.101	24.2
DD4	D155	48	541	886	0.55	0.136	31.0
DD11	A130	30	319	592	1.20	0.100	20.0
DD13	A130	46	314	821	0.80	0.130	29.5
DD14	CM1701	43	428	728	0.60	0.133	25.1
DD20	A1010	34	313	587	0.50	0.137	22.2
DD24	UC1010V	39	511	730	0.94	0.115	23.9
DD25A	UC1018V	49	629	783	0.75	0.121	28.5
DD25B	UC1018V	31	419	514	1.03	0.102	19.3
AA Triax	CDB200	31	348	452	0.50	0.140	18.8
AA4 Triax	TV3400	33	449	377	0.67	0.105	20.4

* The Material is the designation for this laminate in the DOE/MSU Database. All DD series materials are in the ply configuration $[0/\pm45/0]_s$, where the ±45 plies are DB120 fabric.
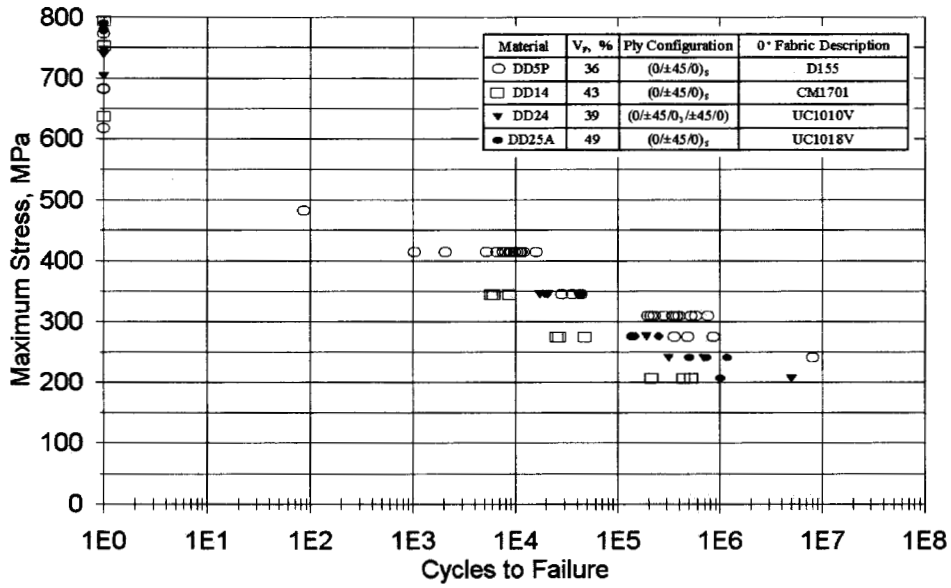
Figure 31. Tensile Fatigue Data Comparing Baseline Laminate (DD5P) With Laminates Based on Other Warp Unidirectional Fabrics, R = 0.1.
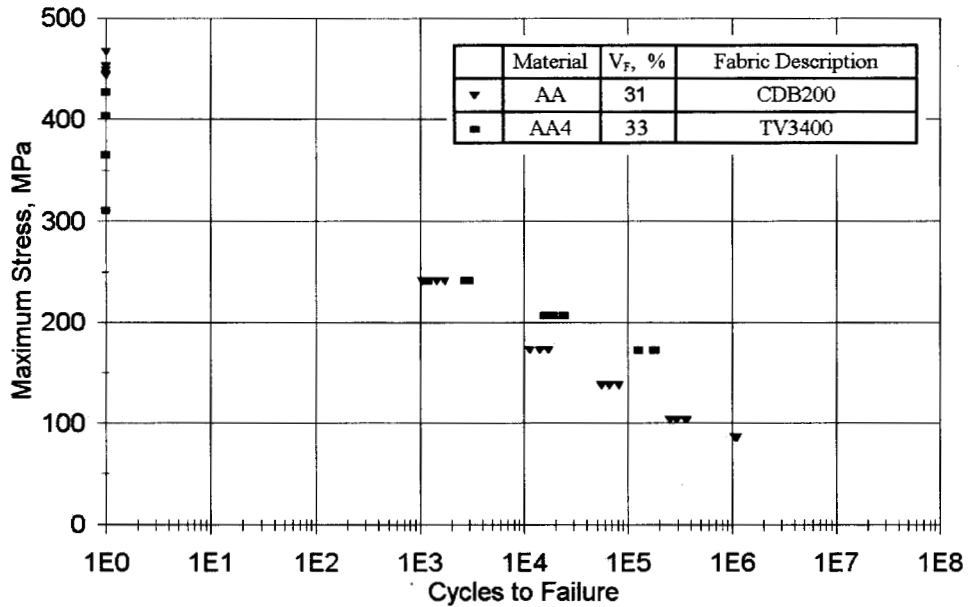
Figure 32. Comparison of Tensile Fatigue Data For Triax Fabric Laminates, R = 0.1.

Table 11. Comparison of Properties for Unidirectional Laminates Containing a Single Fabric Type.

Fabric	V_F (%)	Ultimate Compressive Strength (MPa)	Ultimate Tensile Strength (MPa)	Fatigue strain for 10^6 cycles (R=0.1) (%)	b, (R=0.1) Equation (1)	0° Elastic Modulus (GPa)
D155	40	653	854	1.12	0.102	31.5
A130	36	373	728	1.10	0.091	31.6
CM1701	38	573	796	0.64	0.126	30.5

There is a potential problem with fiber waviness (deviations from straight 0^0 in the plane of the sheet) in most of the fabrics discussed here. This may occur in applications even when it is not present in coupon tests used to establish the database. Effects of fiber waviness on compressive strength are described in Chapter 8.

4.4.3. Delamination Resistance

The delamination resistance has been determined in two types of experiments. First, a direct interlaminar fracture toughness test has been run on unidirectional specimens containing a starter crack. This is an opening mode (Mode I) test using a double cantilever beam specimen. Table 12 compares the delamination resistance for the baseline stitched and bonded fabric laminates. The results show no significant difference in delamination resistance between the two fabrics, eliminating concern that the bonded fabric, with its thin veil mat backing, would provide a favorable path for delamination crack growth.

The second delamination test uses a more realistic geometry of a ply drop, which is typical of a thickness-tapering section of a blade. Results of this type have been presented earlier for a variety of ply drop geometries [12, 17, 34]. Figure 33 compares the rate of delamination growth in fatigue from a single ply drop for laminates based on different fabrics. The ply arrangement in all cases is $[0/0*/\pm45/0]_s$, where the 0* ply is dropped from the specimen at mid-length (see References 12, 17 and 34). Little significant effect of fabric type is evident in Figure 33, with only a slightly more rapid crack growth for the A130 fabric based laminate for this particular ply arrangement. Results for the bonded fabrics are not yet available.

Table 12. Interlaminar Fracture Toughness, G_{IC}, 0°/0° Interface.

Material	Fabric	Initiation G_{IC} (J/m^2)
DD5P	D155	140
DD25B	UC1018V	176
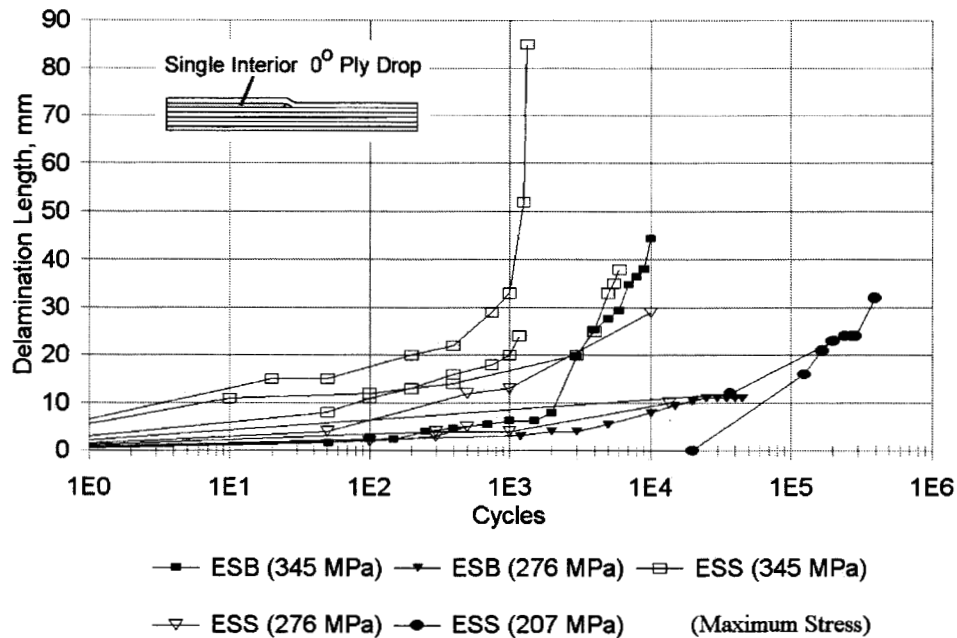
Figure 33. Typical Delamination Length versus Cycle Data for Laminates
ESB (D155 fabric) and ESS (A130 fabric) With a Single Interior Ply Drop.

4.4.4. Manufacturability

Laminates containing the three 0° fabric types, D155, A130, and UC1018V, have also been evaluated for manufacturability by fabricating flat plates at different fiber contents by RTM, and at low fiber content by hand layup. All fabrics are in the same general price range. As indicated in Table 13, all laminates were easily manufactured by hand layup in the 30 to 40 percent fiber by volume range, but the A130 fabric caused some difficulties in handling and wet-out. The D155 fabric laminates were easily manufactured by RTM at both low (30 to 40 percent) and moderate (40 to 50 percent) fiber content ranges. The A130 based laminates were more difficult to mold at the higher fiber content, and the bonded fabric (UC1018V) was difficult at low fiber content and nearly impossible at high fiber content by RTM. The reason for the relatively easy molding of the D155 laminates by RTM is the resin flow paths between the stitched strands (Figure 30), which are not present in the other fabrics. As noted earlier, variations in the bonded fabric are being pursued to improve manufacturability. Additionally, process variations to the RTM method are also being investigated for low permeability fabrics.

4.4.5. European Fabrics

Several European E-glass fabrics (Table 9, Figure 30), said to be used in European blades, were obtained from Ahlstrom. The 0° fabric (Figure 30) has relatively large tows, stitched to a mat. It was thought that the larger tows (compared to the CM1701) might provide properties similar to

Table 13. Manufacturability with Different 0° Fabrics.

Fabric*	Hand Layup (30 to 40 percent fiber volume fraction)	Resin Transfer Molding (30 to 40 percent fiber volume fraction)	Resin Transfer Molding (40 to 50 percent fiber volume fraction)**
D155	Excellent	Excellent	Good
A130	Fair	Good	Fair
UC1018V	Good	Fair	Poor

* Laminate configuration $[0/\pm45/0]_s$, $\pm45°$ layers are DB120 fabric.
** Vacuum assist helps at high fiber content

D155 laminates, but with the 0° strands in the warp direction of the fabric roll. The $\pm45°$ fabric is also pictured in Figure 30. Laminates with 76 percent 42024L/M50 and 24 percent 62002 were prepared with the baseline ortho polyester resin. Materials DD27A and DD27B have fiber contents of 32 and 42 percent fiber by volume. The ply arrangement was $(0/\pm45)_S$. Table 14 and Figure 34 give the results of the static and fatigue tests compared with D155 fabric based laminates like DD5P in Table 10. The compressive static strength is reduced by 34 percent and 48 percent for DD27A and DD27B, respectively, reaching levels similar to those for woven fabrics. The tensile fatigue resistance is also disappointing, with b values and 10^6 cycle strain values similar to D155 or A130 based laminates at much higher fiber contents. It is expected that the low compressive strength is the result of the strand waviness (Figure 30), particularly when impregnated; the poor tensile fatigue resistance appears to be the result of stitching to the mat, locally raising the fiber content in the strand, as discussed in Chapter 11 (similar to CM1701).

Table 14. Fatigue Summary Properties of Materials DD27A, DD27B, Based on Ahlstrom 42024/M50 0° fabric, compared with baseline DD5P.

Material	V_F, %	Ultimate Compressive Strength (MPa)	Ultimate Tensile Strength (MPa)	b, (R=0.1) Equation 1	Strain for 10^6 cycles, %	0° Elastic Modulus (GPa)
DD27A	32	-381	566	0.136	0.61	20.5
DD27B	42	-321	667	0.133	0.60	25.9
DD5P	37	-574	661	0.101	1.16	24.2
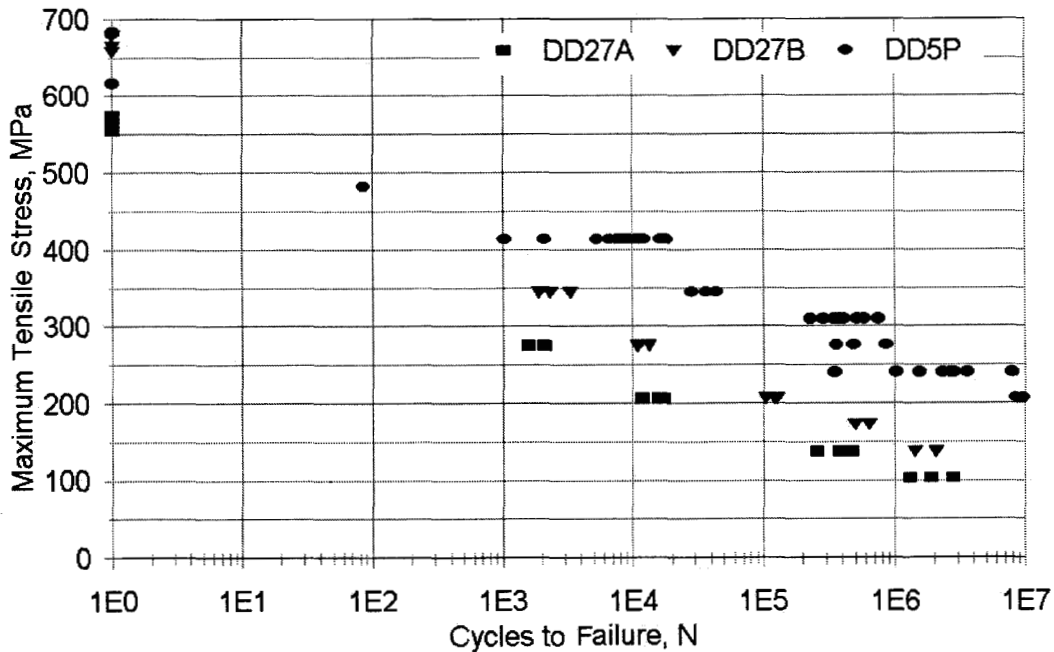
Figure 34. Fatigue Diagram for Materials DD27A ($V_F = 0.32$) and DD27B ($V_F = 0.42$) Compared to Baseline DD5P ($V_F = 0.37$), at R=0.1.

4.5. Conclusions

The results allow some overall conclusions as to the application of these fabrics to wind turbine blades. For blade areas where compression stresses are not limiting, the A130 class of fabrics provide good performance. While low in compression strength, these laminates require very low knockdown factors at structural details in compression (discussed later). For general cases with tension and compression as well as structural detail variations, the bonded fabrics such as UC1018V appear very promising for hand layup, but manufacturability may limit their use for processes such as RTM which require resin flow in the plane of the fabric. The D155 fabric is available in the weft direction of the roll of fabric only, and so cannot be used for lengthwise reinforcement down the blade. Fabrics such as triax and CM1701, based on stitched 0° layers, are appropriate if tensile fatigue is not limiting in the design. They are easily handled and molded. The CM1701 can be used with separate ±45° fabrics to produce a higher 0° fiber content than is available in triax fabrics. Both the CM1701 warp unidirectional fabric and the TV3400 triax fabric provide convenient reinforcement with a moderate sacrifice in tensile fatigue resistance which may be less significant if structural details are present. Compressive strength is also relatively low for these materials, as noted earlier, in part due to fiber waviness. the European fabrics, with large 0° strands stitched to mat, similar to CM1701, showed relatively poor compressive strength and tensile fatigue resistance. Well prepared prepreg materials should provide the best overall properties (Chapter 10.3), but they require somewhat specialized processing as well as incurring the cost of preparing the prepreg product.

71

5. SPECTRUM FATIGUE LIFETIME AND RESIDUAL STRENGTH

5.1. Summary

This chapter addresses the effects of spectrum loading on lifetime and residual strength. Over 1100 tests have been run on a typical fiberglass laminate configuration under a variety of load sequences. Repeated block loading at two or more load levels as well as a modified standard spectrum have been studied. Data have been obtained for residual strength at various stages of the lifetime. Several lifetime prediction theories have been applied to the results.

The repeated block loading data show lifetimes that are usually shorter than predicted by the most widely used linear damage accumulation theory, Miner's sum. Actual lifetimes are in the range of 10 to 20 percent of predicted lifetime in many cases. Linear and nonlinear residual strength models tend to fit the data better than Miner's sum, with the nonlinear providing the better fit of the two. Direct tests of residual strength at various fractions of the lifetime are consistent with the residual strength damage models for several cases. Load sequencing effects are not found to be significant. The more a spectrum deviates from constant amplitude, the more sensitive predictions are to the damage law used. The nonlinear model provided improved correlation with test data for a modified standard wind turbine spectrum. When a single, relatively high load cycle was removed, all models provided adequate correlation with the experimental results.

Additional results for compression, reversed loading, and the unmodified WISPERX spectrum may be found in the forthcoming SNL report [21] or Wahl's doctorial dissertation [43]. The effects of constant amplitude data extrapolation models are also explored in these references, and found to be significant. The residual strength models may provide a more accurate estimate of blade lifetime than Miner's rule for some loads spectra. They have the added advantage of providing an estimate of current blade strength throughout the service life. Another, conservative approach would be to use a residual Miner's Sum, such as 0.1 rather than 1.0.

5.2. Introduction

An investigation of the relationship between spectrum loading and fatigue lifetimes of a typical wind turbine blade fiberglass material has been undertaken for the development of refined design tools. Present design tools for estimating lifetimes of fiberglass materials produce results that may be significantly non-conservative for some loads spectra. These tools or prediction models range from the simple Miner's sum and the various deviations to more complicated ones based upon residual strength [51-59]. Many require testing of the materials to establish "fitting" parameters to obtain the best performance of the model. The objective of this study is to identify cumulative damage laws which provide improved accuracy in predicting lifetime under a variety of loads spectra for wind turbine blade materials. Ease of incorporation into design codes is also a major concern

This program was conducted in a logical progression from simple to complicated spectra; that

is, from constant amplitude loading, to multi-amplitude loading, to a modified standard spectrum. Small dog-bone shaped coupons were manufactured, tested and favorably compared to standard tensile test coupons. Baseline data for the development of stress-cycle (S-N) trends was obtained by constant amplitude fatigue testing of coupons by using computer controlled hydraulic testing equipment. Results of this preliminary testing are consistent with earlier work [2].

Tests were then run using repeated blocks at two stress levels. Initially, this two-block testing was such that the first block contained ten cycles of the higher stress load, followed by a varying number of cycles at a lower stress level, repeated until failure. Two-block testing by some investigators has been limited to the application of a fixed number of cycles of the first stress level, followed by an undetermined number of cycles at a second level, until failure. This reportedly results in either Miner's sums greater than unity for high stress levels followed by low stress levels or Miner's sums less than unity for low stress levels followed by high stress levels [60]. The present work used the more general case of repeated application of two-blocks until failure, and also explored load sequencing effects.

Testing of multi-block spectra was then performed with blocks of three and six stress levels. Finally, coupons were subjected to a modified WISPERX [61, 62] spectrum which has been reported to produce Miner's sums less than unity.

5.3. Nomenclature and Definitions

The linear damage accumulation rule of Miner's sum is frequently applied to fatigue test results and is here defined as:

$$D = \sum_i \frac{n_i}{N_i} \qquad (3)$$

where D is a quantified damage accumulation parameter, n_i is the number of cycles experienced at a σ_i maximum stress level and N_i is the number of constant amplitude cycles to failure at the maximum stress level σ_i and R-value. Typically, failure is predicted to occur when D reaches unity, as originally proposed by Miner [63].

The cyclic loading of a specimen is frequently reported as a maximum stress and an R-value. The R-value is the ratio of the minimum to maximum stress. Several common constant amplitude sinusoidal loading waveforms are shown in Figure 35, along with their R-values.

WISPERX [61, 62] is a European standardized loading spectrum which has been used for analysis of fatigue of wind turbine components. It is provided as a sequence of numbers ranging from 1 to 64, with 25 as a zero value. WISPERX contains 25,663 loading reversal points for 12,831 cycles. An overall visual presentation of the WISPERX spectrum is shown in Figure 36.
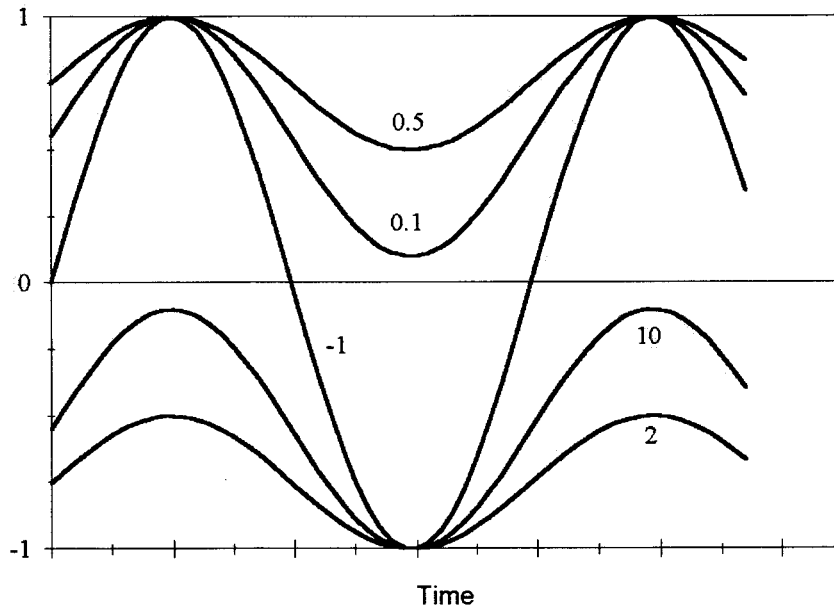
Figure 35. Typical Waveforms With Different R-Values.
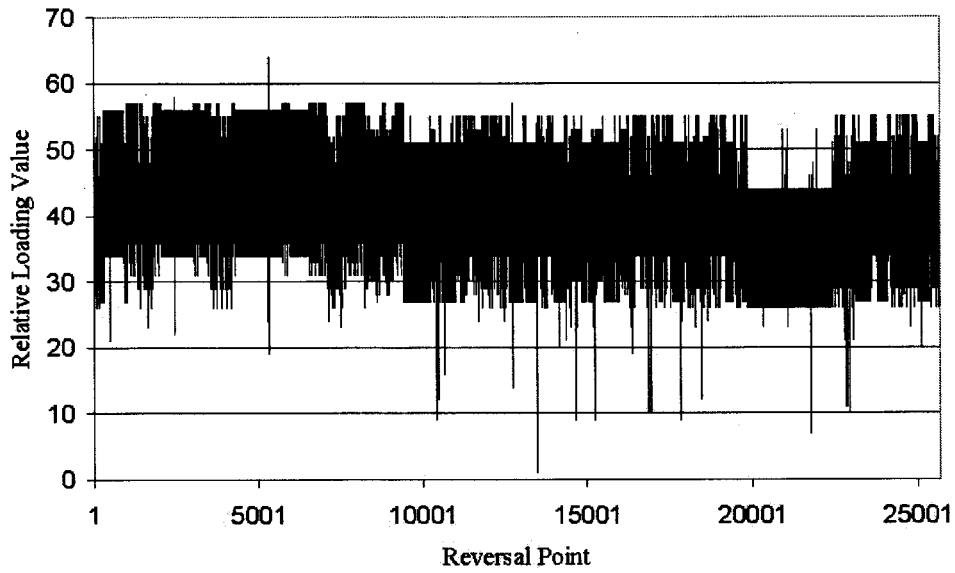
Figure 36. WISPERX Spectrum.

In this study, WISPERX was modified to a spectrum of constant R-value by adjusting the valley reversal point after each peak reversal point. This was done for R-values of 0.1 and 0.5, as demonstrated in Figure 37 for a small portion of the WISPERX spectrum. The WISPERX spectrum was scaled for use with testing machinery control software. The results are shown in Figure 38.

The first modification only included cycles that were tensile-tensile. The results of this modification called the Mod 1 spectrum, are displayed in Figure 39 for R = 0.1. A second modification, that included all peak reversal points, was created. The resultant spectrum, Mod 2 spectrum, is displayed in Figure 40 for R = 0.1. The main thrust of the modification was to create spectra that were of a constant R-value, thereby aiding in the application of the baseline constant amplitude fatigue data for lifetime predictions. Comparison of the Mod 1 and Mod 2 spectra allowed an investigation into the damage contribution of essentially one major event per pass through the spectrum.

—Mod 1 WISPERX, R = 0.1 —Mod 1 WISPERX, R = 0.5 —Scaled Original WISPERX
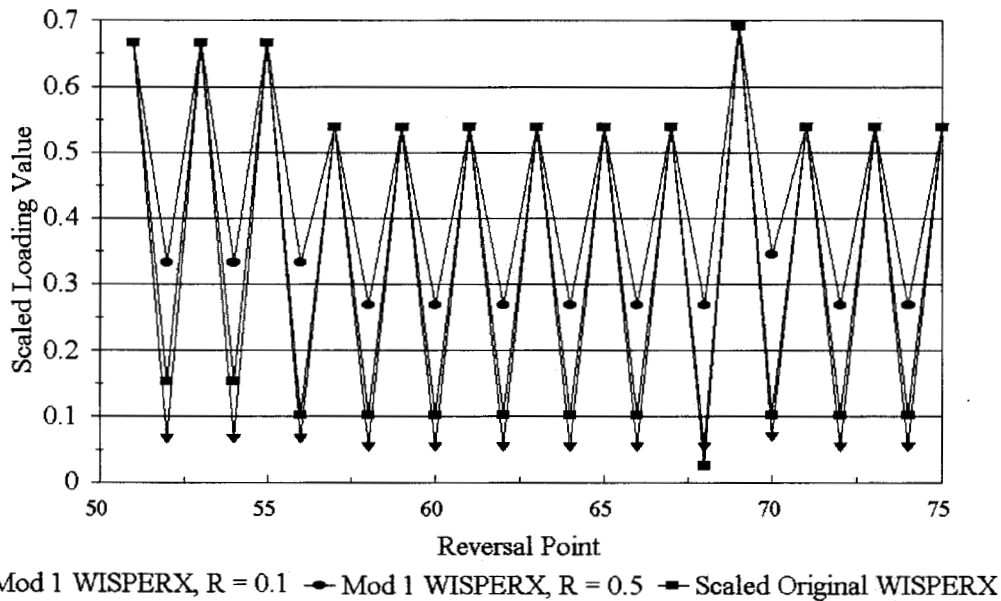
Figure 37. Modified WISPERX Spectrum Example.
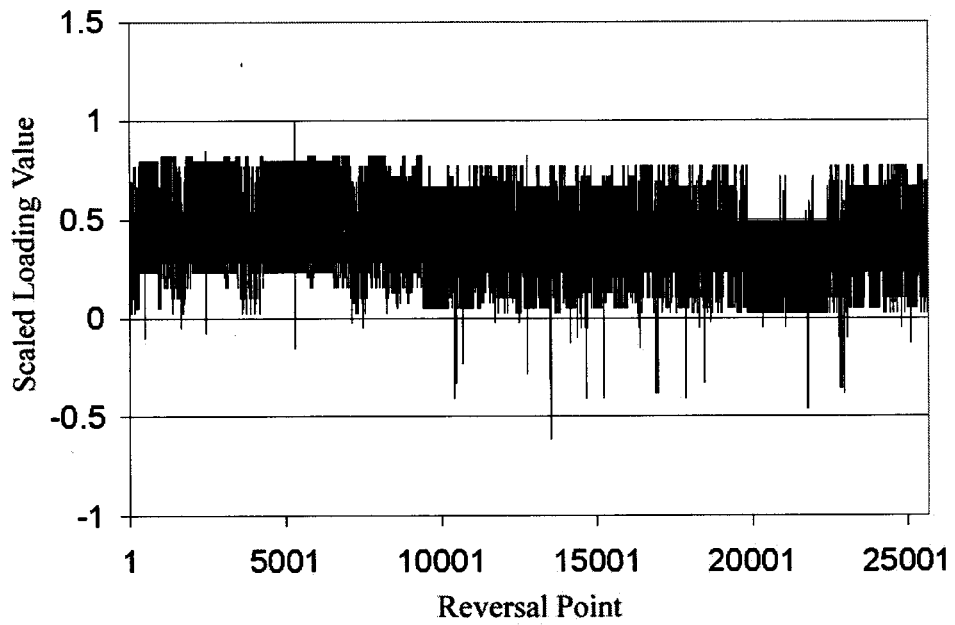
Figure 38. Scaled WISPERX Spectrum.
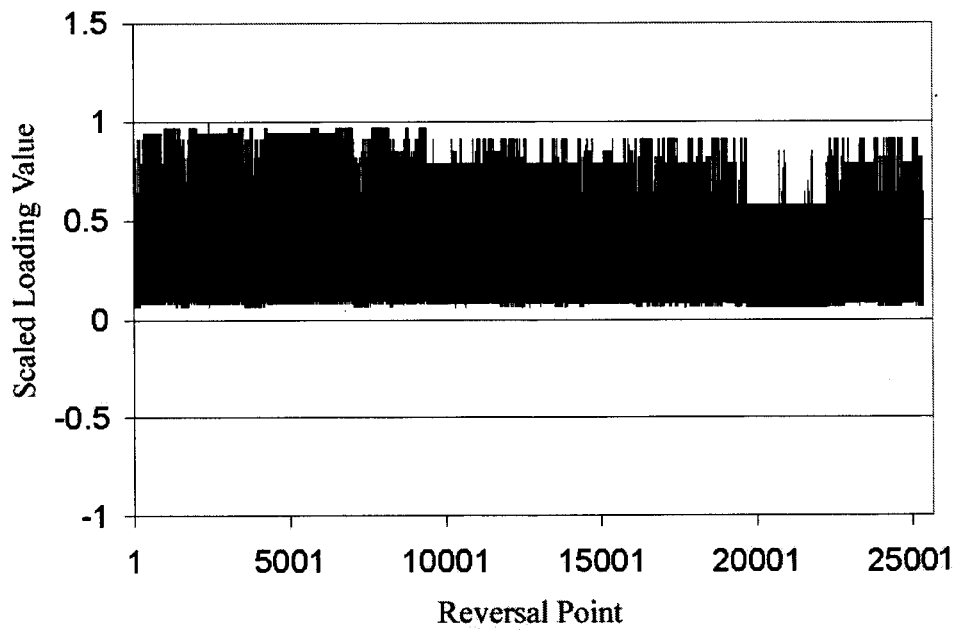
Figure 39. Mod 1 Spectrum for R = 0.1.
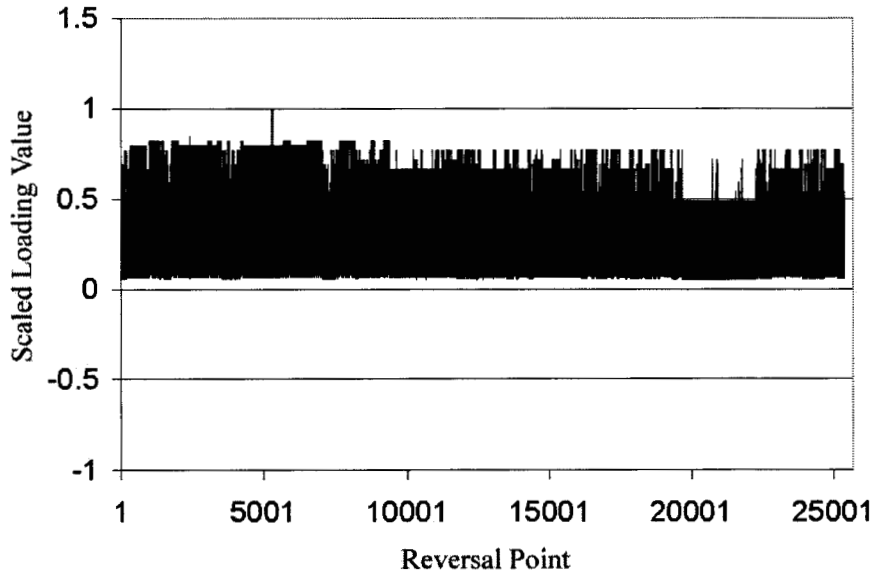
Figure 40. Mod 2 Spectrum for R = 0.1.

5.4. Experimental Methods

5.4.1. Material and Test Specimens

The material, termed DD16 in the database [2], was comprised of Owens Corning D155 and DB120 fabrics in a $[90/0/\pm45/0]_S$ lay-up. Plates of this material were fabricated by a resin transfer molding, RTM, process with Interplastics Corporation CoRezyn 63-AX-051 ortho-polyester matrix to an average fiber volume fraction of 0.36. Details can be found in the current version of the DOE/MSU Fatigue Database and Reference 2.

Tensile-tensile specimen blanks were rectangularly shaped, typically 13 mm wide by 4 mm thick and 64 to 75 mm long. These blanks were then individually machined to a dog-bone style with a pin router and master pattern. Fiberglass tab material was attached to better distribute testing machine gripping forces. The minimum width of the dog-bone gage section was typically 9.5 mm.

5.4.2. Testing Equipment

An Instron 8872 hydraulic testing machine, with an Instron 8800 controller was used to subject the specimen to the spectrum loads. Instron WaveRunner© and RANDOM© * software packages were used to develop and apply the loading spectra. Secondary measurement and recording of the actual loading waveforms were favorably compared to that available from the Instron equipment.

Testing was performed at 8 or 10 Hz, with forced air surface cooling of the specimen to preclude thermal effects.

5.5. Testing and Results

5.5.1 Constant Amplitude Testing

The fatigue results of the single amplitude testing are summarized in the stress-cycle (S-N) diagram, Figure 41, for R = 0.1 and R = 0.5.
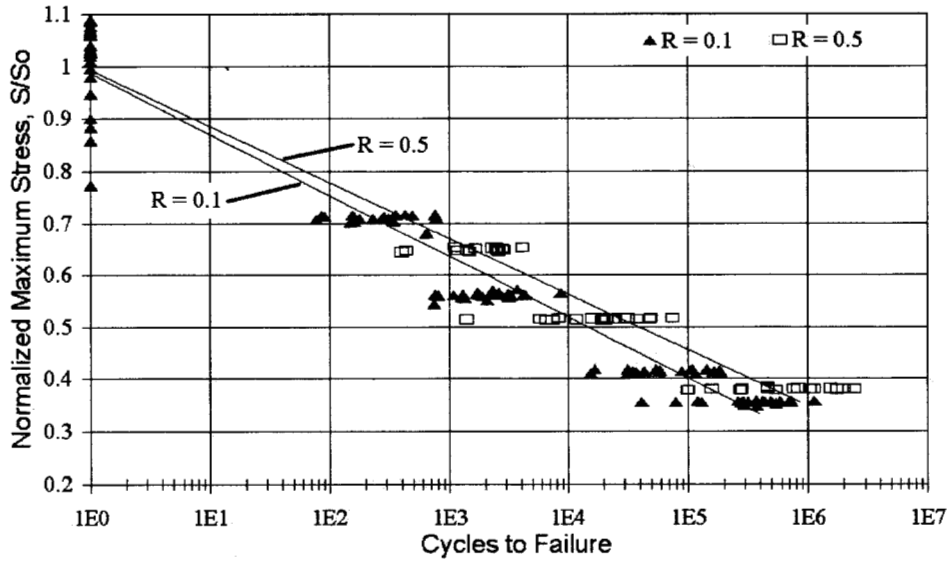
Figure 41. Constant Amplitude S-N Fatigue Data.

The slopes for the two tensile-tensile S-N lines are 0.108 and 0.119 for R = 0.5 and 0.1 respectively. Over 175 tests are represented by the information in Figure 41. Both regression lines have correlation coefficients better than 0.98.

The generic equation [64] for the two lines in Figure 41 is (also equation (1)):

$$\frac{S}{S_0} = 1 - b \log (N) \qquad (4)$$

where S = maximum applied stress, MPa
S_0 = static strength, MPa
N = number of cycles to failure
b = slope or reduction in maximum applied stress for each decade increase in cycles.
for   R = 0.1, S_0 = 578.7 MPa, b = -0.119
R = 0.5, S_0 = 642.2 MPa, b = -0.108

The average data shown in Figure 41 reflect the average cycles to failure at a given load level.

The different S_0 values at R = 0.1 and R = 0.5 reflect different material batches.

5.5.2. Two-block Testing

Two-block testing was performed with both the Instron WaveRunner and RANDOM control programs. This testing was used to study both the effect of a simple spectrum on the fatigue life and the effect of the sequencing of cycles within the spectrum.

Testing of the sequence effect involved applying ten cycles of high stress level within 1000 cycles of a lower stress level. Three cases were chosen: 1) one high amplitude cycle followed by 100 low; 2) ten high amplitude cycles followed by 1000 low; and 3) ten high amplitude cycles randomly interspersed within 1000 low. These spectra are shown, respectively, top to bottom in Figure 42.
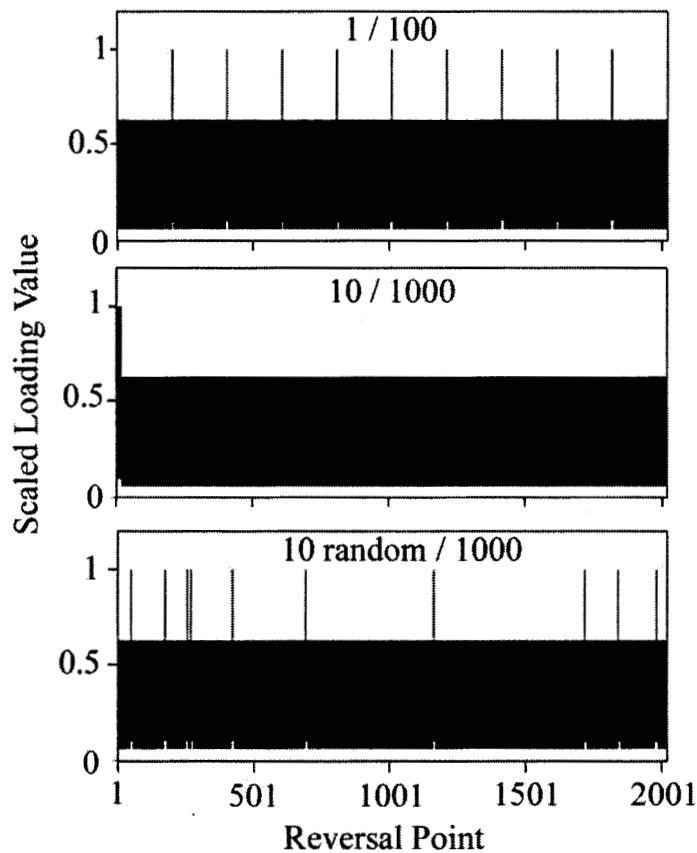
Figure 42. Two-Block Sequencing (sequences shown repeated to failure).

The results of these tests are displayed on the occurrence graph, Figure 43. This figure also shows the constant amplitude results for each stress level, which illustrates the degree of scatter present in typical single amplitude tests, such as those represented by average values in Figure 41. Note the center three sets of data representing the two-block fatigue tests at three different

79

sequences. Statistically, no differences could be found among the results. The 120 tests, 82 two-block and 38 constant amplitude, represented in Figure 43, were all performed for R = 0.1. The high stress level was 325 MPa and the low stress level was 207 MPa.
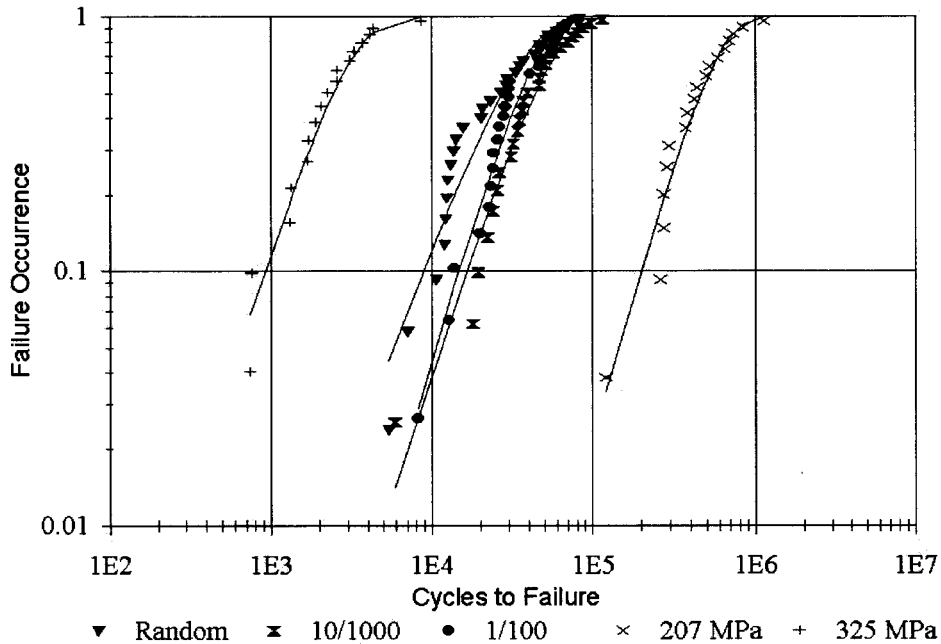
Figure 43. Sequence Effects on Two-block Repeated Spectra, R = 0.1.

Figure 44 depicts these same 82 two-block tests now as a function of Miner's sum at failure. Only four of the 82 tests achieved Miner's sums of greater than one. It is evident that the sum tends to less than unity for two-block loading, causing the Miner's sum rule to be non-conservative.

Additional two-block results were obtained by varying the fraction of high amplitude cycles. A representation of Miner's sum at failure as a function of the fraction of the higher stress cycles shows a trend of unity for fractions of zero and one, with sums less than unity for fractions in between. A typical graph of these results is shown in Figure 45.

The tests summarized in Figure 45 are those of repeated two-block loading with the higher amplitude block of ten cycles run with a maximum stress of 325 MPa and the lower amplitude block of preselected number of cycles at 207 MPa. Several other cases have also been run at different stresses with results which are consistent with Figure 45 [21, 43].
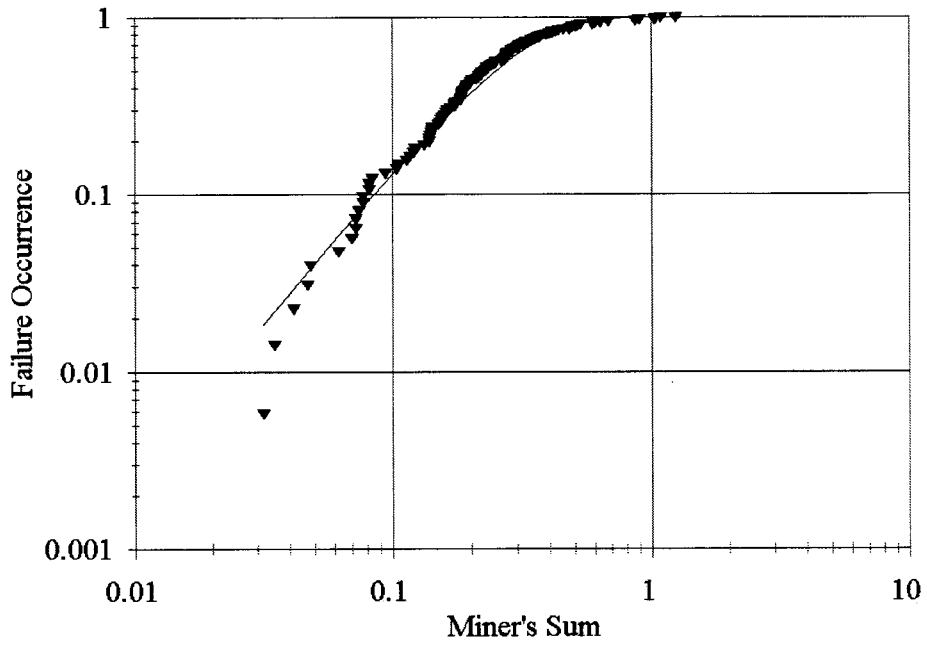
Figure 44. Combined Two-block Miner's Sum Results at Failure, R=0.1.
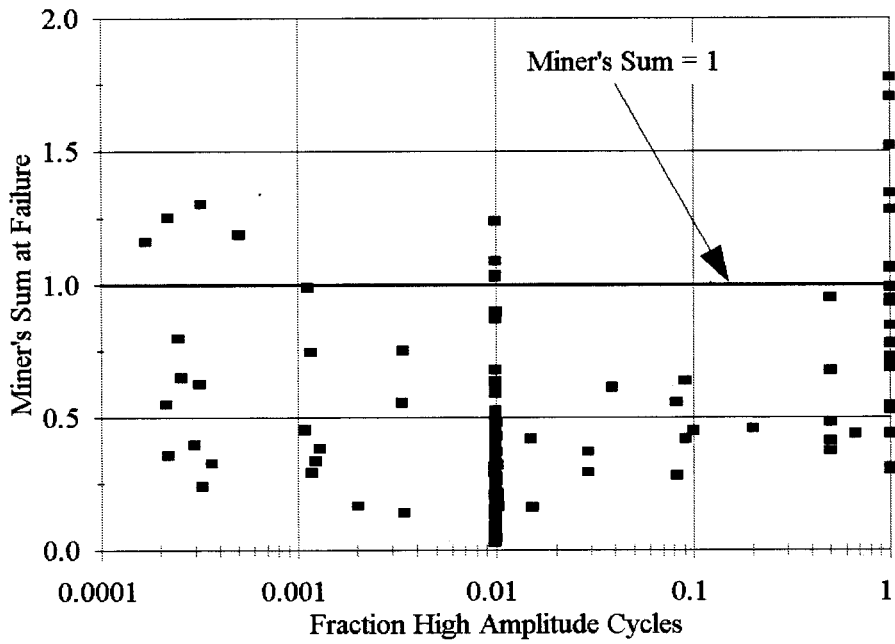
Figure 45. Typical Two-block Miner's Sum for High and Low Blocks of 325 and 207 MPa, R = 0.1.

81

5.5.3. Multi-Block Testing

Testing for spectra with three and six stress levels has also revealed Miner's sums at failure that are consistently less than unity. The three block testing program was constructed as a mix of ten cycles of 414 MPa, ten cycles of 325 MPa, and 100 cycles of 235 MPa in various sequences.

The six block testing consisted of four stress levels arranged into six blocks as:

Table 15. 6-Block Sequence.

Number of Cycles	Percent of Maximum Stress
1000	30
1000	50
400	75
10	100
400	75
1000	50

The three and six block testing were all performed with R = 0.1; results are presented in Table 16 for the three-block and Table 17 for the six-block. Note, all Miner's sums at failure are less than unity.

5.5.4. Modified WISPERX Testing

The WISPERX spectrum was modified to maintain a constant R-value as described earlier. This was done to allow direct use of the constant amplitude baseline data for R-values of 0.1 and 0.5, in the model predictions. Two versions of each, Mod 1 and Mod 2 were described earlier.

The results for the Mod 1 and 2 spectra testing are summarized in Figures 46 and 47 respectively. The trend of longer lifetimes for the R=0.5 loading are also typical for constant amplitude testing (Figure 45). The spectra loads were adjusted relative to the maximum stress in the spectrum following Figures 38 to 40, with only the maximum stress (of the entire spectrum) plotted in Figures 46 and 47.

5.5.5. Testing Summary

The spectrum testing program was implemented to vary the complexity of the spectra, from constant amplitude loading for base line data to multi-block spectra and finally to more random spectra. The latter used two modified WISPERX spectra, Mod 1 and 2. The method of establishing a set of blocks and then repeating these blocks until specimen failure is considered to be more representative of service loading as compared with continuing the final block to failure and not repeating the sequence.

In nearly every test, the Miner's sum at failure is less than unity. The need for improved models is evident.

Table 16. Three-Block Test Results R = 0.1.

Test Number	Sequence Cycles	Load	Actual Cycles	Miner's Sum		
				Actual	Linear Prediction	Non-Linear Prediction
179	10	414	62	0.520	0.770	0.282
	100	325	600			
	1000	235	6000			
489	10	414	113	0.421	0.920	0.657
	10	325	110			
	100	235	1100			
490	10	325	180	0.653	0.918	0.651
	10	414	174			
	100	235	1700			
491	100	235	1600	0.576	0.916	0.648
	10	325	160			
	10	414	153			
492	10	414	123	0.458	0.920	0.657
	10	325	120			
	100	235	1200			
493	100	235	1634	0.599	0.916	0.648
	10	325	160			
	10	414	160			

Table 17. Six-Block Test Results R = 0.1.

Test Number	Sequence Cycles	Load	Actual Cycles	Miner's Sum		
				Actual	Linear Prediction	Non-Linear Prediction
220	1000	97.5	26000	0.397	0.758	0.335
	1000	163	26000			
	400	244	10400			
	10	325	260			
	400	244	10337			
	1000	163	25000			
221	1000	104	8000	0.173	0.747	0.296
	1000	173	8000			
	400	259	3044			
	10	345	70			
	400	259	2800			
	1000	173	7000			
222	1000	124	2000	0.181	0.677	0.203
	1000	207	2000			
	400	311	654			
	10	414	10			
	400	311	400			
	1000	207	1000			
225	1000	104	5000	0.115	0.747	0.296
	1000	173	5000			
	400	259	2000			
	10	345	50			
	400	259	1857			
	1000	173	4000			
226	1000	82.8	48000	0.203	0.814	0.406
	1000	138	48000			
	400	207	19200			
	10	276	480			
	400	207	18968			
	1000	138	47000			
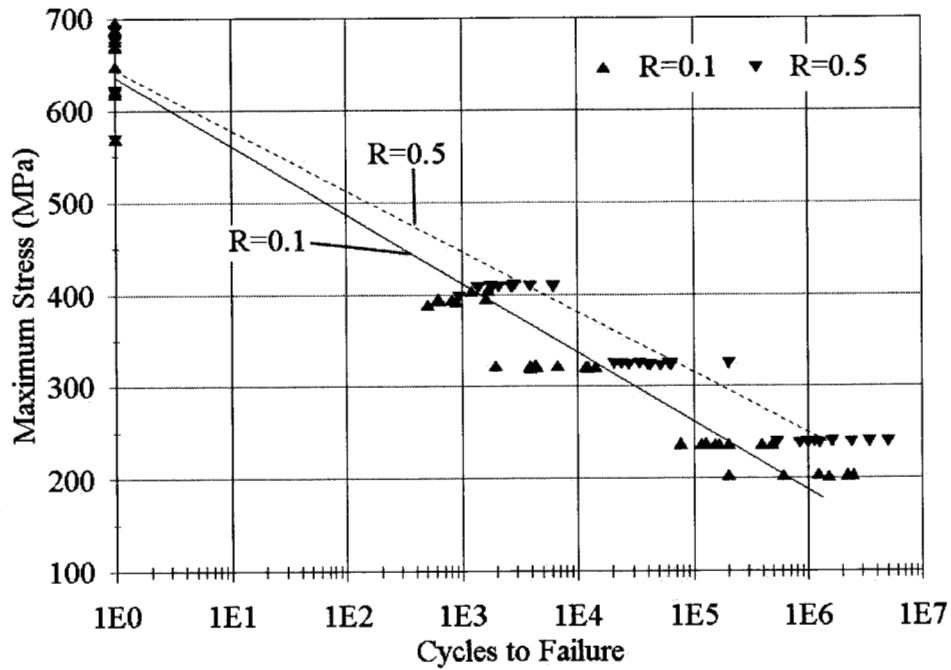
Figure 46. Mod 1 Fatigue S-N (S is the maximum stress in the spectrum), Shown with Trend Lines for the Data Fit to Equation (4).
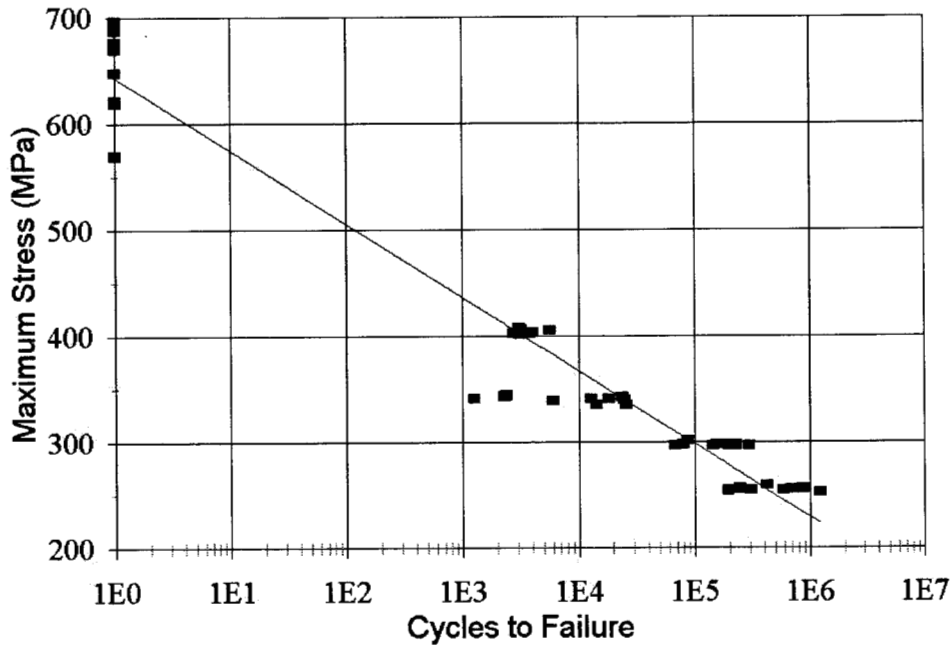
Figure 47. Mod 2 Spectra Fatigue S-N, R = 0.1 (S is the maximum stress in the spectrum).

5.6. Lifetime Predictions

An accurate cumulative damage law is essential to component design under spectrum loading. The fundamental and most widely applied damage law is that established by Palmgren and Miner. Under this law, damage is considered to develop linearly as a function of the number of cycles encountered at specific load levels. As reported throughout this paper, the Miner's sum is consistently less than unity, often on the order of 0.1, for testing under spectra of more than one block.

A component or specimen is considered to have failed when it can no longer support the load intended. Tensile failure was usually a sudden separation of 0° fibers, brooming out from the matrix. One clear deficiency in Miner's sum is that it only accumulates damage and does not consider that the current strength may be exceeded by a particular high stress cycle.

5.6.1. Residual Strength Degradation Models

Let us assume that the strength of a specimen may decrease linearly as the part is loaded cyclically [59]. The result of this assumption can readily be applied to block loading to estimate lifetimes. In Figure 48, the strength and cycles have been normalized to the static strength and cycles to failure, respectively. The maximum stress, in this case, is half of the initial strength. Let N represent the number of cycles to failure at stress level S_i, and n the number of cycles experienced at this level. Let S_0 represent the static strength of the material. The slope of the degradation line is then:

$$m = \frac{S_i - S_0}{N} \tag{5}$$

therefore, at any number of cycles during the stressing of this component, a linear residual strength degradation (LRSD)[59] model will yield residual strength as a function of n as:

$$S_R = S_0 + n \left[\frac{S_i - S_0}{N}\right] \tag{6}$$

which is represented graphically in Figure 48. Also represented is a nonlinear degradation path. The corresponding nonlinear model [53,54] has the following form:

$$S_R = S_0 + (S_i - S_0)\left(\frac{n}{N}\right)^V \tag{7}$$

where: S_R = residual strength at n cycles
  S_0= static initial strength (tensile or compressive)
  S_i=applied stress in fatigue

N=number of cycles to failure at the stress level of σ_i

ν=nonlinear factor, a value of $\nu=1$ reduces Equation 7 to the linear degradation model of Equation 6.

The nonlinear factor affects the shape of the prediction line for the strength degradation (Figure 48). Values less than one cause a prediction of more damage in the early component life; conversely, values greater than one would predict more of the damage to occur later in the life of the component. Upon investigating the results displayed in Figures 49 and 50, factors less than one were considered appropriate.
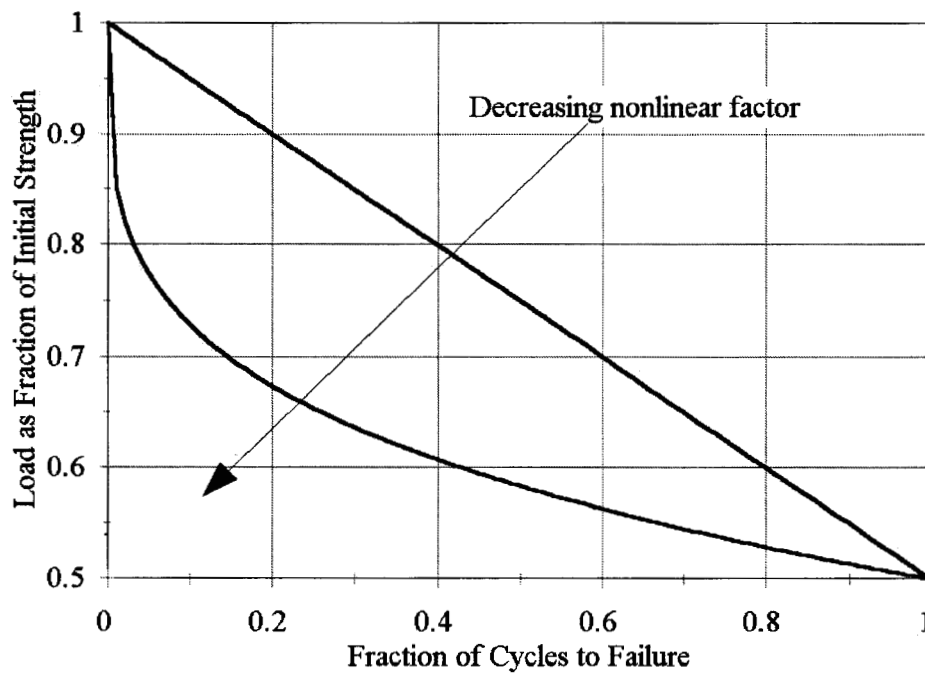
Figure 48. Residual Strength Degradation.

5.6.2. Model Comparison With Data

Figures 49 and 50 depict the results of strength degradation tests under constant amplitude loading for various maximum applied stresses and for R-values of 0.1 and 0.5. Specimens were cycled for a preset number of cycles, then the cycling was stopped. and a strength test was conducted. While the data are complicated by premature failure during cycling of some specimens prior to residual strength testing, the linear and nonlinear models provide reasonable agreement with the data.

Figure 51 depicts the lifetime predictions for Miner's, LRSD, and NRSD rules. The nonlinear factor, ν, utilized in these calculations was 0.265, which was selected for fit. In all cases, the nonlinear rule provides better prediction than the other two rules investigated. This is also true for the multi-block spectra as summarized in Tables 16 and 17. (Testing in compression shows similar results to Figure 51, with the same nonlinear factor. [21, 43])

87

Figures 52 and 53 show comparisons of the Mod 1 spectrum test results with the three damage rules. For this spectrum there is little difference between the three rules and they are all reasonably accurate at lower load levels.
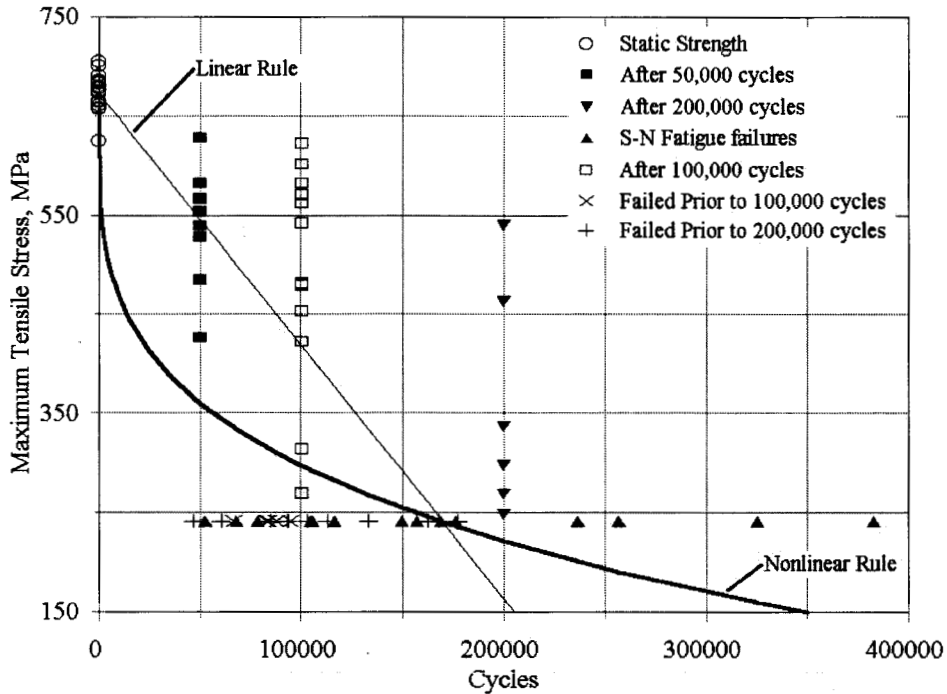
Figure 49. Residual Strength, R = 0.1.

Figure 54 shows that choice of the model is more important for the Mod 2 spectrum, with a single higher load. The nonlinear model fits the data from Figure 47 much more accurately, particularly at higher stresses. As the maximum stress (and other stresses) is reduced, the models tend to converge.

Generally, as a spectrum includes a greater difference in load levels, the damage rule becomes more important. This is illustrated in Figure 55 which shows predictions for two-block repeated spectra with different ratios of low to high block amplitude. When the damage is mostly caused by low stresses, but occasional high stresses occur, then the residual strength models are more accurate and differ strongly from Miner's rule.
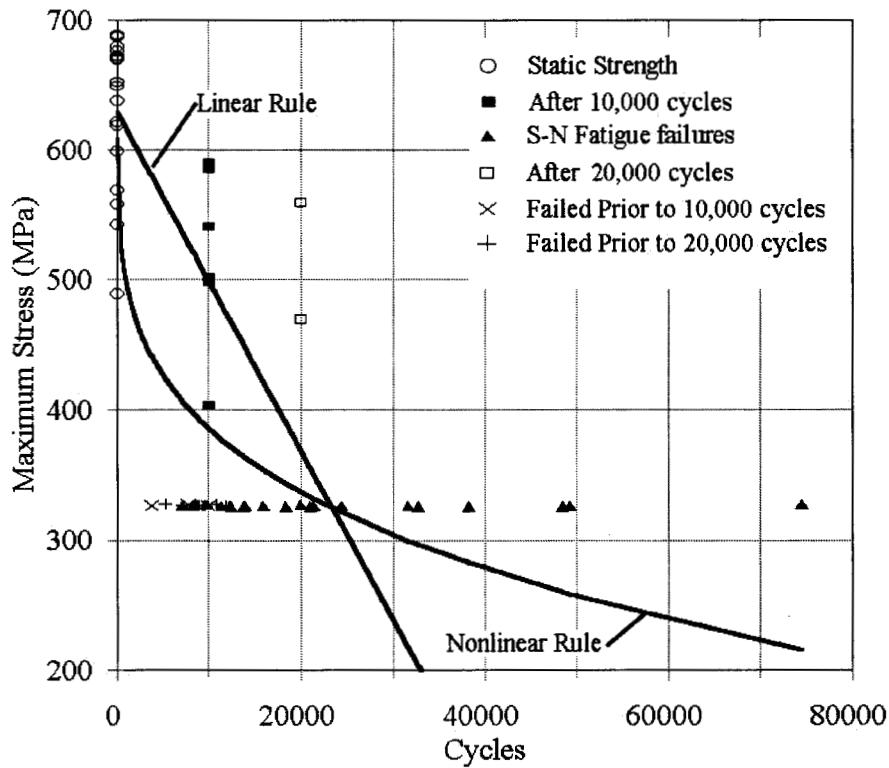
Figure 50. Residual Strength, R = 0.5.
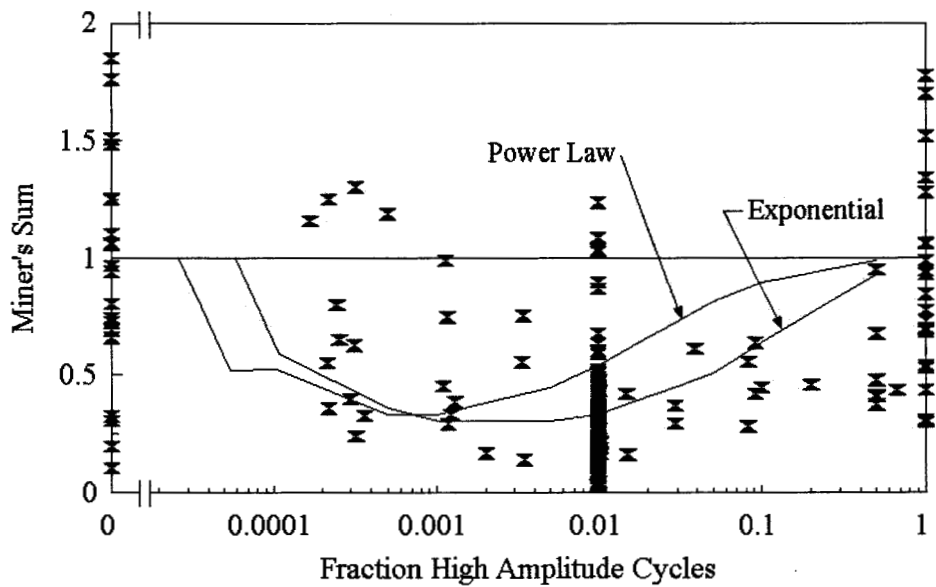
Figure 51. Lifetime Prediction for Two-Block Spectrum at 325/207 MPa
Maximum Stress Levels (R=0.1); Exponential and Power Law Fatigue
Models.
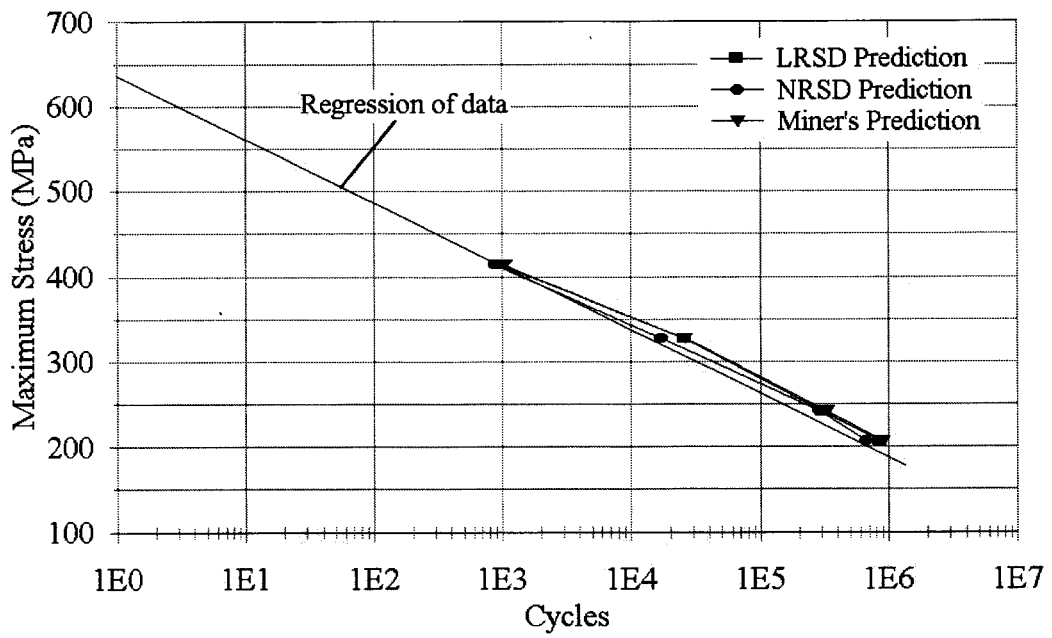
Figure 52. Mod 1 Spectrum Lifetime Prediction R = 0.1.
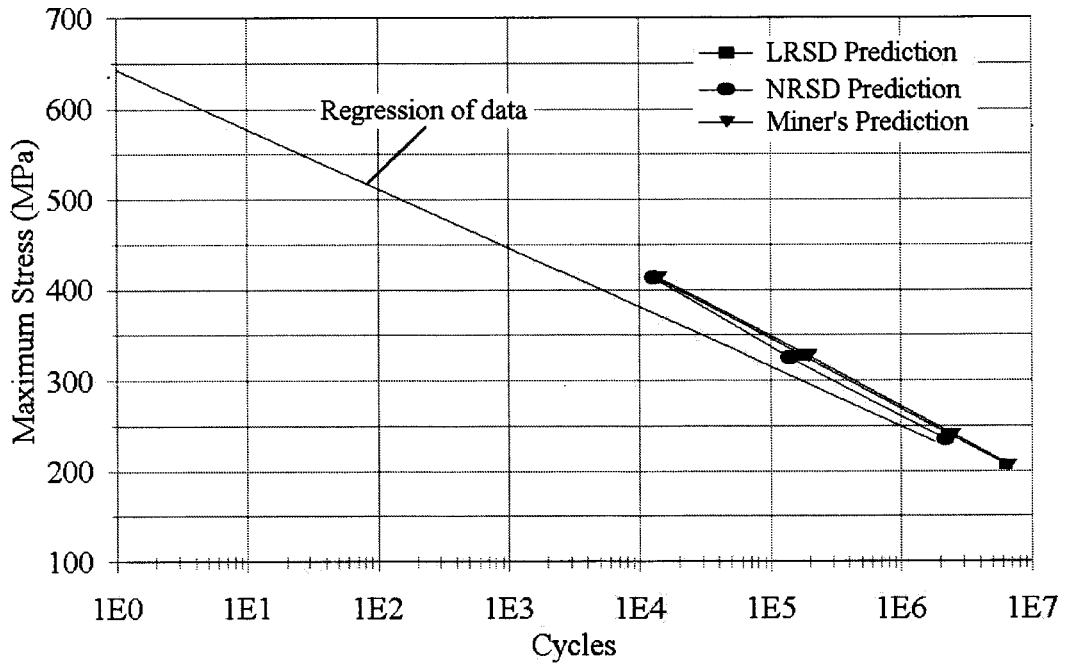
Figure 53. Mod 1 Spectrum Lifetime Prediction R = 0.5.
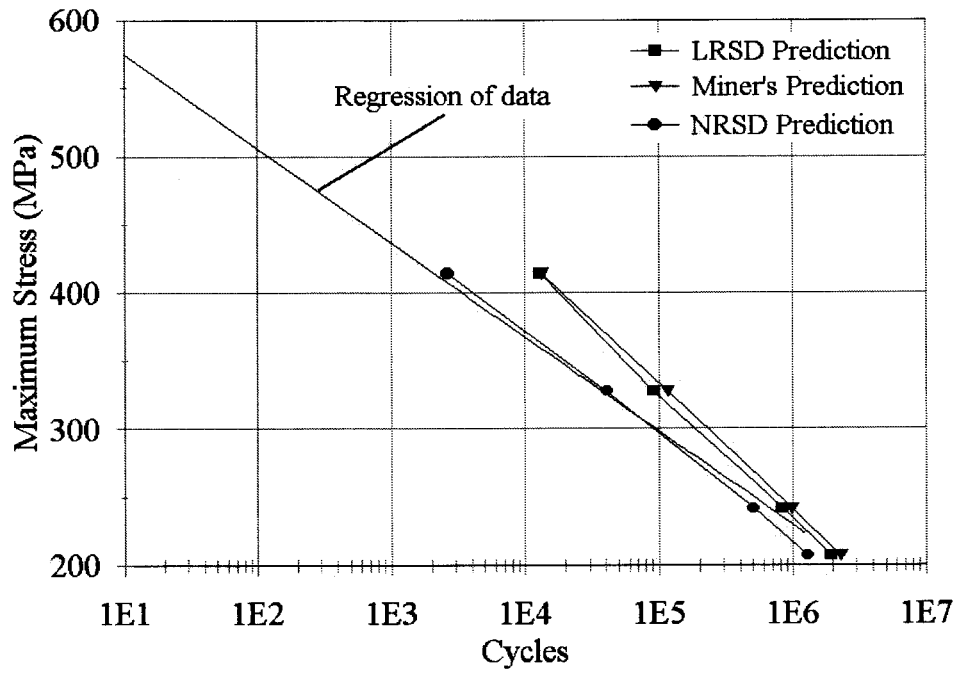
Figure 54. Mod 2 Spectrum Lifetime Prediction R = 0.1.
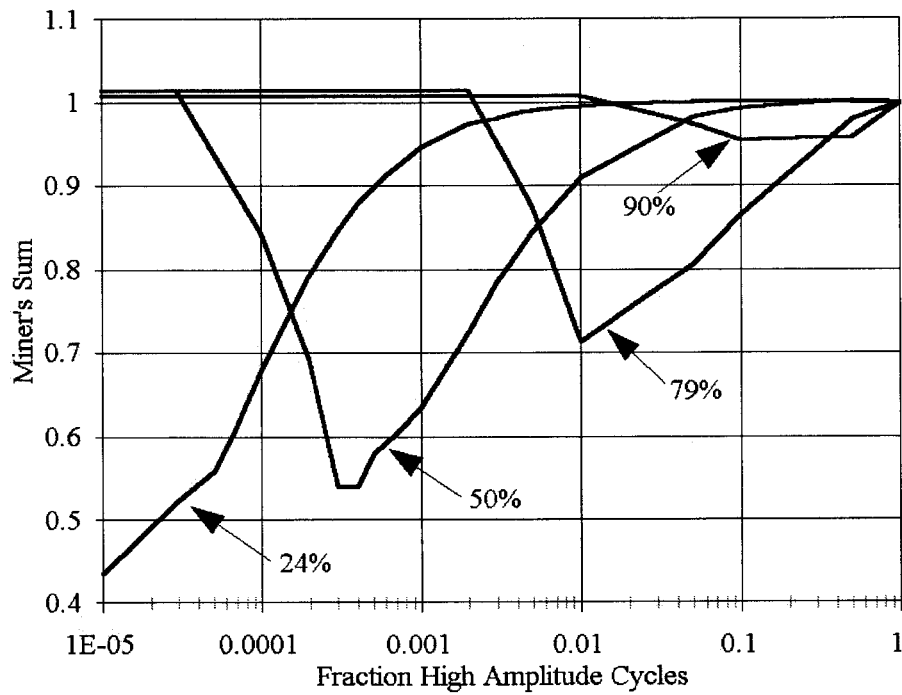
Figure 55. Two-Block Load Level Sensitivity Low-Block Amp as percent of High-Block Amp.

5.7. Conclusions

Spectra involving two or more different stress levels generally result in lifetimes less than that predicted by Miner's sum. Better agreement can be found by the application of residual strength degradation based rules. Although the nonlinear rule introduces an unknown parameter that must be determined experimentally, it does provide a better prediction of lifetimes than the linear model. Sequencing effects of the cycles at different stresses is not significant for repeated block loading. Testing of two modifications of the WISPERX spectrum has demonstrated that the nonlinear residual strength model is more accurate when greater variability is present in the stresses.

As a near-term design recommendation, a conservative approach would be to assume a miner's sum at failure of 0.10 rather than 1.0. This follows the recommendation in Reference 57. In the long-term, it is expected that a more accurate and useful prediction can be developed based on residual strength models. Further testing and model development are required to bring a model of this type into closer agreement with the experimental data; this view is based, in part, on the broader-based results in References 21 and 43.

6. GIGA - CYCLE TESTING AND RESULTS

6.1. Summary

This section describes the development and application of a novel, low-cost, high-frequency fatigue testing apparatus, and its application in obtaining very high cycle data for small impregnated glass strands. The first known tensile fatigue data out to 10^9 to 10^{10} cycles have been obtained using two matrix systems. The results can be represented by a power law S-N trend or an exponential trend with a fatigue limit around 10^8 cycles, or a combination of the two. Both these results and related tests to 10^9 cycles using larger strands support the use of a power law extrapolation of S-N data trends to very low stresses and long lifetimes. This is critical in the application of cumulative damage laws to spectrum loading [21, 43]. Interpretation of the results for larger volumes of material is difficult due to the high static strength and less steep S-N curve for the very small strands. A tougher resin system, 8084 vinyl ester, showed only slight improvements in fatigue resistance at high cycles.

6.2. Introduction

Composite wind turbine blade materials experience between 10^8 to 10^9 significant fatigue (loading-unloading) cycles in their 20 to 30 year lifetime. The design of wind turbines has required use of extrapolations from experimental data due to the lack of data beyond 10^7 or 10^8 cycles, with little guidance as to appropriate extrapolation models. The spectrum fatigue investigation showed two interesting features relating to high cycles. First, significant sensitivity to the fatigue model assumed in fitting the constant amplitude data [21, 43], and second, many of the stresses in the spectrum for overall lifetimes of 10^6 to 10^7 cycles were in the low stress range where no fatigue data exist. Thus, the damage contribution to be assigned to the low stress cycles requires extrapolation of the S-N data.

Testing to high cycles requires high frequencies to be practical, and high frequencies can only be used for very small specimens to avoid hysteretic heating and thermal failure of the polymer based composite [2]. Standard servo-hydraulic testing machines are limited in their frequency, and the actuator rod assembly also has wearing problems; piezoelectric actuators have displacement and thermal limitations, and standard vibration table equipment can be costly. In order to determine the high cycle behavior of impregnated glass strands, it was necessary to build a unique low cost testing apparatus with several test stations.

6.3. Test Equipment

The fiber testing apparatus used various low frequency audio speakers (woofers) as actuators which could handle frequencies as high as 300 Hz. Speakers which were 25 to 30 cm in diameter with audio handling capabilities greater than 100 watts were used. These speakers could deliver a maximum force of approximately 25 N with a displacement of approximately ±5 mm. To ensure some fiber-to-fiber contact and composite action in the unidirectional strand, the number of fibers was maximized to the capacity and frequency of the testing apparatus. With the force capacity of the

apparatus known, it was determined that a strand containing 45 E-glass fibers could be tested. Earlier studies have shown fatigue S-N response similar to laminates when 30 fibers are used [65 - 67]. A total of five test stations were constructed.

Grips (Figure 56) for load transfer to the coupon were constructed from carbon fiber prepreg to minimize the grip mass attached to the speaker; grips generally weighed less than 20 grams including the coupon clamping bolts. The test coupon was clamped in a sandwich friction grip system with the clamping force supplied by two bolts. Polishing paper, 1000 grit with a self adhesive back, lined the internal surface of the grips to ensure coupon gripping with the low clamping pressures generated by the 2 mm diameter clamping bolts. The lower grip assembly was then bonded to both the speaker dome and the cone with Plexus AO425 adhesive. The upper grip assembly was bolted to the load cell on the crosshead, which completed the load transfer path. The crosshead was moveable by two 6 mm bolts, which were used to apply the mean cyclic load to the test coupon. A machinists level ensured that the crosshead was moved parallel with the lower grip assembly.

The load cell chosen for the apparatus was a steel cantilever beam design, Omega Engineering Incorporated, LCL-005. This load cell held calibration and had a very small zero load offset during the long duration tests of a year or more. Other low force, canister type load cells were tried, but their construction out of aluminum limited their use to a few million cycles. Several were broken.

Various data acquisition hardware was utilized, including: computer data acquisition, digital oscilloscopes and an Instron 8500 electronic display tower. A sine-wave frequency generator supplied the waveform to a 120 watt audio amplifier which drove each speaker. Separate frequency generators and amplifiers were used to minimize any electrical noise or crosstalk between the test stations. Approximately 10 to 40 watts per speaker apparatus was required, which allowed for small uninterrupted power supplies to provide clean and continuous electrical power to the equipment.

6.4. Test Strand Geometry

A small strand containing 45 E-glass fibers with an average fiber diameter of 10.6 μm was constructed with fibers carefully removed from an Owens Corning Fabrics, OC-990-BC-2385-4093 roving. These strands were then drawn through a bath of resin and suspended vertically to cure. The final coupon diameter was between 0.09 and 0.1 mm, with an average fiber volume fraction of 0.55. The resin for most tests was an unsaturated orthophthalic polyester resin, CoRezyn 63-AX-051, obtained from Interplastic Corporation. Additional tests were run on the same strands, but with a Derakane 8084 vinyl ester resin. The cured strands were cut to length and bonded to 75 g/m^2 paper tabs using silicone sealant and a structural adhesive, Hysol EA9309.2NA, as shown in Figure 57. The gage length of the strand was 25 mm. The silicone rubber was used to reduce the stress concentration as the strand entered the tab. The final specimen was post cured at 60°C for 2 hours.
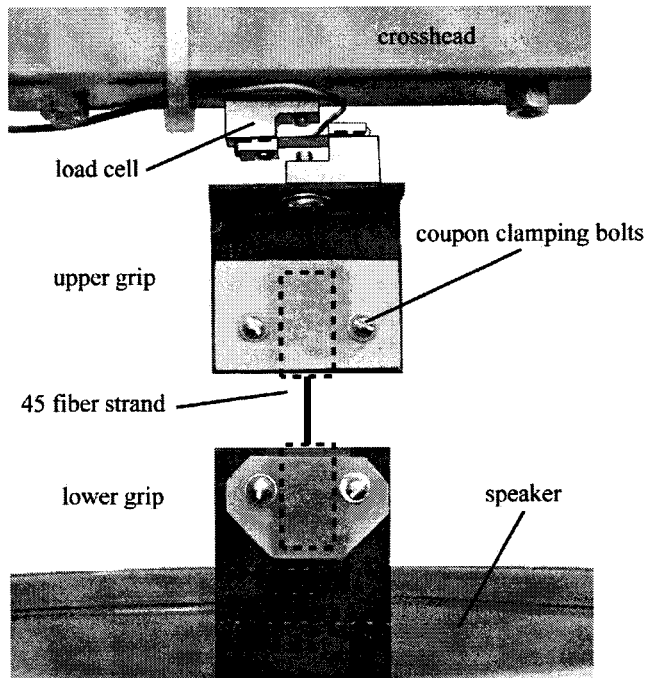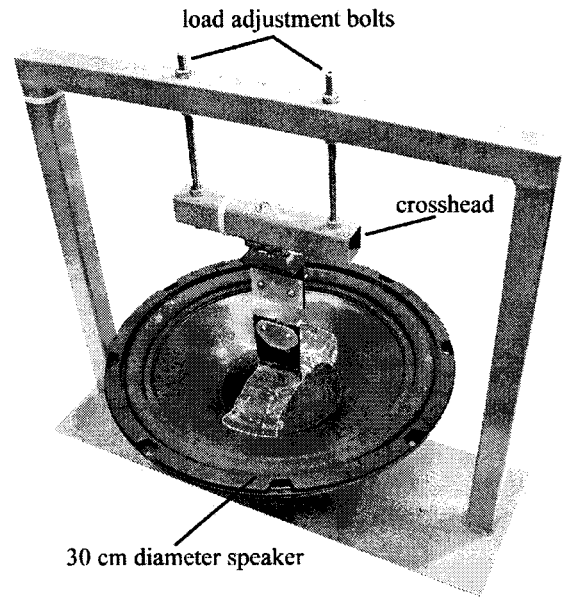
Figure 56. Small Strand Test Apparatus.
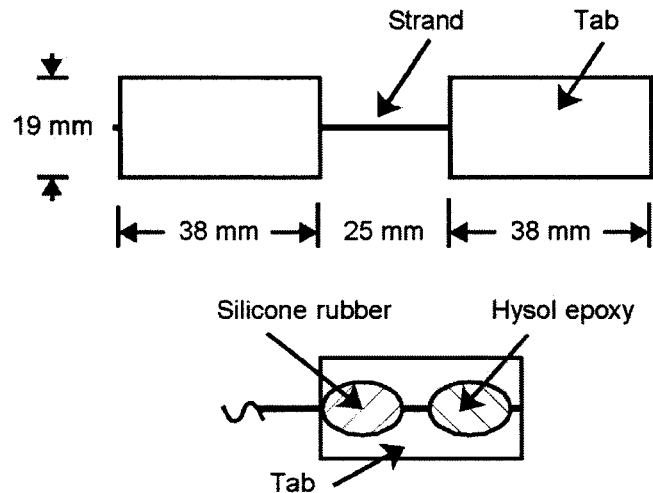
Figure 57. Small Strand Test Geometry.

6.5. Testing Procedures

The specimens were carefully loaded into the grips, aligned with the load train, and clamped into place. The paper tabs extended a millimeter or two outside the clamps, again in an effort to reduce stress concentrations as the strand enters the grips. Alignment was critical for the same reason. Specimen misalignment produced out-of-plane movement of the grips which was easily visible and corrected. The maximum applied loads ranged from 2.94 to 8.83 N for the fatigue tests and 16.67 N for the static tests.

The static tests were performed by attaching a 12.6 volt battery across the speaker terminals (4 ohms), which drove the speaker at a reproducible displacement rate of 140 to 150 mm per second, similar to the displacement rate in fatigue. This produced strand failures in approximately five to ten milliseconds. Fatigue tests were run with a sinusoidal waveform at the highest frequency possible, which was generally limited to 200 Hz due to the acoustical noise. No surface temperature increase was noticeable, as initially monitored by temperature sensitive paints. Coupon failure was defined as the inability of the coupon to hold the prescribed maximum load, which usually coincided with separation of the strand. Coupons which were stopped prior to failure are termed "run outs".

The control mode of the apparatus was modified position control, where the cyclic load was manually adjusted throughout the test to best maintain the loads. Most tests only required daily adjustments. Figure 58 shows the maximum daily error for both the maximum and minimum loads applied to test coupon STR100 over a 55 day period (1×10^9 cycles). In position control, the applied load will drop if the coupon stiffness changes or the coupon slips in the gripping fixture. The frequency of the sinusoidal waveform was varied approximately inversely with the maximum stress level, giving an average displacement rate over a half-cycle of 110 mm/s; the lower frequencies at higher loads limited any hysteric heating.
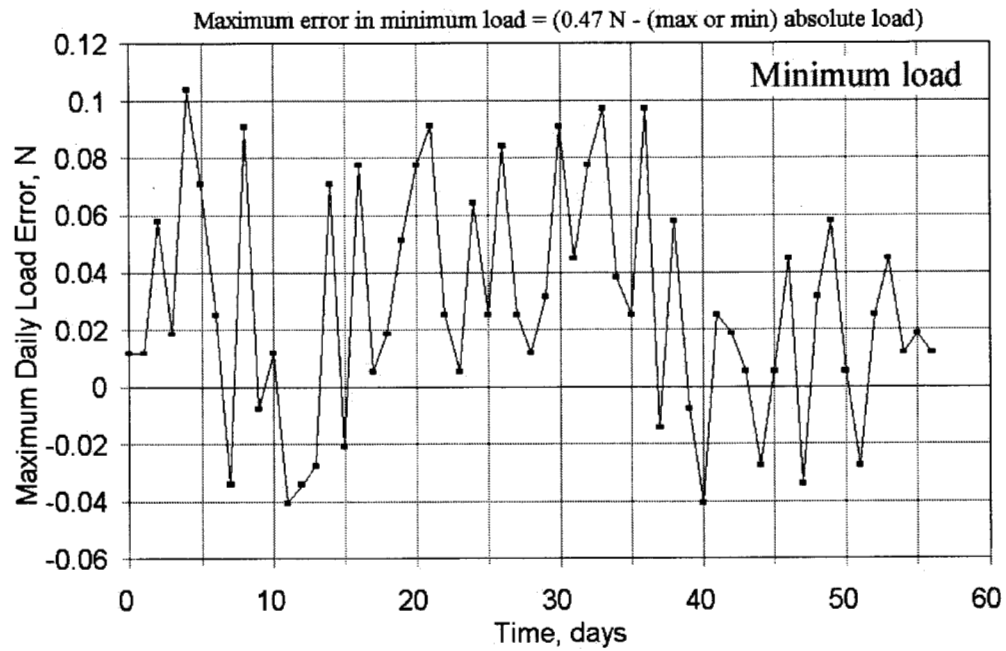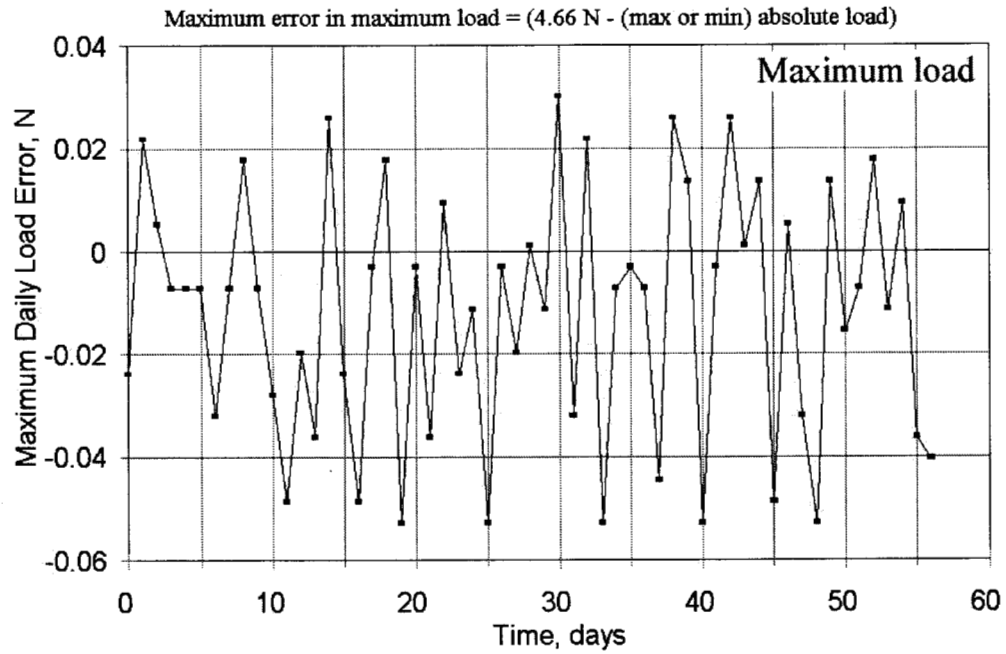
Figure 58. Sample of the Maximum Errors in the Maximum and Minimum Applied Loads for Coupon STR100, Average Maximum Load = 4.66 N..

After testing, a sample of the strand in the tab was removed for microscope examination for number of fibers in the strand and their diameters for calculation of the maximum stress; this determination of the cross-sectional area of the fibers was carried out for samples from every strand. Eight of the test coupons were found to deviate from the required 45 fibers in the gage section (ranging between 42 and 51 fibers); the applied load was adjusted linearly to normalize it to a fiber cross sectional area of 45 fibers. An average cross-sectional fiber area was used in the normalization, since all the coupons were manufactured from the same individual fibers, just at different locations along the length of a 12 meter long roving.

6.6. Results and Discussion

The static and fatigue strand test data are listed in the database [2]. Most of the coupons failed in the gage section, with significant fiber failures (brooming) and transverse matrix cracks. The polyester resin used to impregnate these fibers had an ultimate strain to failure of approximately 2.0 percent [36], and the test coupons showed numerous transverse matrix cracks along the length of the strand. The coupons which were run-outs showed no noticeable matrix cracking or broken fibers in the gage section.

The S-N data are presented in Figures 59 to 62, in terms of load, stress, normalized stress and strain. The high strength and strain to failure of the small strands is also extended to the fatigue resistance, with very high strain levels at high cycles, and a less-steep S-N trend than for larger coupons at similar fiber content.

Figures 63 and 64 compare the normalized S-N data plotted linear-log and log-log, respectively, with exponential and power law curve fits (forced through one-cycle data, not including runouts) Equations [1] and [2], respectively. The power law trend fits the data well, including run-outs. The exponential trend fits only if a fatigue limit or slope decrease around 10^8 cycles is included. A combination of exponential fit at lower cycles and power law fit at higher cycles is shown in Figure 65.

Larger strands, taken from D155 fabric, containing 2000 fibers (Owens-Corning OC 107B-AC-450) were also impregnated with the ortho polyester resin and tested, as described in more detail later in the section on fiber content effects. These were tested in an Instron 8511 servo-hydraulic machine at a maximum frequency of 80 Hz. Figure 66 shows the larger strand data, extending to between 10^8 and 10^9 cycles, fit with the exponential and power law models, and a combination. The data are similar to the smaller strand data in Figure 63. Figure 67 contains a combined plot of the two data sets. The larger strands show a slight flattening in the 10^8 to 10^9 cycle range on a semi-log plot. The large strand data tend to validate the trends for the smaller strands, which can be run to higher cycles due to the higher frequencies (the small strands tests required 579 days to reach 10^{10} cycles).

Comparison of these data with earlier results for standard coupons using the same strands in unidirectional D155 fabric composites is shown in Figure 68. The larger coupons show a lower

98

strength, as discussed in the next section. The laminate results also depend on the fiber content as discussed later, with the lower fiber content showing a normalized S-N slope, b, of about 0.10 (Equation 1). This is the lowest slope measured for glass fiber materials in standard coupons [2]. The strand data show somewhat less steep S-N trends in addition to the higher static strength.

Use of the strand data in blade design is problematical, due to the size effects shown in Figures 67 and 68. At 10^6 cycles, the small strand strains are about 2.0 percent, while the best of the standard coupon materials give a strain in the range of 1.2 percent, and the laminates with higher fiber contents are in the range of 0.6 percent (discussed later). Thus, it is difficult to use the small strand data to establish allowable strains in conventional coupons. However, the small strand data may be useful in establishing the best choice for a curve fit model, exponential versus power law. The power law fit appears to be the best choice at this time, as evidenced in Figure 66.

The small strand tests may also be useful in exploring factors such as matrix selection for high cycle fatigue resistance. Figure 69 presents data for the toughened vinyl ester resin Derakane 8084 described earlier, in comparison to the baseline orthophthalic polyester. The vinyl ester has higher toughness and strain to failure, but approximately the same elastic modulus as the polyester. The data in Figure 69 indicate only a slight improvement with the 8084 at cycles above 10^6. As reported earlier for many systems [2], the matrix has little effect in tensile fatigue resistance out to 10^6 cycles using conventional coupons.
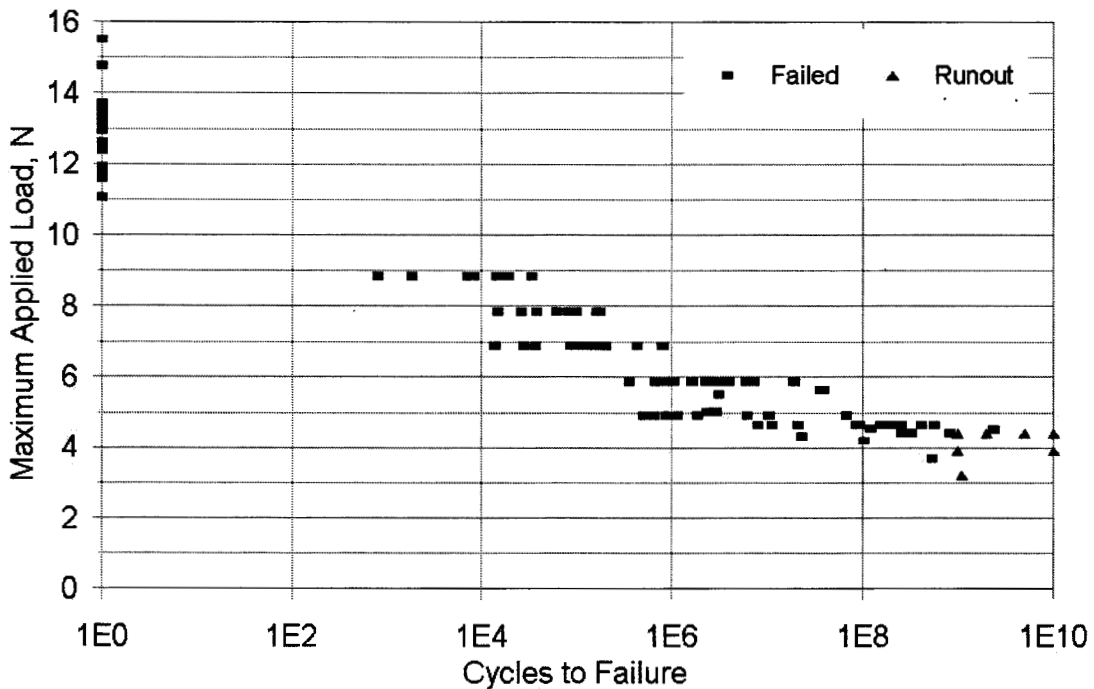
Figure 59. Load-Cycles Fatigue Diagram for Small Strands, Normalized to 45 Fibers, R = 0.1.
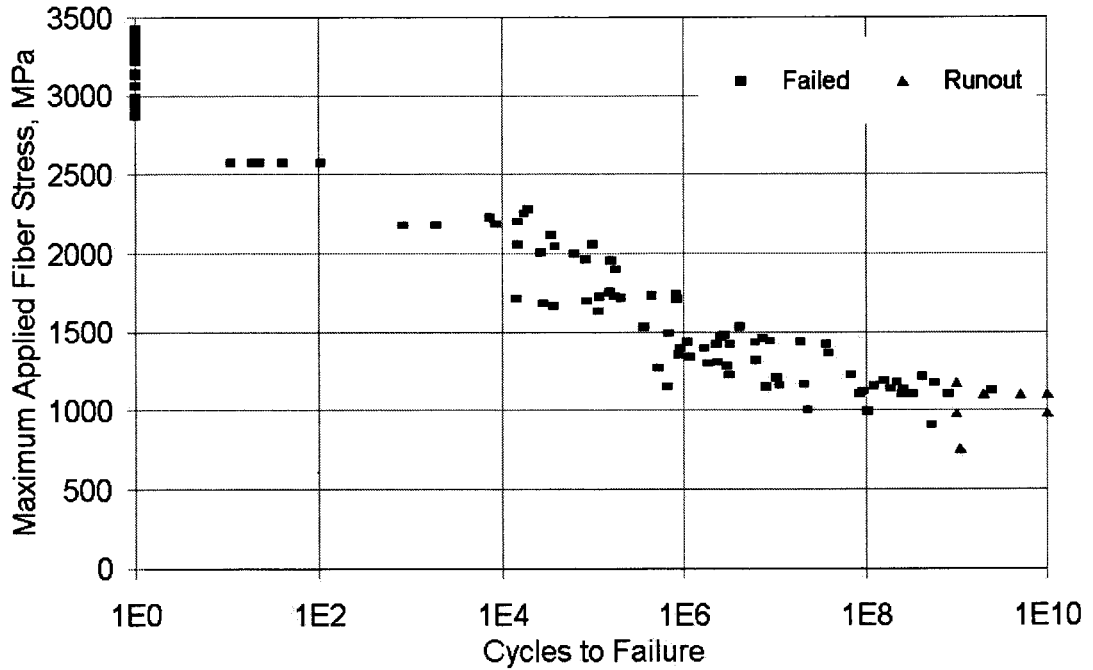
Figure 60. Maximum Applied Fiber Stress versus Cycles for Small Strands, R = 0.1 (using measured cross-sectional area of glass fibers only, excluding resin).
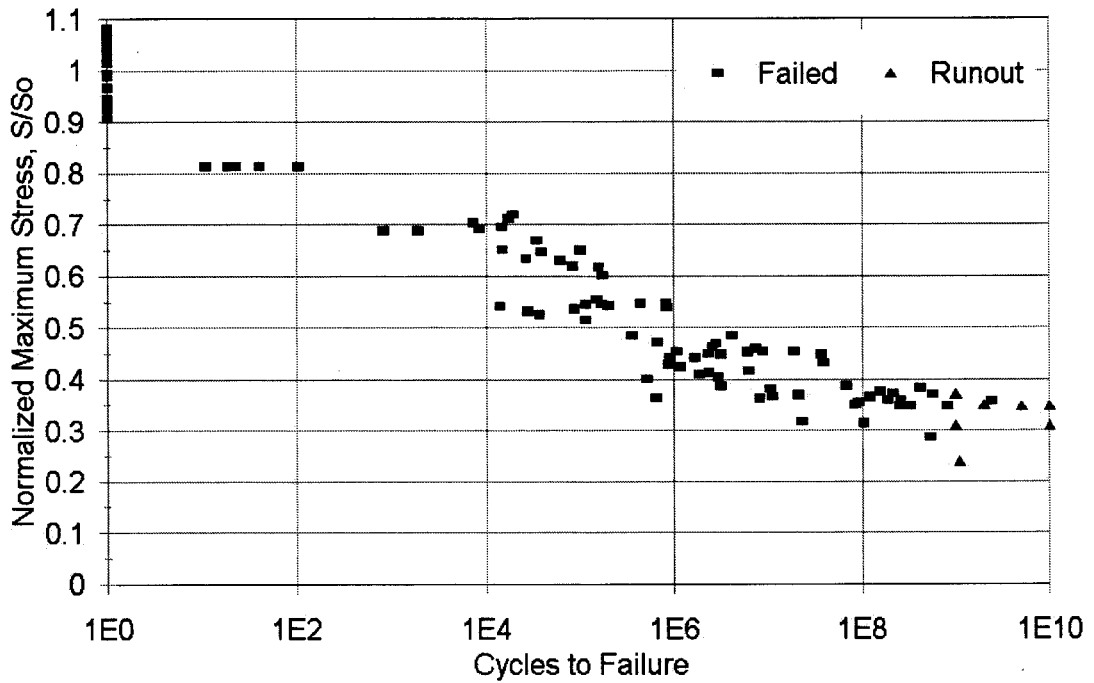
Figure 61. Normalized Maximum Stress versus Cycles Diagram for Small Strands, R = 0.1.
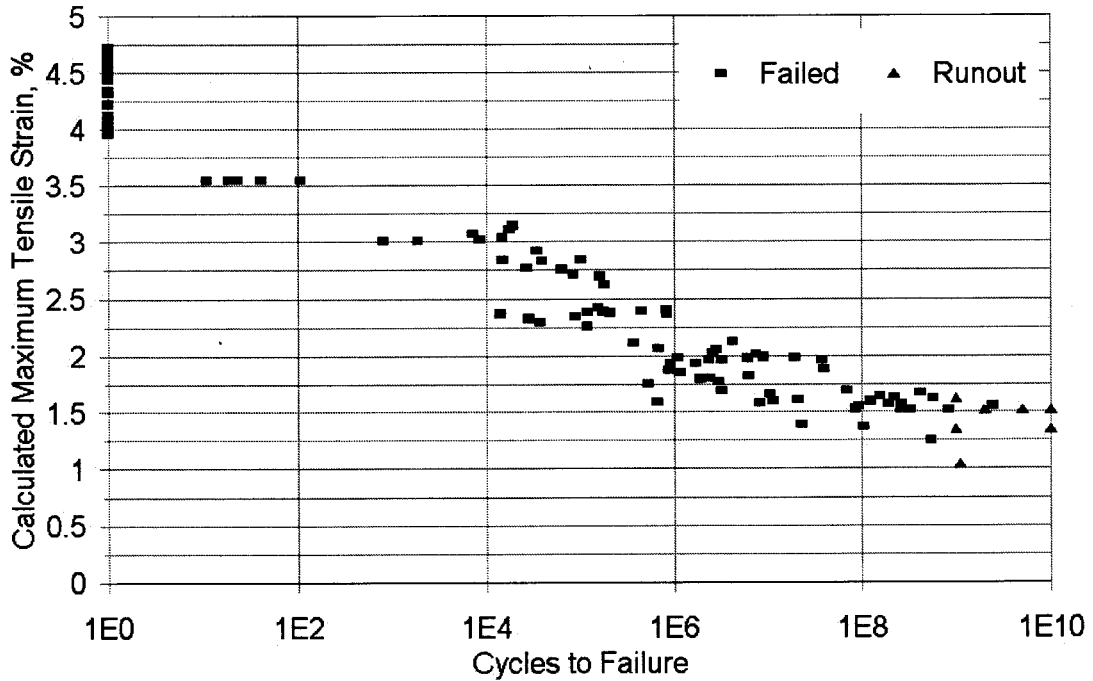
Figure 62. Calculated Maximum Tensile Strain versus Cycles for Small Strands, R = 0.1 (strain calculated by dividing maximum fiber stress by the fiber elastic modulus, 72.4 GPa).
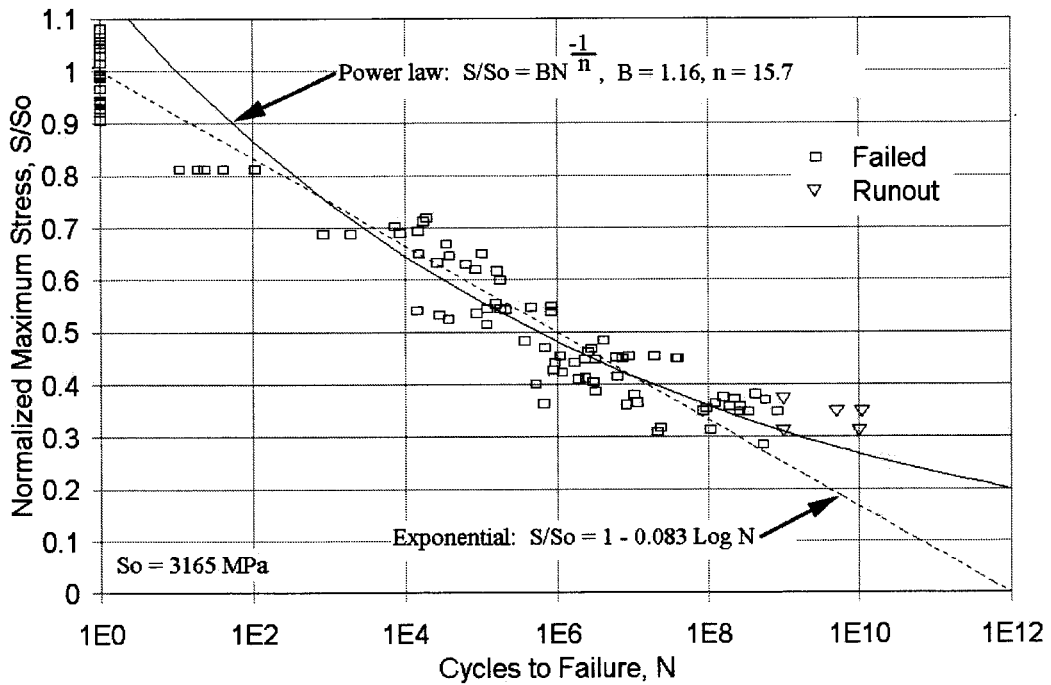
Figure 63. Normalized Tensile Stress versus Cycles for Small Strands with Trend Lines.
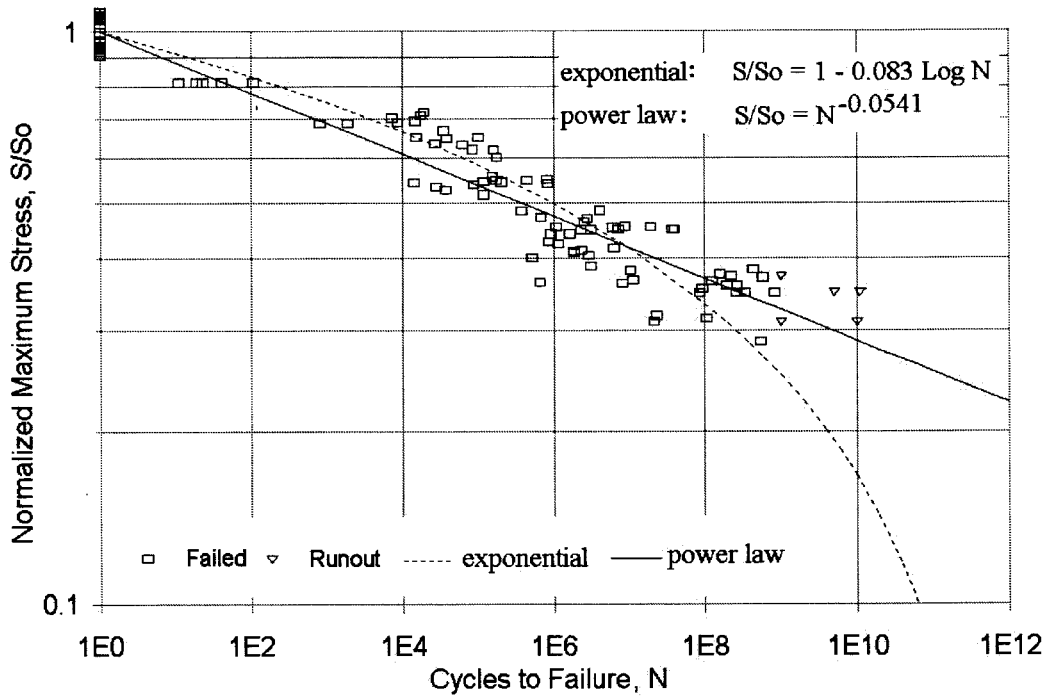
Figure 64. Log Normalized Tensile Stress versus Cycles for Small Strands with Trend Lines.
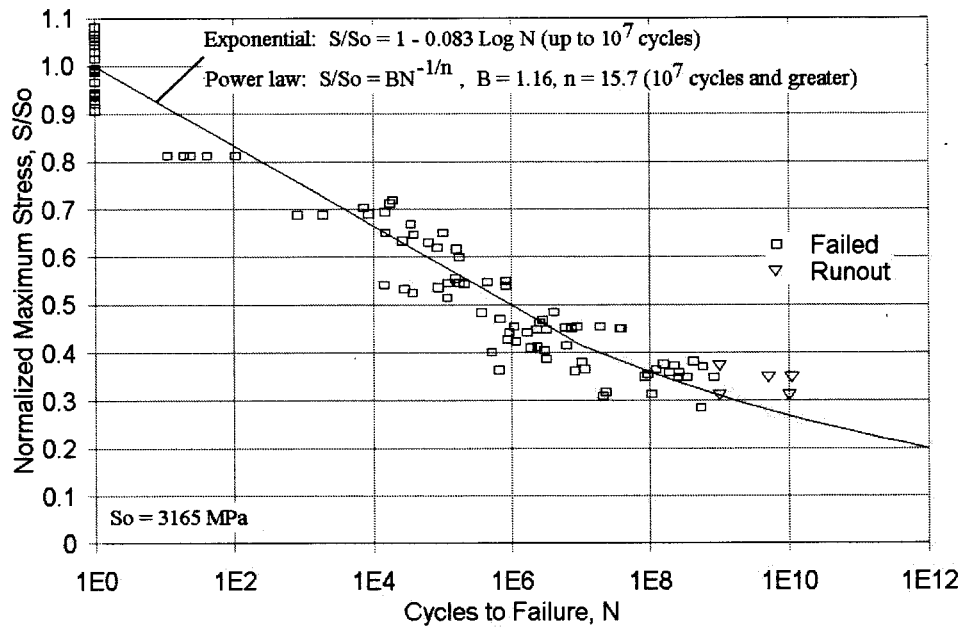
Figure 65. Normalized Tensile Stress versus Cycles for Small Strands with Trend Line.
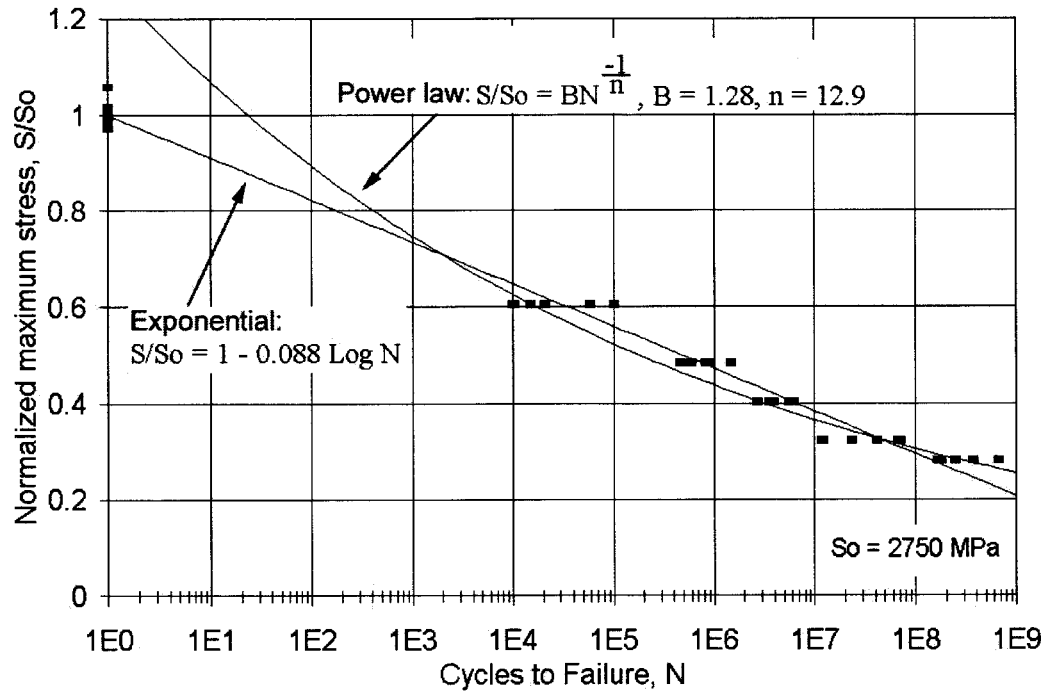
Figure 66. Normalized Fatigue Diagram for D155 Strands with 2000 Fibers.
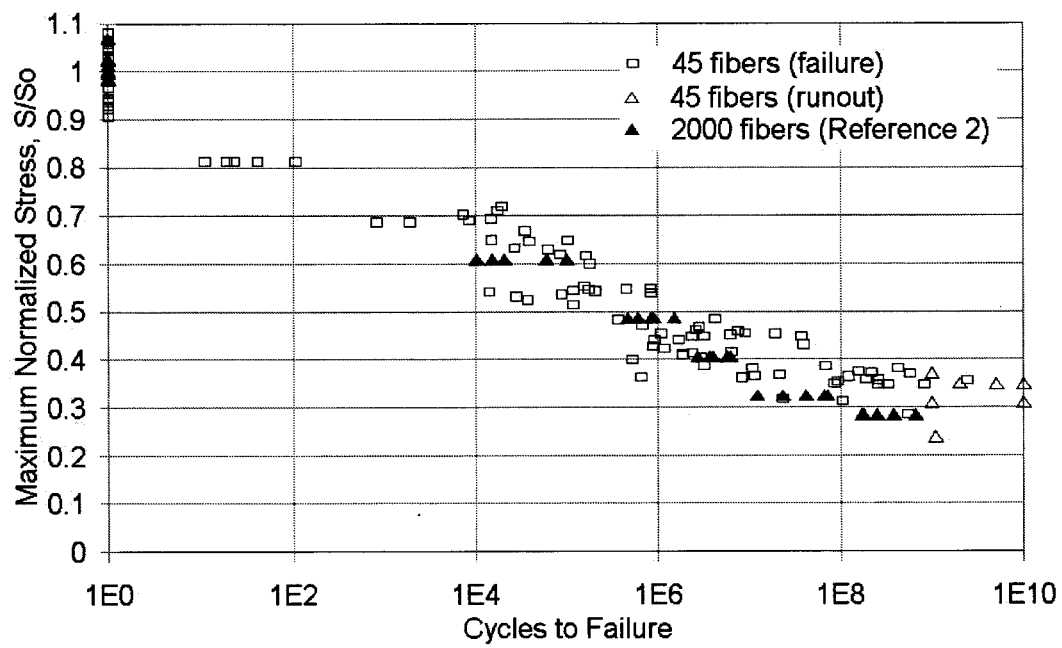
Figure 67. Normalized Fatigue Diagram for Small Strands with 45 Fibers
Compared with Larger 2000 Fiber Strands [2].
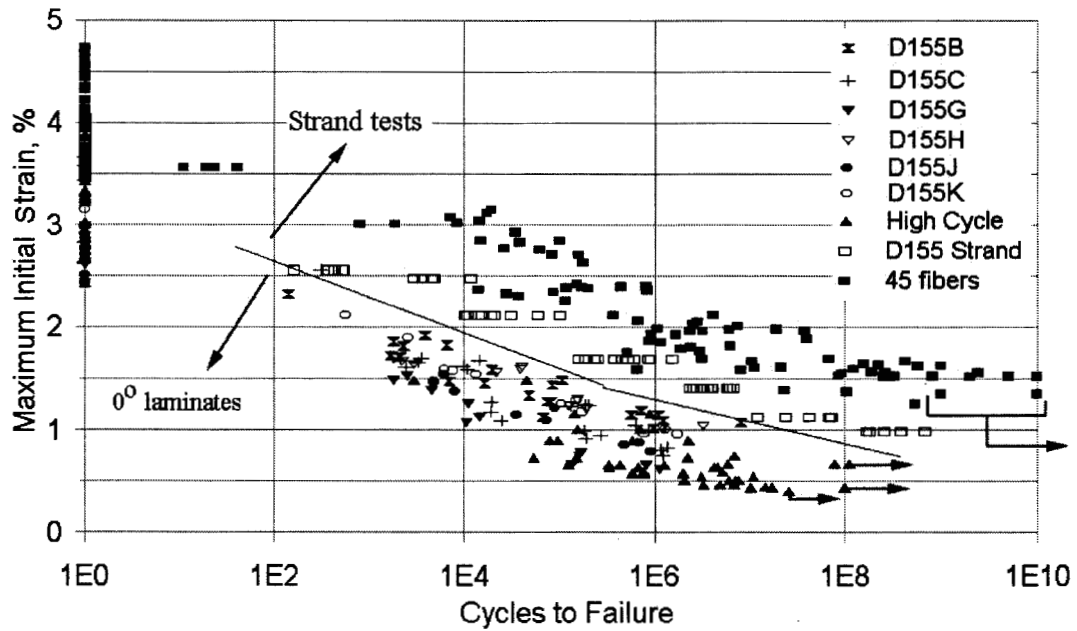
Figure 68. Maximum Initial Tensile Strain for Laminates and Small Strands, R = 0.1.
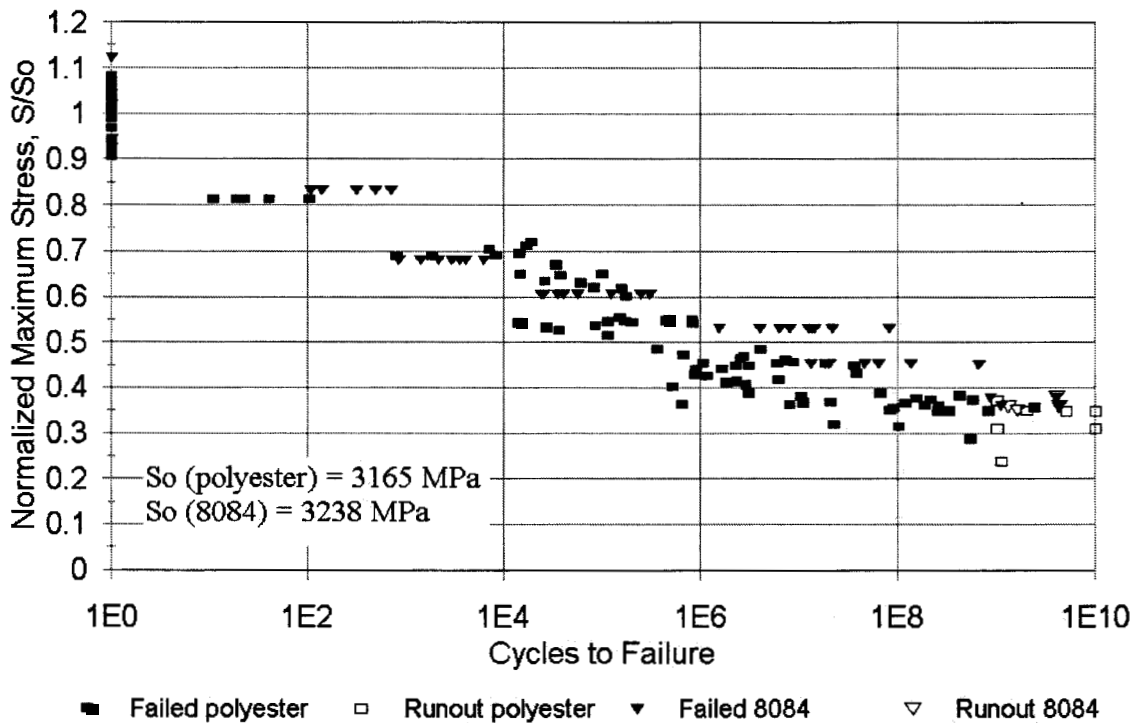
Figure 69. Normalized Maximum Stress versus Cycles for Small Polyester and Vinyl Ester Impregnated Small Strands, R = 0.1.

6.7. Conclusions

Small strand tensile fatigue data have been generated out to 10^{10} cycles with a speaker cone apparatus. The results show much higher static strength and fatigue resistance than for conventional coupons (in the moderate cycle range). The fatigue data support the use of a power law representation or else a fatigue limit around 10^8 cycles. Only small improvements are found at high cycles with a toughened resin.

7. EFFECTS OF STRAIN RATE AND TIME UNDER LOAD ON STRENGTH

7.1. Summary

Static tensile and compressive strength data are presented in the database for a wide range of materials, including different environmental conditions. These data are obtained from standard size test coupons loaded at a high strain rate to be consistent with fatigue strain rates. The high strain rate produces higher strength values than would low strain rates. The use of these strength data in blade design requires consideration of the timescale of loading under extreme wind conditions. If the maximum stress conditions for the blade involve significant time at high stress, such as more than one second, then the timescale of the event should be considered before using strength values in the database.

This section provides a detailed consideration of time under load effects for various laminates. The effects of time under load and strain rate are more significant than expected from earlier investigations. Load transfer between ±45° and 0° plies is sensitive to time under load, and contributes significantly to time effects in addition to the expected static fatigue effects for the glass fibers. Rate effects are significant in compression as well as tension. Knockdown in strength required for longer time durations are additive with factors such as strand waviness in woven fabrics, which reduce compressive strength, and environmental effects.

7.2. Introduction

Static fatigue effects in tension have long been known in composites containing glass fibers, and derive fundamentally from moisture related stress corrosion crack growth in glass [68]. Fiber or composite strength data show a consistent slope with strain rate or time under constant load for time scales varying from impact to long term loading, as in pressure vessels [69]. For composites using E-glass fibers, the tensile strength in clearly fiber-dominated situations (such as unidirectional laminates) is generally reported to decrease by the order of 3 to 4 percent per decade of either decreasing strain rate or increasing time under constant load. Limited data for this so-called static fatigue effect show increased effects if matrix dominated damage is important, as with random mat composites [70]. No previous data are known for time effects on compressive strength, which generally shows a matrix domination.

7.3. Results and Discussion

7.3.1. Stress-Strain Curves

Most of the time effects considered in this section involve laminates with a combination of 0° and ±45° plies. Figure 70 illustrates typical stress-strain curves for specimens of this type. In tension, as the stress increases, the first damage event is matrix cracking in the ±45° plies, which show matrix cracks growing parallel to the fiber direction. Laminate analysis shows this cracking to be dominated

106

by transverse tension in these plies, with a smaller contribution from the shear stress. Cracking in the ±45° plies reduces the laminate overall stiffness, producing a knee in the stress-strain curve. Above the knee, cracking continues as the stress increases. High crack density in the ±45° plies further reduces the secant modulus as shown. Cracking in the ±45°plies shifts more of the load they were carrying onto the 0° plies. Finally, the 0° plies approach their ultimate strain capability, and the laminate fails.
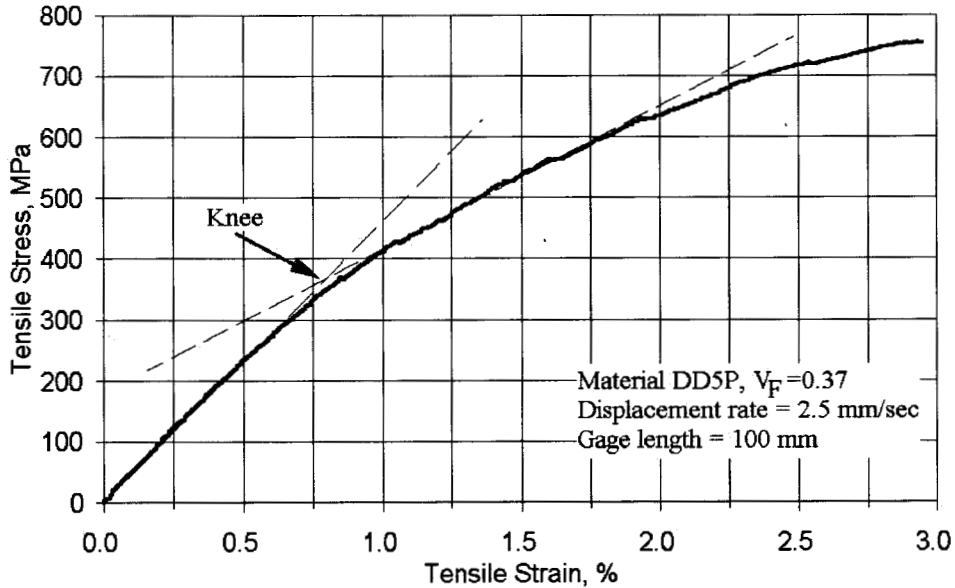
Figure 70. Typical Stress - Strain Curve for a $[0/\pm45/0]_S$ Laminate.

At stresses below the knee, where the strains are equal in all plies, the relative stresses in the 0° and ±45° plies in the 0°direction are approximately

$$\sigma_0 = \varepsilon_C E_0 = \frac{\sigma_C E_0}{E_0 V_0 + E_{45} V_{45}} \tag{8}$$

$$\sigma_{45} = \varepsilon_C E_{45} = \frac{\sigma_C E_{45}}{E_0 V_0 + E_{45} V_{45}} \tag{9}$$

where the subscripts are c: overall composite, 0: 0° plies; 45: ±45° plies and V_0 and V_{45} are the volume fraction of 0° and ±45° plies, respectively. If the ±45° layers become sufficiently cracked that they carry no stress, the stress in the 0° plies will be:

$$\sigma_0 = \frac{\sigma_C}{V_0} \tag{10}$$

Figure 70 is a schematic of the gradual transfer of stress from the ±45° plies to the 0° plies as matrix cracking in the ±45° plies accumulates. If the 0° ply ultimate strain is reached while the ±45° plies carry a significant fraction of the applied stress, σ_C, then the laminate strength will be higher than if the 0° plies carry all of the load. (The strain at failure will be about the same, but the laminate modulus, E_C, will be higher if the ±45° plies carry substantial load.) Cracking in the ±45° plies can be influenced by time under load, fatigue, and environmental effects. The load carried by the ±45° plies is a function of both the intralaminar crack density within the plies and any delamination between plies.

Figures 72 and 73 give the typical tensile stress-strain curves for the 0° and ±45° materials tested independently. The nonlinearity in the ±45° curve occurs both before and after cracking initiates. The high strains reached by the ±45° laminate reflects the need to delaminate the +45° and -45° layers before complete specimen separation occurs. The complex behavior of the ±45° material complicates interpretation of the behavior of the laminates containing both 0° and ±45° plies, particularly at the high stresses where rate effect tests can be carried to failure in a reasonable period of time.

7.3.2. Effects of Strain Rate

Tensile tests were run at varying strain rates for a series of laminates. Figures 74 [1] and 75 give results for tensile and compressive tests, respectively. All tests were run using a ramp loading function (see typical ramp loading function in Figure 76, bottom) with the indicated displacement rate. Note that, in tension, the laminates containing 0° and ±45° plies show steeper normalized slope than do the ±45° materials separately. The compression results in Figure 75 are also significantly rate sensitive, in several cases more so than in tension. Thus, the matrix plays a major role in these trends, in addition to fiber static fatigue.

Additional tests over a wide range of rates were run using the DD5 configuration $[0/\pm45/0]_s$, with a toughened vinyl ester matrix (Derakane 8084) and the baseline polyester (ortho polyester 63-AX-051). The data, shown in Figures 77 and 78, again show a strong rate sensitivity for both matrices, with the polyester the more rate sensitive. The lowest rates in Figure 76 show a decreased slope, possibly indicating an exhausting of the ±45° cracking effect, and a shift to the fiber static fatigue slope.

Figure 79 gives tensile strengths for impregnated strands removed from D155 fabric (see Chapter 10.3) versus displacement rate. These strands do not have a simple linear to failure stress-strain curve as might be expected, but show steps in the curves (Figure 79). The steps appear to relate to both partial strand failures and grip debonding. The data in Figure 78 follow the approximate 3 to 4 percent per log decade slope expected for E-glass dominated materials.

108

4.5 % per decade knee
shift with strain rate

decreasing E_L increases load on 0's
as cracking in $\pm 45^\circ$ plies increase

Stress

Strain

$$\sigma_c \left[1 - \frac{E_0}{E_0 V_0 + E_{45} V_{45}} \right]$$

$$\sigma_0 = \frac{\sigma_c}{V_0} \quad (\pm 45^\circ \text{ plies completely unloaded})$$

progressive $\pm 45^\circ$ cracking
at constant σ_L

Stress in 0° plies

$$\sigma_0 = \sigma_c \left[\frac{E_0}{E_0 V_0 + E'_{45} V_{45}} \right]$$ where E'_{45} is the current
modulus of the $\pm 45^\circ$ plies

progressive $\pm 45^\circ$ cracking
at constant σ_c

Stress in 0° plies

Time after 45's start to crack
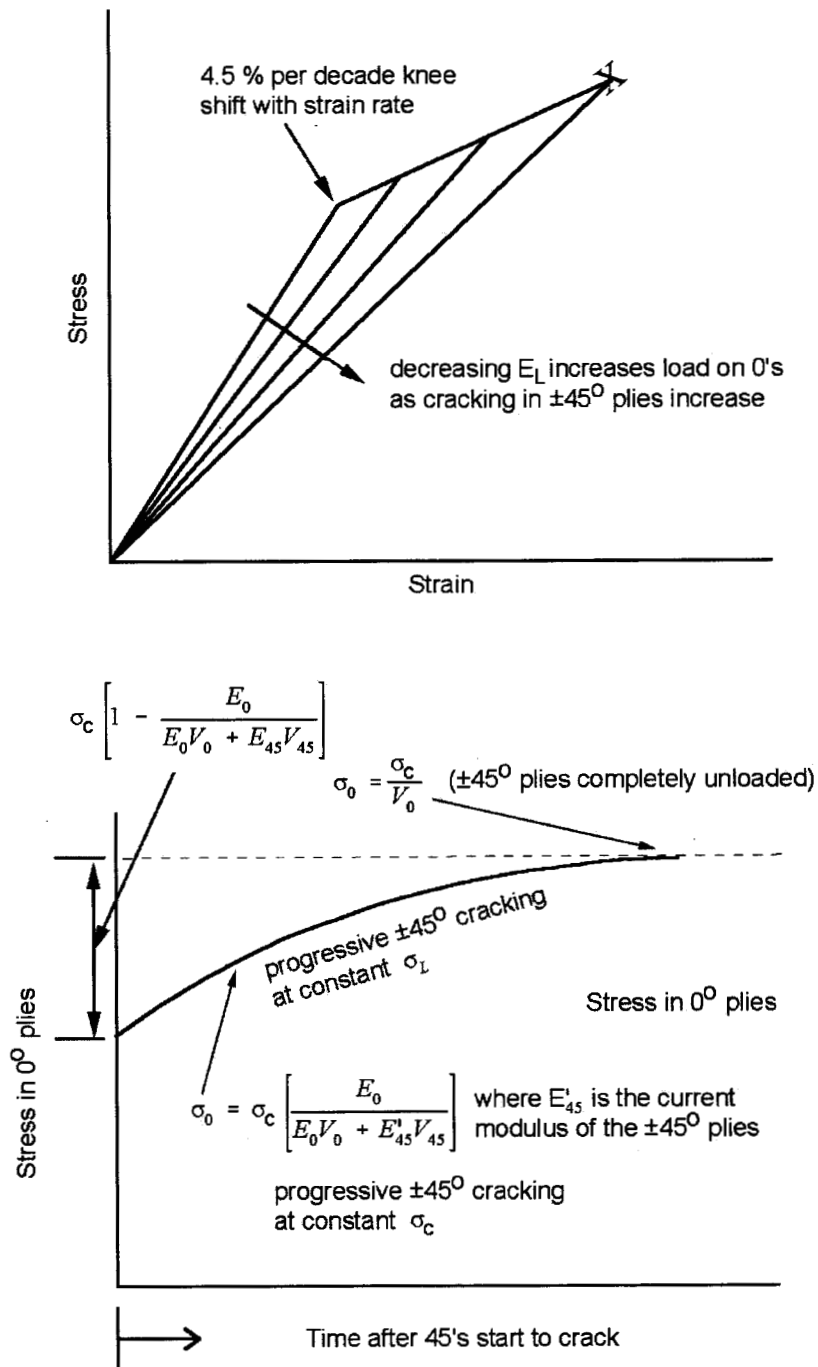
Figure 71. Schematics of Strain Rate Effects on the Stress-Strain Curve (Top) and the Gradual Shift in Load From the $\pm 45^\circ$ plies to the 0° Plies as Matrix Cracking Accumulates in the $\pm 45^\circ$ Plies (Bottom).

109
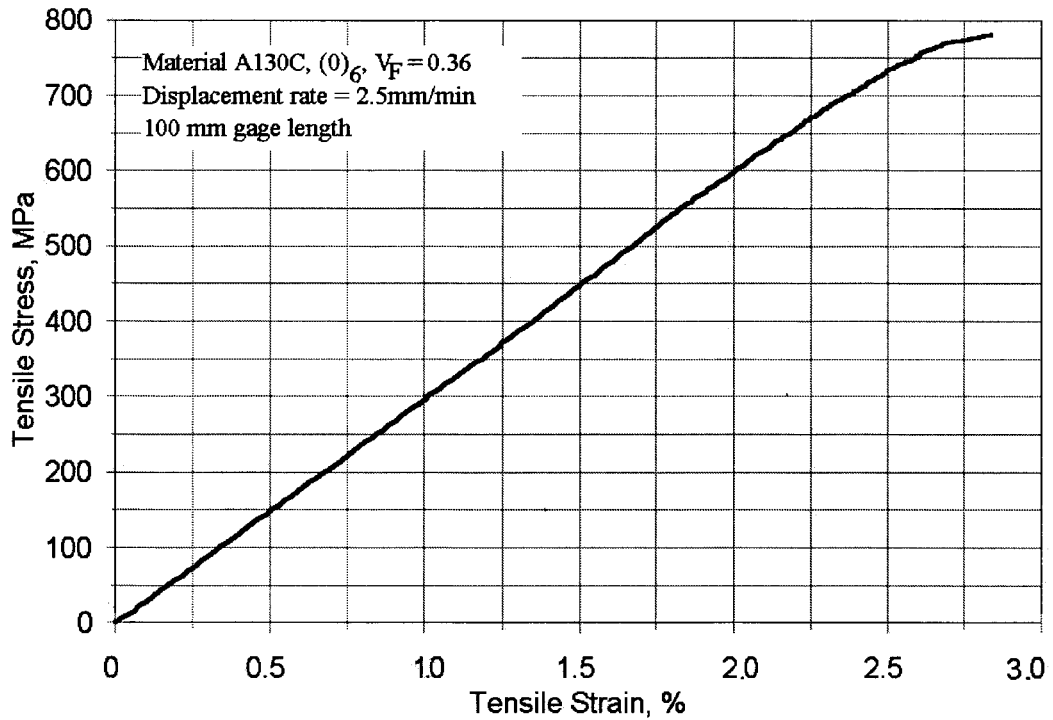
Figure 72. Typical Stress-Strain Curve for a Unidirectional 0° Laminate.
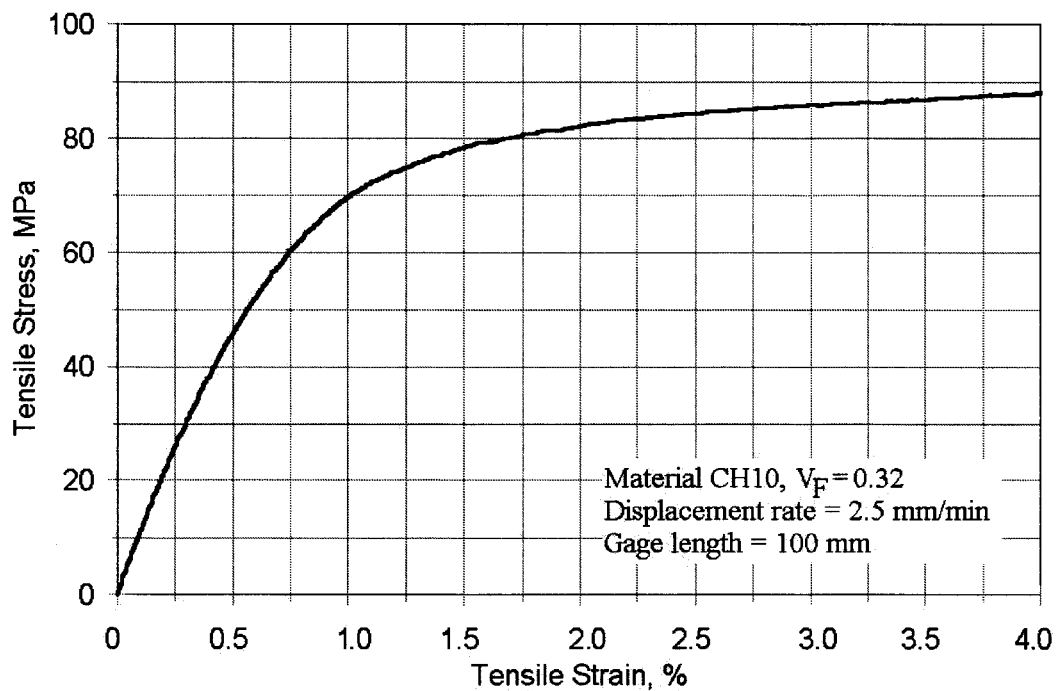
Figure 73. Typical Stress-Strain Curve for a ±45° Laminate.

110
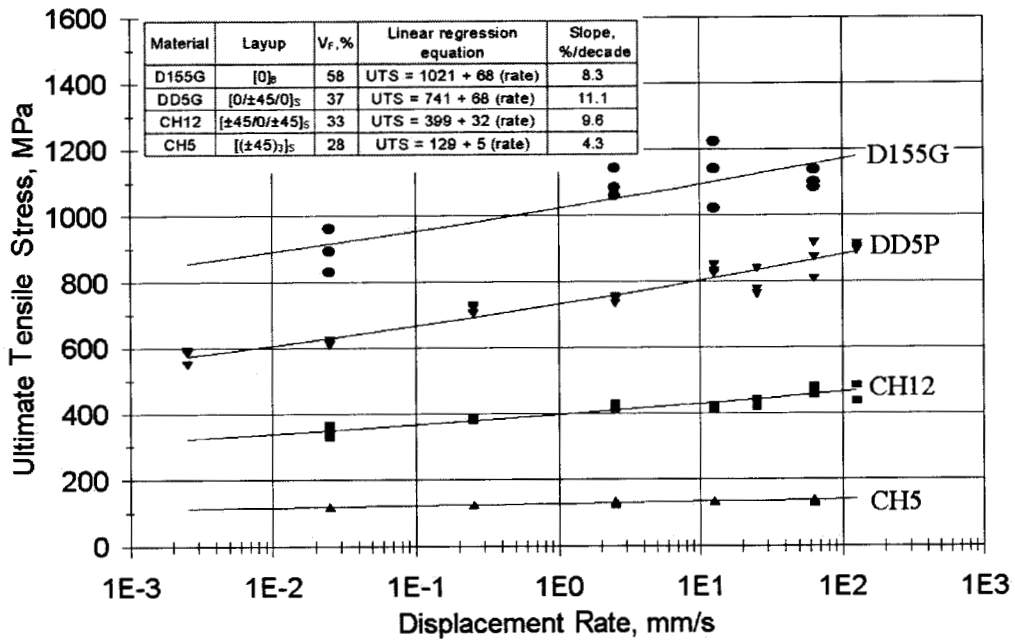
Figure 74. Ultimate Tensile Strength versus Displacement Rate (102 mm long gage section).

Material	Layup	V_F,%	Linear regression equation	Slope, %/decade
D155G	[0]8	58	UTS = 1021 + 68 (rate)	8.3
DD5G	[0/±45/0]s	37	UTS = 741 + 68 (rate)	11.1
CH12	[±45/0/±45]s	33	UTS = 399 + 32 (rate)	9.6
CH5	[(±45)2]s	28	UTS = 129 + 5 (rate)	4.3
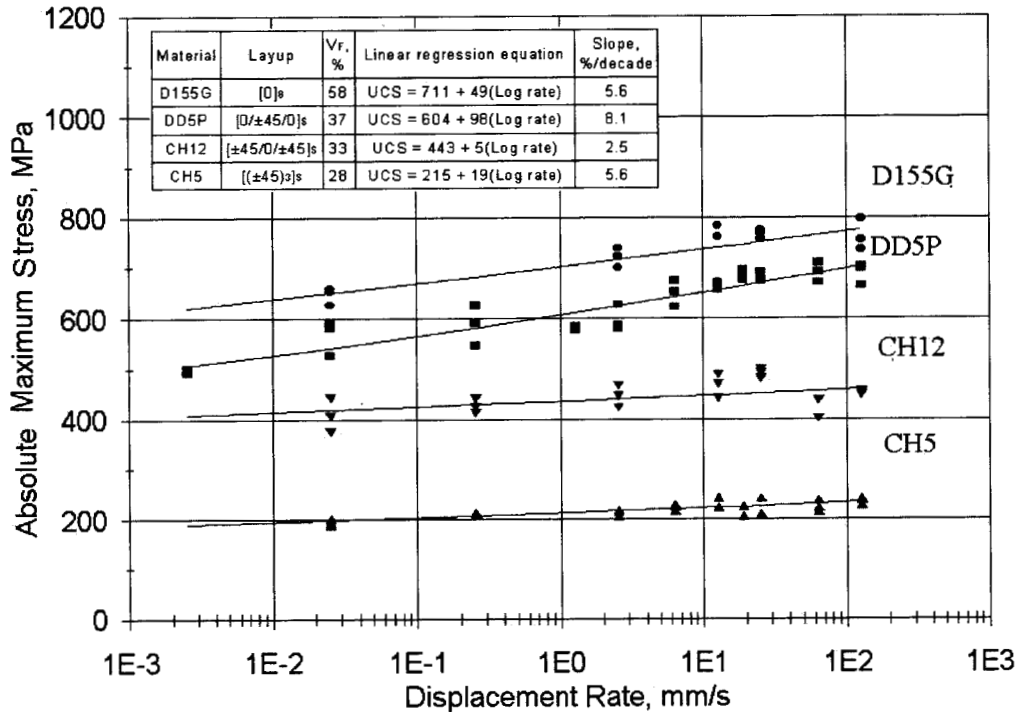
Figure 75. Ultimate Compressive Strength versus Displacement Rate (13 mm long gage section).

Material	Layup	V_F, %	Linear regression equation	Slope, %/decade
D155G	[0]8	58	UCS = 711 + 49(Log rate)	5.6
DD5P	[0/±45/0]s	37	UCS = 604 + 98(Log rate)	8.1
CH12	[±45/0/±45]s	33	UCS = 443 + 5(Log rate)	2.5
CH5	[(±45)3]s	28	UCS = 215 + 19(Log rate)	5.6

111

Constant displacement rate ramp tests

Displacement

decreasing
displacement
(strain) rate

Time

(a)

Constant stress to failure tests

Stress

ramp at 13 mm/s

Time
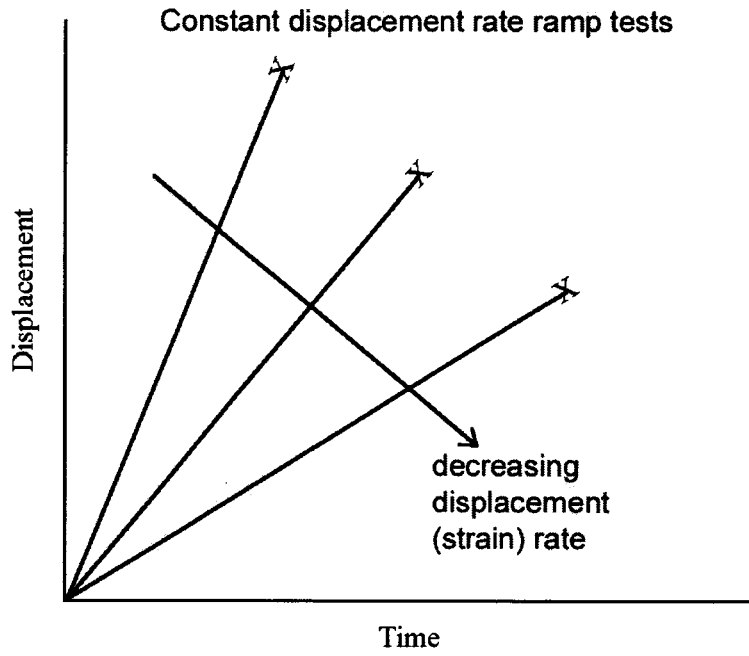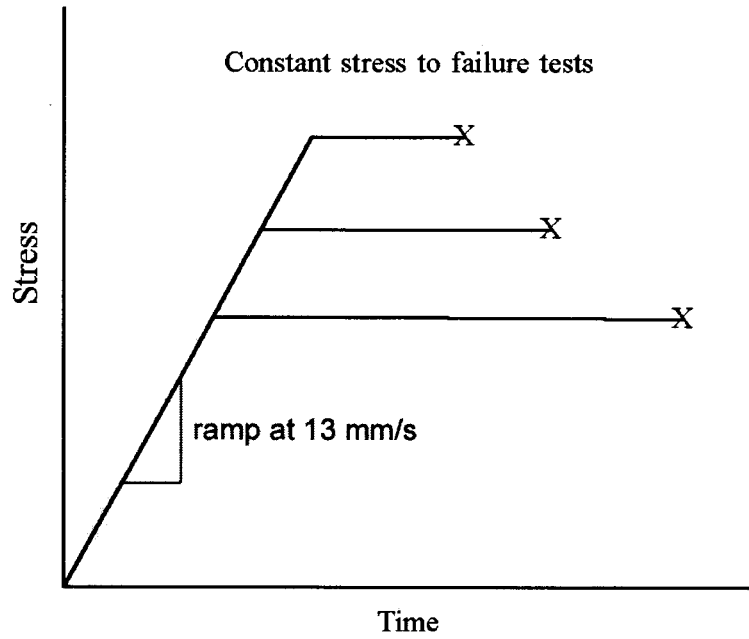
(b)

Figure 76. Comparison of Constant Displacement Strain
Rate and Constant Stress to Failure Tests.

112
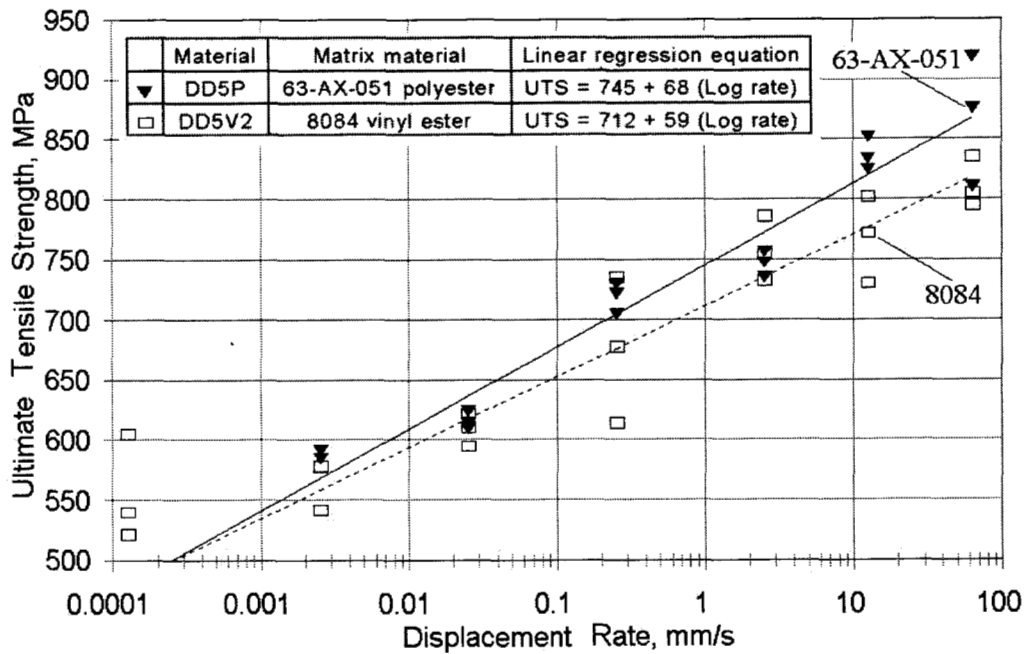
Figure 77. Ultimate Tensile Strength versus Displacement Rate for Two $(0/\pm45/0)_S$ Laminates; One Laminate with a Polyester Matrix and One with a Vinyl Ester Matrix.
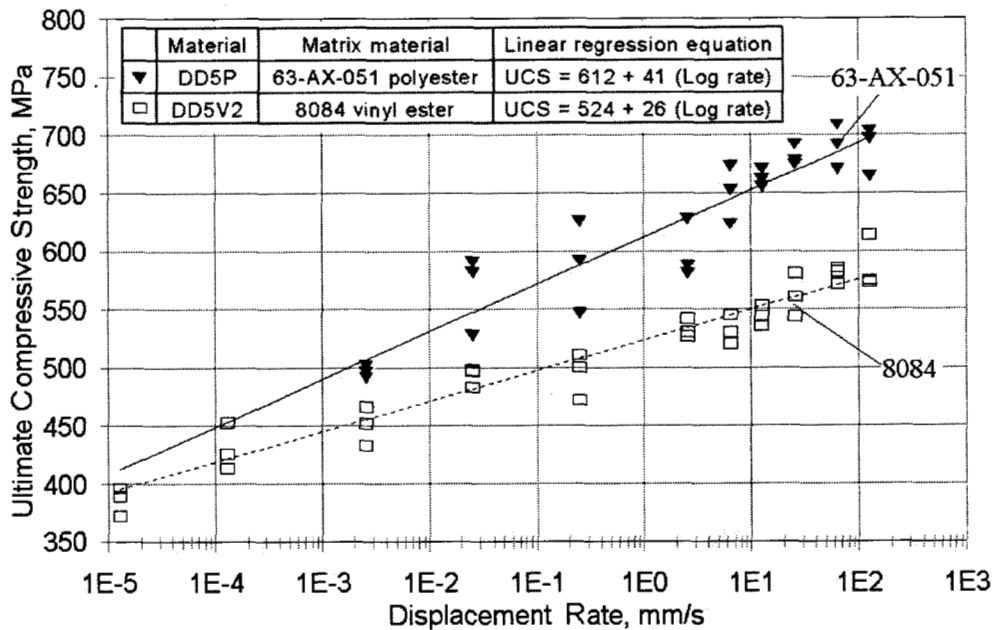
Figure 78. Ultimate Compressive Strength versus Displacement Rate for Two $(0/\pm45/0)_S$ Laminates; One Laminate with a Polyester Matrix and One with a Vinyl Ester Matrix.

113
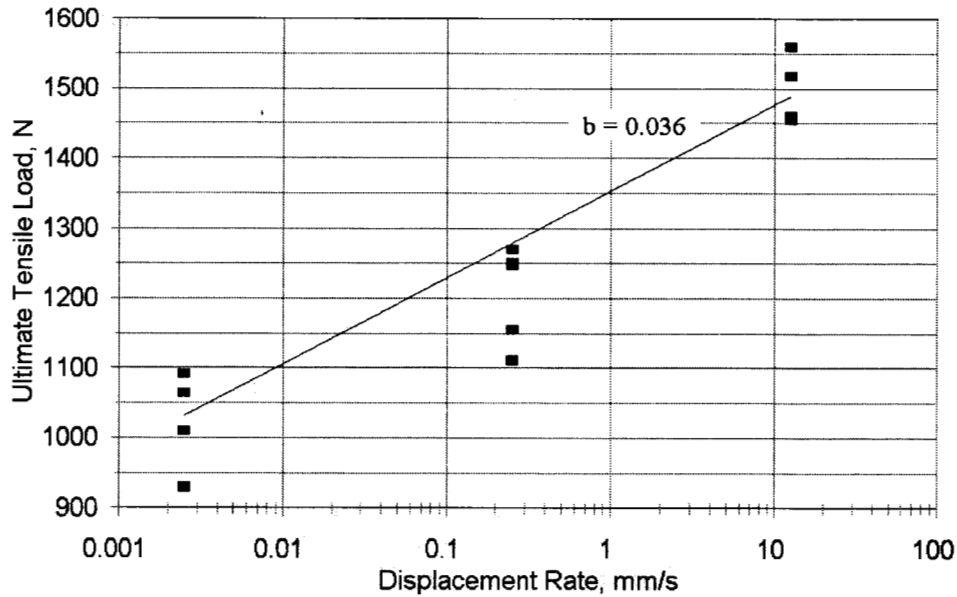
Figure 79. Maximum Tensile Load versus Displacement Rate for an Impregnated D155 Strand.

7.3.3. Constant Stress to Failure Tests

The stronger than expected strain rate sensitivity described in the preceding led to a second series of tests run in a slightly different, and easier to interpret manner. Instead of varying the displacement rate in ramp-type tests to failure, in this series of tests the specimens were loaded rapidly to a predetermined load, then that load was held constant until the specimen failed. Thus, the time to failure at various stress levels was determined (Figure 76, bottom).

Results for time to failure for specimens held at different stress levels for various materials are given in Figure 80. The slopes of the stress-time curves are again much greater than the expected 3 to 4 percent per decade of time expected for E-glass dominated materials, and are in a similar range to the slope observed in the variable strain rate tests. Figure 81 gives the same data, normalized by the database (high strain rate) strength value for that laminate. Table 18 gives a description of each material and the regression equation for the data. For materials not tested for time effects, the database strength values obtained at a higher strain rate, can be discounted proportionally to similar materials in Table 18 for the timescale of interest.

Additional data were obtained by recording the strains during the tests using an extensometer. Figure 82 gives typical strain-time results at constant stress. The increasing strain is consistent with the progressive matrix cracking in the ±45° layers, and the transfer of their applied load to the 0° layers shown schematically in Figure 71.

114
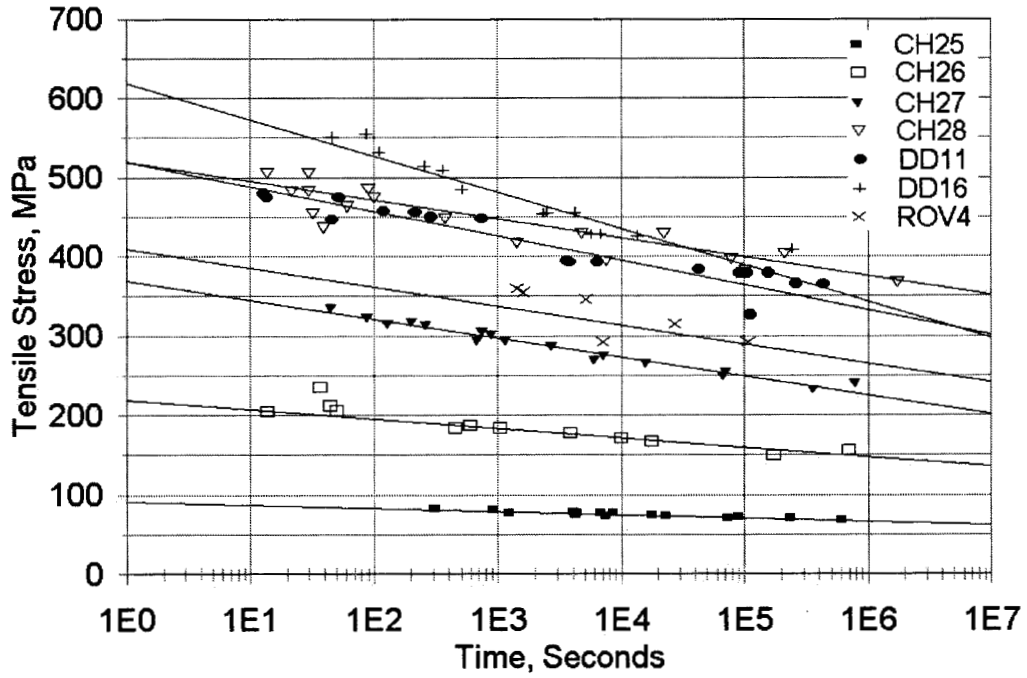
Figure 80. Maximum Tensile Stress versus Time to Failure at Constant Stress.
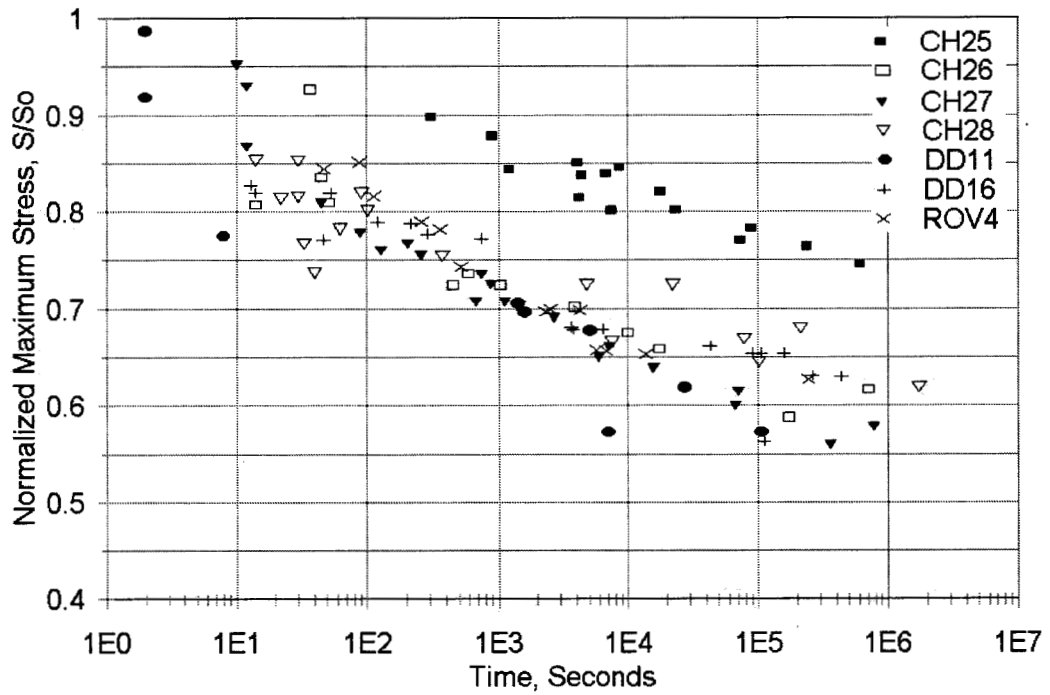
Figure 81. Normalized Maximum Stress versus Time to Failure at Constant Stress.

115

Table 18. Results of Constant Stress versus Time to Failure Experiments.

Material	V_F, %	Layup	S_o, MPa	Regression equation, t = time in seconds	Slope, % / decade
CH25	31	$[\pm45]_7$	92	S = 92 - 4.2 Log t	4.6
CH26	33	$[(\pm45)_3/0/(\pm45)_3]$	260	S = 220 - 12 Log t	5.5
CH27	35	$[(\pm45)_2/0/\pm45/0/(\pm45)_2]$	417	S = 370 - 24 Log t	6.5
CH28	38	$[0/\pm45/0/\pm45/0/\pm45/0]$	597	S = 520 - 24 Log t	4.6
ROV4	52	$[0/90]_6$	486	S = 410 - 24 Log t	5.8
DD11	32	$[0/\pm45/0]_S$	592	S = 520 - 31 Log t	6.0
DD16	41	$[90/0/\pm45/0]_S$	672	S = 620 - 46 Log t	7.4
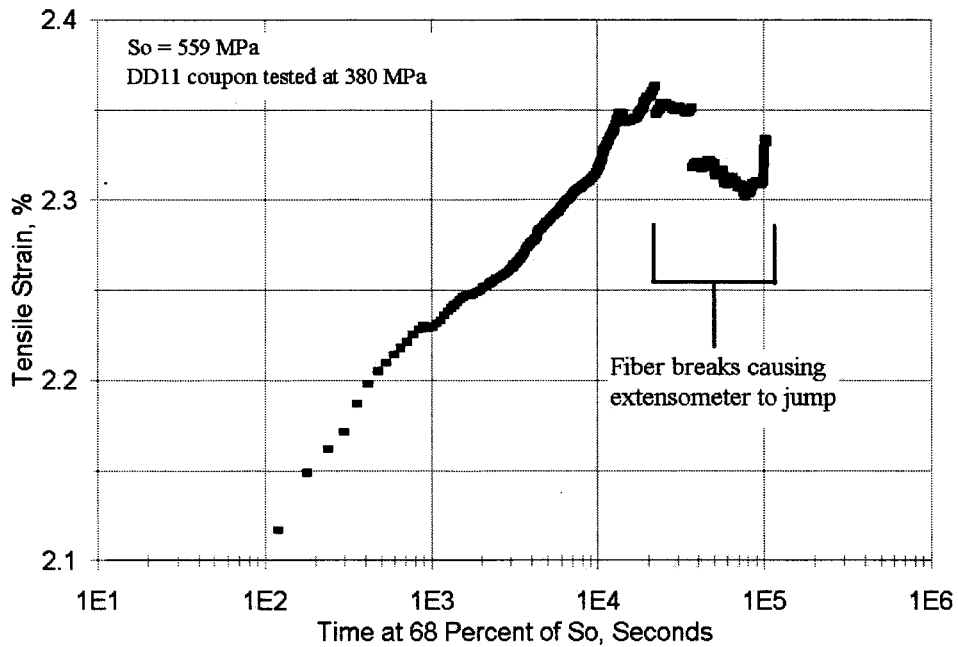
Figure 82. Tensile Strain versus Time to Failure of a $(0/\pm45/0)_S$ Laminate at a Constant Stress of 559 MPa.

116

7.4. Conclusions

The effects of time on static tensile strength, whether strain rate or time under load, are more significant than expected. The tensile strength for coupons with a high 0° content drops by up to 9 percent per decade of time if ±45° plies are present, while the rate is closer to 4 percent if only the 0° material is dominant. The high time sensitivity with the ±45° ply interaction may need to be addressed in using database strength values (obtained at high rates) in static strength design. This is treated as a knockdown on strength in Chapter 8.

The compressive strength is only slightly less rate sensitive than is the tensile strength. The time effects in compression are presumably due to matrix creep.

7.5. Design Recommendation

The results in this section call for a conservative approach to the design of strength-critical parts of the blade. These points are likely to be compression critical for most blades in the extreme loading condition. A conservative approach in tension would to be to assume that the ±45° layers carry no loads and contribute no modulus in the highly stressed parts of the blade. The 0° plies could then be assumed to decrease in tensile strength by 4 percent of their strength per decade of time during the high stress event. For compression, the trend in Table 18 could be used, with the strength chosen to correspond to the timescale of the event (see knockdowns, Chapter 8). For laminates not shown in Table 18, the stress can be normalized by the database strength value, as shown, and a trend assumed for a laminate of similar 0° material content. The modulus in compression could again be calculated assuming no modulus contribution from the ±45° (or 90°) layers.

8. KNOCKDOWNS FOR FLAWS, STRUCTURAL DETAILS, TIME AND ENVIRONMENT

8.1. Summary

Material partial safety factors are an important part of blade design. They are intended to account, in part, for the effects of flaws and geometries not present in normal material test coupons, as well as environmental conditions and time effects. Safety factors can be rendered more rational by exploring specific contributing factors, which is the subject of this chapter.

Laminates fabricated from stranded glass fiber fabrics commonly used in wind turbine blades have been found to exhibit a strong sensitivity to fiber content. The tensile fatigue resistance decreases rapidly over a narrow range of fiber volume fraction as the fiber content is increased. Many manufacturing processes produce fiber contents in this range, and local variations in fiber content around details such as stiffeners are often not well controlled. Thus, the fatigue resistance around structural details may drop precipitously if the fibers are locally pinched during manufacturing.

A second problem associated with structural details is delamination between plies of fabric due to out-of-plane stresses. Delamination can lead to breakdown of a structure directly, often with subsequent buckling, or indirectly, by accelerating fatigue breakdown of the fiber strands. Another, independent type of flaw, fiber waviness, affects compression strength in many types of composites. This is inherent in woven fabrics, and is often introduced by manufacturing processes in otherwise straight-fiber reinforcements. It is particularity difficult to avoid in thick sections.

This chapter explores the static and fatigue strength of a number of real and simulated flaws and structural details which may be associated with local increases in fiber content as well as delamination and waviness. The flaws and structural details investigated include ply drops, skin-stiffener intersections in I-beams, local matrix rich and transverse fiber areas, surface indentation, sandwich panel closeouts and waviness. These are compared to unflawed laminates and laminates containing severe flaws such as through-thickness holes. The results are represented in two ways. First, the stress or strain required to produce a 25 mm delamination in static or fatigue tests in 10^5 cycles is documented for cases which delaminate; and second, as knockdown factors on the ultimate static strain and maximum strain to produce total laminate failure in 10^6 cycles. Two types of 0° fabric are included in most cases. The knockdown factors on static properties ranged up to 4.0, with the worst case being a sandwich panel closeout. In fatigue knockdown factors also ranged up to 4.0 with the worst case being a double ply drop in compression, with a sandwich panel closeout a close second. Extended time under load showed a knockdown of about 1.3, while 50°C/wet conditions produced a knockdown of 1.9 for the ortho-polyester resin in compressive fatigue. Materials with poor initial properties, such as woven fabrics in compression and high fiber contents in tension fatigue, require lower knockdowns than did materials with the best performance.

8.2. Introduction

Structural details are a potential problem in composite material structures for several reasons. They may concentrate stresses simply through geometric effects, as is common with metal structures. They also may produce local changes in reinforcement architecture (fiber packing, bundle spacing, matrix rich regions, etc.) which can cause stress concentrations associated with variations in local material modulus. There is also the potential for local property changes associated with fiber orientation and variations in fiber content, which can lead to premature failure. Thus, the primary structure of a blade, designed for good fatigue performance, could be compromised by the presence of intersecting stiffeners or by ply drops in areas of thickness tapering, with similar effects at ply fabric joints. Figure 83 shows strand packing around a good quality resin transfer molded (RTM) stiffener intersection described in more detail in a later section, and Figure 84 shows a section through a typical ply drop.

A reason for concern is that the fiber content can become locally high as the strands are crowded together in the detail areas. Studies discussed elsewhere [2, 8, 11] have shown a sharp transition in fatigue resistance associated with increasing fiber contents in the range of 40 to 50 percent fiber by volume. Figures 1 through 3 show this transition for typical laminates containing 50 to 100 percent of the fiber in the load (0°) direction, with the remainder of the layers oriented at ±45°. The lines in Figure 1 show normalized S-N trends in the form of Equation [1], an exponential formulation. The results show a change in fatigue coefficient, b, from about 0.10 at low fiber contents, to about 0.14 at higher fiber contents. These coefficients represent the best possible tensile fatigue resistance at low fiber content (b=0.10), and the worst observed resistance at high fiber contents (b=0.14). The concern is that, even if a blade is manufactured for optimum fatigue resistance, the resistance in the structural detail areas could knock the allowable strains down by a factor of two to three due to local fiber crowding. The delamination based design methodology (chapters 12 and 13) for structural details does not take such fiber packing effects into consideration; these must be handled separately for their effects on in-plane strength and fatigue.

Fiber waviness is a fundamental problem in fibrous structures. It has been shown in many studies [44] to strongly reduce compressive strength in aerospace-type composites. Fiber waviness is inherent in woven fabrics, which have been described in detail in the past [2] in this program. However, in-plane waviness is often introduced by local fiber wash during processing by methods such as RTM, and has even been a problem in prepreg based aerospace applications.

8.3. Experimental Methods

All materials were fabricated at MSU by resin transfer molding or hand layup (the latter for sandwich closeouts and waviness specimens). Reinforcing fabrics from Owens Corning Fabrics were used in all cases, with an orthophthalic polyester resin (CoRezyn 63-AX-051) with approximately 2 percent methyl ethyl ketone peroxide as a catalyst. Plates were cured under ambient conditions, followed by a post cure at 60°C for two hours. Details of molding, specimen preparation, and testing can be found in References 17 and 34. These materials are typical of those from hand layup and other processes used by blade manufacturers. The reinforcing fabrics included D155 stitched

119
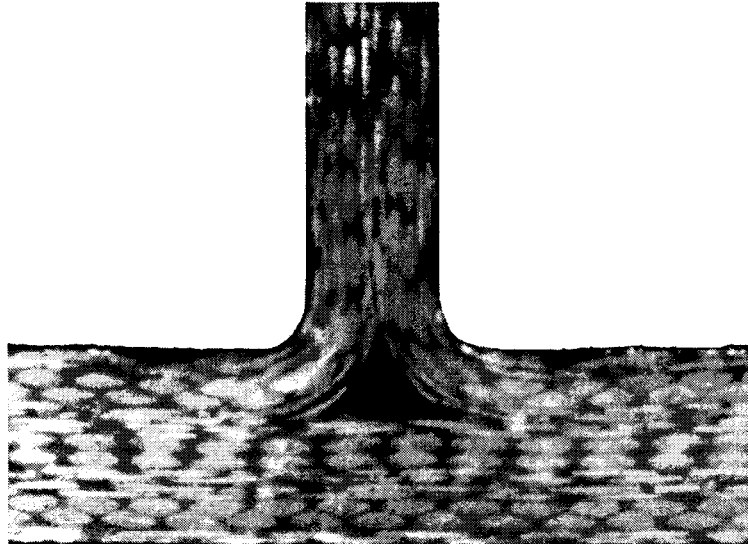
Figure 83. Cross-Section Through Integrally Molded Skin-Stiffener Intersection Showing Fiber Strands for 0° (large strands) and ±45° (small thin strands) Layers.
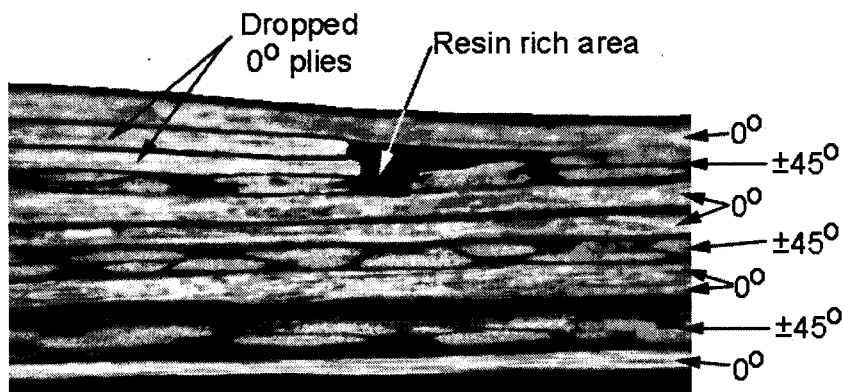
Figure 84. Photomicrograph of Material ESH (Table 19) Showing Resin Rich Region Ahead and Strand Crowding Behind the Ply Drop. ([0/0*/0*/±45/0/(0/±45/0)$_2$], * = dropped plies)

weft unidirectional, A130 woven warp unidirectional, DB120 stitched ±45°, and UC1018V bonded warp unidirectional fabrics.

Structural details were incorporated into the materials during molding in most cases. Ply drops were incorporated in area of thickness tapering as shown in Figure 84. Other features such as surface indentations and matrix rich areas were either molded in or bonded on to simulate possible effects of stiffener intersections, etc., as described later. Actual stiffeners were included in the form of I-beam

120

web-flange intersections, following fabrication procedures described elsewhere (mostly secondary bonding of the stiffener to the flange [3, 7]). Sandwich panels described in a later section are also included in this study.

In-plane fiber waviness was introduced by removing several stitches, then pulling the fabric into a wavy shape. Details of waviness effects and their introduction can be found in Reference 44.

8.4. Results and Discussion

8.4.1. Delamination at Ply Drops

Detailed results for the growth of delamination cracks at various ply drop geometries were reported previously [3, 7]. Other studies involving delamination in standard delamination test specimens and in complex substructural geometries are reported in later sections of this report.

The stress for delaminations to initiate and grow at ply drops is usually far below the strength of the laminate. Figure 85 shows delamination length versus applied tensile stress for the typical ESH configuration which contains two internal adjacent ply drops. Delamination started to grow at about 20 percent of the laminate ultimate tensile strength. Design knockdown factors for static and fatigue loading are included at the end of this section.

Fatigue tests were run under tensile loading (R=0.1) at relatively low cycles, on the order of 10^5, at various maximum stress levels. Table 19 presents a summary of the results reduced to a form which may be of use to designers. The base laminate is identified in the database [2, 13] as DD5, which has a ply configuration $[0/\pm45/0]_s$, with 72 percent 0° layers and an overall fiber content of 37 percent fiber by volume. This material is a typical structural laminate for wind turbine blades and has good tensile fatigue resistance (see Figure 1). Most of the laminates in Table 19 had fiber contents in the range of 30 to 36 percent as detailed in Reference 34.

When plies are added to this approximate laminate configuration, then dropped in the coupon gage section, they are indicated by an (*) in Table 19. Thus, laminate type ESA has an single 0° surface ply dropped , while ESB has a single 0° interior ply dropped. When the data presented in Reference 13 are reduced to obtain an approximate strain to produce significant (25 mm) delamination length within 10^5 cycles, the various laminate types in Table 19 can be compared. A number of methods for improving delamination resistance at ply drops by added reinforcement and tough interlayers are also discussed in Reference 13.

All of the strain levels shown for delamination are above the typical working strains of blades. However, those strain levels might be reached in service in stress concentration areas, and in many cases are well below the fatigue strain capability of the base laminate at the strain level shown. Thus, those strain values below about 1.0 percent would likely produce delamination prior to laminate fatigue failure, as discussed later. The results clearly show that surface ply drops delaminate at much lower strains than interior ply drops (ESA and ESE versus ESB, ESC, and ESF). Dropping two

121

internal plies at the same location produces delamination at lower strains (ESH versus ESB) that are equivalent to a single surface ply drop. Multiple internal ply drops, when spaced at various distances from 13 to 48 mm, rather than at the same spot as in ESH, produced delamination
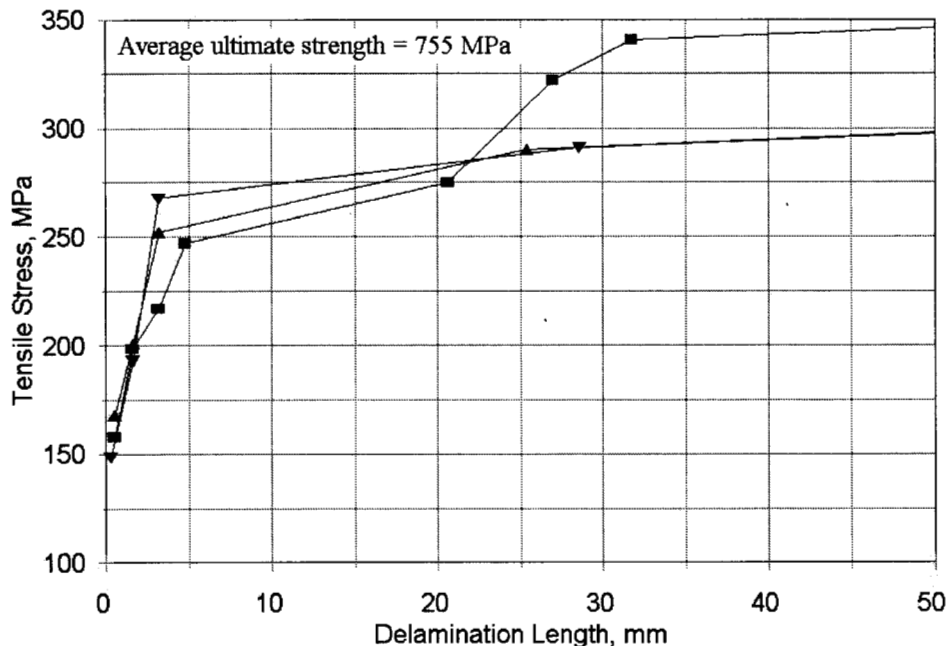
Figure 85. Static Applied Tensile Stress versus Delamination Length for ESH Laminate, with Two Internal Ply Drops.

similar to a single internal ply drop (ESI versus ESB). Figure 85 shows no clear trend with ply drop spacing, with all spacings giving similar results to a single ply drop (ESB), and much better resistance than for a double ply drop at the same location (ESH). It did appear that the delamination rate could approximate that of ESH if the delamination at the closer spacing grew to where they overlapped, producing a geometry like ESH. While complete data are not available to explore this question, a ply drop spacing of at least 25 mm, with interior, single ply drops, should avoid this problem. Also, it should be understood that the fabrics used in this study are relatively light weight, and heavier fabrics would produce effects like the multiple ply drops presented in this study.

A related parameter is the thickness of the plies dropped versus the total laminate thickness. As indicated by modeling [34], delamination is reduced if the percent thickness reduction is smaller, as with a thicker base laminate.

Laminates with ±45° layers dropped were also tested, but these failed in tension prior to any delamination. Thus, it appears that single or double ±45° ply drops with the DB 120 fabric will not produce delamination [34].

122

Two other representations of delamination resistance are given in Table 19, the apparent arrest strain for a growing delamination (typical data shown in Figure 86), and the threshold strain where delaminations were not observed to initiate in the 10^5 cycles tests. These are approximate values from the limited test data in Reference 34. These results generally follow the trends described above for a 25 mm long delamination in 10^5 cycles, but at lower strain values. It should be noted, as shown in the next section, that the ply drop might shorten laminate lifetime in some cases, even if it does not produce any delamination.

Table 19. Comparison of Delamination Resistance of Different Ply Drop Configurations (R = 0.1).

Laminate	Layup (* indicates dropped ply)	Strain for 25 mm delamination in 10^5 cycles, %	Arrest strain[1], %	Threshold strain[2], %
ESA	$[0*/(0/\pm45/0)_s]$	0.6	0.5	0.4
ESB	$[0/0*/\pm45/0/0/\pm45/0]$	1.1	1.1	0.8
ESC	$[0/\pm45/0/0*/0/\pm45/0]$	1.1	1.1	0.8
ESE	$[0*/(0/\pm45/0)_3]$	0.6	0.4	0.4
ESF	$[0/0*/\pm45/0/(0/\pm45/0)_2]$	1.0	1.0	0.7
ESG	$[0*/0*/(0/\pm45/0)_3]$	0.4	--	--
ESH	$[0/0*/0*/\pm45/0/(0/\pm45/0)_2]$	0.7	0.6	0.5
ESI	$[0/0*/0*/\pm45/0/0/\pm45/0]$	1.1^3	1.0	0.7

[1]- no further growth over most of the 10^5 cycles

[2]- no delamination after at least 10^5 cycles. Fabrics: 0°: D155; ±45°: DB120
    Laminates ESO, ESR and ESP not shown, ±45° layers did not delaminate.

[3]- Same as ESB, except multiple ply drops.

8.4.2. Effect of Ply Drops on Fatigue Lifetime

As noted in the introduction, a structural detail such as a ply drop can concentrate stresses, and can also rearrange local reinforcement packing and orientation. This may result in reduced lifetime, whether or not delamination occurs. In fact, some delamination and matrix cracking at stress concentrations, such as holes, in composites is widely recognized to reduce the stress concentration in the load bearing fiber strands, improving the fatigue performance [71].

A comparison of the S-N fatigue data under tensile fatigue for high and low fiber content (V_f) laminates is given in Figure 86, with and without a double ply drop. The high fiber content results are about the same, whether or not there is a ply drop present. The low fiber content laminates, which show much improved fatigue resistance in the absence of ply drops, are adversely affected by the

123

double ply drop, producing a steeper S-N curve which is now similar to the high fiber content cases here and in Figures 1 and 4. Thus, it appears that the more fatigue resistant materials in Figures 2 and 3 (those with lower fiber contents) lose their advantage when used in conjunction with a double ply drop. This may be due to locally higher fiber packing in the ply drop area (Figure 84). The laminates in Figure 87 used weft unidirectional D155 fabric for the 0° layers; similar findings are presented in Reference 34 for the warp unidirectional fabric A130 in similar cases.
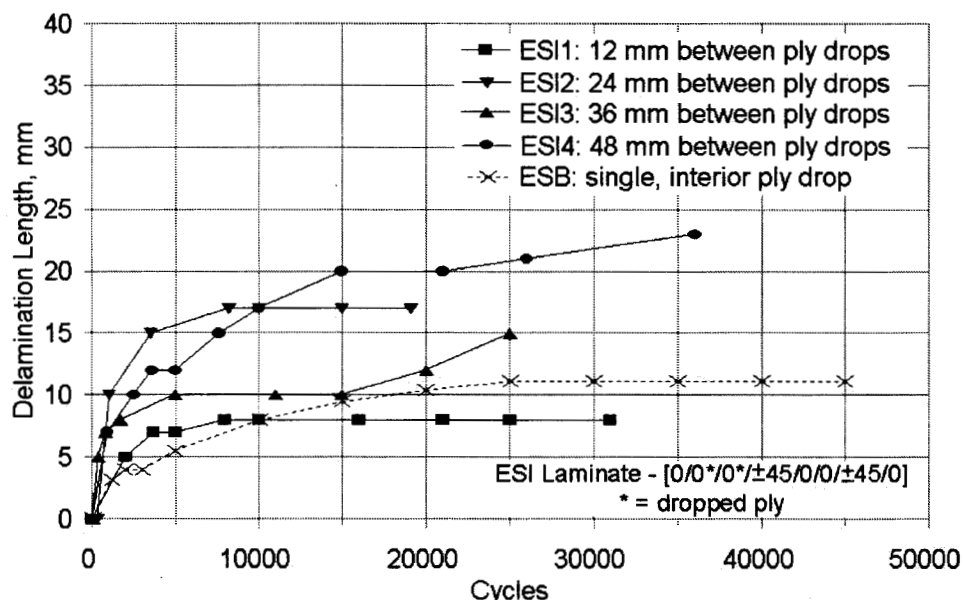
Figure 86. Effect of Different Spacing Between Ply Drops, R=0.1, ESI Laminate (Two 0° ply drops) at 276 MPa.

Somewhat less severe results were obtained when a single layer ply drop was used (ESB) instead of the double ply drop in ESH. Figure 88 compares these two cases. The fatigue resistance for ESB is now about midway between values for good and bad materials in Figures 1 and 4, but the laminates in Figure 88 were at a medium overall fiber content of 44 percent.

Delamination may appear to be significant in terms of compromising the integrity of the laminate. However, when specimens were fatigued to a significant fraction of their lifetime (n/N), then tested for residual tensile strength, Sr, the residual strengths given for individual tests in Table 20, normalized by the initial strength, S_o, are between 0.85 and 0.95. Thus, delamination at ply drops does not severely reduce laminate strength over most of the lifetime range.

Reference 34 presents additional results for ply drops under compression loading and in I-beam substructural elements. In general, strains to produce delamination in beam flanges were consistent with those in the coupon studies. While delamination occurred sooner on the tensile flange than on the compression flange, the compression flange delamination was sudden and extensive. Delamination under compression fatigue will be investigated in more detail in the future.

124

The compressive strength and fatigue resistance are probably also reduced by ply drops due to geometric effects. However, these have not yet been investigated due to difficulties in compression testing of geometries which vary in thickness without premature bending and buckling.

	Laminate	S_c, MPa	V_F, %	
▪	DD7	832	54	no ply drop
●	DD5	724	37	
▲	ESH high	798	52	double ply drop
▼	ESH low	747	35	
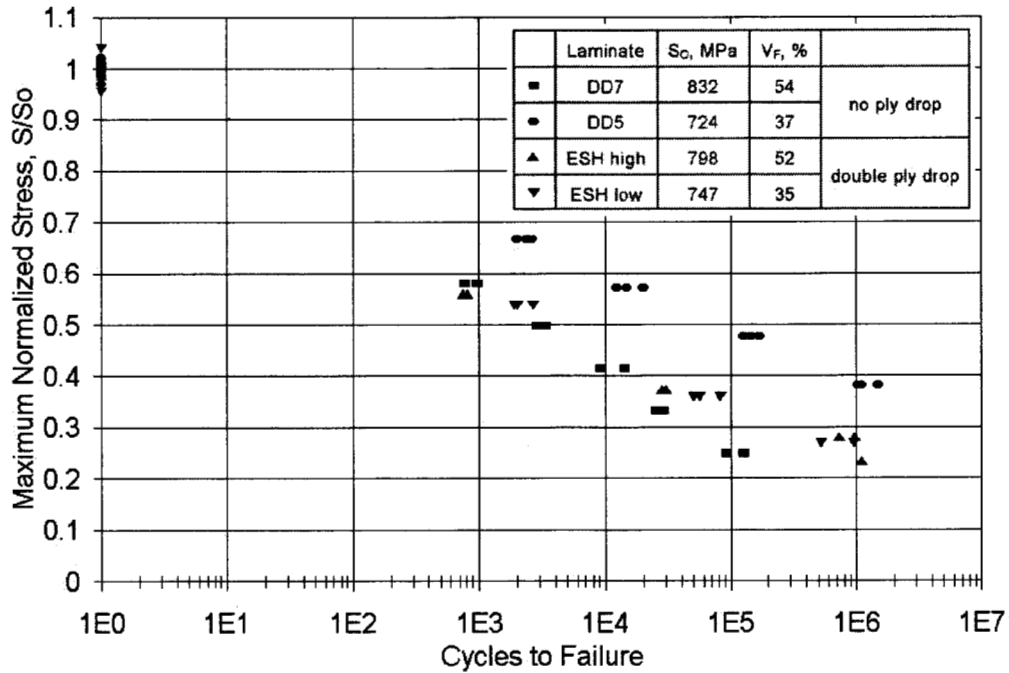
Figure 87. Effect of Fiber Content on the Normalized S-N Data, R=0.1, for Control DD materials [0/±45/0]s Compared to ESH Laminate (Two interior 0° ply drops).

125
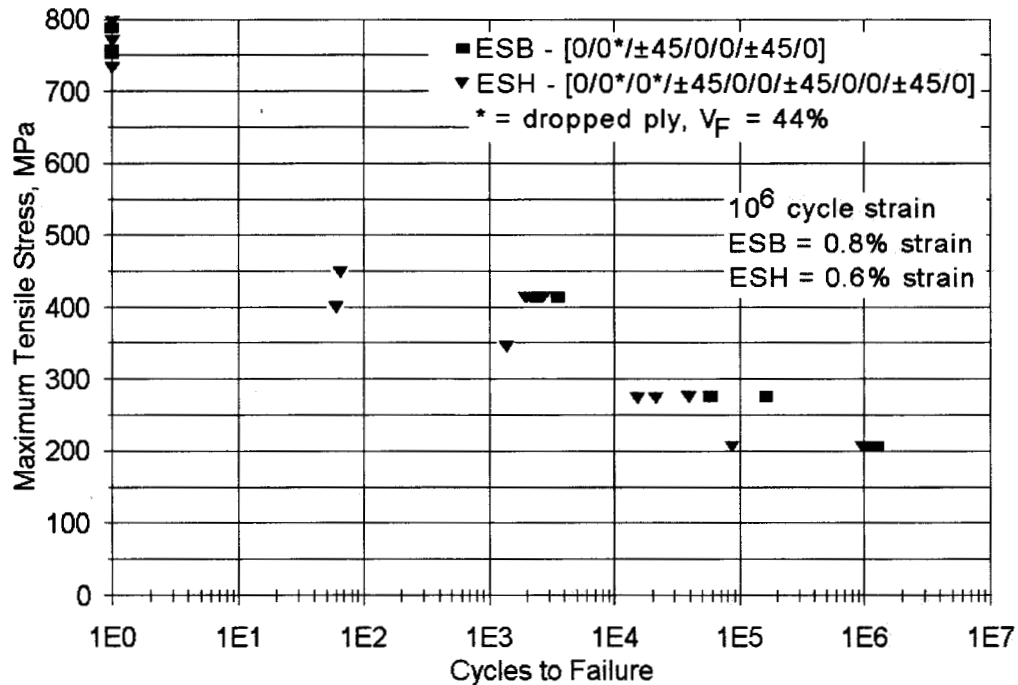
Figure 88. Tensile Fatigue (R=0.1) S-N Curves for ESB (Single 0° internal ply drop) and ESH (Two interior 0° ply drops).

Table 20. Residual Strength of ESH Laminate After Being Fatigued (R=0.1)*

Coupon	Fiber content, %	Maximum stress, MPa	Cycles	n / N_o	Initial strength, S_o, MPa	Residual strength, S_r, MPa	S_r / S_o
ESH 205	36	276	40,000	0.8	703	600	0.853
ESH 213	36	276	20,000	0.4	703	675	0.960
ESH 409	44	207	1,100,000	1.1	746	686	0.920
ESH 404	44	176	1,100,000	0.11[A]	746	717	0.961

[A]- Lifetime estimate used was 10^7 cycles, however test was stopped at 10^6 cycles after no delamination.

* Individual specimen results

8.4.3. Effect of Other Structural Features

As indicated in Figures 89 and 90, a number of cases have been investigated which simulate possible effects of structural details, like stiffeners, on base laminate fatigue resistance. These cases involve variations of resin rich areas, crowding of fibers, and exterior geometry. Fatigue S-N data at R=0.1(tension) have been obtained for all cases, and the strain to produce failure in 10^6 cycles determined; some were also tested in compression (R=10). The knockdown factor for design, F, is

126

the ratio strain without and with the detail present. These ratios have been determined for both static (ultimate strength) and fatigue testing to 10^6 cycles in many cases, as well as conditions for the growth of a significant delamination (25 mm). Thus, the allowable fatigue strain in the design should be reduced by dividing by F if a similar feature is present. Figure 89 gives S-N data for several cases from Figure 90. The base laminate is $[0/\pm45/0]_s$ with V_F =36 percent, which has good fatigue resistance, as shown for comparison in Figure 89.

Composites have remarkable tolerance to many types of flaws which would produce problems in metals. For example, in a cracked 90° material patch simulation, a resin rich area on the order of the laminate thickness, produces no measurable fatigue life reduction, even though a crack grows through the patch early in the lifetime. However, if a thinner 90° ply patch is molded into the interior, it reduces the lifetime significantly, apparently due to the increase in fiber content this forces on the remainder of the laminate in the area (34 to 47 percent fiber). This moves the base laminate into the poor fatigue condition in Figure 1, due to the higher local fiber content.

One of the most severe structural details shown in Figures 91 and 92 is, somewhat surprisingly, a simple molded-in indentation in the laminate surface, caused by a bump on the mold surface. No fibers are cut, but the fibers are locally compressed together to increase the local fiber content from 36 percent away from the indentations, to 52 percent at the minimum thickness. This again shifts the material into the high fiber content, poor fatigue resistance condition in Figures 1 through 4. The surface indentation is intended to simulate the compression of the fibers over a molded-in stiffener, but the surface geometry may also contribute to the effect; local delaminations
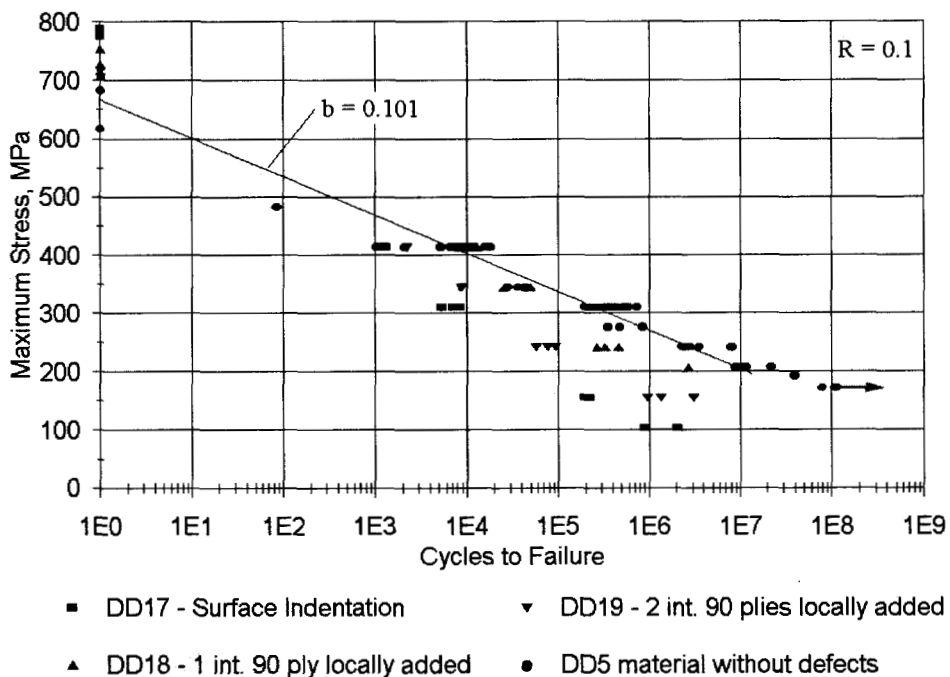
Figure 89. Effect of Defects Which Produce Locally Higher Fiber Content on the Tensile Fatigue Behavior of Baseline Material DD5.

127

at the shoulder of the indentation were observed prior to failure. The case with smooth surfaces, but a similar fiber content increase caused by inserted 90° material may be more representative of typical structure. The knockdown factor here is 1.4 compared to 2.5 for the indentation.

By way of comparison, the I-beam structure shows very little effect on fatigue when the tensile flange fatigue performance is considered [3, 7]. Here, the web is bonded to the flange after molding each part separately, so that no local strand compression occurs, as compared with a molded-in stiffener. As discussed in the previous section, ply drops can have a significant effect on fatigue life, causing significant knockdown factors if the laminate has a low fiber content.

An important aspect of Figure 90 is that the base laminate, except where noted, has a low fiber content, and good fatigue performance. This can then be degenerated to poorer fatigue performance if the local fiber content increases and/or the surface geometry changes, inducing local delamination.

The most severe knockdowns in tension came from the sandwich panel closeout with the standard 30° angle, transitioning to a thin laminate that is described in detail later. The sandwich panel alone causes little loss in tensile strength, but the closeout causes strong geometric effects including delamination and fiber packing effects. This would also be expected to strongly compromise the compressive strength, but the geometry makes compression testing difficult. As noted later, sandwich closeouts may be located in low stress areas, so that their full knockdown effects are not realized.

Detail	Sketch	Knock-Down Strength Factor, F			
		Static Strength		10^6 Cycle Fatigue	
		A130 fabric	D155 fabric	A130 fabric	D155 fabric
Simple coupon (straight material)		1.0	1.0	1.0	1.0
50 mm wide coupon with a 13 mm dia. hole		1.5 (T)	1.5 (T)	2.2 (T)	1.7 (T)
Bonded stiffener beam-web, (bending)			1.0		1.2
Time 100 to 1000 seconds at maximum stress		1.3 (T)*	1.3 (T) 1.3 (C)		
Hot / Wet 50°C / Max. moisture	Ortho polyester 63 - AX - 051		1.0 (T) 1.5 (C)		1.0 (T) 1.9 (C)
Fiber waviness (in-plane) 0° fibers in loading direction — Mild			1.0 (T) 1.2 (C)		
Fiber waviness (in-plane) 0° fibers in loading direction — Severe			1.7 (T) 2.7 (C)		2.7 (C)
Single interior 0° ply drop			1.0 (T) F 1.4 (T) D		1.2 (T) F 2.5 (T) D
Double interior 0° ply drop — $V_F<0.4$		1.1 (T)	1.0 (T) F 3.0 (T) D 1.0 (C) F	1.25 (T)	1.6 (T) F 3.9 (T) D 4.0 (C) F
Double interior 0° ply drop — $V_F>0.4$			1.05 (T)		1.0 (T)
Surface indentation (V_F increased, thickness reduced by 25%)	V_F = 45 - 52% r = 6mm V_F = 35 - 37%	1.0 (T) 1.2 (C)	1.0 (T) 1.4 (C)	2.3 (T) 1.0 (C)	2.5 (T) 1.4 (C)
Locally higher fiber content (2 - 90° plies in center)	V_F = 47% V_F = 34%	1.0 (T) 1.1 (C)	1.0 (T) 1.5 (C)	2.1 (T) 1.0 (C)	1.5 (T) 1.4 (C)
Cracked transverse 90° patch			1.0 (T)		1.0 (T)
Sandwich panel (tension)	balsa	1.02 (T)		1.1 (T)	
Sandwich panel (tension) 30 degree closeout to thin laminate	balsa	4.0 (T) D 2.3 (T) F		3.4 (T) D 3.0 (T) F	

* (T) Tension Loading (R=0.1), (C) Compression Loading (R = 10), (F) Failure, (D) Delamination
Sandwich panel data are based on stress, and are compared to the facesheet material alone.
Delamination indicates conditions where delamination spreads completely across the specimen.

Figure 90. Static and Fatigue Knock - Down Factors for Tension and Compression Laminates Based on D155 and A130 0° Fabrics. (Knock-Down Factor, F, is the Ratio of Strength or 10^6 Cycle Fatigue Strain for Control Laminates Tested at Normal Rates and Environment, Relative to Laminates Containing the Indicated Condition.)
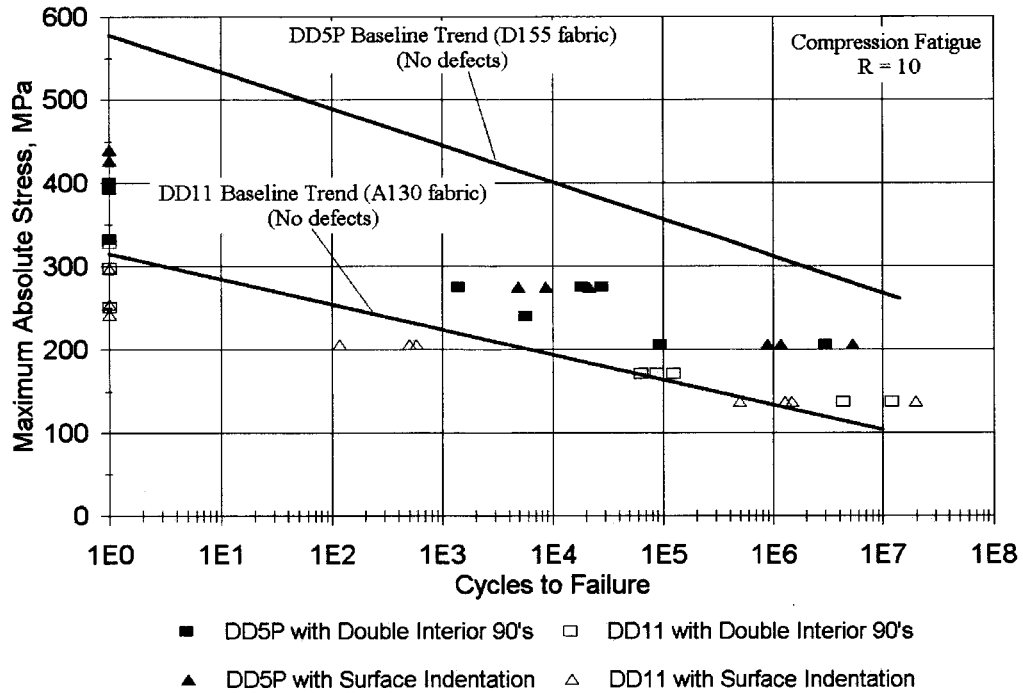
Figure 91. Effects of Surface Indentation and Interior Inclusions on Compression Fatigue Resistance, R = 10.
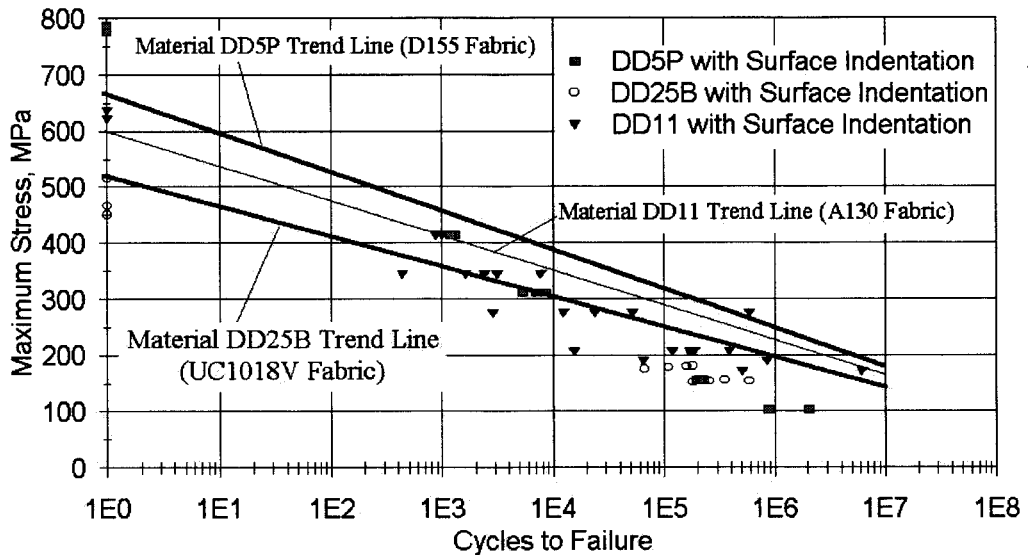
Figure 92. Effects of Fabric Type on Tensile Fatigue For Coupons Containing a Surface Indentation Compared With Trend Line For Base Laminates Without Indentations, R = 0.1

Nearly as important as sandwich closeouts are severe waviness effects. Most strands include

a significant amount of misorientated fibers due to the effects of winding on spools and other factors, which can significantly reduce the compressive strength even if the overall strand is straight. Furthermore, additional waviness due to processing can significantly distort the strands in a local area [72].This is difficult to avoid in many processes, and can be difficult to inspect by nondestructive evaluation. Low levels of waviness do not reduce tensile strength significantly, but all levels reduce compressive strength of otherwise straight fiber laminates (woven fabrics already have significant waviness due to the weave). Severe waviness can strongly reduce both static and fatigue strength under both tensile and compressive loads [44].

8.5. Time and Other Knockdowns

Material safety factors are also intended to include the effects of time and environmental conditions. As noted in earlier sections, both of these factors can significantly reduce the static and fatigue strengths. Unfortunately, time and environmental knockdown factors appear to both be additive to the other knockdown effects. For time effects, several possible durations of extreme loads are listed, as described earlier. Combined hot/wet conditions representative of relatively extreme moisture contents for the particular resin and a maximum temperature of 50 °C are listed. As noted in earlier sections, time and environment can lead to significant knockdowns.

8.6. Conclusions

The various sources of knockdown factors shown in Figure 90 have serious implications for blade design. The most severe factors of 3.0 to 4.0 are more severe than cutting a 13 mm diameter hole through the laminate. These include delamination and failure at sandwich panel closeouts and delamination at double 0° ply drops. The former could be alleviated by changes in closeout design (Chapter 14) or placed in low stress areas. The ply drop effect is more difficult to avoid, particularly if thick fabric layers are used; some delamination at ply drops may be tolerated in blades if it is embedded in the interior of the laminate; however, the limited compression data indicate a serious knockdown in compression fatigue if delaminations grow significantly.

More moderate knockdowns of 2.0 to 3.0 are observed for fiber waviness and features which cause local fiber content increases due to crowding of strands. Surface indentation and internal 90° material inclusions are in the latter category intended to simulate effects near stiffener intersections, etc. The geometry of the surface indentation may be significant, and so the internal inclusion, which is less severe, may be more representative of typical structural details.

The time and hot/wet conditions are less severe, but are additive to other knockdowns; the hot/wet effects would be much lower for other resins (Chapter 3). Secondary bonding of stiffeners and other substructures may avoid the fiber crowding effects simulated for integrally molded cases. Strong geometric changes such as sandwich panels and adjacent matrix rich material need not lead to large knockdowns away from transition areas.

The results from the ply drop experiments indicate that ply drops of the 0° weft unidirectional fabric (D155) need not lead to delamination prior to laminate failure if the following conditions are

131

met: drop only individual plies at a particular point; drop the plies on the interior rather at the surface; and space adjacent ply drops at least 25 mm apart where multiple ply drops are needed. These recommendations are not optimum for manufacturing, but neither are they a major expense. While properly configured ply drops need not lead to premature delamination, they are likely to require a knock down factor in design if the base laminate has a low fiber content and other characteristics such as a high 0° material content [2] which produce good tensile fatigue performance.

8.7. Design Recommendations

Several implications are evident in the fatigue data and knockdown factors for ply drops and other flaws and structural details. First, even some simple variations such as surface indentations can produce a significant increase in fatigue sensitivity and decrease in static strength in laminates with good base material characteristics. Second, it is not clear that a complex composite structure such as a blade can be manufactured without some details of this type. Third, there may be little benefit in choosing fatigue resistant laminate types if they are this sensitive to detail features, and if the poorer-behaving laminates do not show these effects. Further work is needed to explore whether materials such as triax would require only low knockdown factors. In the long run, there is a clear need to develop manufacturing approaches which give control over reinforcement architecture to avoid waviness and strand packing, particularly near structural details. This is particularly important for processes such as resin transfer molding (RTM) which may involve molded-in design details. Testing of more realistic RTM molded blades and substructural elements is planned in future work.

The time and environmental factors are significant, unavoidable in some degree, and additive to other knockdowns. The use of environmentally resistant iso-polyester and vinyl ester resins would reduce the environmental knockdown. The extreme load conditions, involving compression loads, time effects, environment, and often fiber waviness in fabrics may be subject to high additive knockdowns; more study of this topic with realistic load spectra containing time effects is needed.

9. DELAMINATION TESTING AND DATA

9.1. Summary

Delamination between plies is widely viewed as the "Achilles heel" of composite material structures. Failures in blades due to delamination have been observed in both service and full-scale blade tests. Delaminations occur in areas of complex, three-dimensional stress states which are rarely analyzed in detail during design. The resistance to failure due to thickness-direction shear and normal stresses is very low relative to the fiber dominated properties along the primary load paths. Lower cost thermoset resins are brittle, and their composites have low delamination resistance (see Chapter 3). Manufacturing problems such as resin-rich areas and porosity can provide sites for delamination initiation. Environmental factors and fatigue loading can lead to the spread of delaminations at low load levels. In aerospace applications, the delamination problem has been addressed primarily through increased resin toughness (which is costly), conservative designs in structural detail areas, and a variety of rules-of-thumb [73].

Relative to aerospace composites, where delamination problems have been addressed in detail, wind turbine blades tend to be more heterogeneous (thicker plies and stranded fabrics), which may raise both the stresses causing delamination and the material's resistance to delamination growth. The more brittle, low cost resins which are commonly used in blades produce lower delamination resistance, while glass fibers tend to reduce delamination stresses due to the reduced anisotropy relative to carbon fiber composites.

Methodologies for dealing with delamination are described in this chapter, and in later substructure chapters. Test methods which are applicable to blade materials are identified, and test procedures are described which produce conservative measures of delamination resistance. Methods of analysis for both standard delamination tests and complex substructures are described, with applications of the latter in the substructures chapter. Test data are limited to a few cases at this time; these cases relate to the matrix study discussed earlier, and the substructure studies which follow. To use delamination data in the design of structural details, it is necessary to have data for basic opening and shearing modes of delamination growth for the ply interfaces of concern, with the appropriate fabrics, resins, and fiber contents. To date, only limited data have been obtained for static delamination and fatigue crack growth. A simplified procedure of using only initiation values in design is recommended.

9.2. Introduction

Composite materials are relatively strong and durable when loaded such that the fibers carry the loads; however, even relatively small out-of-plane loads can cause separation between plies, where the strength and resistance to crack growth are relatively low. Out-of-plane stresses occur naturally at many types of structural details, as indicated in Figure 93 [74].

133
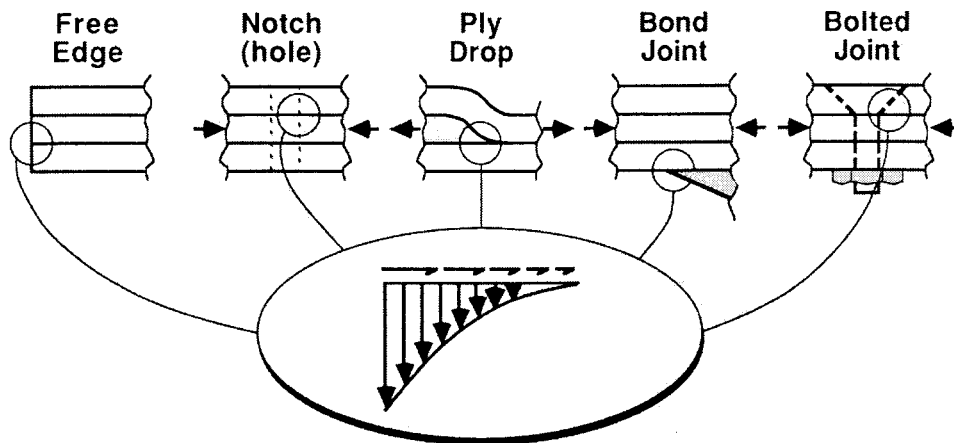
Figure 93. Common Structural Elements which Generate Interlaminar
Stress Concentrations [74].

As with monolithic materials [75], delamination crack growth may be separated into three
independent modes (Figure 94), with mixed-mode cracks common in many geometries. Modes I and
II are the most prevalent in delamination problems, and test methods for pure Mode I and II cracks
have been standardized. Mixed mode crack growth criteria have been investigated as described later,
but their application to blade materials requires validation. The delamination tests can be used for
either static or fatigue crack growth studies. Thus, a database is under development for static and
fatigue crack growth results for various materials parameters. These data can be used in materials
selection, in design rules-of-thumb, and in finite element based structural detail design as
demonstrated in the substructures sections.
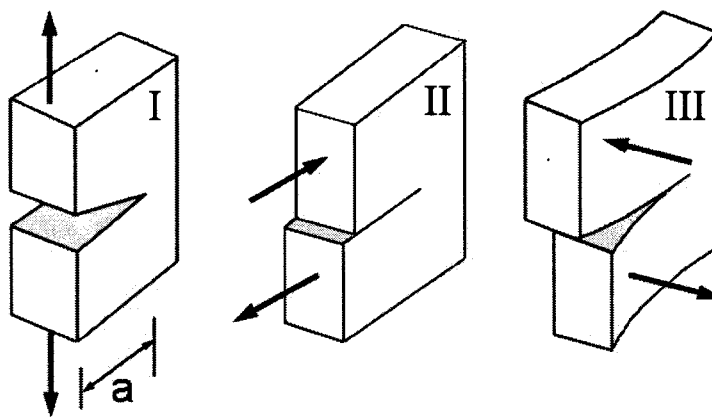
Figure 94. The Three Modes of Cracking, Mode I
(opening), Mode II (sliding) and Mode III (tearing) [75].

134

9.3. Delamination Test Methods

Delamination test methods were discussed briefly earlier with regard to matrix and environmental effects. Tests for Modes I and II are shown in Figures 96 and 97. In aerospace composites, testing of this type has led to greatly improved delamination resistance, primarily through tough epoxy and thermoplastic matrix development. A good review of the use of fracture mechanics in composites can be found in Reference [76].

The second part of this report deals with substructure tests, where delamination is the primary mode of failure. Finite element results for these substructures indicate that most delaminations occur under mixed mode conditions, that is, a combination of Modes I and II. A test method which combines the specimens in Figures 96 and 97 to give controlled mixed mode loading is shown in Figure 98. Test methodologies for this geometry with wind turbine composites are currently under development in the MSU program. Particular thicknesses and crack lengths must be identified to grow cracks with fabric reinforcements and matrices of interest, as many cases exceed allowable displacements prior to crack extension.

For reasons discussed later, it is often necessary to measure the strain energy release rate, G-values (see chapter 9.4) for only short values of crack extension, called "initiation" G_{IC} and G_{IIC}. These are usually the minimum values relative to those measured with greater lengths of crack growth. Measurement of initial crack growth requires careful observation of the crack length during testing, or loading-unloading sequences with inspection for crack length at each step. The lowest values in this study are reported for cases where the crack grew directly from the teflon starter strip with no initial pre-cracking. An alternative method, which is also used for unstable growth in Mode II, follows the 5 percent offset procedure used in ASTM Standard E399 for metals. Figure 98 illustrates this method as applied in ENF tests. Unless noted, tests in this study involved an initial starter crack beyond the teflon strip, introduced by wedge opening prior to loading for both the DCB and ENF tests.

9.4. Analysis of Delamination

A wide range of analysis methods have been developed for delamination tests and for delamination in structural geometries [74]. The most widely used methods are based on modified beam theory (MBT).

One of the most common methods of analyzing and predicting crack growth behavior is the concept of strain energy release rate, G. The basis for G lies in the Griffith criterion, [74], where the condition for crack growth is:

$$\frac{dU}{da} = \frac{dW}{da} \qquad (11)$$

where: U = elastic strain energy
         W = energy required for crack growth

a = crack length

G is also called the crack driving force and equals dU/da. The resistance to crack growth is referred to as the crack resistance, R (not to be confused with the stress ratio, R, in fatigue) and equals dW/da, which is the energy consumed in crack propagation per unit area of crack extension. The condition for growth in Equation 11 can also be read as G = R at crack extension. At or above some critical value of G, the crack will propagate. This critical value must be experimentally determined for each material system. The critical value usually differs for each mode and is denoted with subscripts as G_{IC} and G_{IIC}. In practical terms, materials that are "tougher" have higher critical values of G, requiring more energy to grow a crack in that material.
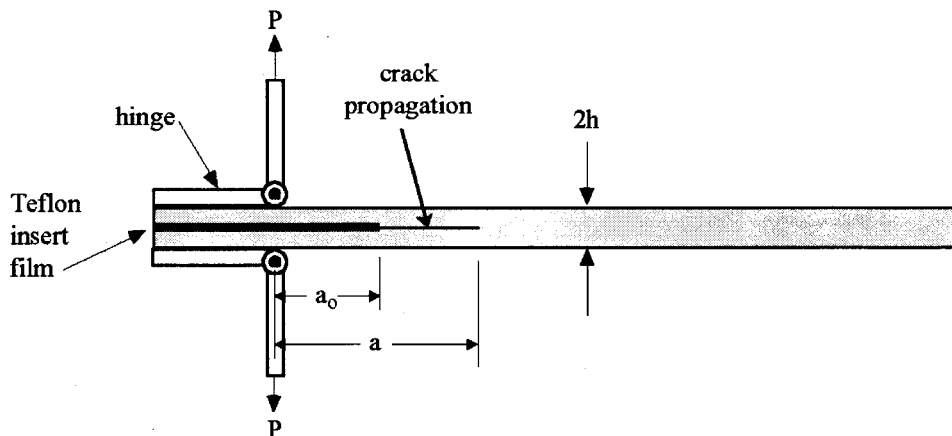
Figure 95. Mode I DCB geometry and loading (ASTM D5528).
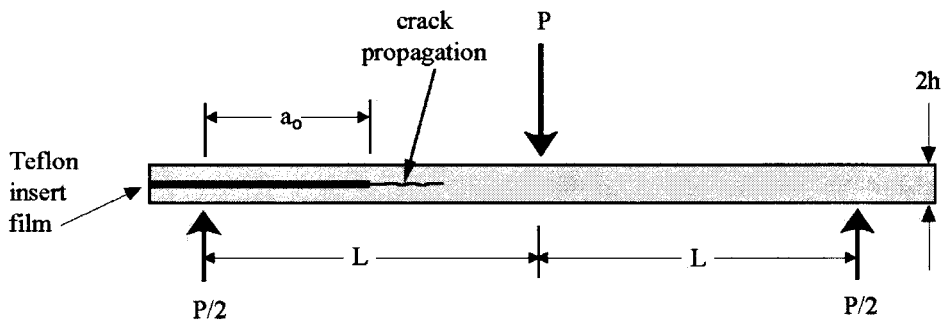
Figure 96. Mode II ENF geometry and loading.

136
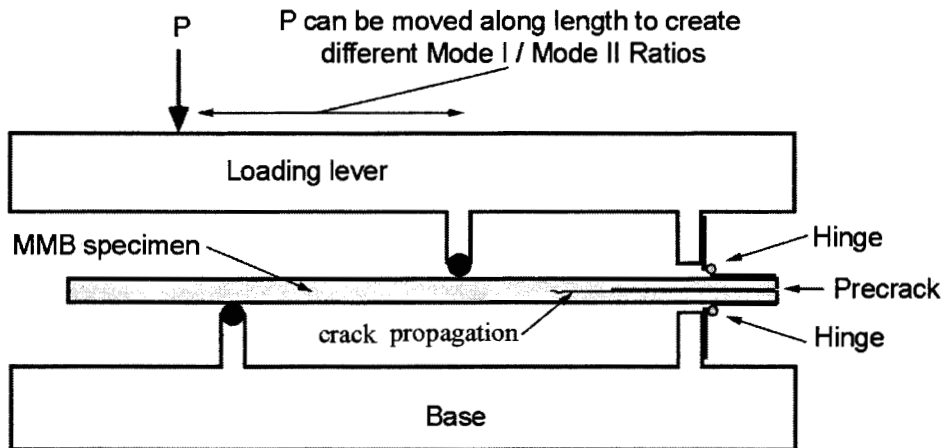
Figure 97. Mixed Mode Bending Test Apparatus.
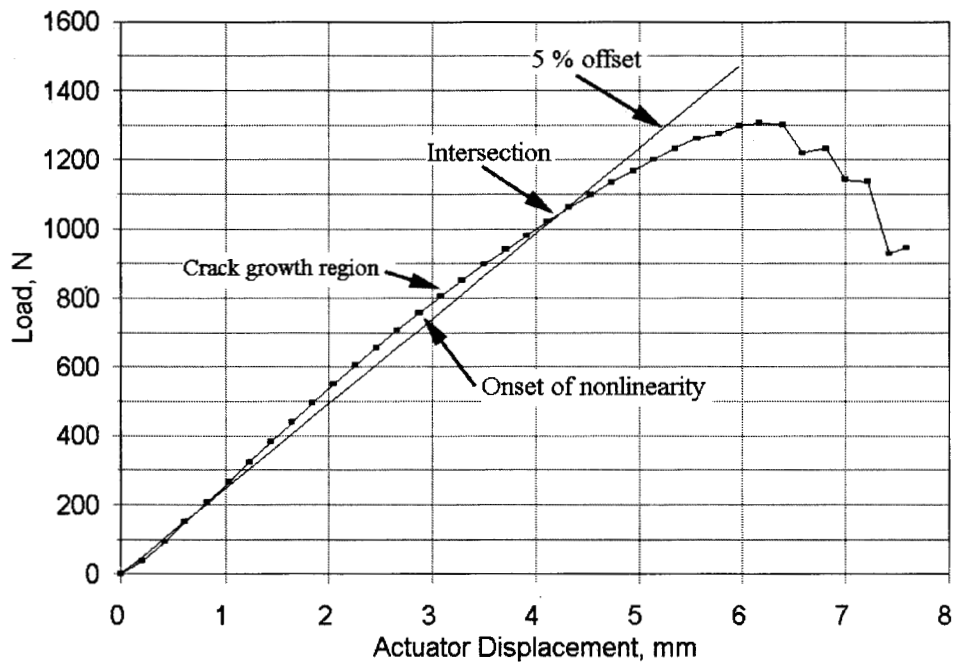
Figure 98. Typical Load versus Actuator Displacement for an ENF
Specimen.

To obtain critical values for G in static loading conditions, a variety of tests are used for the various modes of crack extension. For Mode I fracture, the standard test specimen is the double cantilever beam (DCB) as described in ASTM standard D5528 and shown in Figure 95. The critical strain energy release rate to grow a crack in the material can be obtained by the use of the load versus displacement curve of the test and the modified beam theory (MBT) method [76]:

$$G_{IC} = \frac{3\,P\,\delta}{2\,b\,a} \,, \tag{12}$$

where: P = critical load at crack propagation
      δ = displacement between DCB cantilever arms at critical load
      b = specimen width
      a = crack length measured from the center of the load pins

The end-notched flexure (ENF) test has emerged as the standard test method for measuring Mode II type crack growth, although questions remain as to crack closure problems. Typical specimen geometry and loading for an ENF specimen are shown in Figure 96. This specimen produces shear at the mid-plane of a composite loaded in three-point bending. When a critical load is reached, the crack advances, usually in an unstable manner [34]. A formula used to calculate G_{IIC} based on beam theory [77, 78] is given by:

$$G_{IIC} = \frac{9\,P^2\,a^2\,C}{2\,b\,(2\,L^3 + 3\,a^3)} \,, \tag{13}$$

where: P = critical load at propagation
      a = initial crack length measured from support point
      C = specimen compliance (= center point deflection/P)
      b = specimen width
      L = one-half support spacing distance

9.4.1. Analytical Prediction of Strain Energy Release Rate

Many analytical methods have been developed for use with finite element analysis (FEA) to predict strain energy release rates in each mode of crack extension. Two popular ways to calculate G are by (1) calculating the change in strain energy in an FEA model with an associated crack extension (virtual crack extension - VCE) [77], and (2) calculating the energy required to close a crack front by a small increment (virtual crack closure technique-VCCT) [79 - 82]. Both methods have gained acceptance, but the virtual crack closure technique has emerged as the preferred method. It has the benefit of allowing separate G calculations for each mode of crack extension.

The VCCT is based upon Irwin's hypothesis that the energy absorbed during crack extension (da) is equal to the work done to close that crack by the same incremental amount. This is the concept of the crack closure integral [74, 83]. Rybicki and Kanninen [83] applied this concept to the calculation of strain energy release rates with the finite element model. It has subsequently been

138

expanded for use with most common element types in FEA [84, 85].

The VCCT can be applied by two different methods. The one-step VCCT (VCCT-1) only requires one finite element run to calculate the G. This has obvious benefits in saving computing time for detailed analyses with long solution times. In this method, the forces at the crack tip are multiplied by the displacements behind the crack tip. Different formulas have been derived for the various finite element formulations [85]. A schematic of VCCT-1 for a 2-dimensional 8-node quadrilateral element formulation is presented in Figure 99. The formulas for G_I and G_{II} from Reference [85] are presented as Equations 14 and 15 where u and v are the nodal displacements in the x and y directions, F is a nodal force, i through m are node numbers, and Δ is the element width (Figure 99).

$$G_I = \frac{-1}{(2\Delta)[F_{yi} \ (v_m - v_m') \ + \ F_{yj} \ (v_1 - v_1')}$$ (14)

$$G_{II} = \frac{-1}{(2\Delta)[F_{xi} \ (u_m - u_m') \ + \ F_{xj} \ (u_1 - u_1')}$$ (15)

This technique may be used with a variety of element types and does not require the use of a quarter point nodal placement element with a stress singularity at the crack tip. No stresses are used in the calculation and it may be utilized with a relatively coarse mesh. Rybicki and Kanninen [83] found good results for the calculation of stress intensity factors with the VCCT-1 method and constant-strain elements at ratios of crack length to crack extension (a/da) as low as 5. Martin [86] has reported that when using the VCCT-1 technique, there was no mesh size dependency if the crack was grown within the same material type, but found that if the crack grew at a bimaterial interface, the calculations were mesh size dependent. However, he gave no recommendations for acceptable (a/da) ratios. Values for (a/da) ratios from 50 to 200 have been recommended for general fracture mechanics analysis with FEA [87].

The two step VCCT (VCCT-2) uses two successive FEA runs to calculate G values. The first analysis is performed with the specified loading on the structure, while the second analysis uses unit loads at the nodes immediately behind the crack front to close the crack by some amount. Details of the VCCT-2 method can be found in References 35, 88 and 89. Since the VCCT-1 method was found to be both faster and in better agreement with experimental data in this study [35], it has been used throughout the substructure studies.

The FEA virtual crack closure methods have been tested against the modified beam theory Equations 12 and 13, and applied in the skin-stiffener substructure studies reported in later sections. Results presented in this section were determined by Equations 12 and 13.

139
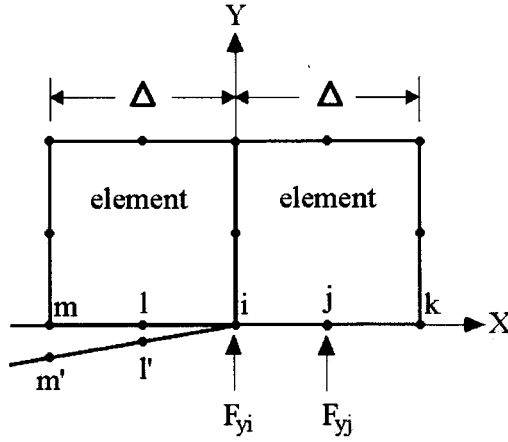
Figure 99. VCCT-1 schematic with
8-node quadrilateral elements.

9.4.2. Mixed-Mode Fracture Criteria

Delaminations in composites often have a mixed mode interaction at crack fronts. Once a database of fracture toughness has been established for Mode I and Mode II, a mixed-mode fracture criterion must be established for use in the complex architectures. Russell and Street [78] proposed a form of

$$\left(\frac{K_I}{K_{IC}}\right)^m + \left(\frac{K_{II}}{K_{IIC}}\right)^n = F \tag{16}$$

for the interaction of stress intensity factors in modes I and II. The coefficients m and n are determined by curve-fitting and the K values are the stress intensity factors and c indicates the critical value for unstable crack growth. The K values are proportional to the square root of the G values [75].

Reeder [90] used a parallel formulation based on the G-values which are actually measured in delamination tests. This can be expressed in terms of fracture energies as

$$\left(\frac{G_I}{G_{IC}}\right)^{\frac{m}{2}} + \left(\frac{G_{II}}{G_{IIC}}\right)^{\frac{n}{2}} = F \tag{17}$$

where the coefficients m and n are determined by curve-fitting. When F is greater than 1.0, crack growth occurs. Equation 17 has been applied in this study for static delamination, and extended to fatigue crack growth by using the G_I and G_{II} for a particular crack growth rate, in place of the static fracture values G_{IC} and G_{IIC}.

140

9.5. Results and Discussion

9.5.1 Modes of Crack Growth

Testing for delamination resistance is often complicated by crack extension which is not self-similar. That is, the crack does not extend in a simple flat planar fashion from the starter crack which is included in the test specimen. Often, the first millimeter or two is self-similar, particularly if there is a matrix rich area ahead of the teflon film used as a starter crack. As the crack extends, the adjacent plies may form cracks in the matrix and interface above and below the delamination plane, or strands may debond from the adjacent plies, sometimes bridging the crack. These phenomena can significantly increase the resistance to propagation of the main crack relative to a simple self-similar extension of the main crack between the plies. The interpretation of delamination resistance is greatly complicated due to these associated cracks and debonding. While this has been observed in Mode I in prepreg materials [50], it is more common the more heterogeneous the microstructure becomes. A major concern is that, in an application with mixed-mode cracks and different far-field stresses, the benefits of the secondary crack phenomena may not be realized, and the crack resistance may be much lower. The most self-similar crack resistance tends to occur between 0° plies, where the crack extends parallel to the fibers.

Figure 100 shows schematics of crack paths from tests involving a 45°/90° interface (the other plies are ±45°) relative to the crack path. Interfaces involving 45° and 90° plies show extensive secondary cracking; they are common in stiffener-type substructures as discussed later. The Mode I (DCB) crack contains extensive matrix cracking in the ±45° plies, away from the main crack (Figure 100A). In fatigue crack growth (Figure 100B) the lower stresses result in a significant reduction in secondary cracking in Mode I. This reduction in secondary cracking in fatigue has also been observed in prepreg materials [50]. In Mode II, ENF specimens (Figure 100C), reduced secondary cracking is observed, and in fatigue in Mode II (Figure 100D) no secondary cracking is observed.

9.5.2. R-Curve Results

The extensive secondary cracking in Mode I results in an increasing crack resistance as the crack extends, termed R-curve behavior [75]. Figures 101(a) and 101(b) show the increasing value of G_{IC} calculated as a function of the length of crack extension from the initial starter crack ($a^*=a-a_o$). Figure 101(a) gives the least increase in crack resistance for a [0°/0°] interface, while a crack between +45° and -45° plies shows much greater R-curve behavior. In comparison, the data in Figure 101(b), covering a much shorter range of crack extension, show similar data for cracks between +45°and +45°, and +45° and 90° plies. Each of these figures include data from several tests specimens; the fabrics were D155 0° plies, DB120 ±45°, and the ortho-polyester matrix with a fiber content in the 30 to 40 percent range. The matching fracture surfaces from the +45°/-45° interface are shown in Figure 102, indicating extensive strand debonding.

141
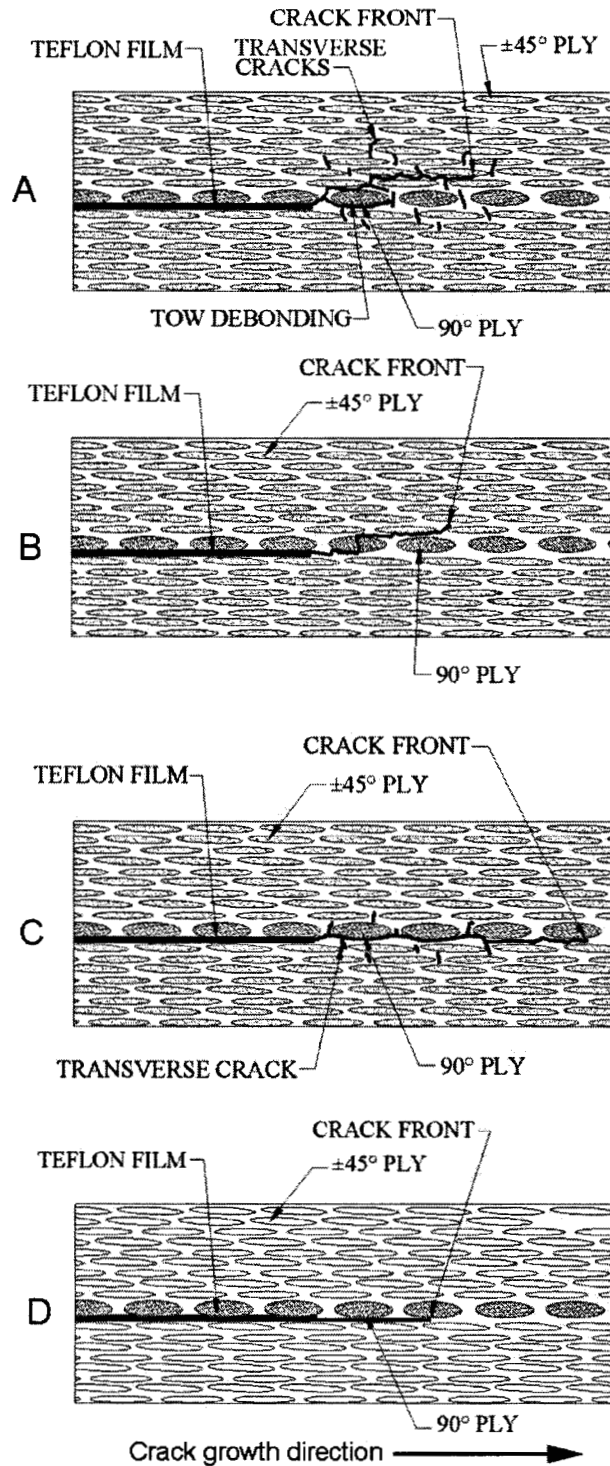
Figure 100. Details (Sketches of Actual Observations) of Crack Growth in a (90°/45°) Interface Under (a) Static DCB Testing, (b)Fatigue DCB Testing, (c) Static ENF Testing and (d) Fatigue ENF Testing [40].

Figures 101(a) and (b) demonstrate that the G_{IC} value can increase by several-fold within the

142

first 10 mm or so of crack extension. The figures also demonstrate the great scatter which is typical of G_{IC} and G_{IIC} test data. the G value varies with the force squared (or force multiplied by deflection), which inherently increases the degree of scatter over properties which are proportional to stress. The G value also represents the very local area near the crack tip, which tends to vary more than do macroscopic domains.

The strong R-curve behavior observed in Mode I, combined with the DCB test geometry, lead to very stable crack extension in Mode I, with further crack extension requiring the application of increased force and/or displacement. Mode II cracks show much less R-curve behavior, and the ENF test specimen geometry leads to unstable crack extension in most Mode II tests.
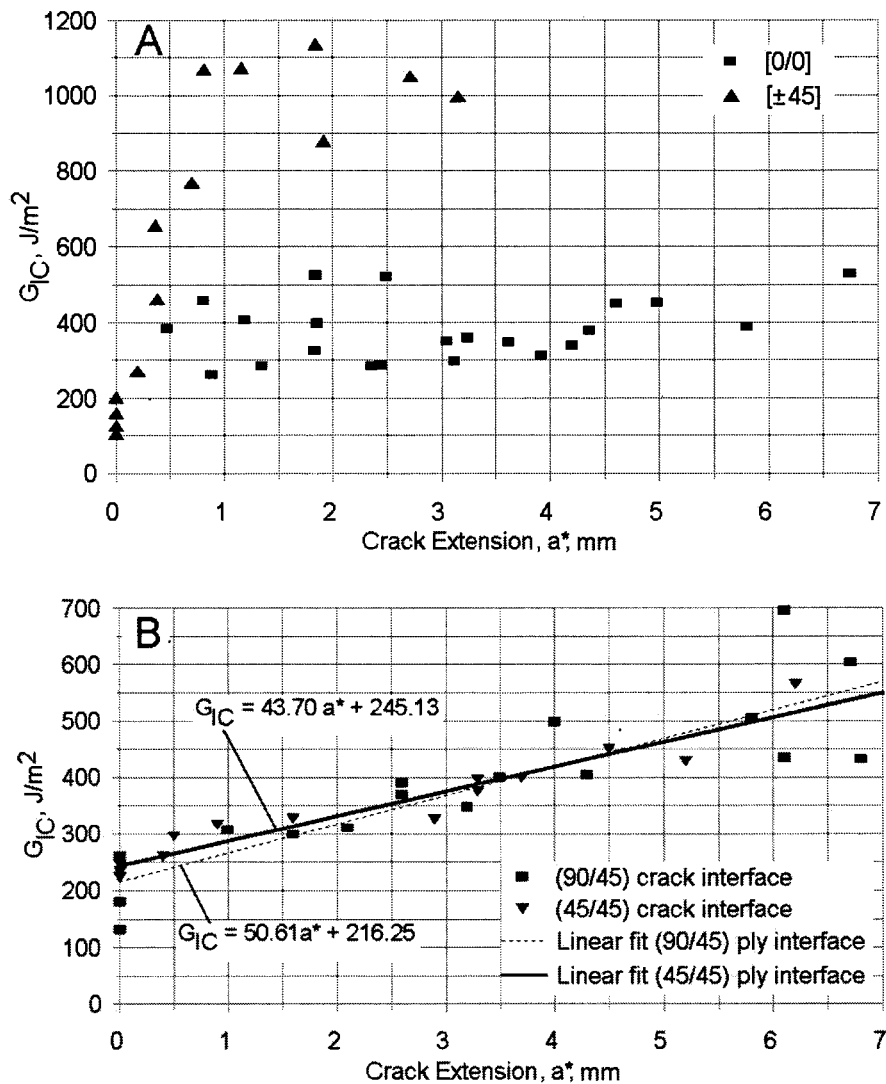
Figure 101. R-Curve Data for (a) (±45) and (0/0) interfaces (calculated with the MBT method) and (b) (+45/+45) and (90/45) interfaces [40].

143
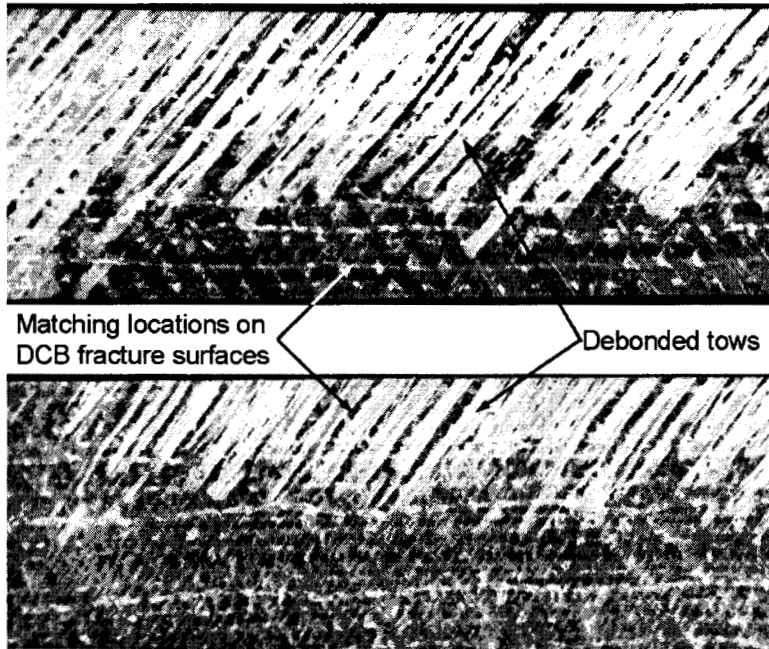
Figure 102. Fracture Surface for a $(\pm 45)_{10}$ DCB specimen.

9.5.3. Test Protocol and Design Philosophy

The strong R-curve behavior in Mode I complicates testing and the use of the data in design. Differing geometries and loads, as well as mixed-mode crack growth, may reduce or eliminate the R-curve effect, resulting in the much lower crack resistance evident for initial crack extension. Effects of this sort appear to be occurring in some of the substructure studies, when delaminations are observed to initiate in the structure (Chapter 13, Figures 163 and 164); they often show little or no secondary cracking if the overall crack length is short, and their growth conditions suggest that the R-curve effect shown by DCB specimens for that extent of crack extension is not present.

Another complicating factor involves fatigue crack growth. As the G_I and G_{II} values are reduced, the extent of secondary cracking decreases. During slow fatigue crack growth, the G values may be an order of magnitude lower than the G_{IC} or G_{IIC} values. This greatly complicates fatigue crack growth testing, since any increase in crack length, if it increases G, may arrest the crack due to greater secondary cracking. With the high crack growth exponents observed in delamination, this produces an extreme case of the well known overload crack retardation effects observed in metals [75].

As a consequence of these factors, it was decided to limit delamination tests and design recommendations to the lower G_{IC} and G_{IIC} values observed in the initial stages of crack growth, up to two millimeters of extension. Even that limitation allows some R-curve behavior, as evident in Figures 101a and 101b. This philosophy requires testing of a new specimen for each data point, whereas multiple points can be obtained from one specimen if R-curve effects are allowed. Testing for initiation G-values was discussed earlier.

144

In fatigue crack growth, the growth rate is measured only for the first five millimeters or less of crack growth. Only one crack velocity is obtained for each specimen at a particular maximum G-value. This procedure is consistent with that adopted (for similar reasons) with carbon/epoxy prepreg laminates in Reference 50. However, fatigue crack growth cannot be reduced to initiation only, since it inherently involves extension distances of the same crack front.

9.5.4. Static Test Results

The static test results for G_{IC} and G_{IIC} are given in Table 21 for selected cases. Both the initial and average (after 2 mm of crack growth) G_{IC} values are listed. As described in the resins section, tougher resins like 8084 vinyl ester and SC14 epoxy show significantly higher delamination resistance in both modes. G_{IIC} values are higher than G_{IC} values for all systems, as expected from the literature. Tests on 0° unidirectional materials (with a 0°/0° interface) gave the lowest values of G_{IC}, and showed the least complications from secondary cracking; this orientation is used to evaluate different resins and environmental effects. For orientations other than 0°/0°, there is always concern that even the initiation G_{IC} involves some secondary cracking, which may raise the apparent value above the case for a crack in that interface, but with no secondary cracks, which could occur in service. This issue is discussed further in the section on skin-stiffener intersection fatigue, Chapter 13.

Table 21. Mode I and II Results from Various Studies (tested at ambient conditions).

Resin	V_F, %	Crack interface	G_{IC} initial, J/m^2	G_{IC} (ave), J/m^2	G_{IIC}, J/m^2	Reference
Derakane 8084(V)	36	[0/0]	344 (7)	595 (133)	2638 (567)	[36]
Derakane 411C50 (V)	36	[0/0]	234	396	2557	
System 41(E)	36	[0/0]	219 (22)	231 (38)	3776	
SC-14 (E)	36	[0/0]	638 (58)	638 (157)	3223 (520)	
Iso-polyester 75-AQ-010	36	[0/0]	200 (23)	321 (96)	1359 (459)	
Ortho-polyester 63-AX-051 (P)	40	[0/0]	153 (10)	196 (99)	977 (229)	[34]
	40	[0/0]	----	490 (3)	1430 (35)	
	40	[+45/-45]	----	780 (4)	2270 (53)	
	36	[0/0]	138 (56)	379 (81)	1293 (259)	[35]
	26	[+45/-45]	140 (41)	1028 (97)	2001 (286)	
	35	[45/45]	249[1] (75)	462 (107)	----	[40]
	35	[90/45]	273[2] (41)	420 (75)	942 (261)	
	36	[0/0]	176[3]	-----	-----	

NOTE: values in brackets indicate the standard deviation. 0° and 90° fabrics were D155 and 45° fabrics were DB120, both from Owens Corning Fabrics, except as noted.
[1] The average initiation G_{IC} from the starter strip was 236 J/m^2.
[2] The average initiation G_{IC} from the starter strip was 191 J/m^2.
[3] Using UC1018V unidirectional fabric.

9.5.5. Fatigue Crack Growth

Fatigue crack data are also available for a limited range of materials, shown in Figures 103 and 104. The data are represented in terms of the Paris Law, Equation 18 [75].These data are similar in nature to those for prepreg based materials in the literature, in terms of crack growth exponent, n, where

$$\frac{da}{dN} = A\ (\Delta G)^n \tag{18}$$

and A is a constant. It should be noted that it is often impossible to obtain self-similar crack extension in the desired ply interface, as cracks migrate to other interfaces, particularly in fatigue.
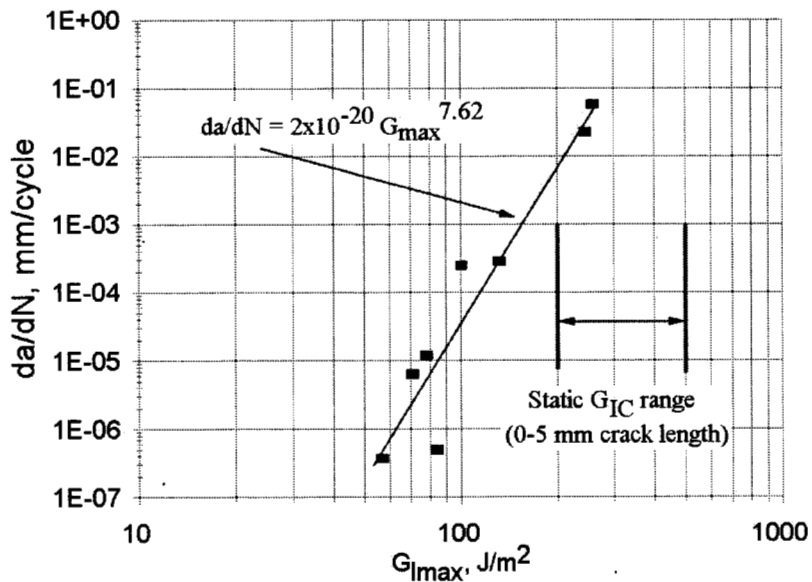
Figure 103. Mode I - (da/dN) versus G_{Imax}. [(±45)$_9$/90/(±45)$_8$] Laminates Cracked in the (90/45) interface. Short Crack Data (less than 5 mm), R = 0.1, DCB Specimens.

146
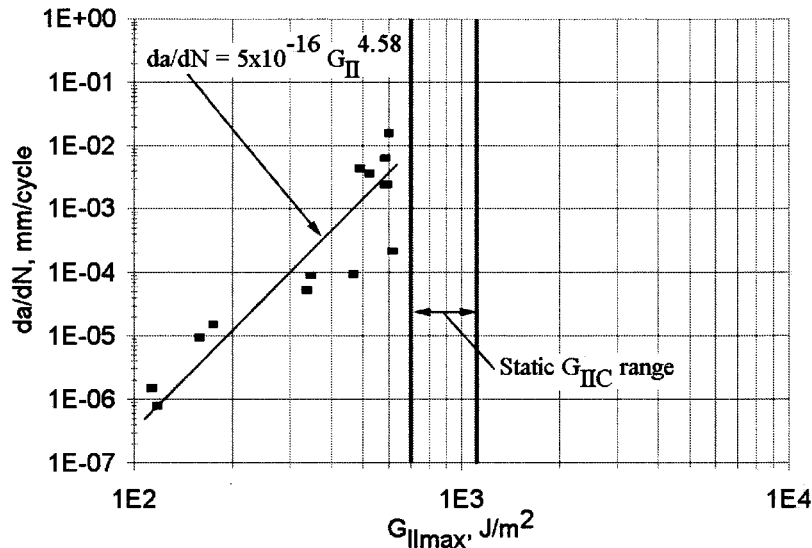
Figure 104. Mode II - (da/dN) versus G_{IImax}. $[(\pm 45)_9/90/(\pm 45)_8]$ Laminates Cracked in the (90/45) interface, R = 0.1, ENF Specimens.

9.6. Conclusions

This section describes initial efforts in this program in the area of delamination testing, analysis, and interpretation. The heterogeneous laminates used in blades, with typical fiber orientations in structural details, show significant complications from R-curve effects in opening mode, DCB tests. Values of G_{IC} increase rapidly, due to secondary cracking and strand debonding, as the crack extends even a few millimeters. Initiation values of G_{IC} are preferred as a conservative measure in case secondary cracking is suppressed in service. G_{IIC} values are obtained with less complications, and are much higher than G_{IC} values from the same laminate, as expected from literature results.

As noted earlier, tougher resins produce higher values of both G_{IC} and G_{IIC}. Studies involving substructures discussed earlier (under resins) and later show that substructure structural integrity also increases for tougher resins.

9.7. Design Recommendations

As later results in the skin-stiffener studies illustrate, naturally forming delaminations in substructures with mixed-mode cracks may show no secondary cracking. The use of initiation values of G_{IC} are recommended for both design and materials selection. Beyond this, it is advisable to obtain G_{IC} values for $0°/0°$ interfaces, as secondary cracking may be unavoidable in DCB tests with other orientations. G_{IIC} values are less complicated, but use of $0°/0°$ interface values are justified for this case as well.

147

10. OTHER DATABASE ADDITIONS

10.1 Overview

This chapter contains results for several types of materials not previously available in the database. Data are presented in separate subsections for carbon fiber and carbon/glass hybrid laminates; glass fiber composites with well-dispersed fibers (compared with stranded fabric reinforcement); sandwich panels; injection molded carbon fiber/thermoplastic matrix composites; and useful relationships between molding pressure, ply thickness, and fiber content for most materials in the database.

The carbon fiber results focus primarily on the large tow, low cost carbon fabrics. Most of the results are for hybrid laminates with carbon 0° plies and glass ±45°plies. There were difficulties with fabrication and testing in some cases and tests are on-going. Results to date indicate good performance in tension for static and fatigue properties. Fatigue stress and strain levels in tension are better than those for all glass laminates, as is the elastic modulus, as expected. The compression data are disappointing when viewed in terms of strain levels for static and fatigue properties. While prepreg materials, with relatively well dispersed and well aligned fibers, show longitudinal compressive ultimate strains above 1.0 percent, woven fabrics with large tows are in the 0.6 to 0.7 percent range, and stitched fabric is in the 0.7 to 0.8 percent range. Million-cycle compression fatigue strains are in the range of 0.35 to 0.45 percent for the woven fabrics and 0.55 to 0.6 percent for the stitched fabrics. The fabrics were tested with a vinyl ester matrix. The carbon fabric compression strains fall well below values for glass fabrics, and may be sufficiently low to be a limiting factor in blade design.

New data for impregnated strands and prepreg laminates with well dispersed glass strands support the earlier view that the transition to poor tensile fatigue resistance with increasing fiber content (reviewed in the background section) is related to the stranded architecture of the fabrics. While this transition occurs around 40 percent fiber by volume in stranded glass fiber laminates, it is shifted to the 60 percent fiber by volume range when the fibers are well dispersed, as in prepreg laminates. This is explored further in Chapter 11.

Sandwich panel construction is used to raise the bending and buckling resistance of thin airfoil skin areas in most blades. If this construction is used in high stress areas of blades, it must withstand the same strain levels as do adjacent primary structures. A typical sandwich panel with glass fiber laminate skins and balsa core was subjected to static and fatigue testing. The results show very similar tensile ultimate and fatigue strengths when compared to the base laminate without the core. Chapter 14 deals with the greater problem of transitions between the sandwich panel and plain laminate.

Static and fatigue testing was also done on an injected molded carbon fiber/thermoplastic matrix material. Test specimens were cut from small turbine blades. The results show relatively good stiffness, strength and fatigue properties compared with typical database glass fiber laminates.

However, these materials are probably not appropriate for large blades due to relative brittleness and probable molding related problems in thick sections.

A final part of this chapter provides data for most database materials, relating molding pressure and ply thickness to fiber content. These data can be useful in initial mold and process design, to obtain desired fiber contents (associated with weight and mechanical properties).

10.2. Carbon Fiber Laminates and Hybrids

10.2.1. Introduction

Carbon fibers have the potential to improve the efficiency of blade designs due to their increased modulus and strength and reduced density and tensile fatigue sensitivity relative to glass fibers. The potential of carbon fibers depends strongly on their price, which has been dropping as production shifts to larger tow (strand) sizes. Carbon fiber composites have been the subject of intense research for many years due to their attractiveness for aerospace applications, and an extensive database of static and fatigue properties is available in the open literature [72, 73]. However, few data are available for the new, lower-cost large-tow forms of carbon fibers, particulary in fabrics, or for matrix materials of interest in blade applications.

The higher modulus of carbon fibers is critical to their use in blades, since, for the same blade outer geometry and bending stiffness, EI, the material can be made thinner, reducing the moment of inertia, I, to the extent that the modulus, E, is increased. Also, the thinner and less dense composite reduces the weight of the blade.

The advent of larger tow, lower cost carbon fiber materials in both prepreg and woven fabric (Figure 105) forms has led to the possibility of economical laminates which are all carbon or at least all carbon in the 0° plies. On-going tests are designed to investigate the potential of these materials for blade applications. This section provides results and discussion for the materials tested to date, but a full set of data is not yet available.

10.2.2. Results and Discussion

10.2.2.1. Carbon Fiber Composites

Literature fatigue data [71] for small-tow carbon fiber/epoxy prepreg composites indicate much improved tensile fatigue resistance over glass fiber composites; the fatigue coefficient, b, in Equation 1, is usually in the range of 0.04 compared with 0.10 to 0.14 for all glass fiber composites. Compression fatigue data [91] are similar to those for glass, with b-values in the 0.07 to 0.08 range. Both tensile and compressive ultimate strengths are usually higher than for glass, while corresponding strain values are lower.

Figures 106 and 107 gives tensile and compressive stress and strain based fatigue data, respectively, for a large-tow carbon fiber unidirectional composite with a vinyl ester matrix, fabricated by RTM. This is material UNI25 in the database. The tensile data are in the expected range for both static strength and ultimate strain, and fatigue coefficient, b. The compression ultimate strength and strain results are relatively low, apparently due to the fabric weave (as noted earlier, woven glass fiber composites have much lower compressive properties than do straight-fiber stitched fabrics or prepregs). The compressive ultimate strain is in the range of 0.6 percent, and fatigue strains at 10^6 cycles are in the 0.4 percent range. A similar fabric, UNI21, produced somewhat lower results, but the loose weave resulted in significant fiber wash during processing. Results presented in the following section for a stitched large tow carbon fabric, Toray ACM-13-1, showed some improvement in compressive strains. Table 22 gives unidirectional elastic and strength properties for a large tow carbon fiber system compared with common glass fiber materials.

Large tow carbon/epoxy prepreg data given by material suppliers show compression ultimate strain values above 1.0 percent [92]. It is expected that stitched fabric performance, possibly with an epoxy resin, might also reach the 1.0 percent range. Whether large blades can be manufactured without significant fiber waviness remains to be seen; experience with carbon fabrics in the RTM process at MSU has been that it is difficult to obtain good quality laminates without some fiber waviness.

Zoltek UNI21   Zoltek UNI25 (XP33FBUD25)

Toray ACM - 13 - 2   Toray UT - 70 - 60

1 cm
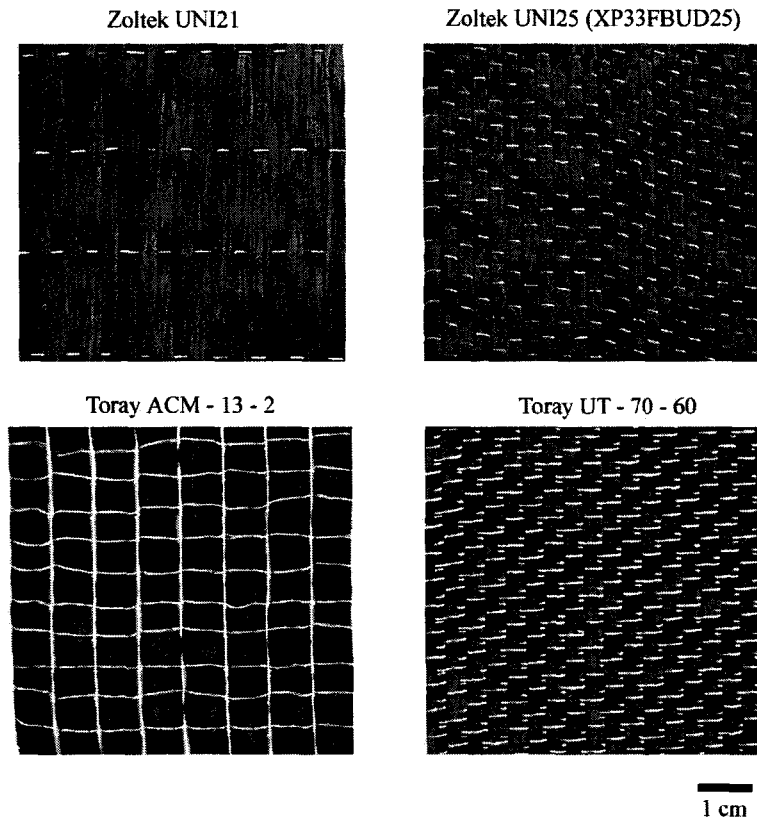
Figure 105. Woven Large Tow Carbon Fabrics.

150
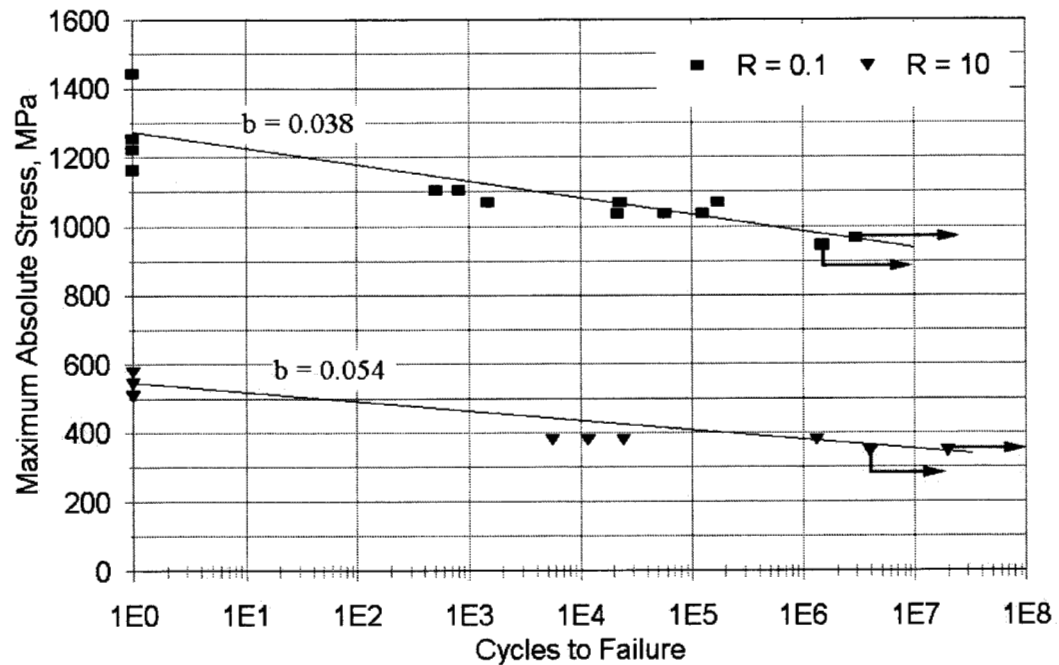
Figure 106. S-N Diagram for Large Tow Unidirectional 0° Carbon Fiber/Vinyl Ester Composites (UNI25 and UNI25A in the Database), R = 0.1 and 10.
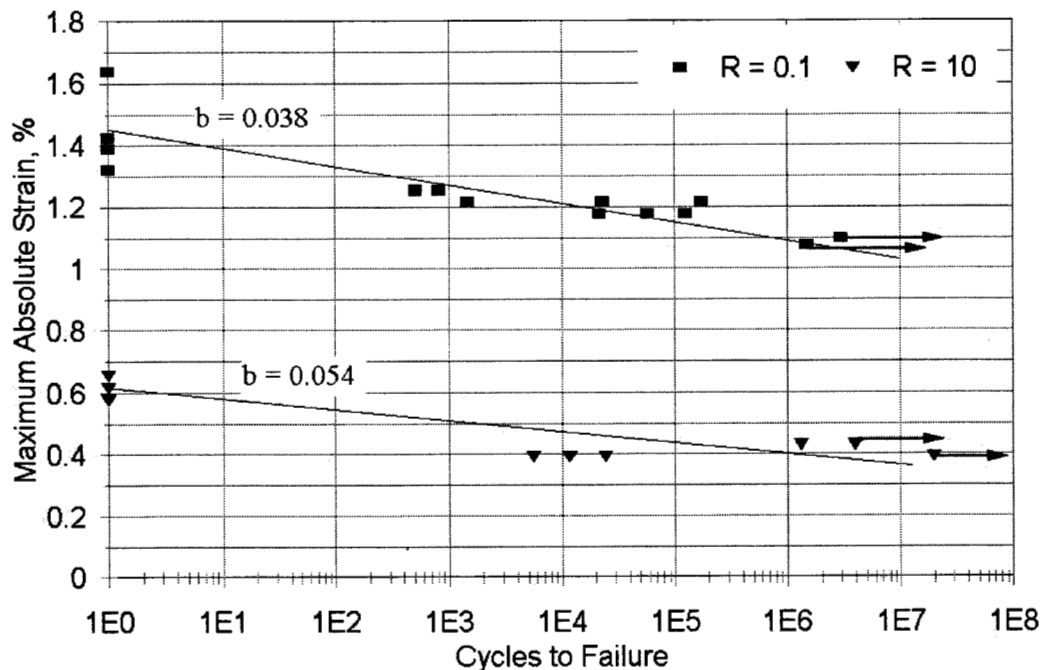
Figure 107. Fatigue Strain Diagram for Large Tow Unidirectional 0° Carbon Fiber/Vinyl Ester Composites (UNI25 and UNI25A in the Database), R = 0.1 and 10.

151

Table 22. Elastic Constants for Glass and Large Tow Carbon Unidirectional Fabrics

| | | | Longitudinal Direction | | | | | | | | Shear | Transverse Direction | | | |
| | | | Elastic Constants | | | | Tension | | Compression | | | Tension | | Compression | |
Fabric	lay-up	V_F %	E_L GPa	E_T GPa	ν_{LT}	G_{LT} GPa	UTS_L MPa	ϵ_U %	UCS_L MPa	ϵ_U %	τ_{TU} MPa	UTS_T MPa	ϵ_U %	UCS_T MPa	ϵ_U %
A130 Glass	$[0]_8$	45	36.3	8.76	0.32	3.48	858	2.53	-334	-0.92	85.3	33.8	0.39	-93.3	-1.05
D155	$[0]_6$	45	35.0	8.99	0.31	4.10	987	2.83	-746	-2.02	97.7	27.2	0.32	-123	-1.67
UNI25	$[0]$	45	89.7	6.80	0.27	----	1213	1.35	-535	-0.60	--	20.5	0.31	-100	-1.47

* See Database for testing details.

10.2.2.2. Carbon/Glass Hybrids

Mixed 0° Layers

The approach of using a combination of carbon and glass fibers in the 0° direction was explored in earlier tests (Materials CG and DD23 in the database). The purpose of these tests was to investigate whether a relatively low amount of carbon, replacing some 0° glass fibers, could improve the tensile fatigue performance at high cycles. Figures 108 and 109 show the predicted and experimental performance in terms of failure strains. Since both the glass and carbon fibers must operate at the same strain level, the component with the lowest strain capability will fail first: carbon at high strains and glass at low strains, in tensile fatigue. The experimental data for a 32 percent carbon material (CG) confirm this expected trend. While the carbon might survive the failure of the glass at very low strains, it is doubtful that fiber failure would be allowed in a conservative design.

While the carbon would significantly raise the material stiffness and stress capability if used in significant amount, tensile fatigue failure at low stresses would still be limited by the glass component. There would also be some complications caused by the difference in coefficient of thermal expansion between glass and carbon, which would cause some residual tensile strain in the glass if high cure temperatures were employed. However, the thermal tensile strain in the glass should be less than 0.1 percent, using published coefficients of thermal expansion.

Carbon 0° Layers with Glass ±45° Layers

The more likely scenario is to use all carbon in the 0° layers, with glass in the less critical ±45° layers. This should reduce the cost relative to all carbon composites, while providing nearly the same tensile and compressive strength, stiffness, and fatigue resistance as an all carbon laminate. The shear stiffness and buckling resistance would be reduced by use of the glass off-axis materials.

152
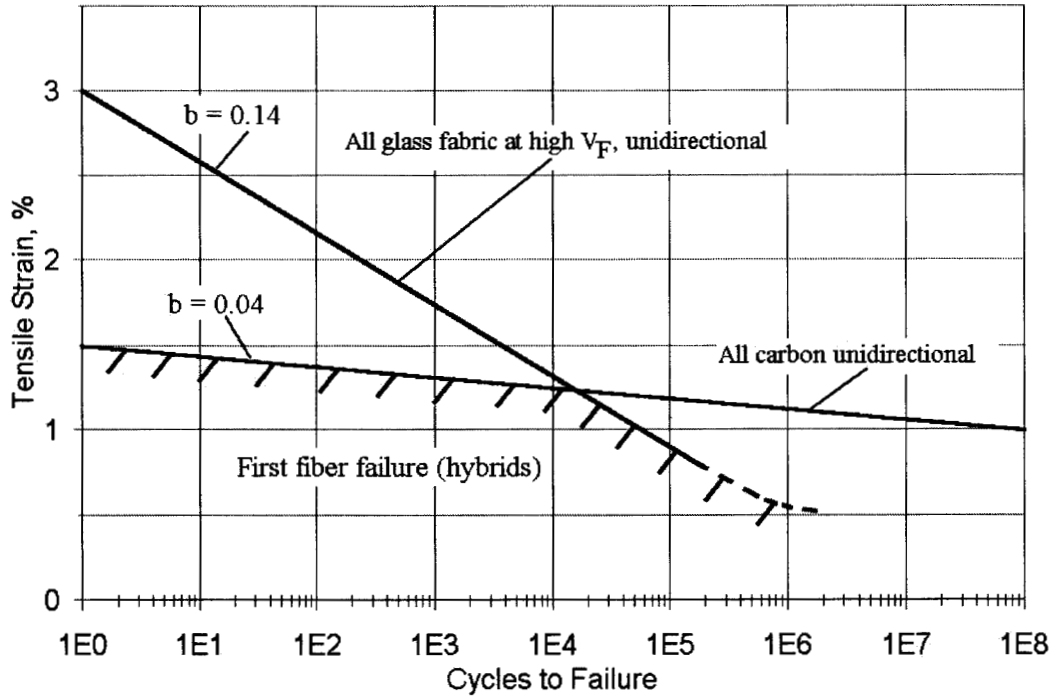
Figure 108. Predicted First Fiber Failure Strain Envelope in Tensile Fatigue for 0° Hybrids Containing, D155 Glass Fabric and AS4 6K Carbon Fabric.
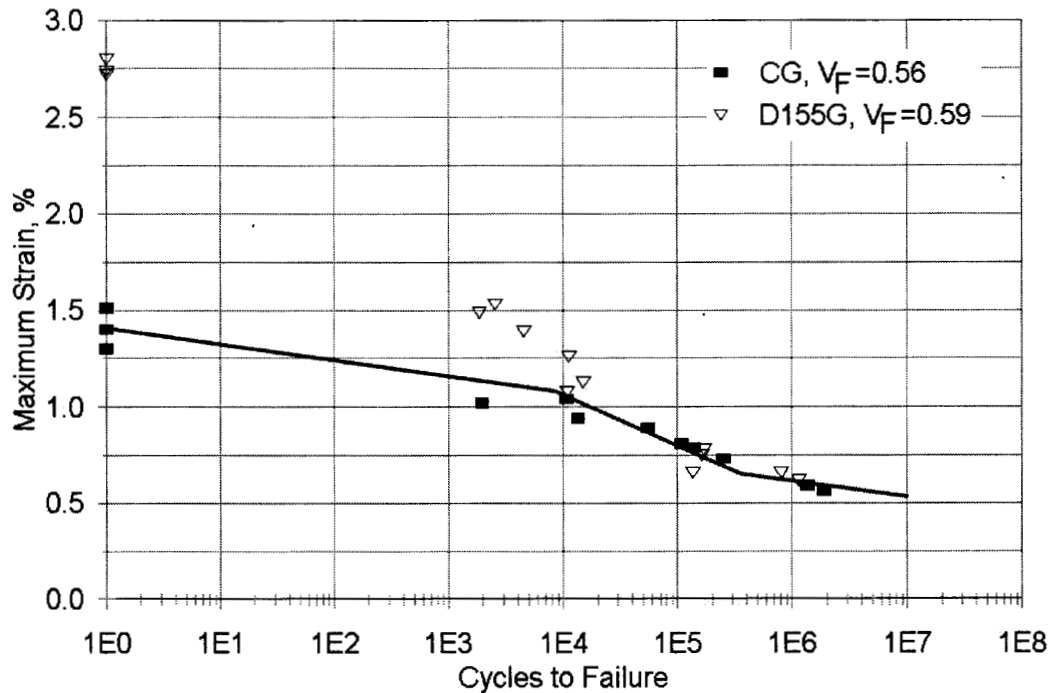
Figure 109. Tensile Fatigue Data for Hybrid Material CG [$(0_{2G}/0_{2C}/0_{3G})_s$, 32% Carbon, V_F=0.56, Vinyl Ester Matrix] where 0_G layers are D155 Glass and 0_C Layers are AS4-6K Carbon, Compared to All D155 Material D155G (V_F=0.58).

153

Figure 110 provides data for strain versus cycles to failure in compression fatigue for composites in the configuration ($\pm 45_G/0_{3C}/\mp 45_G$), with glass $\pm 45°$ plies and Toray large tow stitched carbon fabric ACM-13-2 $0°$ plies (Figure 105). The figure shows that the epoxy matrix provides somewhat improved compressive strength and fatigue resistance relative to vinyl ester. The results with the vinyl ester matrix show moderate improvement over the woven large tow carbon data in Figure 107, with further improvement using the epoxy matrix.
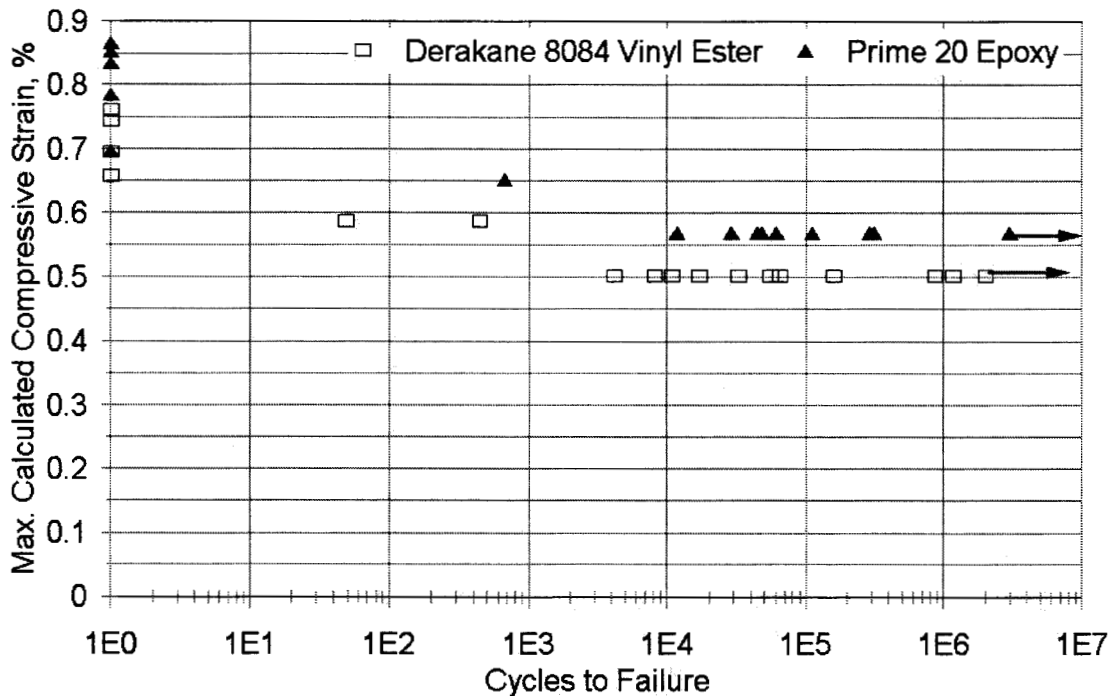
Figure 110. Hybrid Compression Fatigue Data for Vinyl Ester and Epoxy Matrices, Material CGD4 with a Ply Configuration ($\pm 45_G/0_{3C}/\mp 45_G$), $0°$ Fabric is Toray ACM-13-2 Carbon and $\pm 45°$Fabric is DB120 Glass, 76 Percent $0°$ Material by Volume, R=10.

10.2.3. Conclusions

Early data for large tow, low cost carbon fiber composites with a vinyl ester resin show good tensile fatigue performance, but marginal compression fatigue performance. The compression static and fatigue data are lowest for the woven fabrics, and improve for stitched fabrics. Prepreg composites with large tows, and epoxy resins may provided improved performance. The compression results indicate that caution should be exercised in using these fabrics for blade applications; further testing and full consideration of statistics and knockdown factors are needed to gain confidence with the large tow carbon fiber materials.

154

10.3. Tensile Fatigue of Composites With Well Dispersed Fibers

10.3.1. Introduction

Figures 1 through 4 in the background section demonstrated the strong dependence of tensile fatigue resistance on fiber content for fabrics with distinct strands. At higher fiber content, in the range of 40 to 45 percent fiber volume, the slope of the S-N curve, b, increases significantly, and the maximum strains which can be withstood for 10^6 cycles decrease significantly. This study was intended to obtain data for composites with well dispersed fibers in impregnated strands which were sufficiently small to avoid testing problems, as well as in prepreg laminates. The purpose was to observe whether composites without discrete strands might provide better tensile fatigue performance at high fiber contents, and to better understand the performance of stranded fabrics.

10.3.2. Experimental Methods

Strands were removed from the D155 fabric and inserted into a small diameter tube. Resin was then drawn into the strand, forming a circular cross-section at the desired fiber content. Fiber content was varied by changing the diameter of the tube or by adding additional fibers from the strand, which normally contains about 200 fibers. The impregnated strands were cured and removed from the tube. Test specimens were prepared as shown in Figure 57, and tested at frequencies up to 80 Hz. These strands differed from those reported in Figure 57 in that, while the strands in Figure 57 contained approximately 50 percent fiber by volume, they were simply impregnated and hung vertically to cure, without control over the cross-sectional shape or fiber content.

Additional tests were run on Hexcel M9.6/32%/1200/G (0°) and M9.6/35%/BB600/G (±45°) glass/epoxy prepreg laminates in the ply configuration (±45/0/±45) with 50 percent 0° material. These laminates were vacuum bag molded at 90°C for twelve hours, and tested in a dogbone geometry with a gage section width of 20 mm and thickness of 1.9 mm. This is Material GGP4 in the database. The commercial prepreg composite was tested as a baseline laminate with well-dispersed fibers in the 0° plies, at a fiber content of 53 percent fiber by volume.

10.3.3. Results and Discussion

The results for the strand specimens with varying fiber content are given in Figure 111. This Figure can be compared with Figure 1 given in the background for laminates fabricated with stitched fabrics D155 and DB120. The strand data show a similar increase in fatigue sensitivity at the highest fiber content. However, The strands, with uniformly dispersed fibers, show this transition at much higher fiber contents, with clearly increased fatigue sensitivity in the range of 60 percent fiber volume (Table 23) compared with the transition in Figures 1 and 2 in the 40 percent fiber by volume range.

The commercial prepreg material with well dispersed fibers and a fiber content of 53 percent shows a fatigue sensitivity coefficient, b (Equation 1), of 0.11 (Figure 112), similar to the strand data at 50 to 55 percent fiber by volume. This trend is similar to that in Figure 2 for D155 fabric laminates

with the fabric stitching removed, which also produced much lower tensile fatigue sensitivity in the range of 50 to 60 percent fiber by volume, compared with the stitched fabric.
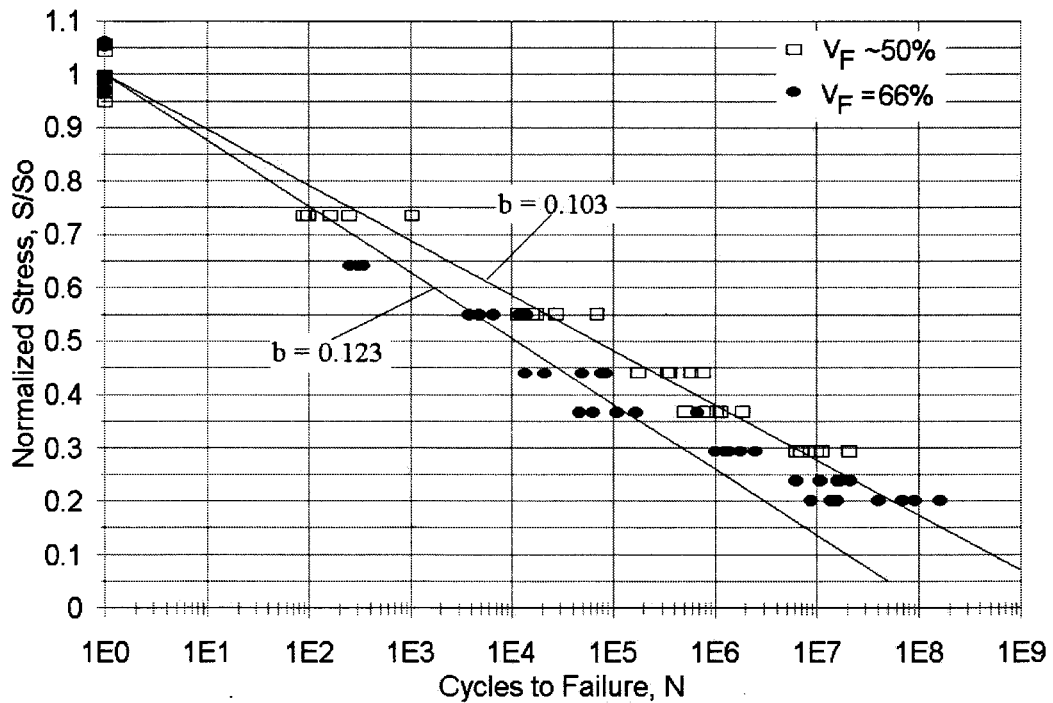
Figure 111. Tensile Fatigue (R=0.1) for Impregnated D155 Strands with Two Different Fiber Volume Fractions.

Table 23. Summary of Impregnated D155 Strands at Different Fiber Volume Fractions.

V_F, %	Fatigue Coefficient, b, (Equation 1)	10^7 strain, %
50	0.103	1.19
56	0.108	1.07
61	0.112	1.05
66	0.123	0.93
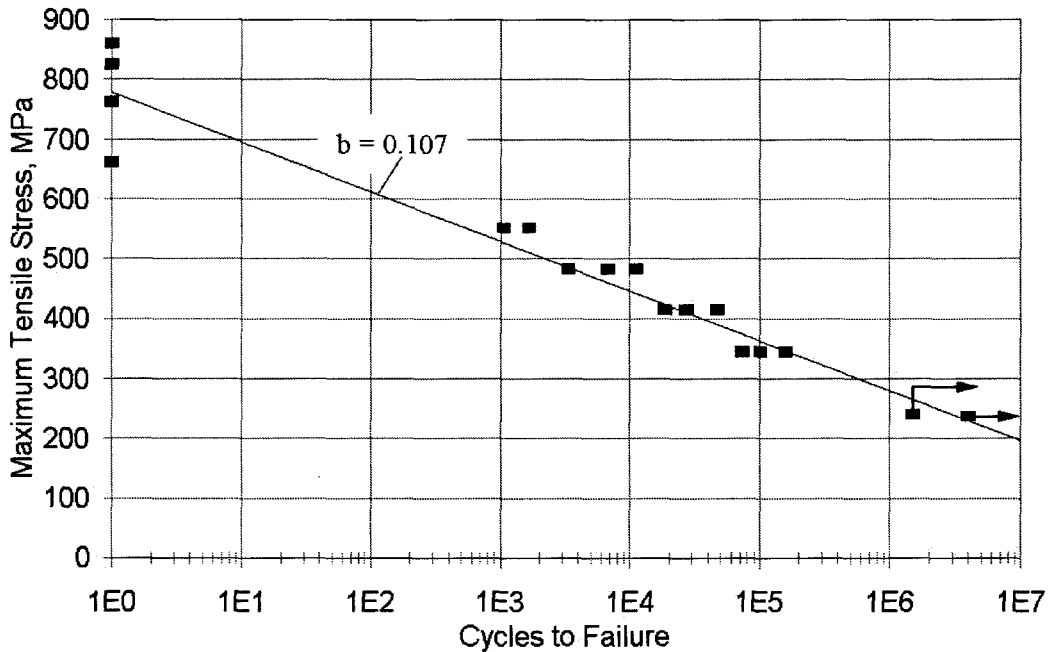
Figure 112. Tensile Fatigue Data for Prepreg Material GGP4 with a Layup of (±45/0/±45) at a Fiber Volume Content of 53 Percent, R=0.1.

10.3.4. Conclusions

Tests with composites containing uniformly distributed fibers show no transition to greater fatigue sensitivity in the range of 40 percent fiber by volume. Thus, the transition to poor tensile fatigue resistance in the 40 percent fiber by volume range, found for all stranded fabrics tested, appears to be caused by discrete strand fabric architecture with resin rich areas between strands. The data given in this section show the beginnings of a similar transition for composites with well dispersed fibers in the range of 60 percent fiber by volume. Earlier data for bonded fabrics and for D155 fabric with the stitches removed support this view. Chapter 11 explores this issue further.

157

10.4. Sandwich Panel Performance

10.4.1. Introduction

As noted earlier, sandwich panels are used to increase the bending stiffness of the blade skin, to resist skin buckling. However, sandwich panels often extend into high stressed portions of the blade and must operate on the same strain levels as the primary structure. Their static or fatigue failure could precipitate blade collapse. The later substructure section addresses the greatest problem with sandwich panels, the structural details associated with transitions from sandwich construction to normal laminate. This section (and the database) provides tensile static and fatigue data for a typical sandwich panel, in comparison to normal laminate structure, away from closeout areas.

10.4.2. Experimental Methods

Plain (control) laminates and sandwich panels were fabricated by hand layup using the A130, woven 0° fabric, DB120, stitched ±45° fabric, and the CoRezyn 63-AX-051 ortho-polyester resin with 2.0 percent MEKP catalyst, all described previously. The core material was Contourkore CK100 AL600/10 with a density specified as 150 kg/m³, by the manufacturer, Baltek Corporation. The plain laminate configuration was [±45/0₂/±45]. For the sandwich panel, the core was inserted at the mid-thickness of the laminate, yielding [±45/0/balsa/0/±45]. Although the balsa is surface treated to reduce permeability, it still absorbed some resin, and resin rich areas are formed where the balsa is scored to make it formable. A summary of processing details and properties for the balsa and laminate plies is provided in the sandwich terminations section of this report; complete details are available in Reference 42.

Considerable test method development was required for sandwich panel testing [42]. Among the problems encountered is that normal hydraulic gripping of the ends of a specimen, crushes the core material. The test geometry used for tension tests of the sandwich panel and plain laminates are shown in Figure 113 and failed specimens are shown in Figure 114. The grip area of the sandwich panel was filled with solid laminate in place of a core, and a tab covered the intersection of the balsa and solid laminate area. Gripping was outside of the tab area. This arrangement combined with the dogbone shape, resulted in the desired gage-section failures.

10.4.3. Results and Discussion

Table 24 gives static tensile strength data for the plain laminate and the sandwich panels. The strength of the sandwich panel was calculated based on the cross-sectional area of the facesheets only, ignoring the core; the facesheet thickness was assumed to be the same as for the plain laminate, with the same fiber content of 36 percent by volume. The precise thickness and fiber contents for parts of the sandwich panel are difficult to establish with any precision [42]. The strength and modulus values for the sandwich panel calculated with these assumptions slightly exceed those for the control laminate, apparently due to slight stiffening from the core. The ultimate strain values are nearly identical, suggesting that the laminate behavior is unaffected by the presence of the core.

158
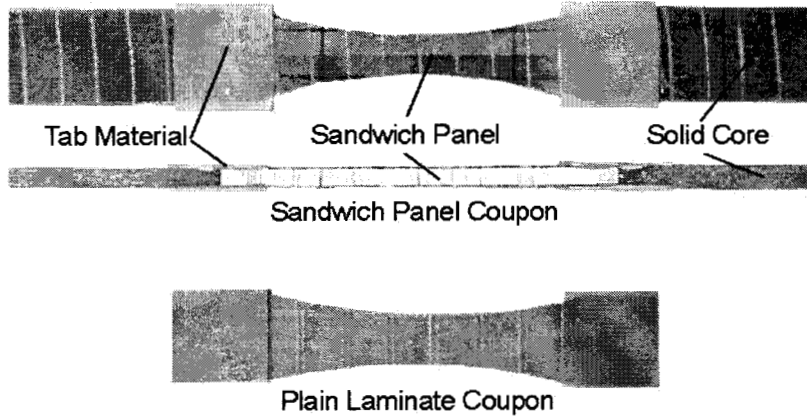
Figure 113. Tensile Sandwich (Top) and Plain Laminate (Bottom) Coupons.
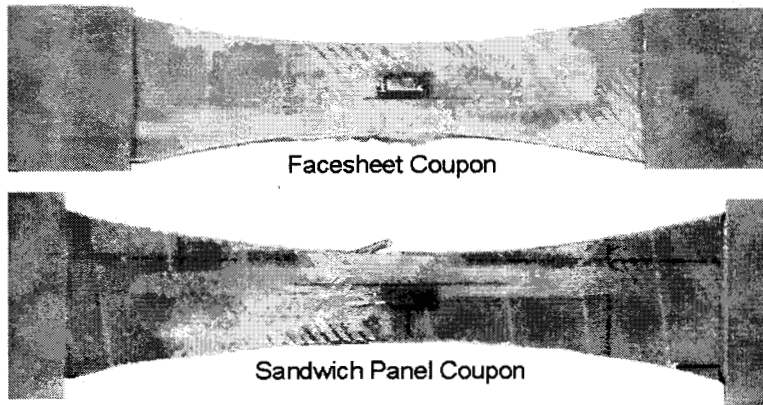
Figure 114. Static Test Specimens at Fiber Failure for Plain Laminate (Top) and Sandwich Panel (Bottom).

Table 24. Static Tensile Properties for Sandwich Panel and Control Laminate

	Longitudinal Strength, MPa		Longitudinal Strain, %		Longitudinal Modulus, GPa	
	Average	Std. Dev.	Average	Std. Dev.	Average	Std. Dev.
Control Laminate	383	9.6	2.68	0.09	18.09	1.23
Sandwich Panel	409	7.4	2.64	0.05	21.13	0.27

159

Table 25 and Figure 115 give the tensile fatigue results for the facesheet control and sandwich panel tests. Both materials performed well in tensile fatigue relative to other database materials. In particular the core, which formed obvious cracks during fatigue, did not delaminate from the facesheets except very locally, at matrix cracks.

Table 25. Fatigue Results for Control Laminate and Sandwich Panel.

Material	UTS, MPa	b	10^6 cycle strain, %	E, GPa
Control Laminate	383	0.084	1.05	18.09
Sandwich Panel	409	0.093	0.85	21.13
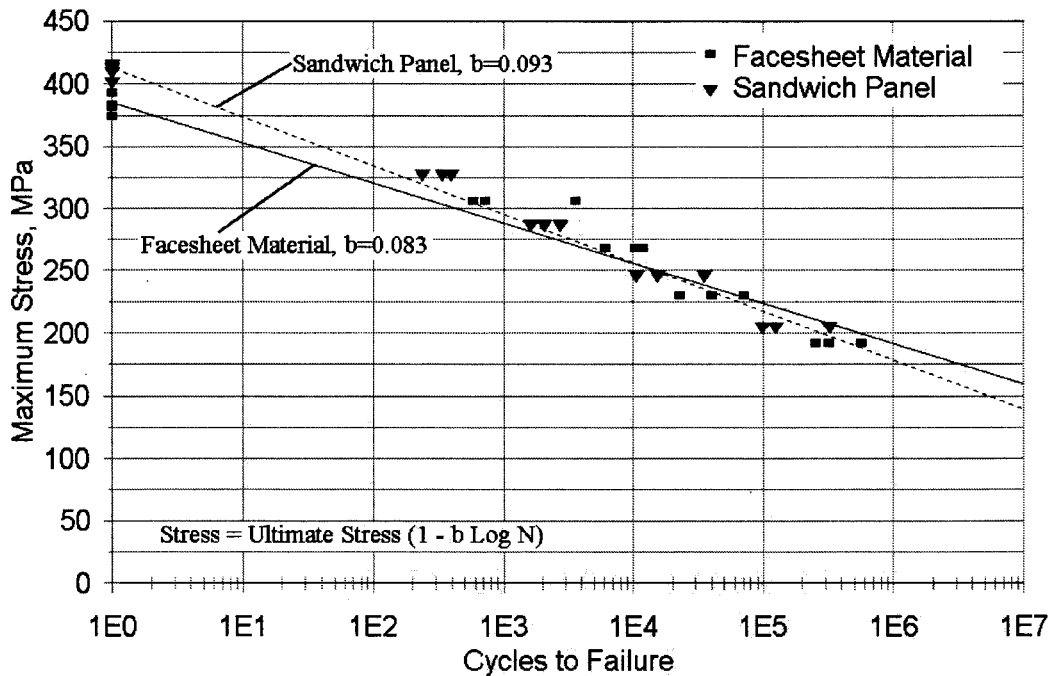
Figure 115. S-N Tensile Fatigue Data for Control Laminate and Sandwich Panel Specimens, R=0.1.

10.4.4. Conclusions

Sandwich panel materials show similar strength, modulus, and tensile fatigue resistance to baseline laminates. The transition areas to normal laminate do not perform nearly as well, as shown in Chapter 14.

10.5. Injected Molded Materials

10.5.1. Introduction

Injection molded thermoplastics containing short (less than 1 mm) glass or carbon fibers are widely used materials in many applications such as automotive. These materials generally [93] have a fiber volume fraction below 0.30, variable fiber orientation, and very short fibers which limits their mechanical properties. However, injection molding is a process which produces net-shape products at high production rates. The use of carbon fibers and longer fibers raises the properties. However, their relative brittleness and low strain to failure (despite using ductile thermoplastic resins) appears to limit their use to small blades. For larger blades, it would also be difficult to produce the desired fiber orientation in thicker sections. Despite significant reinforcement provided by the fibers, their failure is generally matrix dominated in tension, and fatigue trends with carbon fibers do not reach the levels found with continuous carbon fibers [71].

10.5.2. Results and Discussion

The material tested (material HH in the database) was reinforced with carbon fibers and supplied in the form of small injection molded blades. Test specimens were cut from near the blade tip as shown in Figure 116; test specimen geometry is shown in Figure 117 and broken specimens are shown in Figure 118. Failure modes are brittle- appearing cracks orientated normal to the maximum tensile stress direction. It should be noted that the direction and position tested would be expected to have the highest mechanical properties in the blade due to the thin cross-section and the material flow direction (down the blade length). The properties obtained were a fiber volume fraction of 0.21, tensile elastic modulus of 19.6 GPa, and ultimate tensile strength of 147 MPa. The ultimate strains in tension are low, as expected from the literature [71], in the range of 1.0 percent. Figure 119 shows typical stress-strain curves for this material, determined in this study, with a summary of material properties listed in Table 26. (Each specimen was removed from a different blade, and so a measure of the material variability is also included in these results.) Figures 120 and 121 show the tensile S-N fatigue data in terms of stress and strain respectively. The fatigue coefficient, b, from Equation 1, is 0.063, better than for continuous glass fibers, but not as good as for continuous carbon fibers. The significant nonlinearity of the stress-strain curves creates a discrepancy in fatigue, so the strain fatigue data trend was not fit through any static data.

10.5.3. Conclusions

Tensile test results for the carbon fiber reinforced thermoplastic injection molded material show good strength and modulus, but low strain to failure, typical of this class of materials. The fatigue performance is better than for many glass fiber laminates. Due to their brittleness, and poor fiber orientation in thick parts, injection molded materials are appropriate only for small blades.
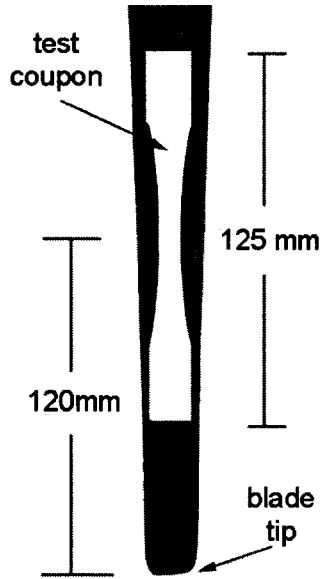
Figure 116. Test Coupon
Blade Locations.
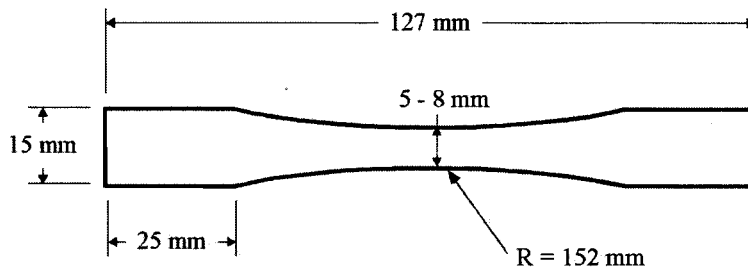
Figure 117. Material HH Test Coupon Geometry.
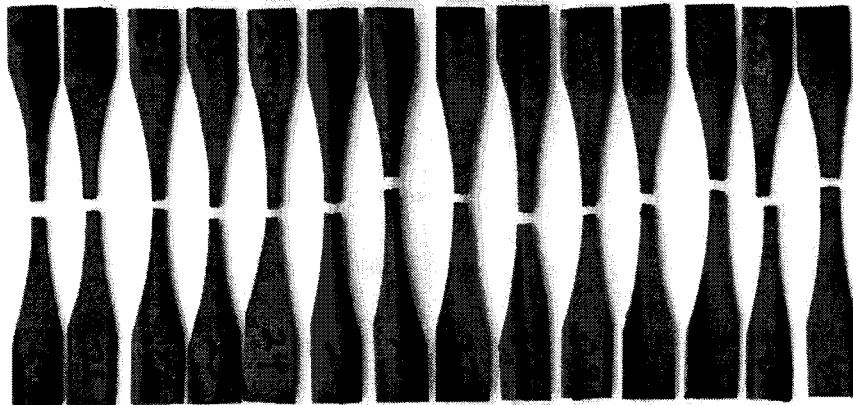
Figure 118. Typical Tension Coupon Static and Fatigue Failures.

162
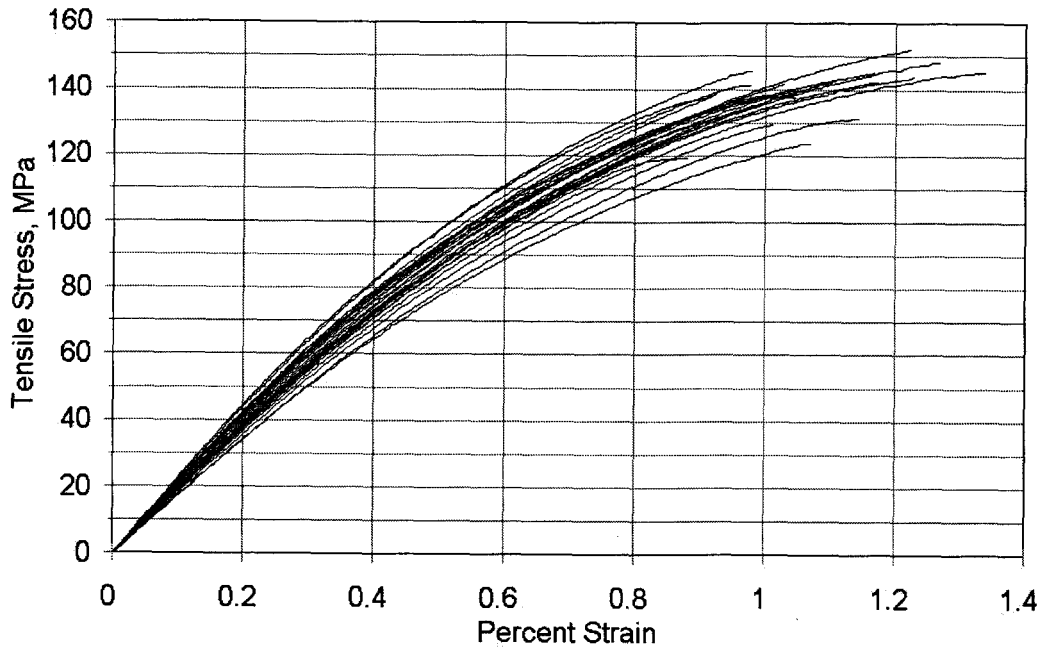
Figure 119. Typical Stress-Strain Curves for Injection Molded Carbon
Fiber/Thermoplastic Material (HH).

Table 26. Summary of Material Properties for Material HH.

b	Ultimate Tensile Strength, MPa		Ultimate Tensile Strain, %		Elastic Modulus, GPa	
	Average	Std. Dev.	Average	Std. Dev.	Average	Std. Dev.
0.056	140	8	1.07	0.12	19.84	1.46
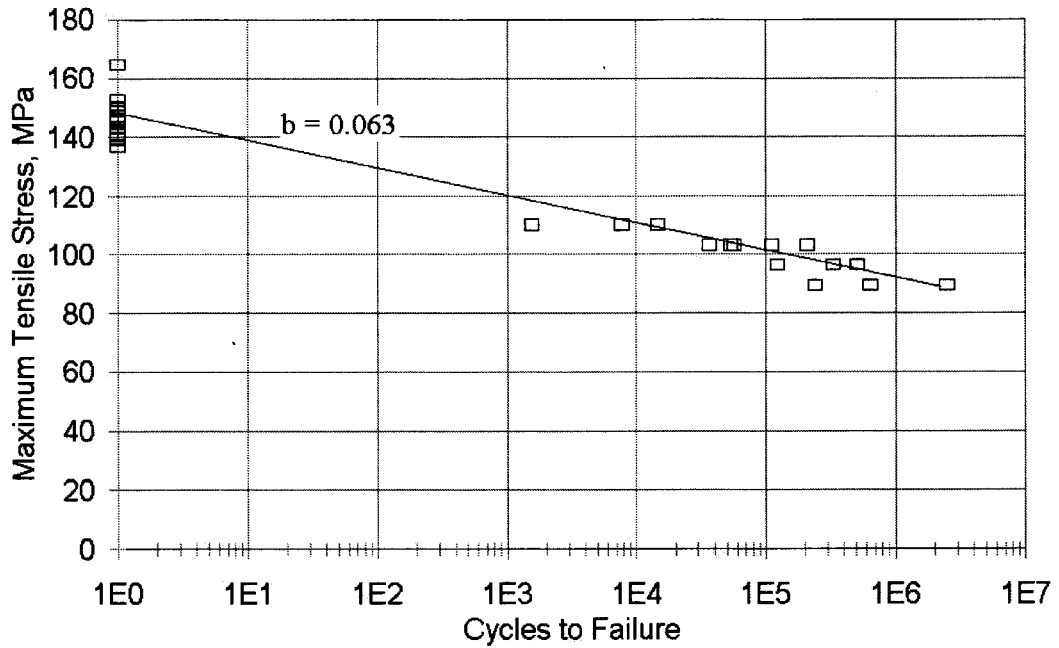
Figure 120. Fatigue S-N Data for Injection Molded Carbon Fiber/Thermoplastic Material (HH), R = 0.1.
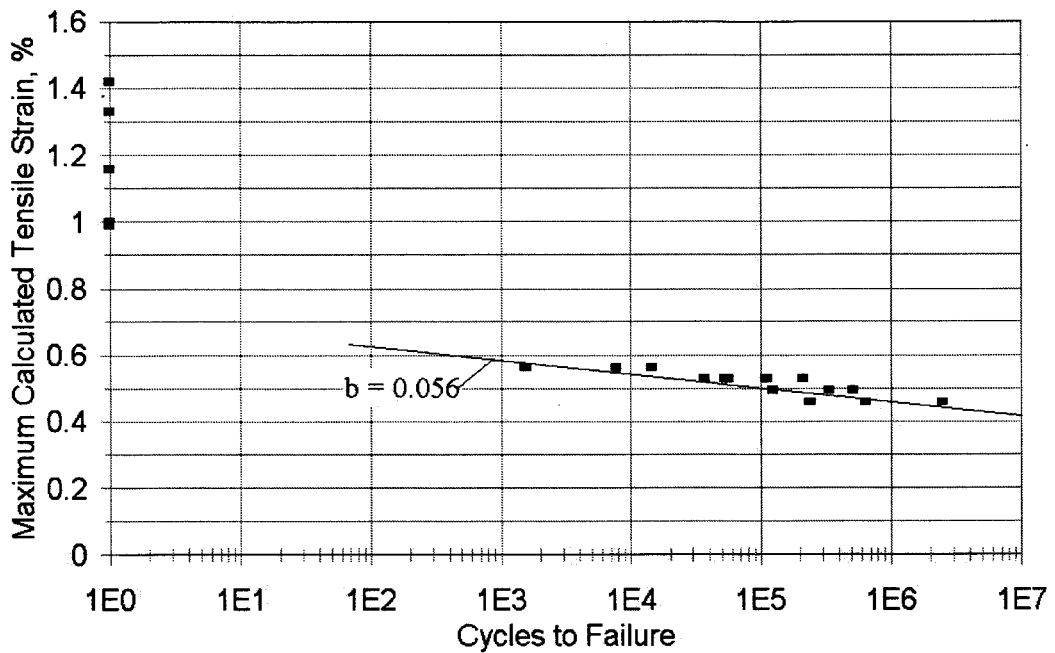
Figure 121. Calculated Strain versus Cycles to Failure for Injection Molded Carbon Fiber/Thermoplastic Material (HH), R = 0.1, (assumes E = 19.8 GPa).

164

10.6. Ply Thickness, Fiber Content, and Molding Pressure Relationships

10.6.1. Introduction

Previous sections have indicated the critical importance of fiber content to properties. It can be difficult in practice to achieve the desired fiber content in a composite part. This is a brief summary of a study relating ply thickness, fiber content and molding pressure for most fabrics in the database. The purpose was to simplify manufacturing procedures so that target fiber contents can be readily achieved, and the fiber content can be accurately determined from the thickness. Complete data are available in the database.

10.6.2. Experimental Methods

Flat composite plates, approximately 20 by 35 cm in dimensions, were manufactured using hand layup procedures on a flat, level aluminum plate. The fabric was impregnated with isothalic polyester resin, and, well before the resin had started to cure, steel weights (14 total, each with a fabric influence area of 6.45 cm^2) were placed on the uncured composite surface to generate different through-thickness pressures between 0.84 and 71.4 kPa. The different pressures were generated by square steel bars of different heights. A top view of the experimental setup is shown in Figure 122. A Teflon sheet (0.1 mm thick) was placed between the steel weights and the fabric to ensure separation after curing. The steel weights were placed on the fabric after it had been wet out to avoid dry friction problems (and poor wet-out areas) in the fabric. Composite plates were manufactured with one, two and three plies, utilizing the same fabric and fabric orientation, which allowed for different ply strand nesting (consolidation) geometries. After curing, the plate was sectioned and the thickness of the individual areas were measured by averaging measurements of each side. Some minor thickness variations on the coupons did occur due to irregularity of the pressure distribution due to the fabric and surface stitching (hard versus soft contacts). There was no influence of the individual steel blocks on the adjacent blocks due to the Teflon film or the fabric.

For the test coupons with two or three plies, the thickness of the test coupon was divided by the number of plies to obtain the average ply thickness. There is some error in this method at low (less than 25 percent) fiber volume fractions, as the matrix rich regions between the plies is included in this thickness. At higher fiber contents, where fiber nesting occurs, the average ply thickness may be less than it would be without nesting, especially with fabrics having large spaces between strands. Thus, in a laminate with adjacent plies of other orientations, nesting will not occur, and the ply thickness may be greater than obtained here.

10.6.3. Results and Discussion

Table 27 lists the best fit equations for ply thickness versus fiber volume percent for each reinforcing fabric. These equations are best suited for initial design thickness until a laminate is constructed. Depending upon the fabric and stacking with adjacent layers, the thickness can change due to fiber nesting. Different fiber stacking (and nesting) possibilities in some unidirectional

165

laminates are shown in Figure 123. The nesting variations shown at constant fiber content are typical variations observed when different parts of a laminate are sectioned, using fabric D155. The right side of the figure shows the effects of increasing fiber content for a fabric with widely-spaced strands, D092.
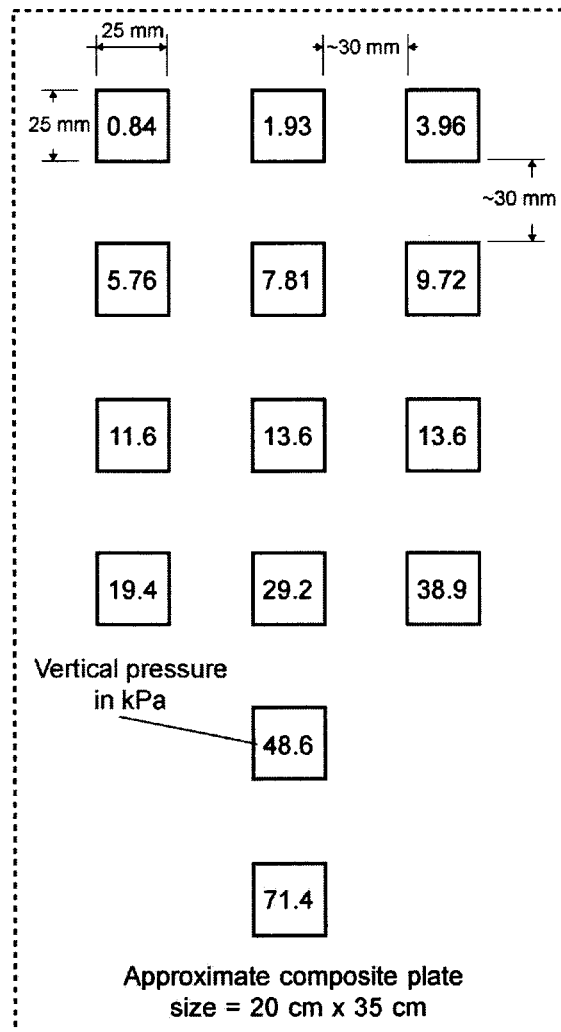
Figure 122. Steel Block (25 mm x 25 mm) Placement on Composite Test Laminate with the Generated Pressures in kPa.

Table 27. Glass and carbon fabric ply thickness versus fiber volume empirical regression equations (The theoretical relationship is $t = A \, V_F^{-1}$, where A is the volume of glass in the ply).

	1 ply	2 plies	3 plies
Unidirectional fabrics			
A060	$t = 7.87 \, V_F^{-1.0823}$	$t = 8.7105 \, V_F^{-1}$	
D092	$t = 12.207 \, V_F^{-0.9999}$	$t = 12.205 \, V_F^{-1}$	$t = 12.205 \, V_F^{-1}$
A1010	$t = 13.811 \, V_F^{-0.996}$	$t = 13.765 \, V_F^{-1}$	
A130	$t = 18.653 \, V_F^{-1.0363}$	$t = 16.236 \, V_F^{-1}$	$t = 16.238 \, V_F^{-1}$
D155	$t = 21.556 \, V_F^{-0.9303}$	$t = 20.947 \, V_F^{-0.9815}$	$t = 20.666 \, V_F^{-0.9999}$
UC1018V	$t = 25.124 \, V_F^{-1}$		
U1701	$t = 25.285 \, V_F^{-1}$		
A260	$t = 34.703 \, V_F^{-1}$	$t = 34.9 \, V_F^{-1}$	$t = 34.038 \, V_F^{-1}$
42024L/M50	$t = 50.355 \, V_F^{-0.9998}$		
UNI21	$t = 40.106 \, V_F^{-1.0001}$		
UNI25 (XP33FBUD25)	$t = 47.988 \, V_F^{-1}$	$t = 47.988 \, V_F^{-1}$	
±45 fabrics			
62002	$t = 16.298 \, V_F^{-1}$		
DB120	$t = 13.573 \, V_F^{-0.9898}$	$t = 14.969 \, V_F^{-1.0178}$	$t = 14.113 \, V_F^{-1}$
DBM1204B	$t = 17.333 \, V_F^{-0.9999}$		
DB240	$t = 25.299 \, V_F^{-0.9448}$	$t = 31.189 \, V_F^{-1}$	$t = 30.594 \, V_F^{-1}$
DB400	$t = 50.657 \, V_F^{-1}$		
0/90 woven roving and triaxal fabrics			
0/90	$t = 18.994 \, V_F^{-0.9392}$	$t = 22.372 \, V_F^{-0.9827}$	
CDB200	$t = 27.451 \, V_F^{-1}$		
TV3400	$t = 45.099 \, V_F^{-0.9999}$		
NOTE: t = ply thickness in mm, V_F = desired fiber volume content in percent			
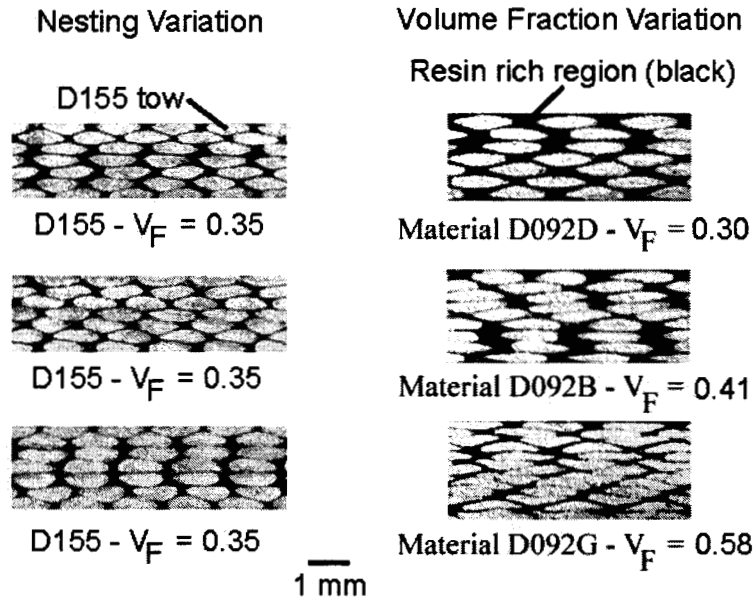
Figure 123. Stacking and Nesting Geometries of Unidirectional Fiber Bundles.

The theoretical prediction for ply thickness versus fiber volume fraction would take the form

$$t = \frac{A}{V_F} \tag{19}$$

where t is the ply thickness and A is the volume of solid glass. Figure 124 compares data for D155 fabric with this relationship, showing excellent agreement. The empirical relationships in Table 26 are all close to the theoretical prediction. Presented in Figures 125 through 132 are the ply thickness versus fiber volume percent and the through-thickness pressure versus fiber volume percent for selected reinforcing fabrics used in the database; data for other fabrics can be found in the database. The ply thickness versus fiber volume percent graphs are all similar, with regards to one, two or three plies in the composite. The maximum margin of error on these relationships was estimated at ± 5 percent and is dependant upon uniformity of the fibers across the ply; voids between fiber bundles will tend to cause fiber nesting if adjacent plies are available to fill the voids. Some fabrics (±45's, A1010, D155) can also have their areal weights altered as the fabrics are tensioned or compressed in the mold.

The through-thickness pressure versus fiber volume percent graphs have greater differences between the one, two and three ply tests than does the ply thickness. Fiber nesting causes through-thickness pressure increase (spikes) to occur at higher fiber contents in composites with two and three plies. The single ply data give the uniformity of the fiber distribution, and any hard contact points present in the basic reinforcement geometry. Low fiber contents at the same pressure indicate that the fabric architecture has large voids which must be filled by adjacent plies (if available), or that

168

excessive pressure is necessary to flow the fabric strands sideways to fill the voids. Either way, these voids hinder the achievement of higher fiber contents. Hard contact points, generated by stitching threads or fiber intersections in woven fabrics, cause a large increase in the through - thickness pressures as the contacts interact with adjacent plies or mold surfaces. This is most noticeable in the A130 fabrics at fiber contents above 43 percent, when the thermoplastic weft weaving thread penetrates the composite surface, causing raised bumps on the surface. The D155 fabric (Figure 126) has an abrupt pressure change (termed a pressure transition) at approximately 38 percent, which is almost vertical, and is caused by the stitching contacting the mold surface; this locally compresses the D155 strands under the stitch. These compression points are shown in Chapter 11 to reduce fatigue performance. With multiple layers, this effect can be somewhat reduced due to fiber and stitching nesting.

Heavier fabrics (A260, UNI21) will have a higher fiber contact pressure transition point due to a more uniform strand distribution. For example the A260 fabric starts to transition at approximately 52 percent fiber. Lighter fabrics have greater difficulty in maintaining a uniform areal weight without voids or stitching discontinuities; the A060 fabric transitions at a fiber content of 32 percent.
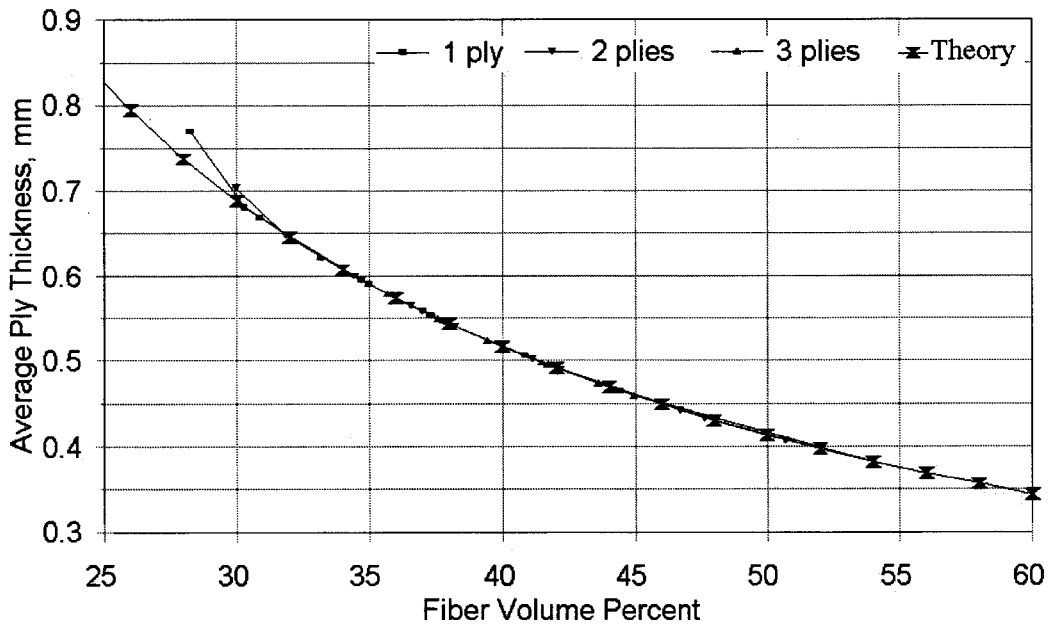
Figure 124. Average Ply Thickness versus Fiber Volume Percent for D155 Fabric Unidirectional Composite. Data versus prediction from Equation 19; see Table 27 for parameter A.
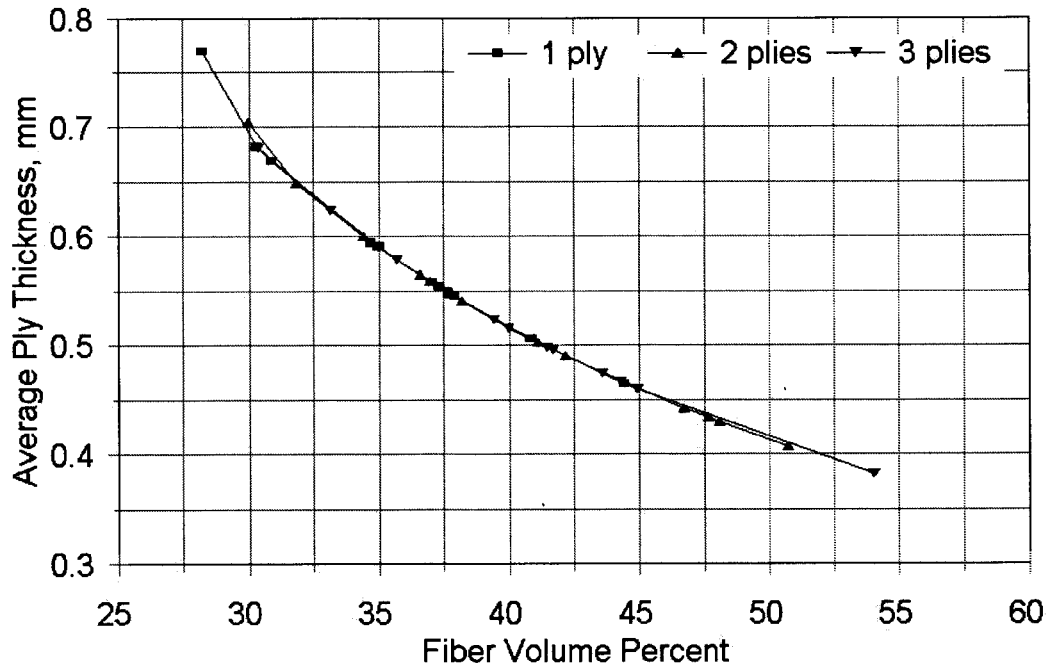
Figure 125. Owens Corning D155 Ply Thickness versus Fiber Volume Percent.
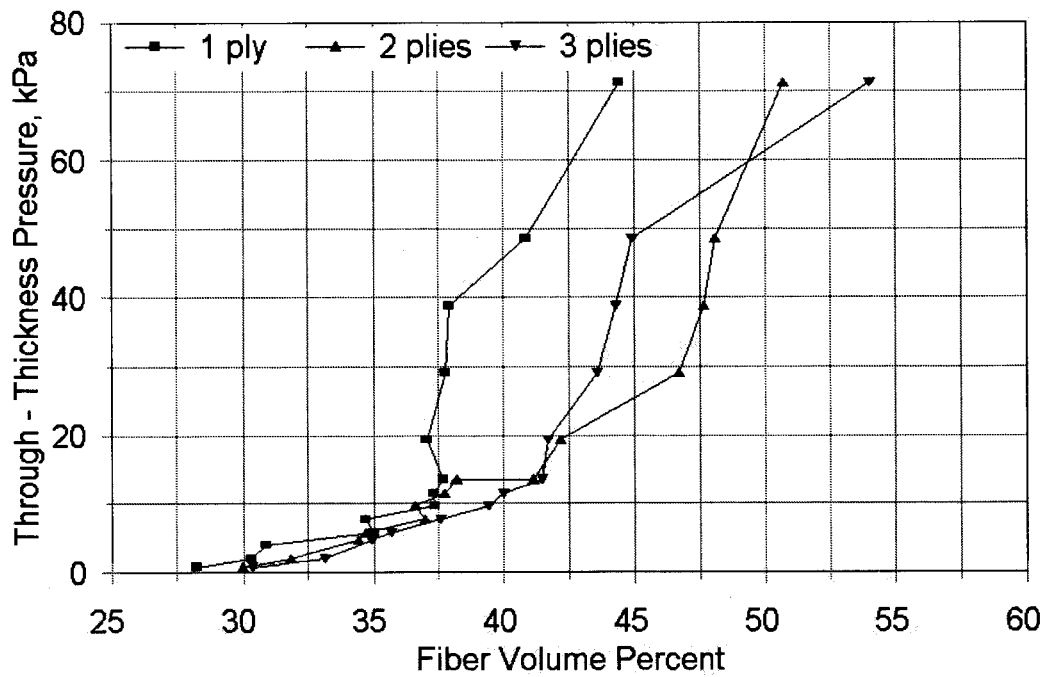
Figure 126. Through - Thickness Pressure versus Fiber Volume Percent for Fabric D155.

170
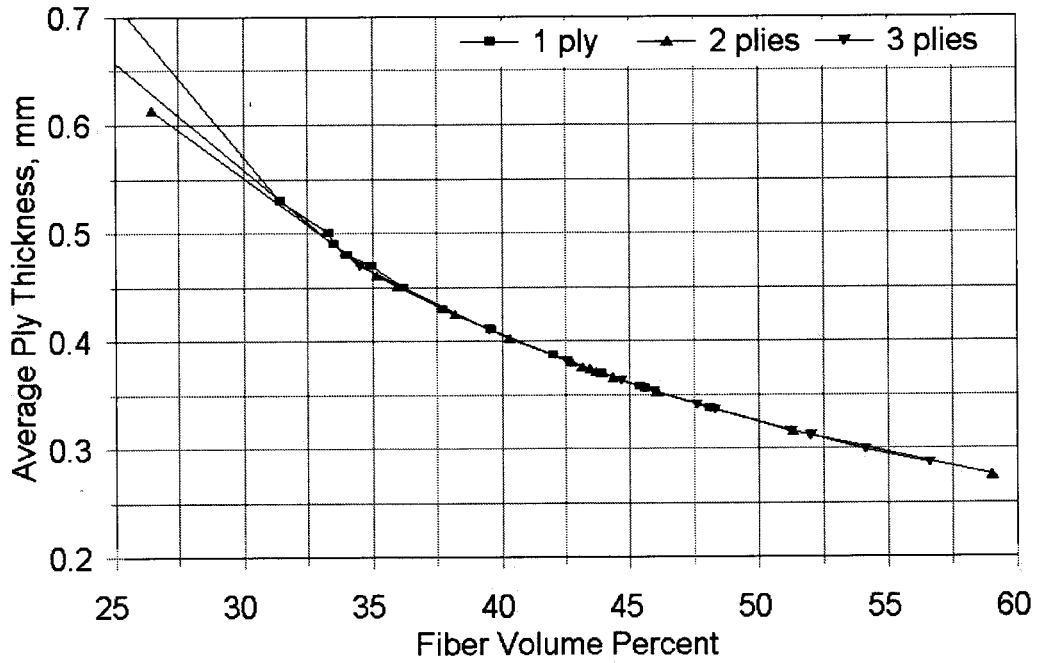
Figure 127. Owens Corning A130 Ply Thickness versus Fiber Volume Percent.
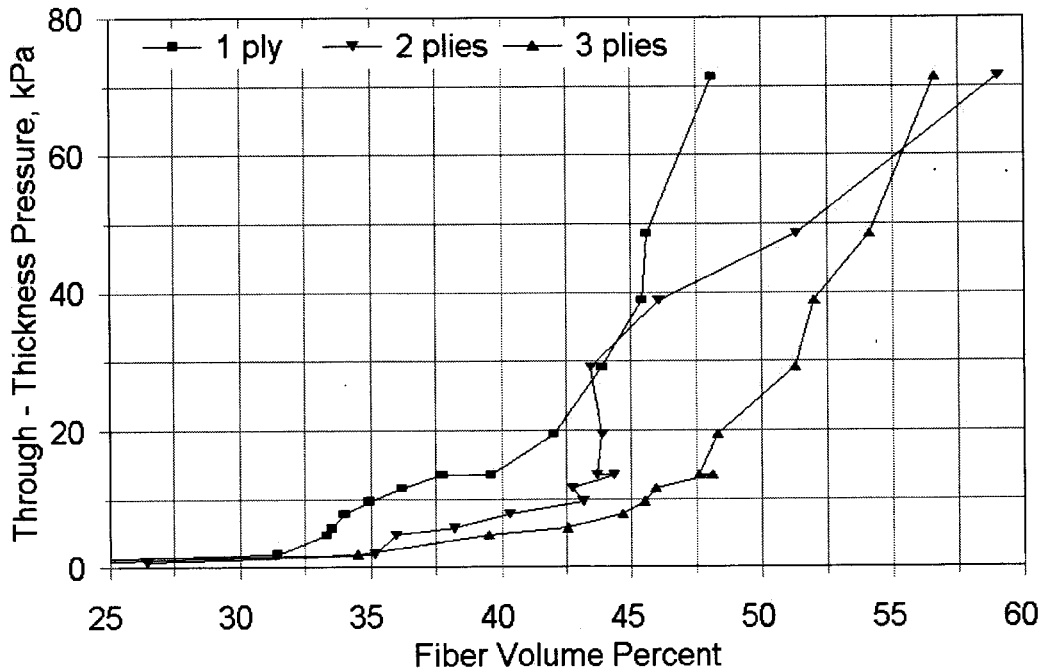
Figure 128. Through - Thickness Pressure versus Fiber Volume Percent for Fabric A130.

171
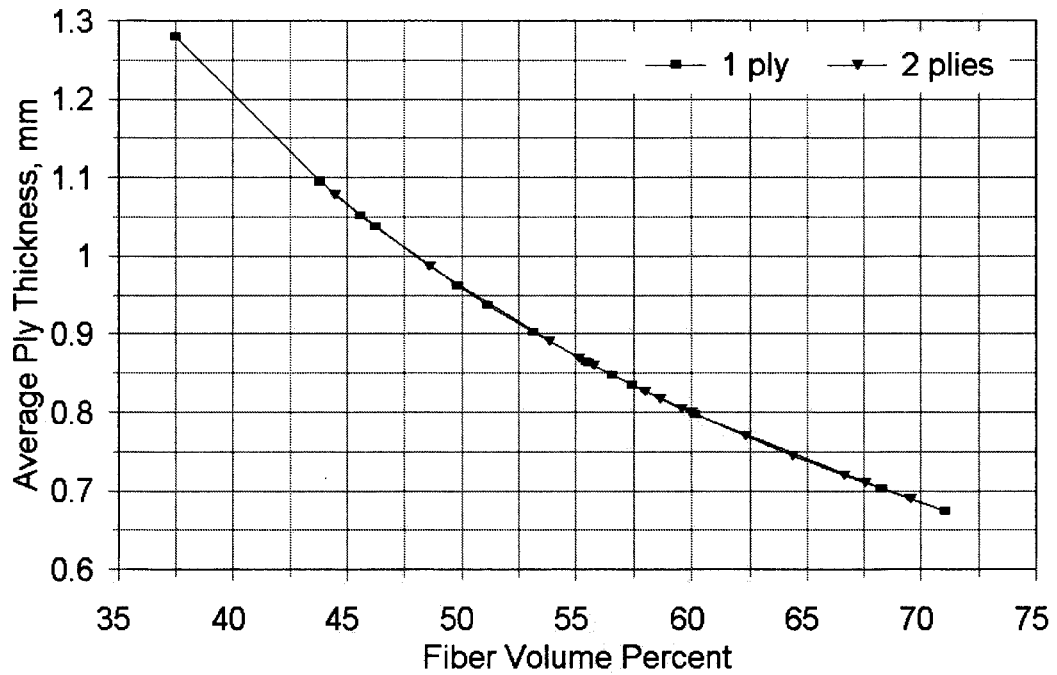
Figure 129. Zoltek UNI25 (XP33FBUD25) Ply Thickness versus Fiber Volume Percent.
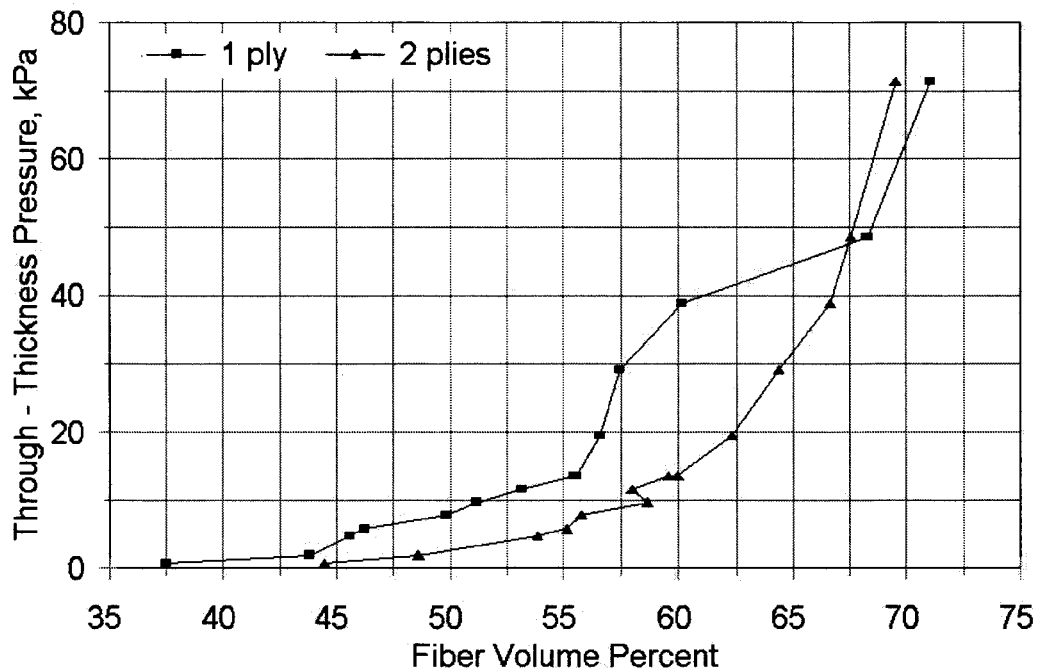
Figure 130. Through - Thickness Pressure versus Fiber Volume Percent for Fabric UNI25 (XP33FBUD25).

172
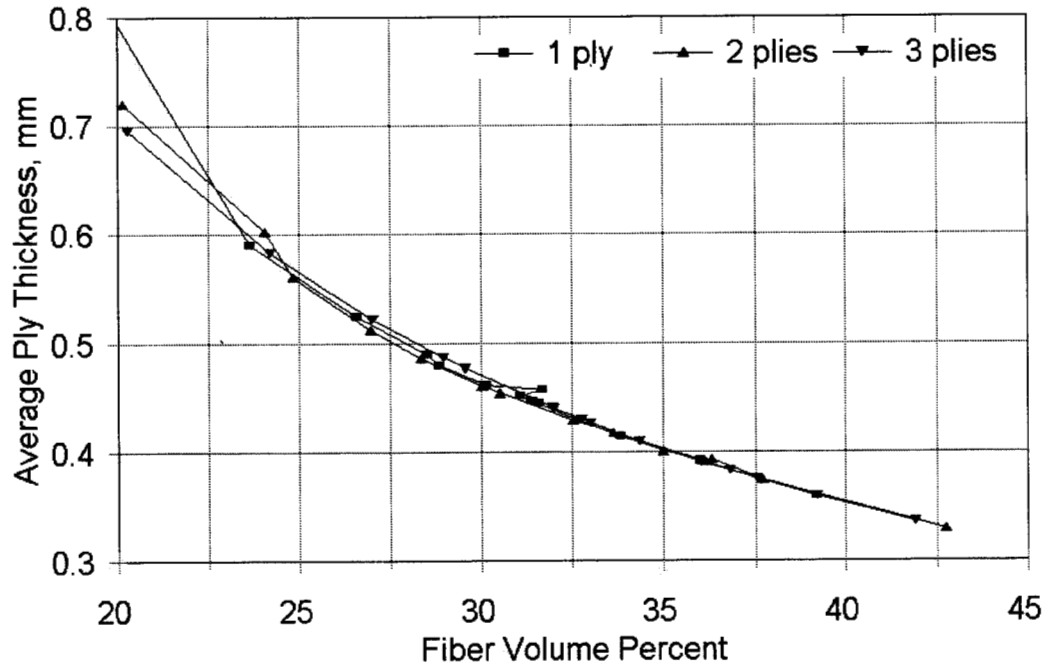
Figure 131. Owens Corning DB120 Ply Thickness versus Fiber Volume Percent.
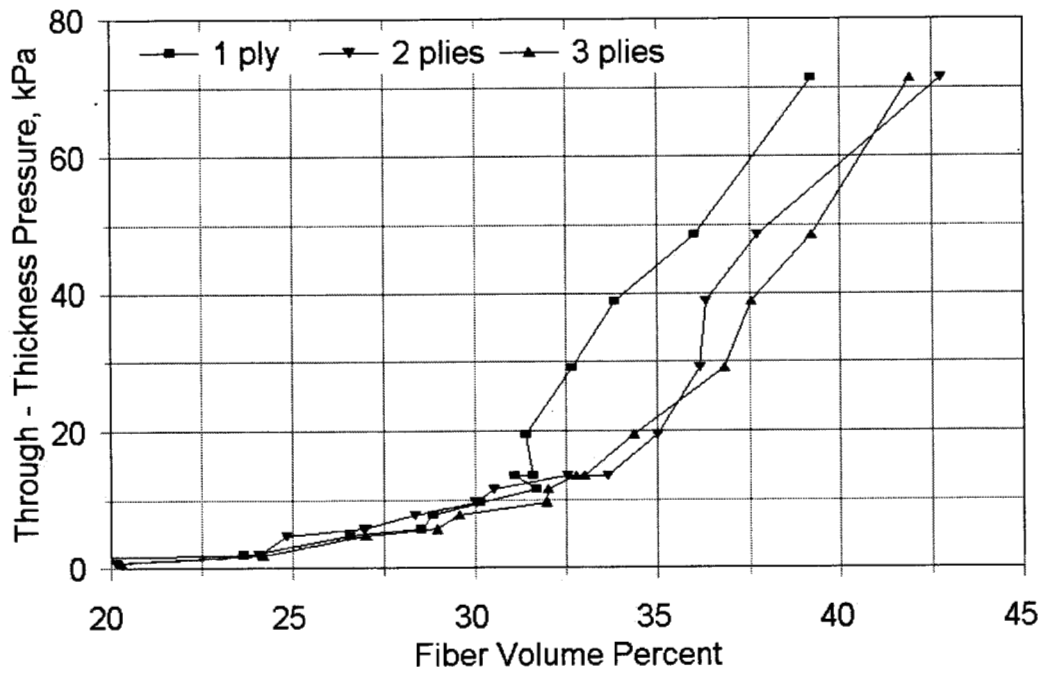
Figure 132. Through - Thickness Pressure versus Fiber Volume Percent for Fabric DB120.

173

10.6.4. Multidirectional Laminates

When plies of different fabrics are stacked together, the actual fiber content in each ply may differ from the overall average. This different ply fiber content effect is shown in Figure 133 for the material DD sequence having the configuration $(0/\pm45/0)_S$. In Figure 133, following the 20 kPa pressure line, the fiber content in the DB120 fabric is about 33 percent, while the fiber content in the D155 ply is about 42 percent, while the overall laminate is about 37 percent. The individual ply thicknesses (0 and ±45) in these graphs, when added together, may not equal the composite thickness due to matrix rich regions between the plies, or to fiber nesting. The separate plies were measured from the test coupons under the microscope. Additional weights were used to generate higher pressures (Figure 134), and these high pressures were part of the problem encountered in molding the high fiber content DD materials. The high molding pressures used to manufacture these composites also introduce a question as to whether fiber damage occurs. The DD materials with a fiber content above 60 percent did have a slightly reduced UTS/V_F ratio. However, the main concern with high fiber contents is the tensile fatigue, as discussed later.

The current database contains data for all materials tested in terms of fiber content, thickness, and variations and tolerances for these parameters. Also included is a table giving the fiber content where the pressure starts to transition, about 20 kPa, and the tensile properties may decline for glass fiber materials.
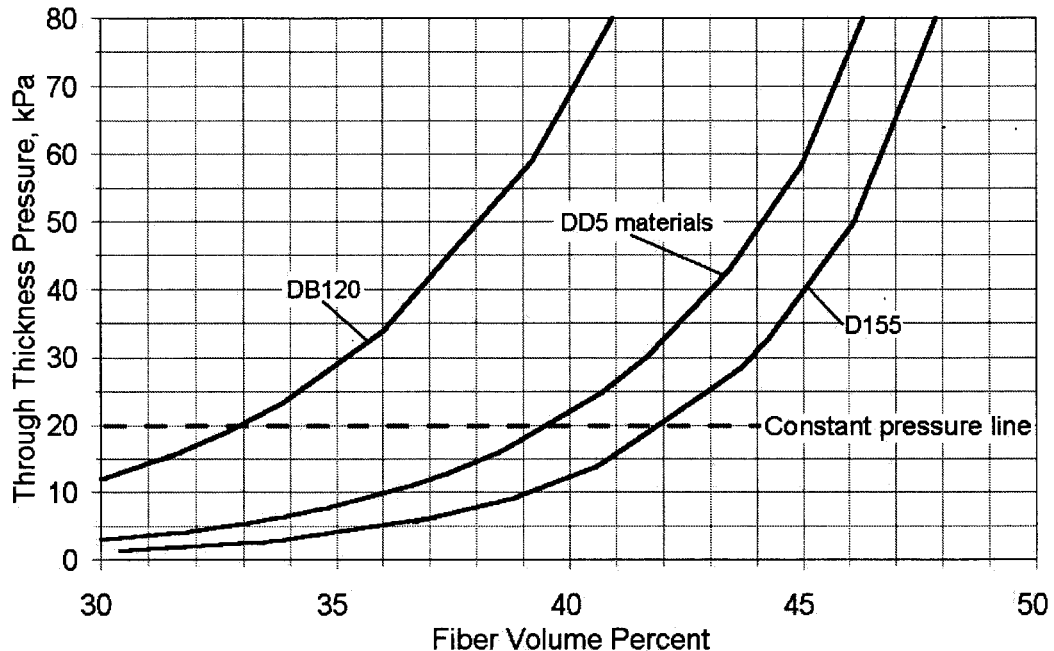
Figure 133. Through - Thickness Pressure versus Fiber Content for DD Materials $(0/\pm45/0)_S$, 0° Plies are D155, ±45° Plies are DB120; Low to Moderate Pressures.

174
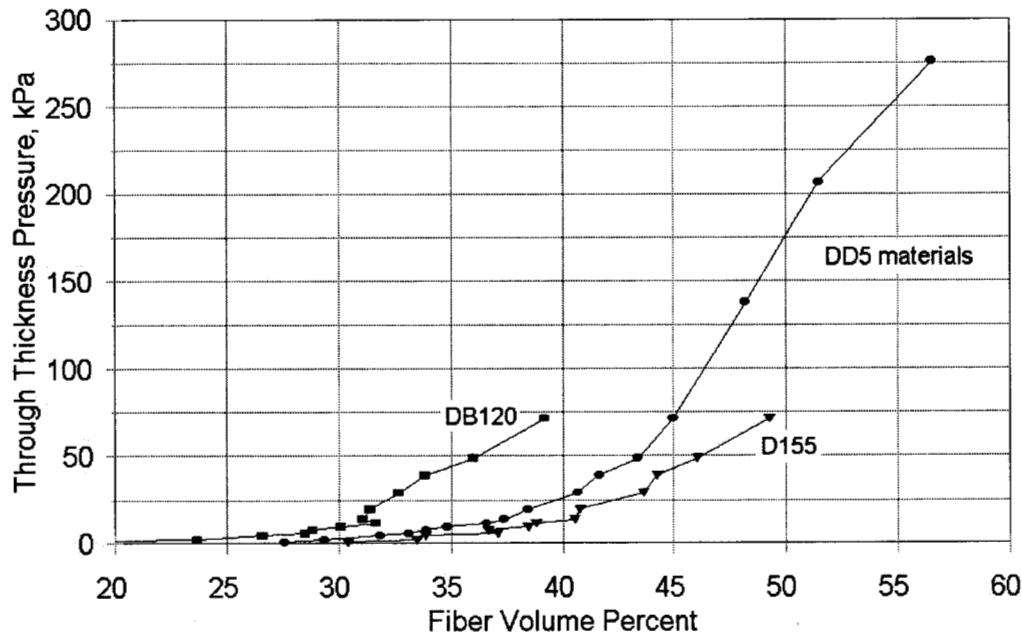
Figure 134. Higher Through - Thickness Pressure versus Fiber Volume for DD Materials, 0° Plies are D155, ±45° Plies are DB120; Higher Pressures.

10.6.5. Conclusions

The relationships in Table 27 allow convenient determination of the fiber content for each fabric, knowing the molding pressure. The relationships also allow for quick verification of the values listed in the fatigue database, and where discrepancies were found, additional matrix burn off tests were performed to confirm the accuracy of the database values. Some fiber content corrections were made in the current version of the database.

If a composite is manufactured with the same fabric for all the plies, the fiber volume fraction will be the same in each ply. This is also the case for most prepregs. However, when combinations of different fabrics are used, the local fiber content may be different in different plies, and corrections in the ply properties must be performed to accurately predict the material behavior. This point has been illustrated for the DD series of laminates in the database.

10.6.6. Design Recommendation

The data can be used to obtain the expected laminate thickness and individual ply fiber contents for a particular molding pressure. For multidirectional composites the common factor is the through-thickness pressure, which must be the same throughout the preform (neglecting fabric weight). The fabric thickness for each ply can be determined from the graphs or tables at the same through-thickness pressure and added to obtain the total composite thickness. The corresponding ply fiber volume fraction can be used to obtain the ply properties. This approach is developed further in Reference 41.

175

11. INTERPRETATION OF DATABASE TRENDS: FIBER CONTENT EFFECTS ON TENSILE FATIGUE

11.1. Summary

The transitions to poor tensile fatigue performance with increasing fiber content have been discussed in earlier sections. Materials with well dispersed fibers (strands and prepreg) have been found to provide good tensile fatigue resistance up to 60 percent or more fiber by volume. The stranded fabric architectures, which constitute most of the database materials, show such a transition in the 40 percent fiber volume content range, with the transition occurring at about two percent lower fiber content for multidirectional laminates than for unidirectional materials with the same 0° reinforcing fabric. Section 10.6 clarified the later trend, since the actual fiber content and ply thickness is higher in the 0° plies when laminates contain ±45° plies with most fabrics, since the ±45° absorb more resin.

This chapter explores the origins of the difference between stranded fabrics and materials with well dispersed fibers, in terms of the fiber content where the transition in tensile fatigue resistance occurs. Detailed microscopy analysis has been carried out for laminates with different fiber contents. As expected, the fiber content within strands is much higher than the average fiber content of the laminate. Furthermore, as the average fiber content increases, the local fiber content within the strands also increases significantly, particularly near stitch or weave crossover points. The strands also distort significantly at higher fiber contents.

The results of this study, and data presented earlier, clearly show that the transition in tensile fatigue resistance is related to increases in the local fiber content within the strands of the ±0° plies. While some fabrics, such as A130, are less severe in this respect than others, such as D155, all stranded fabrics have problems at high fiber contents, particulary near stitch or weave points. To obtain good tensile fatigue resistance in glass fiber laminates at average fiber contents in the 50 to 60 percent by volume range, it is necessary to use materials, like prepreg, with well dispersed fibers.

11.2. Introduction

Figures 1 through 4 in the background section illustrate the transition from good to poor tensile fatigue resistance as the fiber content increases in the range of 40 to 45 percent by volume for fabric with discrete strands. The transition occurs at a slightly higher fiber content for unidirectional materials than for laminates containing 0° and ±45° layers (when the ±45° layers are tightly stitched to 0° layers as in triax fabrics, the transition occurs at much lower fiber contents [2]).

The transition for 0° materials has been difficult to understand, and was earlier related to cracking in the matrix or ±45° layers [2]. Results given in section 10.3 for strands of varying fiber content, and for prepreg laminates with a uniform fiber distribution, have shown no transition in this fiber content range, maintaining good fatigue resistance up to the range of 60 percent fiber by volume. This chapter provides detailed results for the internal structure of stranded fabrics, which are intended

to identify the causes of these effects.

11.3. Fiber Packing

An ideal composite lamina would have all the glass fibers aligned straight and parallel to each other and to the load path, with just enough spacing between the fibers to prevent fiber-to-fiber contact. For this to occur, the arrangement of fibers would be in a uniform geometry, such as a square or hexagonal array. If all fibers are round and have the same diameter, these arrangements would have a theoretical maximum fiber volume fractions of 0.79 (square) and 0.91 (hexagonal), shown in Figure 135. Random packing arrangements have a maximum fiber volume fraction which is between these limits and has a maximum value of approximately 0.82 [94]. Practically, the fibers will involve a range of diameters, 10 to 20 μm, which could increase these fractions slightly. Increasing the fiber volume fraction is usually advantageous, as it increases the primary properties: longitudinal elastic modulus and tensile strength of the lamina. Above a fiber volume fraction of approximately 0.7, the transverse properties of the composite will degrade, as fibers contact each other and stress concentrations increase [95]. The stress concentrations around the fibers are higher when the fiber transverse modulus is higher relative to the matrix modulus. Thus, carbon fibers, with a low transverse modulus relative to glass, have lower transverse stress concentrations, and often subsequent higher transverse and shear strengths. In a well bonded composite, a matrix material which would yield at a lower stress would decrease the local stress concentrations.

11.4. Strand Deformations in Fabrics

Glass fabrics are constructed using glass fiber strands or tows, which contain hundreds to thousands of continuous glass fibers, 10 to 20 μm in diameter, without any definite twisting of the fibers. These tows are stitched or woven together to form a fabric, which allows the fabric to be handled during manufacturing. Fiber handling during fabric manufacturing significantly reduces the fiber strength, as shown later. The properties of the fibers can be further reduced by the stitching thread tightness, and the spacing of the stitching or weaving. The stitching pinches the tow and causes a slight curvature of the fibers on the outside of the glass strand as the diameter locally decreases. This curvature of the fibers introduces a bending stress in the fibers at the stitch, but it is postulated that the major effect is that the stitch decreases the average distance between fibers and causes the number of fibers in virtual contact, in that area, to increase. Virtual contact means that the fibers appear in contact in micrographs; whether a thin matrix layer is present between the fibers is unknown.

The reinforcing fabrics have bundles of glass fibers separated by an area without fibers which forms resin rich areas between the tows in stitched fabrics, and both above and below weave crossover points in woven fabrics. It is the presence of this resin rich channel between the tows which reduces the overall fiber content, and hence the lamina properties. (The spaces do greatly lower the fabric permeability, which helps in manufacturing methods like RTM.) In order to increase the fiber content, the elliptical fiber bundle cross section must be compressed and forced to spread out across the width of the lamina to fill this channel. The stitching or weave crossover points inhibit this spreading. Figure 136 shows three different magnifications of Material PP, which used 3M-SP250

prepreg (no stitching or weaving), compared with a unidirectional composite with D155 stitched fabric. The prepreg material shows a uniform distribution of fibers with no large resin rich
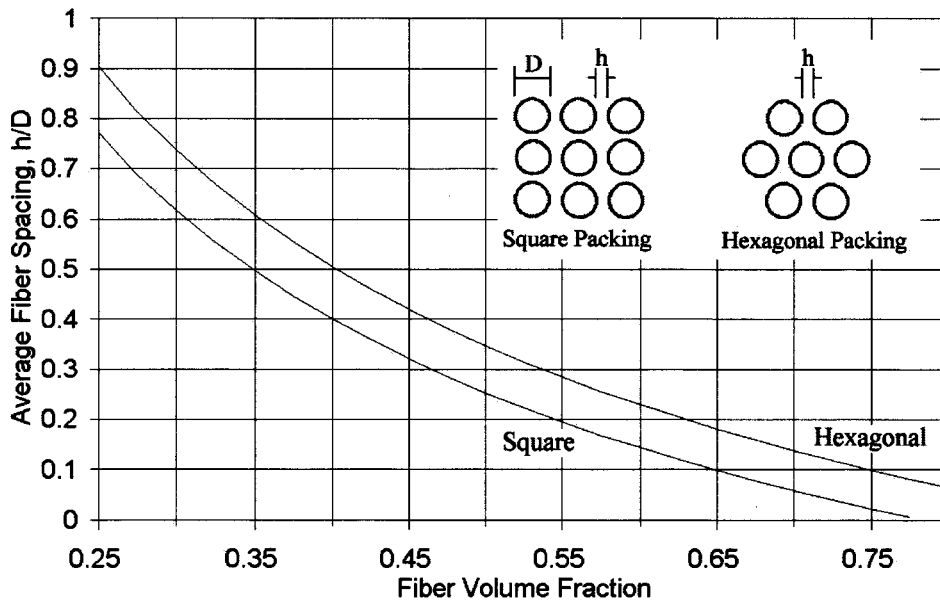
Figure 135. Fiber Volume Fraction versus the Average Fiber Spacing in a Composite with Theoretical Square and Hexagonal Packing Geometries [94].

regions; the D155 composite, because of the stitching, has large resin rich regions between the tows. Figure 137 shows the D155 confined tow area versus the overall ply fiber content for materials DD6, DD2 and DD7. As the composite fiber content increases, the cross-sectional area of the individual tows decrease (as expected), squeezing out the excess resin. The D155 fabric tows in Figure 137 start to interact and fill the matrix rich regions in the adjacent plies, and thus the elliptical tow cross-section geometry deforms. If this deformation of the tow is not uniform along the length, where the tow enters and exits the resin channel in the adjacent ply, a rotation of the strand occurs. The figure shows that the fiber content inside the fiber strand does not change as significantly as the average composite fiber content, and that the fiber content in the strand changes along its length (x-axis) due to the periodic presence of stitching.

Figure 137 shows that the stitching causes up to an increase of 10 percent in the local fiber volume fraction (from $V_F = 0.58$ to 0.68) of the strand contained within the stitching in the DD6 material; the DD7 material exhibited only a 2 percent increase (from $V_F = 0.70$ to 0.72). The determination of strand fiber contents at higher individual ply fiber contents was not performed due to the difficulty in determination of the boundaries between adjacent strands. Figure 138 shows the number of fibers in direct contact with adjacent fibers versus the ply fiber volume fraction, both within and between stitching threads. A large increase in the number of fibers in contact occurs in the 0.31 to 0.42 average fiber volume fraction region, which also coincides with the region where most of the composites in the database start to decrease in fatigue resistance. It should be noted that the D155 tow has stitching every 4 to 6 mm, which means that the tow fiber content varies between a maximum and a minimum value every 4 to 6 mm.

178
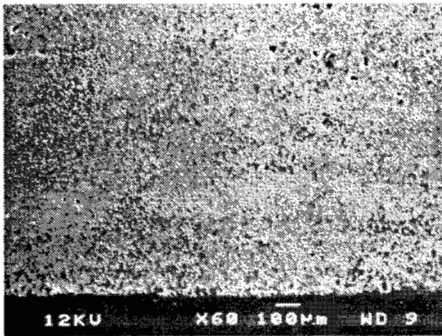
Prepreg (60X magnification)
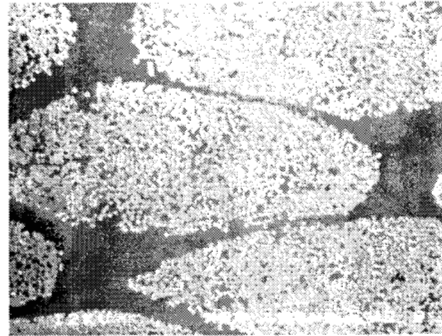
D155 (60X magnification)
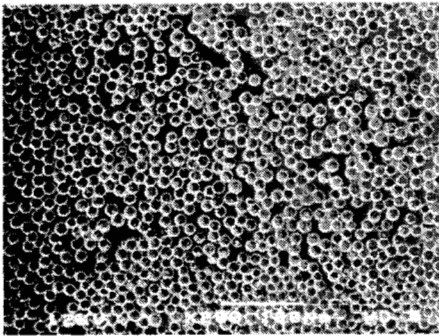
Prepreg (200X)
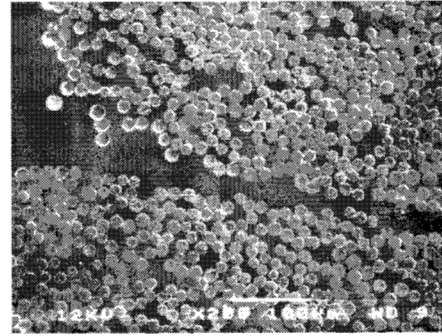
D155 (200X)
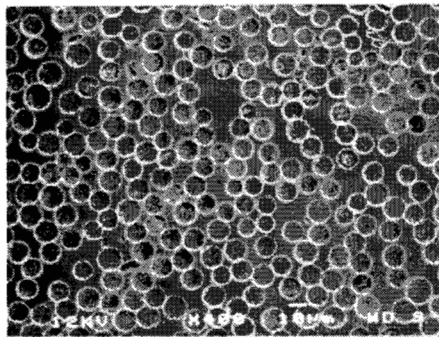
Prepreg (400X)
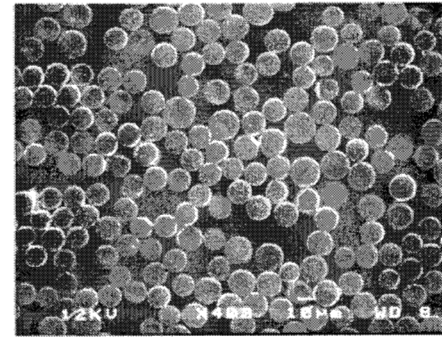
D155 (400X)

Figure 136. Micrographs of Prepreg and D155 Fabric Composites.
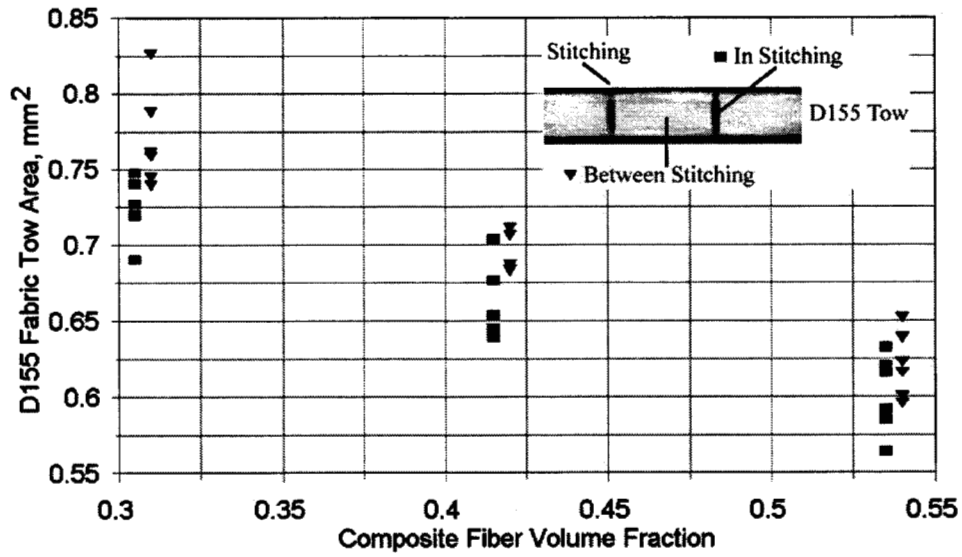
Figure 137. Composite Fiber Volume Content versus D155 Confined Fiber Tow Area in Materials DD6, DD2 and DD7.
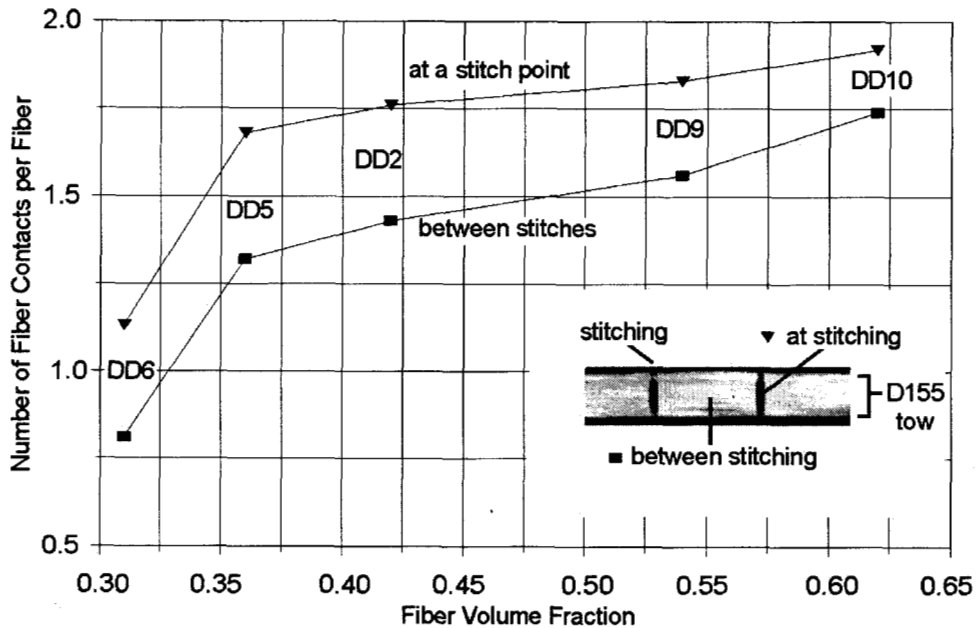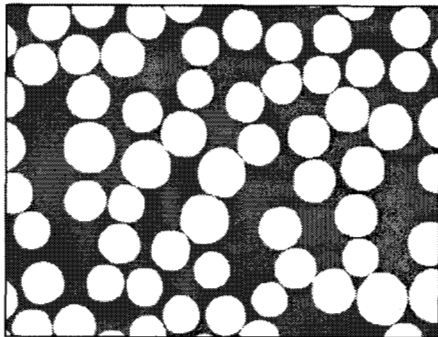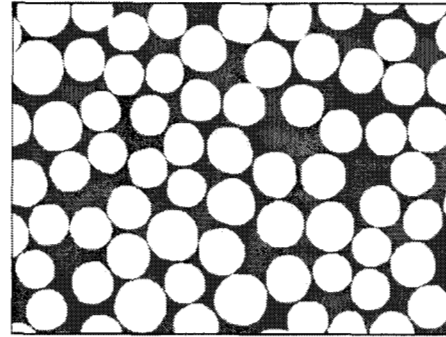
Figure 138. Composite Fiber Volume Fraction versus Average Number of Fibers in Contact with Each Other for Materials DD6, DD5, DD2, DD9 and DD10.

Since the fabrics are stitched or woven with a regular spacing, the tows can be stacked with strands in or out of phase with the adjoining plies. Figure 123 showed three possible stacking possibilities. Each has some degree of tow compression and elliptical shape deformation with increasing average fiber content as the tow interacts with adjacent tows. The D092 fabric is a lighter fabric with a larger distance between the fiber tows and thus larger matrix rich regions. With the tows stacked directly in phase with each other (strands on top of each other) the resin rich areas can extend continuously through the composite thickness. When the tows are out of phase with the adjacent tows, the resin rich areas between the tows are partly filled in by deformed tows from adjacent layers, allowing for higher fiber contents. Figure 123 showed the D092 fabric at fiber volume fractions of 0.30, 0.41 and 0.50. At a fiber content less than approximately 0.30, the tows in all the fabrics are

separated from the adjacent plies by a continuous matrix layer, and therefore do not have any direct fiber contact with the tows in the adjacent ply. As the fiber content is increased, the tows start to contact the tows in adjacent plies, causing elliptical tows to flatten out and fill the resin rich areas between the adjacent plies. Increasing the fiber content further causes the tows to deform in the width direction, filling in resin channels between the tows, within the ply. If this deformation is restricted by the weave or stitching, a pinched region along the strand will exist.

Since the stitching is physically on the surface above and below the tow, the stitch introduces additional "hard points" of contact, which cause localized pinching of the fiber tow as well as adjacent tows in contact with this stitching. This situation causes additional points of pinching. In the DD series of materials listed in the database, the stitching in the D155 fabric starts to interact with the adjacent plies at a fiber volume fraction of approximately 0.36. This interaction effect is illustrated in Figure 139. Since the stitching thread is also on a regular spacing, the stitching in one ply can contact the stitching in an adjacent ply, creating another hard contact point or location of increased bundle fiber content. Figure 140 shows the interaction of the plies when the stitches are stacked on top of each other. The stacking of the stitching causes the plies to be separated more at the stitch points than between the stitches, causing the fibers to collapse into the resin rich region, creating a small fiber angle which might reduce the localized compressive strength. The figure shows the effects of removing the stitching thread from the D155 fabric. Without the restrictions of the stitching thread, the glass fibers disperse and form a more uniform geometry similar to the prepreg materials, minimizing the size of the matrix rich regions in the ply.

Material DD6 - V_f = 0.36, Stitching between 0° and 45°
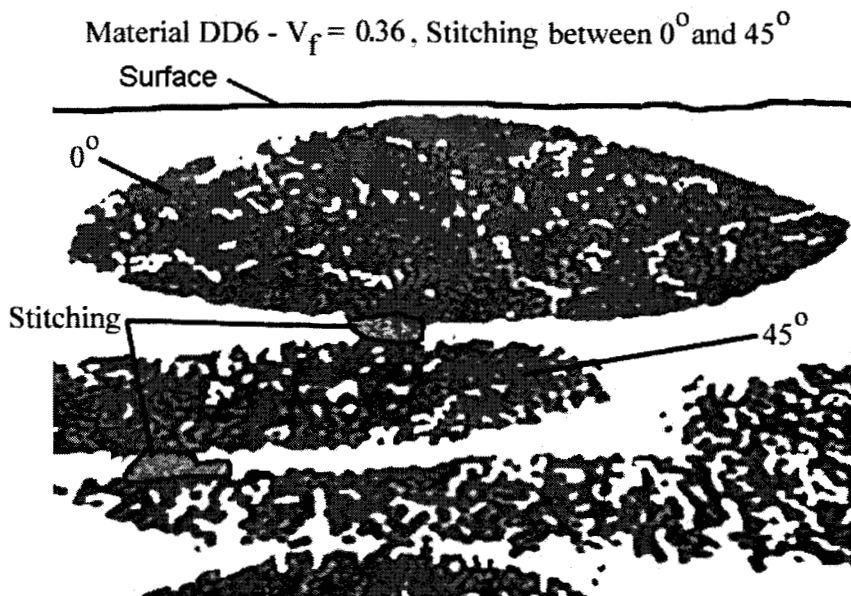
Figure 139. Fabric Stitching Interaction with Adjacent Plies.

The A130 fabric, which has a woven architecture shown in Figure 141, uses the same glass

roving that is used in the D155 fabric. This fabric is woven around a weft glass strand which is coated with a thermoplastic hot melt adhesive. During fabric weaving, this thermoplastic bead is woven into the fabric. Heat is applied to melt the thermoplastic to encapsulate the glass strands in direct contact with it, locking the fabric architecture together. The bonding of the matrix materials to this thermoplastic bead is poor. Cracks readily form at the interface of this bead and the matrix for all the resin systems in the database.
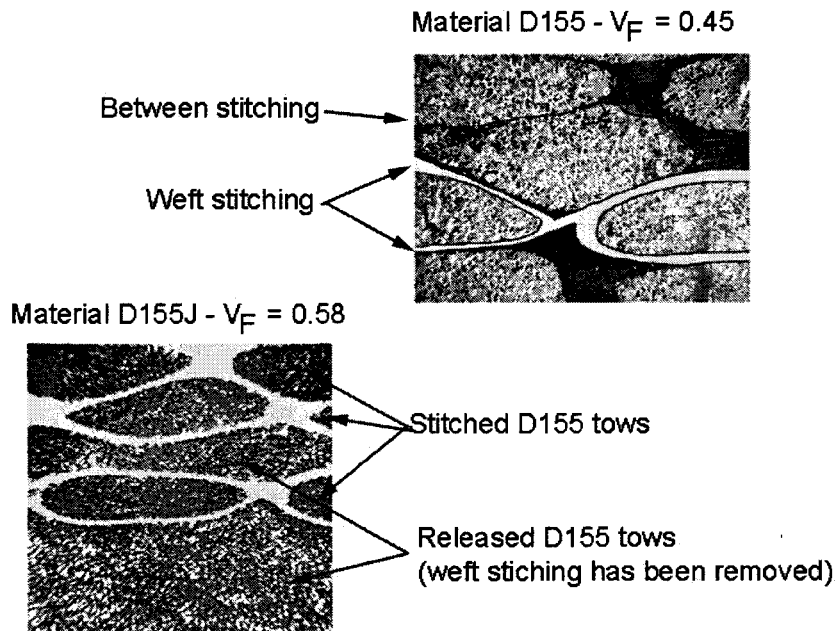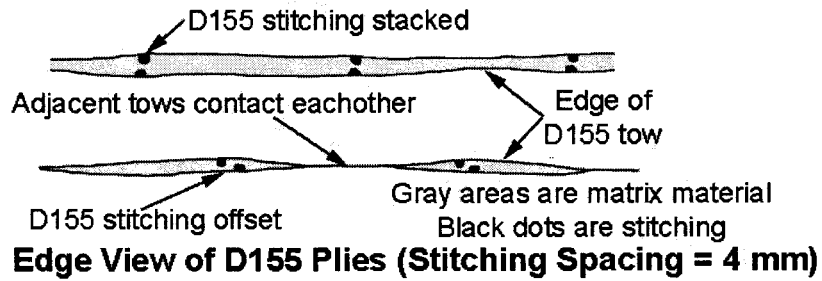
Figure 140. Fabric Stitching Interaction with Adjacent Ply Stitching and the Effects of Removing the Stitching.

A130 Fabric

Thermoplastic bead around weft thread

Fiber Direction

Tow

1 mm

Weft glass strand with thermoplastic bead (woven underneath 0° tow)

Outline of matrix cracking around thermoplastic bead

DD11-107, 414 MPa, R=0.1
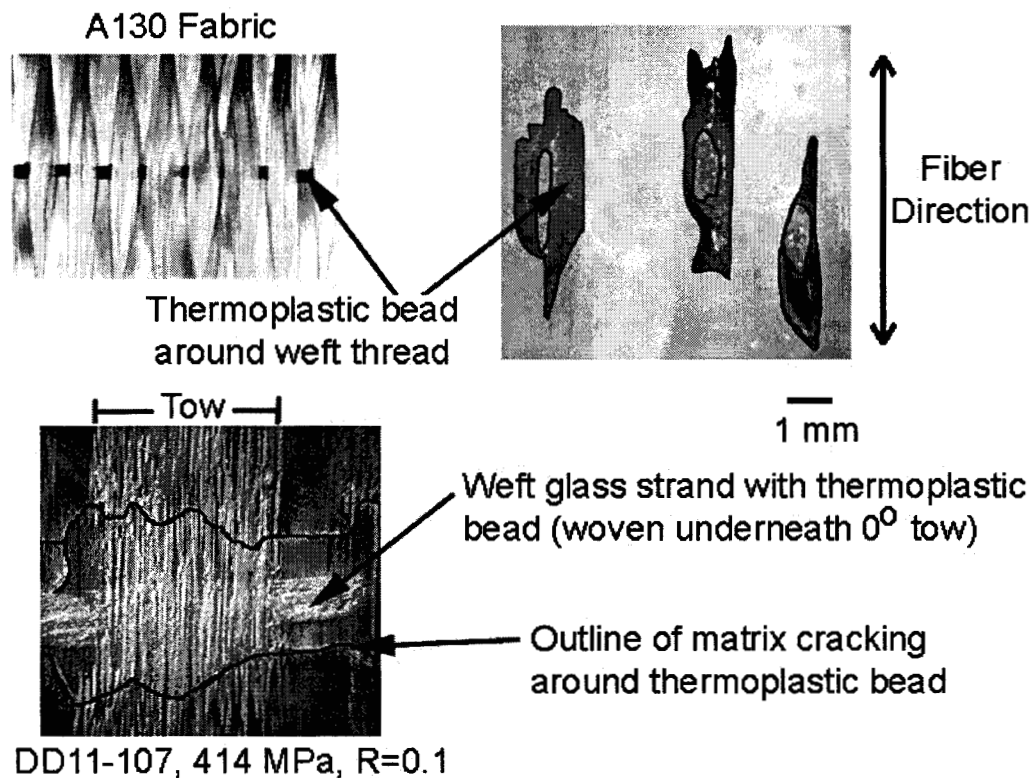
Figure 141. A130 Fabric with Woven Architecture with Cracking Around the Thermoplastic Bead in Coupon DD11-107 after Fatigue Testing, R=0.1.

11.5. Conclusions

This study documents the micro-structural changes in stranded fabric laminates as the overall fiber content is increased. The strands distort significantly and increase in local fiber content as the overall fiber content increase. The fiber content is significantly higher near stitch points, where strand failures are usually observed. The number of fiber-fiber contacts also increase significantly as the fiber content increases. The thermoplastic bead used in the woven fabrics does not bond well to the matrix, and serves as a site for matrix cracking. These results support the view that good tensile fatigue performance at high overall fiber contents requires well dispersed fibers, rather than stranded fabrics.

The average fiber content where the tensile fatigue transition occurs, about 40 percent fiber by volume, produces a local fiber content within the strands, at stitch points, of about 65 to 69 percent for D155 fabric. this corresponds to the fiber content range where composites with uniformly dispersed fibers begin their transition to poor tensile fatigue resistance (Chapter 10.3); local compaction at stitch points from adjacent plies also become significant in this range, and this is also the range of fiber content where the pressure during fabrication must be increased sharply (Figure 126). These findings clearly indicate that most stranded fabrics are best used below an average fiber

184

content of about 40 percent by volume, even though higher contents can be achieved in some processes.

PART B: SUBSTRUCTURE STUDIES

Substructure studies were designed to explore four areas: (1) validation of use of the DOE/MSU database in design and analysis of blade substructures, (2) identification of critical materials issues to be addressed in the database, (3) development and validation of methodologies for designing complex structural detail areas where delamination is the dominant failure mode and (4) to provide standard test specimen geometries for structural integrity, which could be used for comparison of different resins, reinforcement, and processing methods. Choice of structural details was influenced strongly by the design/manufacturing effort centered on the AOC 15/50 blade as part of the Montana DOE EPSCoR program. This blade and the substructure areas explored are shown in Figures 142 and 143. In addition to the areas shown, studies also included ply drops in thickness-tapering areas and a variety of simulated flaw types related to manufacturing irregularities which were discussed earlier. While these substructure geometries were derived from the AOC 15/50 blade design, the geometries are generic to most blades constructed from composite materials. The parametric studies were intended to provide guidelines and methodologies applicable to a broad range of designs.

The substructure studies generally followed a similar format: selection of geometry, fabrication, testing, finite element analysis, and parameter variation. This was intended to explore and validate methodologies for substructure design and analysis, and to develop rules-of-thumb for design and materials selection, where possible.

As noted in the background section, a major study [3] had been concluded prior to the work described here. That study was focused on the development of an I-beam substructural element (Figure 144) for parametric studies and validation of database and analysis methodologies. The beam study demonstrated that, under tensile and fatigue loading, the predicted strength, lifetime and mode change (tension/compression) predictions based on database properties and FEA analysis were generally in agreement with experimental data. Fifty-two beams were tested and analyzed. However, the study was focused on the flange and web areas rather than the details of transition areas, and did not include the key aspect of delamination in the detail areas, which is the main focus of the three studies reported in this section.

An additional study has been carried out on the root section, which for the AOC 15/50 blade involved steel stud inserts. Reference [96] describes this study in detail. The primary focus of the study was manufacturing, but a significant amount of static and fatigue strength data were also generated. A representative test specimen containing one stud was developed (Figure 145), and analyzed by FEA. In the final design, only stud failures in the attachment bolts could be generated under tensile ultimate and fatigue loads, despite oversized bolts relative to the design. Reference [96] contains all data except the final few fatigue tests, which also resulted in repeated bolt failures. Thus, the specimen was over designed, and no useful composite strength or fatigue life data were generated, which could be used to validate the design methodology. As a result, this effort is not presented in detail in this report.
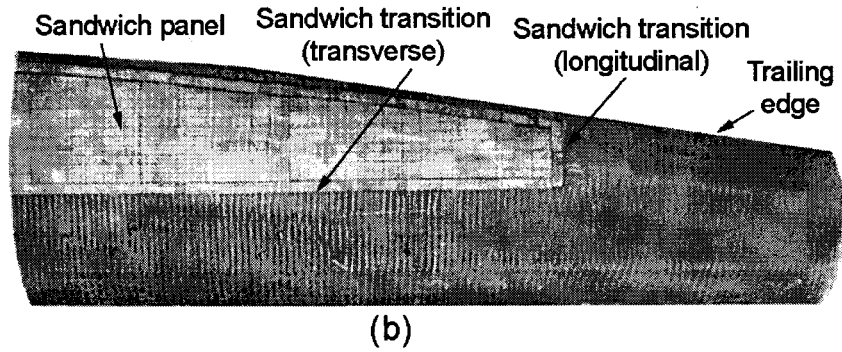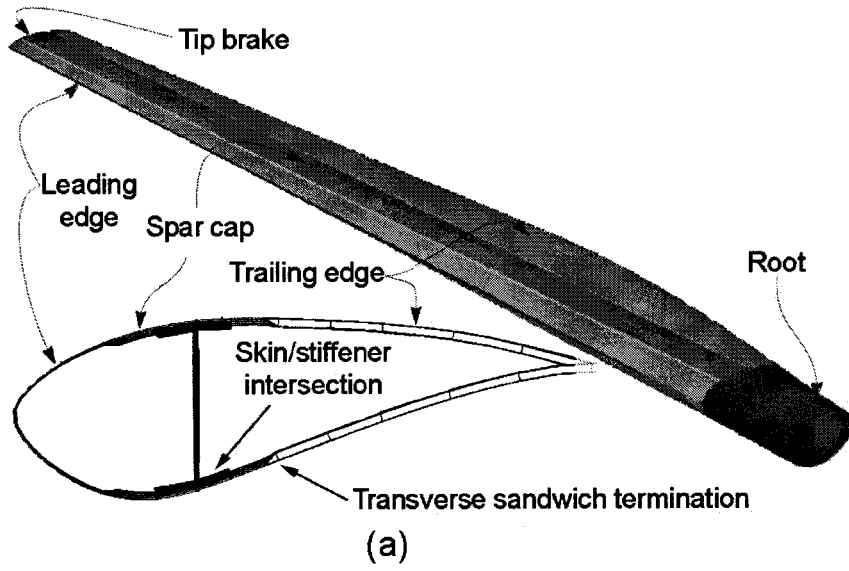
Figure 142. Top View of an AOC 15/50 Wind Turbine Blade Segment.
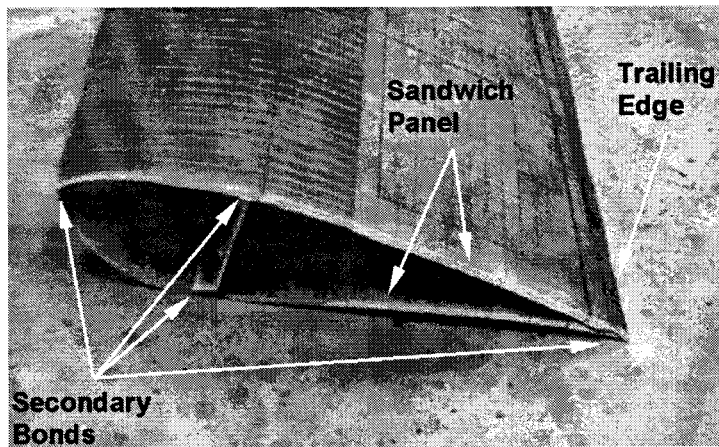
Figure 143. Section View of Wind Turbine Blade Showing Sandwich Construction in the Trailing Edge.
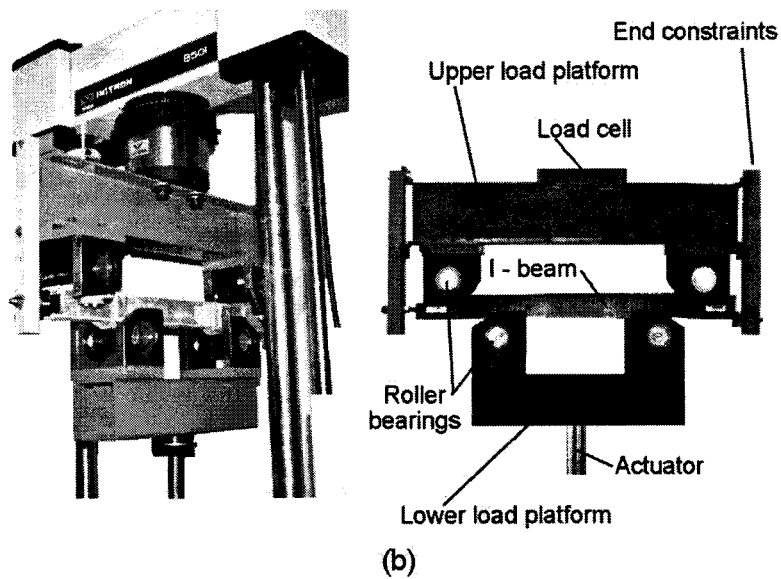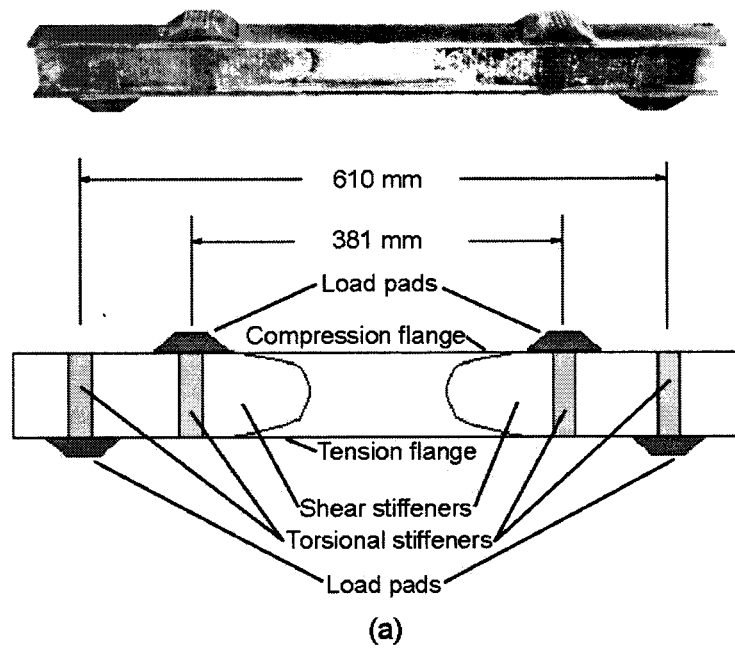
Figure 144. (a) Photo and Schematic of the Composite I-Beam Section and (b) The Four-Point Testing Apparatus and Setup from Reference 3.
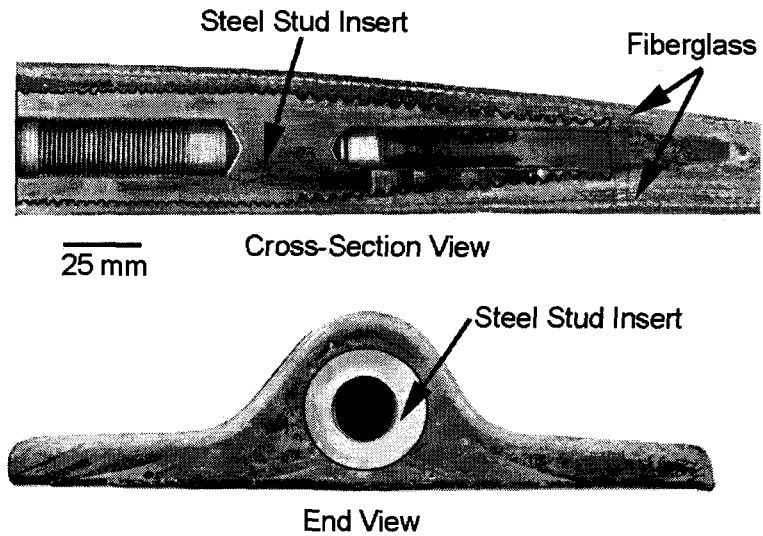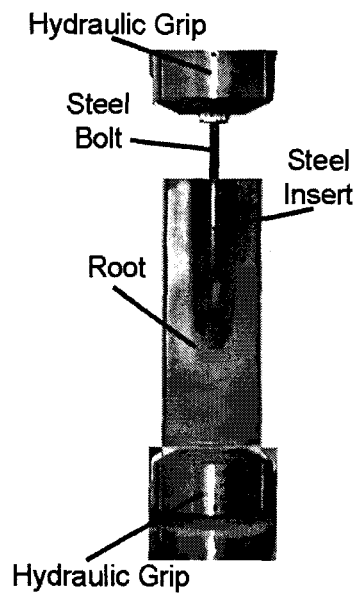
Figure 145. Blade Root Stud Insert Specimen (a) Cross-Section and End View and (b) Test Photograph, from Reference 96.

12. SKIN/STIFFENER INTERSECTION: STATIC TEST DEVELOPMENT

12.1. Summary

Most composite blades contain some type of internal stiffener spar, as shown in Figure 142. The goals for this study were to combine experimental testing with finite element analysis (FEA) to establish design guidelines and develop accurate FEA methods for predicting skin-stiffener fracture loads and locations. A follow-on study reported in the next chapter explored the fatigue response. An additional goal of the study was to establish a structural integrity test geometry for materials and manufacturing evaluation.

A strength-based failure prediction with FEA results was adequate to predict damage onset in the stiffener samples in regions without high stress gradients. However, a fracture mechanics approach was necessary to analyze the flange tip region. Good agreement with experimental delamination initial growth loads was obtained by using the one-step virtual crack closure technique (VCCT-1) to calculate strain energy release rate values. These values were used with the linear interaction criterion for crack growth to predict propagation loads. An initial crack length of less than 0.2 mm and a crack length to crack extension ratio (a/da) of greater than 20 provided good results for the modeling of damage onset at the flange tip. The use of R-curve data for predicting the extension of large delamination produced generally conservative results.

Experimental fracture toughness tests showed that delamination growth resistance was higher for cracks propagating at a ±45 degree ply interface than for cracks between two 0° plies. Increasing the skin bending stiffness and matrix material toughness produced large increases in pull-off loads. Increasing the flange thickness and the adhesive bond-line thickness caused the damage location to change from the web/flange bend region to the flange tip. This was due to the increasing geometric discontinuity at the flange tip, which created high interlaminar stresses. Detailed design recommendations are presented.

12.2. Introduction

The common internal stiffener spar used in the structural design of blades (Figure 142) is usually an I-beam or C-channel. The interface between the spar flange and skin surface is often the site of fracture and delamination growth in composite wind turbine blades. Fracture initiates here due to high out-of-plane stresses and stress concentration areas, combined with the low transverse and out-of-plane strength of composite materials. Areas such as the stiffener flange tip may develop unbounded local stress fields (in continuum models) due to the geometric mismatch between the flange and skin, Figure 146. Such areas cannot be analyzed with strength-based criteria. These factors make skin-stiffener detail regions a critical design component in wind turbine blade structures. This section describes the development of a standard test specimen geometry used to evaluate design methodologies and materials comparisons, the latter discussed in Chapter 3 under resin evaluation.

190

12.3. Experimental Methods

12.3.1. Materials

There were two main categories of specimens investigated in this study. The first group was comprised of delamination specimens as described in Chapter 7. These specimens were used to collect basic delamination data for various fabrics and interface layup configurations. The second group consisted of specimens that represented blade substructures in the skin-stiffener detail regions. These specimens were tested using various loading conditions, manufacturing methods, resin materials, geometries, and fabric layups.

All materials were processed using RTM as described in detail in Reference 35. The resin was the ortho-polyester with a postcure at 60°C for two hours. The reinforcing E-glass fabrics were Owens-Corning stitched D155 fabric for the 0^0 layers and stitched DB120 for the ±45 layers, also from Owens-Corning. T-section specimens were either RTM molded as a single unit, or the skin and stiffener were secondary bonded, as discussed later.

The DCB and ENF delamination specimens were fabricated as flat plates with a Fluoro-Peel Teflon release film at the mid-plane to serve as the crack initiation film. Three lay-ups were tested:. $(0)_{10}$ at a fiber content of 36 percent by volume, $[(0)_2/(45/-45)]_S$ at a fiber content of 34 percent, and $(45/-45)_{10}$ at a fiber content of 26 percent. Both specimen types were cut from flat plates with a diamond blade saw to a standard specimen size of 2.5 cm width by 18 cm length. Data were reduced using both MBT and FEA virtual crack closure methods described in the delamination section of this report.

12.3.2. Tests Methods

A variety of experiments were performed to develop this test method for structural integrity evaluation. The test specimens varied in stiffener geometry, materials, delamination interface lay-up, skin and flange stiffness, manufacturing method, and loading cases. A list of the lay-up schedule used for the skin and flange for each specimen type is presented in Table 28, and a summary of the test matrix and a description of the various specimen types are presented in Table 29.

Two different T-mold configurations were used to produce the skin-stiffener specimens. The geometry and loading for the first batch of specimens, referred to as the "thin-flanged" specimens, is shown in Figure 146. The diagram for the "thick-flanged" specimens is displayed in Figure 147. The different designs were utilized to investigate specimens displaying different failure modes. The thin-flanged specimens were expected to display initial damage at the web-flange fillet region, followed by delamination toward the flange tip. In contrast, the thick-flanged specimens were anticipated to fail at the flange tip area, with a delamination then progressing toward the web centerline. The ability to predict this different failure behavior for different geometries could then be established with the FEA models.

The thin-flanged stiffeners were manufactured two ways. They were either co-cured in the

mold with the skin, or secondarily bonded to the skin with an adhesive. The secondary bonded type was molded with a layer of release film at the skin and stiffener intersection. The flange and skin cured in the same mold, but did not bond together due to this film layer. This film layer is easily removed after molding since it does not bond to the resin. To investigate bonding issues, two different adhesives were compared, and the bond-line thickness was varied considerably. The adhesives used were the Dexter Hysol EA 9309.2NA epoxy and ITW (Illinois Tool Works) Plexus methacrylate A0425.

Table 28. Ply Orientations and Laminate Identification Codes for Substructure Tests.

Laminate Configuration*	ID Code	Thickness, mm
Thin-flanged Specimens		
$[\pm45/0_2/\pm45]_2$	S1 (skin)	4.5
$[\pm45/0_2/\pm45]$	F1 (flange)	1.6
Thick-flanged Specimens		
$[\pm45//0_2/\pm45]$	S2 (skin)	1.6
$[90/0/\pm45]_s$	S3 (skin)	2.8
$[(\pm45/0_2/\pm45//0_2/\pm45)_s/\pm45/0_2/\pm45]$	F2 (flange)	10
$[(90/0_2/\pm45/0_2/\pm45)_s/\pm45/0_2/\pm45]$	F3 (flange)	10
$[\pm45/0_2/\pm45]_s$	Web (all)	4.5

*Thick-flanged layups include $[\pm45/0_2/\pm45]$, which is half of the web layup continued onto the top of the flange cap section. The 0° direction is along the blade length, into the paper in Figure 146.

Flange and skin ply layups were varied to track influences of bending stiffness and delamination interface lay-up on stiffener performance for the thick-flanged specimens. In addition, by varying the interface plies, FEA predictions could be validated more thoroughly, since toughness has been observed to change with delamination ply interface orientation [34].

The static pull-off tests were performed in the displacement control mode on an Instron 8562 servo-electric testing machine. Data were collected and graphed for load versus actuator displacement, Figure 148. In addition, initial fracture load, maximum load, and maximum displacement were manually recorded to verify each plot used in subsequent analysis and to compare specimen performance. The term "load" in the context of the T-section stiffeners tests refers to the force per unit width on which the force is applied, expressed as N/cm (Figure 146); The nominal testing width was 5 cm in all cases. Initial damage onset was taken as the point where either the load-displacement curve became non-linear, or the load suddenly dropped by more than 2.6 N per cm of width. This correlated well with audible and visual damage onset values.

192

Table 29. T- Specimen Substructure Test Matrix.

Geometry from Table 28		Manufacturing			Number of Specimens [1]	Motivation
Flange	Skin	Bonding	Matrix Material	Delamination Interface Layup		
Thin-flanged Stiffeners						
F1	S1	Co-cured	Polyester	(±45)	11 (T) 3 (C)	Baseline pull-off specimens, investigate damage initiation and growth
F1	S1	Co-cured	Polyester	(±45)	3 (T)	Investigate compressive behavior and damage location
F1	S1	Secondary Bonded (0.15 mm bond) (Hysol Epoxy)	Polyester	(±45)	12 (T)	Investigate performance changes with secondary bonding of skin to stiffener
F1	S1	Variable Bond Thickness (Hysol Epoxy)	Polyester	(±45)	11 (T)	Investigate performance changes with variable bond-line thickness
F1	S1	Secondary bonded (Plexus Methacrylate)	Polyester	(±45)	6 (T)	Investigate bonding of commonly used commercial adhesive
F1	S1	Co-cured	Polyester/PET	(±45)	4 (T)	Investigate delamination resistance of different matrix materials
F1	S1	Co-cured	Polyurethane	(±45)	3 (T)	
Thick-flanged Stiffeners						
F2	S2	Co-cured	Polyester	(±45)	6 (T)	Investigate specimens exhibiting flange tip failures, vary the skin stiffness and interface lay-up
F3	S3	Co-cured	Polyester	(0/0)	3 (T)	
NOTE: 1 (T) = Tension tested, (C) = Compression tested						

193
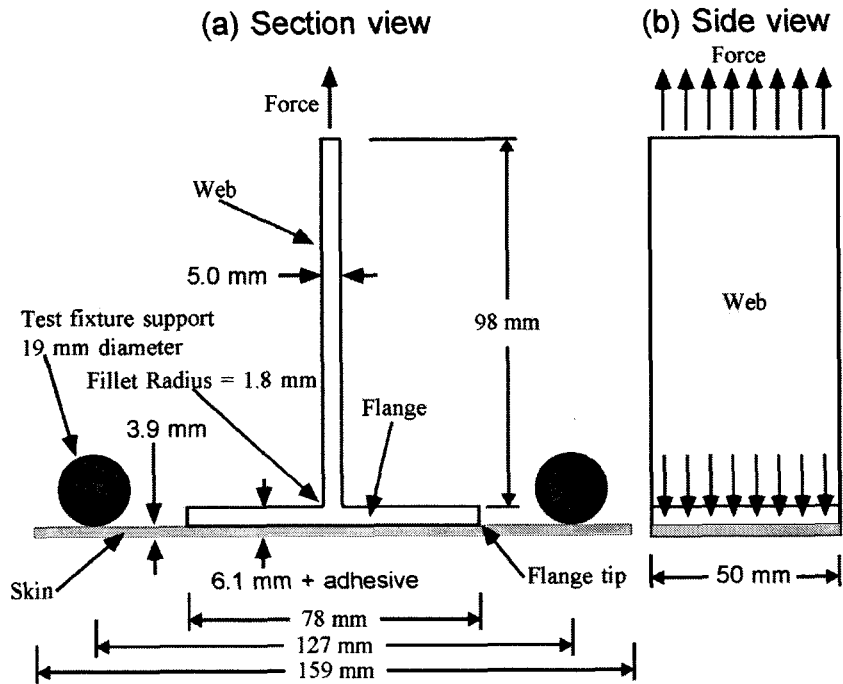
Figure 146. Geometry and Loading for Thin-Flanged Stiffener Tests.
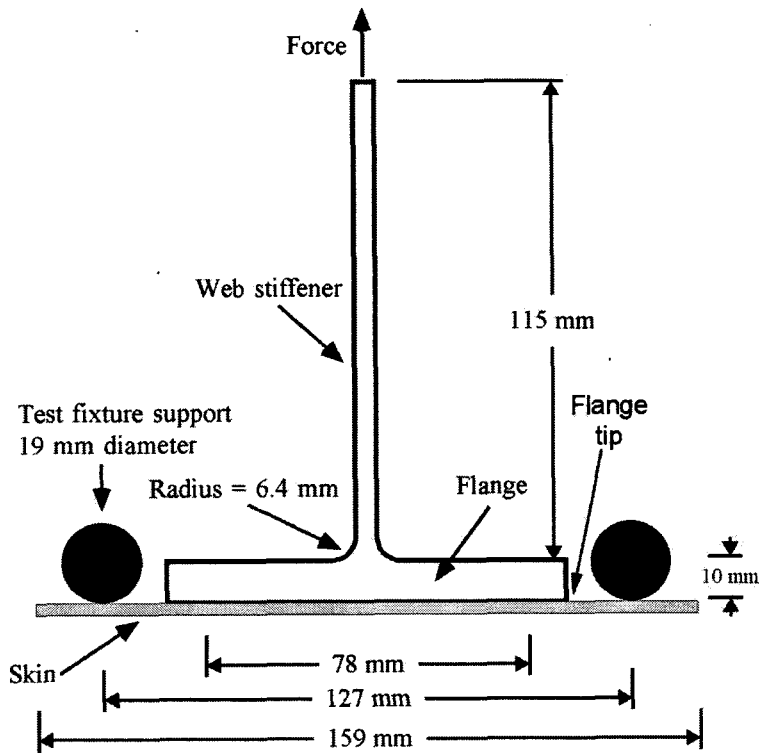
Figure 147. Geometry and Loading for Thick-Flanged Stiffener Tests.

194
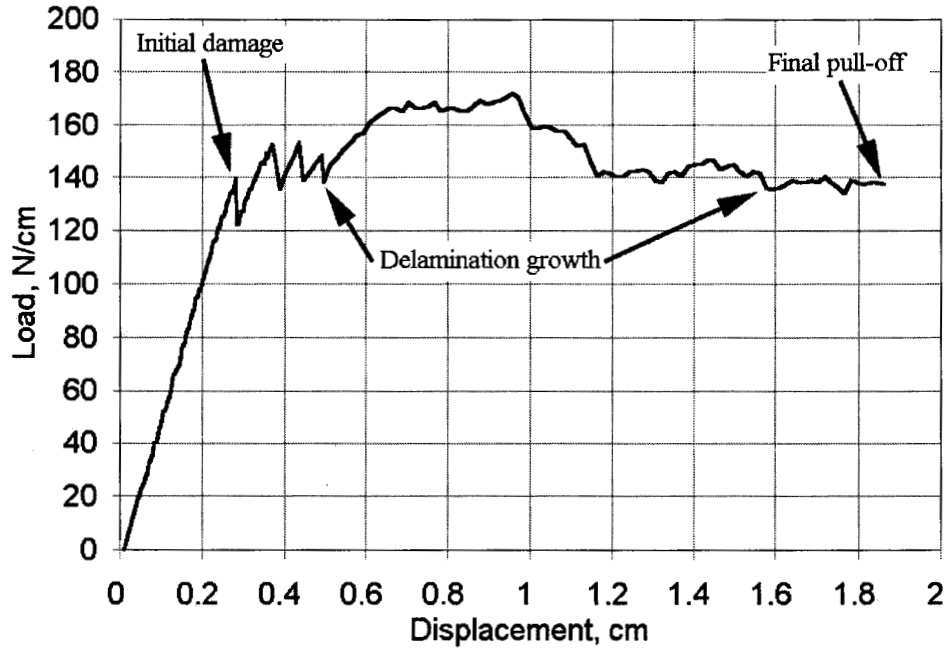
Figure 148. Typical Load-Displacement Curve for Thin-Flanged Stiffener Pull-Off Test.

12.4. Results and Discussion

12.4.1. Thin-Flanged Specimens

The first series of tests provide a comparison of the one-piece T specimens with two-piece specimens which were secondary bonded with a thin bond-line (0.15 mm adhesive layer). The adhesive used in these tests was the Hysol EA 9309. Upon loading, the stiffeners developed cracks at the web/flange fillet area. The initial damage was visible (Figure 149) as transverse cracking in the bend surface ±45° layer (1), whitening underneath the surface plies (2), and transverse cracks through both 0°plies in the bend (2). Actual cracks in Figures 149 and 150 were traced over with a computer drawing program to enhance visibility in the photographs. Many tests were stopped immediately after initial cracking was audibly detected to discern the failure sequence. A black dye marker was rubbed on the bend surface and specimen edges and wiped off to better observe any crack formation. The dye clearly showed transverse cracking on the bend region surface, as well as transverse cracking in the two 0° plies within the bend region (Figure 149). In addition, the transverse cracks appeared to initiate the slight delaminations between the 0° ply and the surface ±45° ply. It was concluded that the transverse cracks happened first because some of the tests exhibited the transverse failure without the small delaminations being present. It is possible that the small delaminations were due to dynamic effects of the fast fracture in the 0° plies. Based upon these observations, it was impossible to determine whether the surface ±45° crack or the 0° transverse crack occurred first.

After initial damage, other cracks formed in the bend region (Figure 150), followed by the

horizontal delamination (3), which formed within the uppermost skin ±45° fabric ply and grew all the way to the flange tip region. A vertical delamination (4) also formed at the web centerline and grew upward toward the loading grips. This damage sequence was the same for all co-cured and thin bond-line specimens.

The results for initial damage and maximum pull-off load (Figure 148) showed essentially no change between the co-cured and secondary bonded specimens (Table 30). The one-piece specimens had an average initial damage load of 85.5 ±15.3 N/cm, while the bonded stiffeners had an average initial damage load of 87.7 ±7.6 N/cm. The average maximum loads reached during the tests were 133 (±4) and 132 (±9) N/cm for the one and two-piece specimens, respectively. Thus, the presence of a thin layer of adhesive has no significant effect on the damage sequence or load carrying capability, relative to a specimen molded in a single piece.

A strain gage was mounted on the bottom skin surface to measure the transverse strain during the pull-off tests. At an applied load of 66.7 N/cm, the strain across the specimen width was 0.028 percent. Linearly scaling this strain up to the initial damage load of 85.5 N/cm gives a strain at damage of 0.0359 percent. This strain is quite low, and while non-zero, it seems to justify a plane strain rather than plane stress assumption for the FEA models.
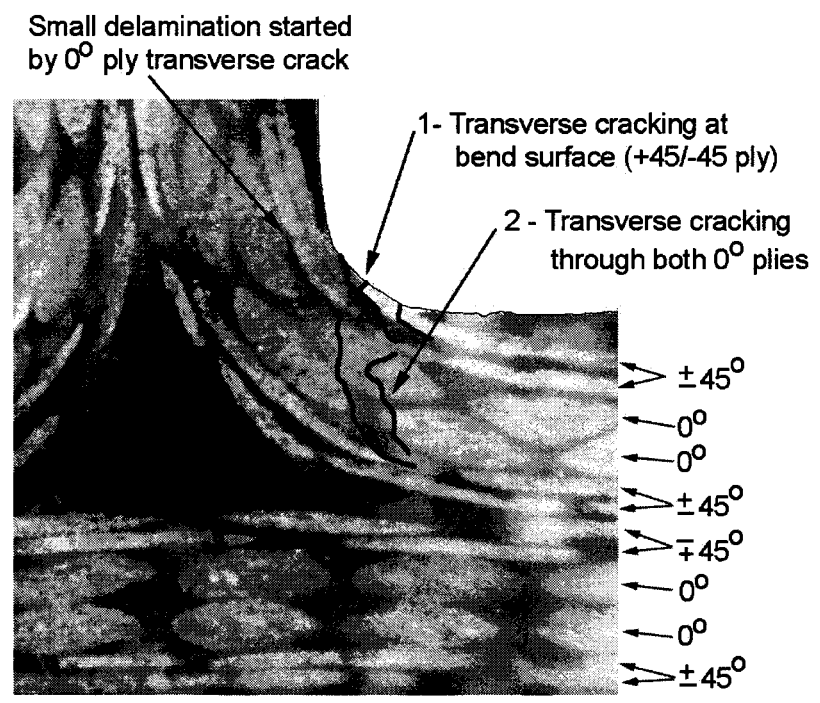
Figure 149. Initial Damage at Web/Flange Fillet Area in Co-Cured Thin-Flanged Stiffener T-Specimens.

196
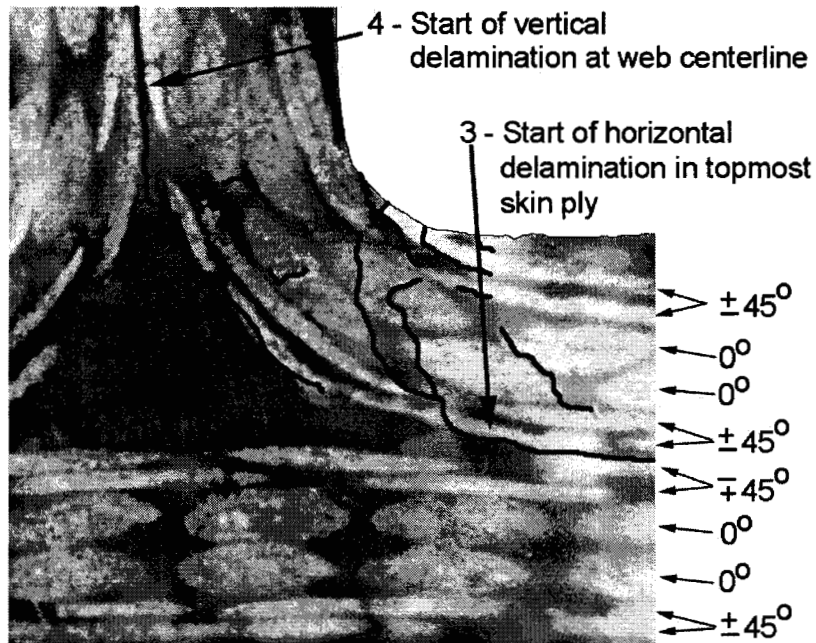
Figure 150. Formation of Major Delaminations at the Bend Region in Thin-Flanged T-Stiffeners.

Table 30. Test Results for Bonded and Co-Cured Thin-Flanged Stiffeners.

Specimen Type	Initial Damage Load, N/cm	Standard deviation	Maximum Load N/cm	Standard deviation	Number of tests
Co-cured	85.5	15.3	133	3.9	11
Secondary Bonded (0.15 mm adhesive)	87.7	7.6	132	9.2	12

Some observations about the specimens and the delamination surface help to explain these results. Increasing the skin bending stiffness has been shown to increase the pull-off load [86]. In particular the higher bending stiffness translates into lower out-of-plane deflection, and lower through-thickness stresses and strains in critical areas. In the tests represented in Table 30, skin bending stiffness remained constant. In addition, the overall bending stiffness of the specimens does not change appreciably with the addition of such a thin bond-line. It was calculated that the bending stiffness (D_{11} term) for the flange and skin added together only increased from 222 N-m to 237 N-m with the addition of the 0.15 mm bond-line. Also, the delamination was observed to grow within the topmost skin ($\pm45°$) ply underneath the adhesive layer. The crack never grew within the adhesive itself. This behavior was also observed by Minguet et al. [86] in bonded stiffener pull-off tests. They concluded that this was reasonable due to the increased toughness of the adhesive compared with the matrix material. This appears to be the case with the polyester/E-glass system as well. The maximum pull-off load occurred once the delamination was beyond the web/flange fillet area and within the top-

197

most skin ply. Since the delamination was propagating in exactly the same location and material in both specimen types, the result of nearly identical maximum pull-off loads is understandable.

To investigate bond-line thickness effects, specimens were made with an adhesive layer thickness ranging from 0.15 mm to greater than 6.0 mm. In addition, a few specimens were bonded with a widely used methacrylate adhesive (Plexus A025).

The results of the bond-line thickness tests are presented in Figure 151. It is evident from the graph that, as bond thickness increases, both initial damage and maximum loads increase. This is in agreement with the previous discussion about the influence of bending stiffness on pull-off load. As bond thickness continues to increase, the bond distance separates the skin and flange. As a result, moment of inertia and bending stiffness increase. At a bond thickness greater than 4 mm, a transition in failure location occurred. For the specimens with approximately 6 mm bond thickness, the initial failure location was at the flange tip, rather than the web fillet radius (Figure 146), as in all previous specimens. The transition to a flange tip failure is consistent with the fact that the peel stress at the flange tip increases as the geometric mismatch between the skin and flange increases [80, 81, 85]. No damage was observed at the web fillet radius area for the 6 mm bond specimens. The initial damage load at the flange tip and maximum load were coincident for these specimens. These results indicate that little or no stable crack growth under static loading would occur for this type of geometry, since the initial damage load was also the maximum load.

The results for the Plexus methacrylate adhesive indicate that it performs as well as the Hysol in terms of initial damage load, and possibly better for the maximum pull-off load (Figure 151). The same damage progression was observed in the Plexus specimen group as in the Hysol bonded specimens.
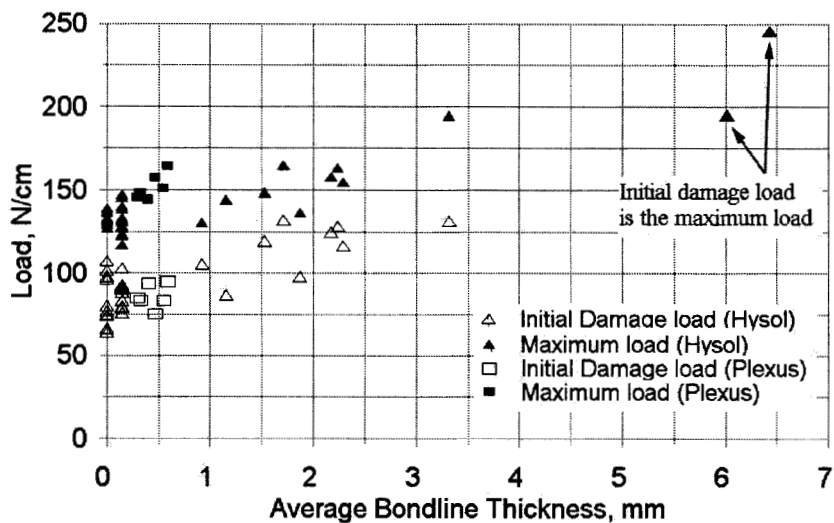
Figure 151. Pull-Off Strength versus Bond-Line Thickness for Thin-Flanged T-Specimens.

12.4.2. Thick-Flanged Specimens

Co-cured thick-flanged specimens (Figure 147) were tested to investigate a skin-stiffener configuration that exhibited flange tip failure. This flange configuration was expected to be dominated by the singular stress zone at the flange tip. This would aid in the development of analysis techniques for these regions with FEA methods. The stiffener was produced with a very thick-flange, formed by adding additional plies underneath the standard flange of the thin-flange design.

Skin thickness and skin-stiffener interface ply orientation were varied to examine the effect on initial damage load and delamination resistance of the specimens. The motive behind these lay-ups was to have two different cases for validating the FEA predictions. The delamination resistance of the polyester/E-glass materials changed with variations in interface layup. The goals of the testing were to collect accurate data for load at damage onset, and load versus delamination length. Once this was established, the FEA predictions could be validated.

The configurations for the thin-skinned and thick-skinned specimens (both with a thick flange) are listed in Table 29. In Table 31, the skin bending stiffnesses and initial damage loads are listed for both specimen types.

The results of the static pull-off tests confirmed the trends of increasing initial damage loads with increasing skin bending stiffness. The thin skin specimens had an average initial damage load of 58.7 ±5.6 N/cm, while the stiffer thick skin specimens showed an average initial fracture load of 153 ±8 N/cm. The flange tip was always the location of fracture onset in both specimens. After initial fracture at the flange tip, the delamination progressed along the skin-stiffener interface plies toward the specimen centerline (Figure 152). No damage was observed in the web-flange fillet area.

Table 31. Initial Damage Loads for Thick-Flanged Stiffener Tests.

Specimen Type	Skin D_{11} (N-m)	Initial Damage Load (N/cm)	Standard Deviation	Number of tests
Thin Skin	9.36	58.7	5.6	5
Thick Skin	71.8	153	7.5	3

To gather data for load versus delamination length, the specimens were loaded until the delamination was observed to propagate. The test was stopped, and the crack length on the left, right, front, and back sides of the specimen were measured using the same dye penetrant method used for the DCB tests. After each crack extension, the procedure was repeated. This allowed each test to start with a known value for crack length. The resulting load versus displacement plot was then used to find the load for propagation at that crack length. These values were later used as test cases for the FEA models.

199
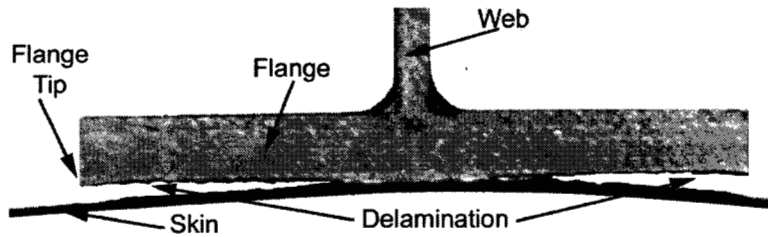
Figure 152. Photograph of Flange Tip Delamination for
Thick-Flanged, Thin Skin Stiffener Specimens.

A problem was encountered in most specimens as the delaminations grew beyond the initial crack onset at the flange tip. In most cases, the crack on one side, left or right, started to dominate, and would propagate farther toward the centerline at the same load case than the other crack. The crack fronts were quite constant across the specimen width on each side, however. The variation in crack lengths make the data beyond initial failure somewhat suspect. However, the initial damage loads are still valid in all cases. Once the crack begins to grow at one location, and propagates into the structure, the strain energy release rate at the longer crack tip should be higher due to the longer moment arm caused by the longer delamination length. This should keep the longer crack propagating more than the short crack.

12.5. Comparison of Finite Element Predictions and Experimental Results

12.5.1. Numerical Results

The results of numerical modeling performed with the ANSYS 5.3 finite element analysis (FEA) code are presented in this section. The analysis techniques and results are discussed with regard to their impact on detail region design. The DCB specimens were modeled to establish predictive capability for strain energy release rates (G) with the VCCT methods and to investigate the effects of modeling parameters such as mesh sizing and crack length to crack closure distance (a/da) ratio on G calculations. Once established, these techniques were applied to skin-stiffener models to predict damage onset and propagation behavior. This technique is described in Chapter 7.

Analysis techniques appropriate for each specimen type were applied to determine predictive capability with FEA. The FEA models used 2-D plain strain, 8-node quadrilateral elements (PLANE82). Comparisons of FEA model displacements with experimentally observed values were used to validate basic model performance, and stresses and strains were calculated to determine likely sites for damage initiation. A strength-based failure approach was used in areas where stress singularities were not present. The load to initiate fracture was determined by multiplying the applied load by the ratio of ultimate strain to applied strain, since stress and strain increase linearly with load for a linearly elastic material. In regions with a singularity, such as the flange tip, a fracture mechanics analysis was required. This involved calculating strain energy release rate values and the use of the linear interaction criterion (Equation 17) for crack growth. The load at damage onset was calculated by multiplying the applied load by a ratio determined from the linear interaction criterion. This ratio

200

is based upon the fact that strain energy release rate increases with the square of the applied loading (explored in the next section). This technique is presented in more detail for the benefit of designers and analysts in Reference 35. The FEA predictions for damage initiation load and location were compared with experimental results to validate these design approaches for different specimen configurations.

12.5.2. Delamination Modeling

The results of the DCB modeling showed that the VCCT-1 method in ANSYS is the preferred tool for predicting G values with FEA [35] (see Chapter 7). The VCCT-1 has good mesh size stability and only requires one FEA analysis to calculate G for all modes of crack growth. In contrast, the VCCT-2 method needs an initial analysis to load the structure, and one additional run for each mode of crack extension. This means that, for a structure with Mode I and II loading, the VCCT-1 method will be at least three times faster than the VCCT-2 method. This fact further increases the utility of the VCCT-1 approach for designers. The VCCT-1 predicted values also match the experimental data better than the VCCT-2 techniques. Full details of the study involving numerical methodology and mesh size effects can be found in Reference 35.

12.5.3. Thin-Flanged Stiffeners

The two prime areas of interest for damage onset were the web/flange fillet radius area and the flange tip region. These areas have typically served as damage initiation sites in pull-off tests [80, 81, 83, 86]. The damage initiated at the bend region (Figure 149) in every test case performed in this study. The verification of the slope of the load/displacement behavior for the FEA model showed good agreement with the average experimental slope. The FEA value differed from the experimental average by only -2.4 percent [35].

The first site investigated for damage was the bend region. Experimental observations (Figure 149) of initial damage showed transverse cracks in the surface ±45° ply and the 0° plies beneath them. These cracks seemed to form at roughly the same load since both cracks were present after initial damage detection. The strain in the plies at the bend was calculated by FEA at the experimentally observed damage initiation load of 85.5 N/cm. Because this was a 2-D analysis, the strain components in the FEA global axes were applied as laminate loads in a composite analysis program to get fiber longitudinal and transverse stresses and strains for comparison with material strength data. The database strength data for the D155 and DB120 materials presented in the next section were used to predict damage. The maximum in-plane strain in the bend region was in the +45 degree surface ply. The strain components had to be viewed in a local cylindrical coordinate system for the bend region rather than the global system. This local system was necessary to properly align the material properties as they curved from the web to the flange area. Typical strain contour plots in the bend region are presented in Figures 153 and 154. In the bend region local coordinate system the X-direction is the radial (R, or through-thickness) direction, the Y-direction is following the curved region (θ or tangential), and the Z-coordinate is out of the page. There was no Z strain component

since this was a plane strain analysis. The maximum in-plane tangential strain at the bend was 0.60 percent within the +45°surface ply. The 0° ply directly beneath the surface (±45°) fabric had a tangential strain of 0.36 percent. The radial (through-thickness) and shear strains in these plies were not high enough to cause damage. The radial strain component in the surface (+45°) ply was -0.43 percent, with an allowable compressive strain for this material of −1.21 percent. The maximum radial strain observed was 0.18 percent at the web centerline, which is below the ultimate transverse strain value in tension of 0.30 percent for this material. The maximum observed XY shear strain was 0.10 percent, while the ultimate transverse shear strain allowable is 2.06 percent.

The appropriate strains were applied to the +45° and 0° plies with a laminate analysis program. Failure was determined by applying both the maximum strain and the quadratic (Tsai-Wu) failure criteria. The results are presented in Table 32. The maximum strain criterion predicts that fracture will occur when the strain in any direction equals the ultimate strain allowable in that direction. The quadratic criterion is based upon an interaction of the various stress states in the laminate [94]. The quadratic failure criterion will not directly predict the failure mode as will the strain criterion. The maximum strain criterion predicted fracture in the +45°surface ply at 94.0 N/cm, or 10 percent above the experimental average load. The quadratic criterion predicted damage onset at 70.9 N/cm, or 17 percent below the experimental average. Thus, these point stress and strain based predictions bound the experimental average value. The failure mechanism in the bend surface +45° ply was predicted as transverse tension failure with the maximum strain criterion.
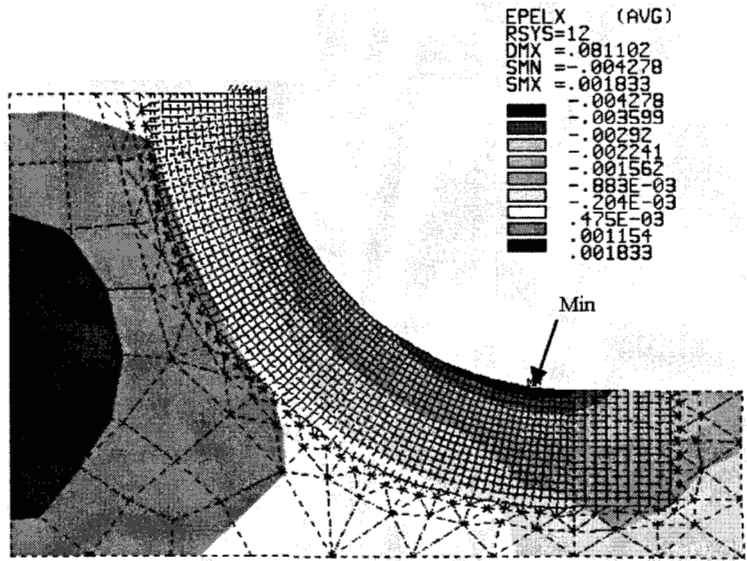
Figure 153. Radial Strain Plot in the Bend Region for the Thin-Flanged Stiffener Model.
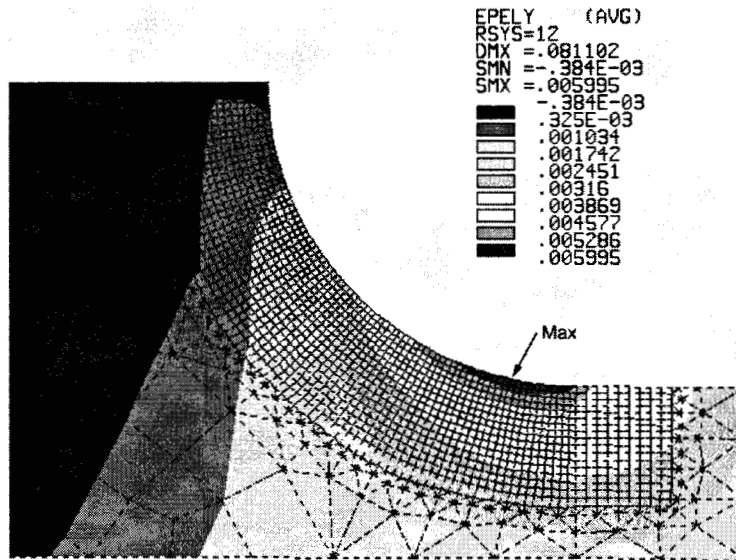
Figure 154. Tangential Strain Plot in the Bend Region for
the Thin-Flanged Stiffener Model.

Table 32. Point Stress Failure Prediction in the Bend Region for the Thin-Flanged Stiffener
Specimens.

Fracture Location	Experimental Initial Damage Load, N/cm	Maximum Strain Criterion Prediction N/cm	Quadratic Criterion Prediction, N/cm
+45° Bend Surface Ply	85.5	94.0	70.9
0° Bend Region Ply	85.5	93.1	92.3

Experimental observations showed that a transverse crack formed in the 0° plies in the bend
at the same time the crack in the ±45°surface plies formed. Tests were stopped immediately after
initial damage was detected and both cracks were present. The strains were analyzed in the 0° plies
to see if they were at the failure point as well. When the 0° ply strain was input into laminate analysis,
the predicted damage load was 93.1 N/cm with the maximum strain criterion. This is 8.9 percent
higher than the experimental average. The quadratic criterion predicted 92.3 N/cm, or 8.0 percent
above the experimental average. These load values are nearly identical to the prediction for the ±45°
surface ply fracture with the maximum strain criterion. Therefore, it is not surprising that both cracks
seemed to form simultaneously during the experimental testing.

The next area analyzed for initial damage was the flange tip termination. This region does not
lend itself to a strength-based prediction due to the existence of a singularity in the peel stress (see
the delamination section). To circumvent this problem, a fracture mechanics approach was utilized

203

to predict initial fracture load. This method assumes that, immediately after damage onset, there will be a crack of finite length in the structure. Furthermore, it assumes that the load to propagate this very small crack is the same as the fracture onset load without the crack present. Values for G_I and G_{II} can be calculated by modeling a very small crack at the likely damage location and then applying a load case and a VCCT prediction method. The values for G are then used with an appropriate mode interaction criterion (Equation 14 or 15) to predict the crack propagation load. The linear interaction criterion was used in the following analysis.

The first step is to verify the existence of a singularity type of stress field to make sure this technique is warranted. At the experimental damage onset load, the peel stress at the flange tip (in the last element at the tip) was calculated to be 260 MPa. This is thirteen times greater than the peel strength of a typical E-glass/polyester composite, and yet the flange tip showed no damage during the tests. In addition, the maximum peel stress value in FEA was increasing with every mesh refinement. There was clearly a need to analyze the flange tip with a fracture mechanics approach due to the flange tip peel stress singularity.

A 0.155 mm long crack was modeled at the interface between the skin and flange at the flange tip. The elements were refined to give an (a/da) ratio of 20. This was based upon the results from the DCB analyses that showed good predictive ability for G_I and G_{II} even at this low (a/da) ratio. The VCCT-1 method was applied to calculate G in Modes I and II. The output value for G_I was 25.8 J/m^2 while G_{II} was 14.7 J/m^2. A load for crack extension of 195 N/cm is predicted using the linear interaction criterion (Equations 14 and 15), and the initiation values for G_{Ic} and G_{IIc} of 140 J/m^2 and 2001 J/m^2. This is much higher than the observed load to cause damage at the bend region of 85.5 N/cm and is well above the maximum load of 133 N/cm reached in the pull-off tests.

This analysis predicted that damage would not initiate at the flange tip for pull-off loading with the thin-flanged stiffeners. This was known a priori from experimental testing. However, this type of analysis will be essential for predictive design work for skin-stiffener detail regions with different geometries. If a fracture mechanics approach were not applied to the flange tip, large errors in the damage onset load predictions would occur. In this case, a stress-based analysis would have incorrectly predicted both the damage initiation load and the location within the structure. This example illustrates the importance of applying fracture mechanics to perform damage onset predictions in regions of very high stress gradients. It is essential that designers recognize situations where point-stress based strength approaches are invalid. This should prevent the failures that have resulted from such detail region design oversights.

12.5.4. Thick-Flanged Stiffeners

12.5.4.1. Thick Skin with (0/0) Interface

Initial Fracture

The thick-flanged skin-stiffeners were co-cured in two configurations. One utilized a thick

skin with a (0°/0°) interface (T5200 series) while another had a thin skin and a (±45°) interface (T5000 series). Note that the 0°/0° interface is for a delamination growing in the 90° direction (relative to the 0° fiber), between two 90° plies. The thick-flanged stiffeners were tested in a tensile pull-off mode. The results for initial damage onset and maximum loads fot the thick-flanged stiffeners were presented in Table 31.

The thick-flanged stiffeners were modeled in ANSYS and the FEA models were used to predict displacements, damage onset, and crack propagation behavior. The FEA results for the T5200 stiffeners are presented in Table 33. The model yielded a good prediction for displacement at damage onset load when compared with the experimental average. The FEA displacement was 0.615 mm, or 1.3 percent less than the experimental average. This indicates that the FEA geometry and material properties were modeled correctly.

Table 33. Experimental versus FEA Results for Displacement at Average Experimental Damage Onset Load.

Specimen type	Experimental displacement mm		FEA displacement, mm	Percent difference in predicted displacement
	Average	Std. Dev.		
T5000 [45°/-45°] Interface	1.086	0.144	1.034	-4.8
T5200 [0°/0°] Interface	0.623	0.038	0.615	-1.3

The next step was to predict the damage onset at the flange tip region. Both the VCCT-1 and VCCT-2 corner node loading techniques were employed to predict strain energy release rates. The same method used for the flange tip analysis of the thin-flange specimens was utilized for the T5200 specimens. The existence of the stress singularity at the flange tip was verified by observing large increases in peel stress at the flange tip with successive mesh refinements. The peel stress (not converged) at the experimentally observed fracture onset load was 261 MPa after the final mesh refinement. This was well above the peel strength for polyester/E-glass of 24.9 MPa. This verified that a point stress strength-based approach would not work and that a fracture mechanics solution was necessary at the flange tip. Viewed differently, this indicates that this part of the specimen would have failed by a strength-based criterion, and a crack geometry should be inserted. This then requires a fracture mechanics analysis.

A crack length sensitivity study was conducted at the flange tip for small crack lengths and low (a/da) ratios for the VCCT-1 technique. The results of this study (Figure 155) show that the G values are fairly stable down to a crack length of 0.04 mm with an (a/da) ratio of five. It should be noted that both the crack length and the (a/da) ratio are changing in Figure 155 with (da) constant at 0.008 mm. In addition, much of the decrease in G with decreasing crack length is probably due to the low (a/da) ratio and not the change in modeled crack length.

Two different initial crack sizes and corresponding (a/da) ratios were modeled to predict initial damage at the flange tip. The first crack had an (a/da) ratio of 26.0 and a length of 0.201 mm. The second crack was slightly smaller with an (a/da) ratio of 20.0 and a length of 0.156 mm. The results for the initial damage load predictions at the flange tip for the T5200 specimens are presented in Table 34. The VCCT-1 method with the 0.201 mm crack model predicted an initial damage load at the flange tip of 141 N/cm, while the 0.156 mm crack prediction was 142 N/cm. The experimental average damage load was 153 N/cm.

Because the FEA predictions are dependent on the interlaminar fracture toughness values, it is worth investigating the predicted damage loads using $\pm$ 1 standard deviation for G_{Ic} and G_{IIc}. The change in predicted fracture onset load with the 0.210 mm crack length was +25.9 and –32.4 N/cm, and with the 0.156 mm crack model was +26.1 and –32.5 N/cm. The experimental average damage load falls well within this predicted range.
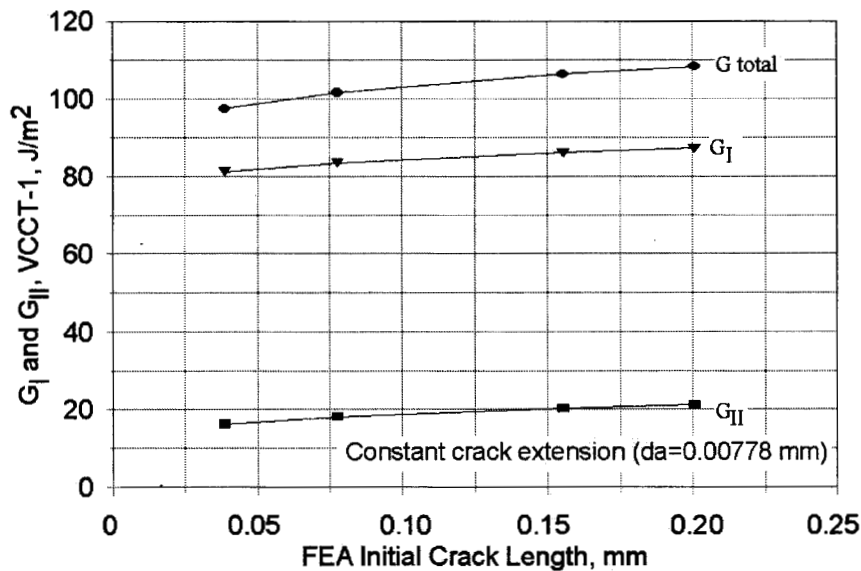
Figure 155. G_I and G_{II} at Flange Tip versus Ratio (a/da).

Overall, the prediction of fracture onset using the VCCT-1 method for the T5000 and T5200 series specimens is very good. Table 33 indicates excellent agreement in the load-displacement curve prior to fracture. Table 34 indicates very good agreement in the load for the onset of delamination propagation.

The VCCT-2 technique was also used with the same model for the 0.201 mm initial crack. The predicted fracture load [Table 35] with this method was 152 N/cm, which is only a -0.5 percent difference from the experimental average fracture load. However, based upon the results from mesh sensitivity studies, the VCCT-2 technique is not recommended, especially at such low (a/da) ratios.

Table 34. Initial Damage Load Predictions at Flange Tip Using VCCT-1 Method.

Specimen Type	Ratio (a/da)	FEA Crack Length (a, mm)	Experimental Fracture Onset N/cm		VCCT-1 Prediction N/cm [1]	% Difference in Predicted Fracture Load
			Average	Std. Dev.		
T5000 [45°/-45°] Interface	5	0.26	58.7	5.6	52.0 +7.0 / -8.2	-11.4
T5200 [0°/0°] Interface	26	0.201	153	8	141 +25.9 / -32.4	-7.4
T5200 [0°/0°] Interface	20	0.156	153	8	142 +26.1 / -32.5	-6.8

[1] Predicted using average G_{Ic} and G_{IIc} with $\pm$ values calculated using $\pm$one standard deviation for G_{Ic} and G_{IIc}.

Table 35. Initial Delamination Growth Predictions at Flange Tip Using VCCT-2 Method.

Specimen Type	Ratio (a/da)	FEA Crack Length a = mm	Experimental Fracture Onset, N/cm		VCCT-2 Prediction N/cm[1]	% Difference in Predicted Fracture Load
			Average	Std. Dev.		
T5000 [45°/-45°] Interface	5	0.26	58.7	5.6	55.3 +7.5 / -8.7	-5.8
T5200 [0°/0°] Interface	26	0.201	153	7.5	152 +27.7 / -34.8	-0.5
T5200 [0°/0°] Interface	20	0.156	153	7.5	NA	NA

[1] Predicted using average G_{Ic} and G_{IIc} with $\pm$ values calculated using $\pm$one standard deviation for G_{Ic} and G_{IIc}. NA -Not Available, no FEA performed for this case.

207

The good predictive results in this case are probably due to the variance in material fracture toughness data. These results show that the VCCT-1 method is always more conservative than the VCCT-2 corner node method in predicting damage load because it predicts higher G values for a given loading case. To reiterate, the VCCT-1 method is preferred for calculating G values with FEA due to its stability with respect to mesh sizing and its consistently higher calculated values for G, compared to the VCCT-2 corner node method. The better agreement between the experimental results and the VCCT-2 predictions in the present case should not be used as an endorsement of this technique.

Delamination Progression

Once damage has initiated at the flange tip, the delamination grows at the skin-flange interface toward the web. This growth was modeled with FEA by releasing coupled nodal sets to achieve the desired crack length. The crack length was chosen as the longest crack in the experimental specimens at a given propagation load. This was due to the observation that once a crack started at the left or right flange, the longest crack would propagate first in subsequent tests. The results for delamination growth predictions are displayed in Figure 156.
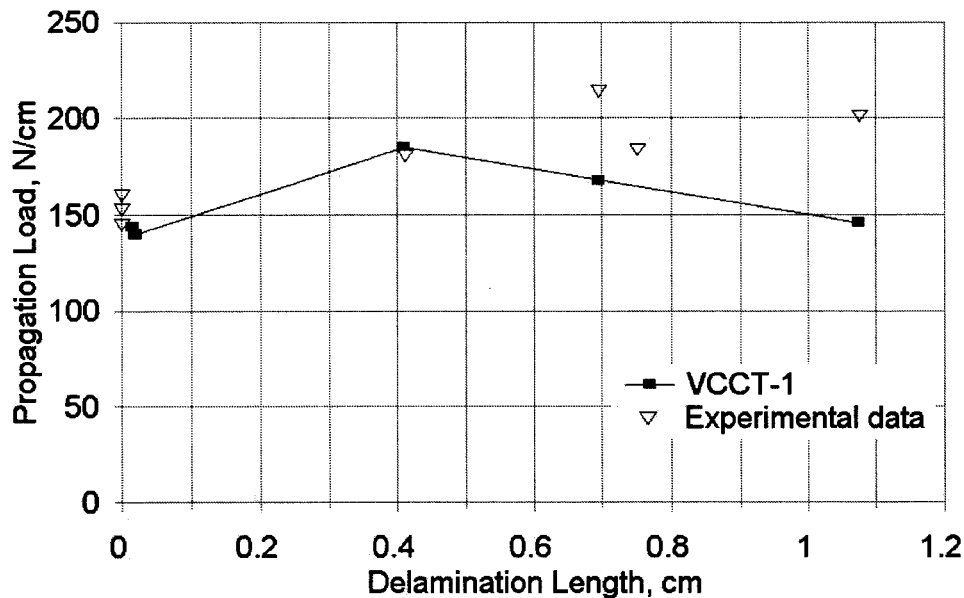
Figure 156. Predicted Propagation Load versus Delamination Length for T5200 Specimens.

208

Individual data points from experimental tests are plotted along with the FEA predictions for those delamination lengths. The G_{Ic} values used in the linear interaction criterion (Equation 17) varied with crack length. The values used were the average values taken from the MBT R-curve data presented in the delamination section. The predictions in Figure 156 are for the VCCT-1 method only. The predicted load for propagation at a crack length of 0.4 cm is nearly identical to the experimentally measured propagation load. Beyond 0.4 cm, the predictions are lower than the experimental results. This may be due to the different crack lengths at the right and left flange tips during the experimental tests. This behavior was observed to be more prevalent at longer delamination lengths. The material at the delamination interface may also be tougher in the stiffeners than the DCB test results. This would result in low estimates for crack propagation loads.

12.5.4.2. Thin Skin with (±45) Interface

Initial Fracture

The same type of testing and analysis was applied to the thin-skinned (T5000 series) specimens. These specimens were tested to investigate the influence of skin bending stiffness and validate the predictive ability for crack growth at a ±45° interface.

The FEA displacement prediction (Table 33) at the experimental damage onset load was 0.103 cm, while the experimental average was 0.109 cm. This shows that the FEA model is approximately 5 percent more compliant than the average stiffness for the experimental specimens.

The prediction for the damage onset load with the VCCT-1 method was presented in Table 34. The predicted value of 52.0 N/cm was 12 percent lower than the experimental average of 58.7 N/cm. However, if one standard deviation were used for G_{Ic} and G_{IIc}, the predicted damage load was 59.0 N/cm. The VCCT-2 method once again predicted lower G values and a higher fracture load [35]. The 2-step method predicted damage onset at 55.3 N/cm, which was below the experimental average by 5.8 percent.

The (a/da) ratio used for the T5000 predictions was only five, with an initial crack length of 0.26 mm. These parameters may be slightly outside of the desired range for damage onset modeling as determined from the DCB mesh sensitivity studies. This was the smallest mesh sizing that could be accomplished for this model, however. The ply layers at the interface were different thickness in the skin and the flange. This caused problems during the mesh refinement process. As the element sizes were reduced by a factor of 2, 4, 8, etc., the element widths were no longer identical on both sides of the interface. The corner and mid-side nodes were then no longer coincident and the VCCT method could not be used. This problem may be avoided by forcing the elements on both sides of the interface to have the exact same width and thickness during the modeling process. If this condition is enforced, then mesh refinements will produce elements of identical size with coincident nodes. These coincident nodes are then coupled together as nodal pairs with identical degree of freedom values to define the crack length.

Delamination Progression

A prediction of delamination growth beyond initial damage was performed by combining the FEA model with the material toughness values from (±45) DCB R-curve results in Figure 101. This interface shows severe R-curve behavior in terms of the increase in G_{IC} with crack extension. G_{Ic} values on the R-curve were assumed to follow a linearly increasing relationship from 140 J/m^2 at 0.0 cm to 1028 J/m^2 at 1.0 cm of crack extension, and then to be constant at 1028 J/m^2, for longer lengths. The predictions for crack growth loads (Figure 157) are consistently lower than the experimental values. This may be due to errors in material toughness data or lack of symmetric crack growth in the T-specimens. The load predictions appear to be about 20 percent lower than the experimental results below 0.8 cm, and get slightly better around 1 cm. The predictions for G_{Ic} would be extremely low if the R-curve toughening behavior were not taken into account. In fact, based upon Figure 157, it seems that the material in the T5000 specimens is actually tougher than the values used from the DCB R-curve. However, slightly different conditions, producing other G_{II}/G_{I} ratios, could greatly reduce the R-curve effect in practice, as could variations in processing or fabric architecture.
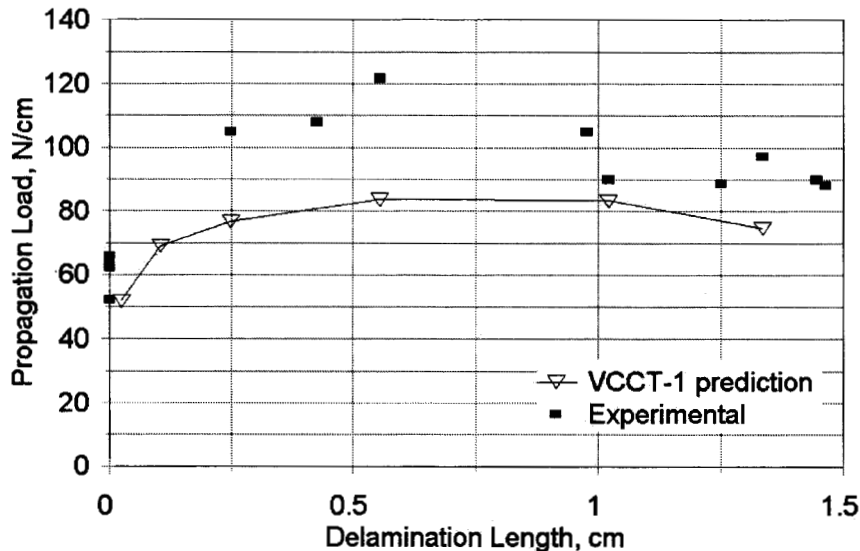
Figure 157. Predicted Propagation Load versus Delamination Length for T5000 Specimens.

12.6. Conclusions

The T-section geometry has been developed as a test specimen for structural integrity studies. While the tensile loading condition differs significantly from the actual stiffener loads in blades, the test is easy to conduct and contains the elements of damage initiation and delamination growth which are critical to structural detail performance. Different configurations of the test allow the shuffling of initial damage from the fillet area to the flange tip, and from intraply failure to delamination failure. Different ply stacking arrangements, matrix materials, and fabrics can be employed to optimize designs. The design methodology demonstrated for this loading can be applied to other loading

conditions and geometries such as ply-drops, but the breath of applicability has not been determined for other cases.

Combinations of point-stress strength-based approaches and fracture mechanics predictions were shown to provide good results for determination of damage initiation loads and locations. The strength-based approach was used to analyze damage onset in areas without high stress gradients. The fracture mechanics method was applied to areas of very high stress gradients such as the flange termination area. These methods can also be applied to three-dimensional analyses with the use of appropriate formulas for G with different element types like composite layered shell elements. The predictive results also showed the need for accurate material strengths and interlaminar fracture toughness data and G_I/G_{II} interaction criteria to determine fracture onset loads. Delamination progression depends heavily on R-curve behavior. Actual design procedures should be conservative and the best assumption is no R-curve behavior, simply using the initiation G_{IC} and G_{IIC} values.

Other findings of this section are that the initial damage location changed from the fillet area in the thin flange geometry, to the flange tip in the thick flange geometries. In the former case, a stress gradient was low, and damage initiation, in the form of matrix cracking in the plies, was predictable using a point-stress strength criterion. Thick flange geometries damage initiated in the form of delamination at the flange tip, and the high stress gradient required a fracture mechanics based prediction. The FEA prediction in both cases was in good agreement with experimental results. The thin flange geometry was investigated with secondary bonding as well as one-piece RTM molding. For thin bondlines, the behavior was unaffected by the adhesive, thicker bondlines produced increased peel strength due to the increasing thickness and moment of inertia.

12.7. Design Recommendations

Several recommendations for materials selection and geometry of T-stiffener structural details can be identified. For delamination resistance, utilize dissimilar fabric ply orientations at delamination prone interfaces in composite skin-stiffener intersections. For example, placing ±45 degree plies together is better than a (0°/0°) interface. However, interface plies oriented at 90 degrees to the primary strain should be avoided due to their propensity to form transverse cracks, which may initiate delaminations. Toughened matrix materials should be used in all areas that will encounter significant interlaminar stresses (see matrix section).

Thin flanges should be used whenever possible to increase delamination onset loads. This minimizes the geometric mismatch between the skin and flange at the flange tip. The stiffness of the flange laminate in the loading direction should also be minimized. This lowers the stiffness discontinuity between the skin and the flange. In particular, ratios of flange to skin thickness from 0.5 to 1.5 should be avoided [85]. The stiffener flange tip should always be tapered by at least 45 degrees. It should never be manufactured with a 90 degree block edge. Tapering reduces the geometric discontinuity at the flange tip, which lowers the interlaminar peel and shear stresses in this region [83, 86]. In areas where the skin may encounter bending loads, use a higher bending stiffness laminate in the loading direction to keep out-of-plane deflections to a minimum. This will increase delamination onset loads at the skin-stiffener interface. Use the largest practical web/flange transition radius to

lower the stress concentration in the bend region. This radius will be dictated by the overall stiffener size and manufacturing issues.

Several recommendations for numerical modeling can also be made. In predicting damage initiation, use a standard strength-based approach to calculate damage onset in regions that do not contain stress singularities or very high stress gradients. A quadratic strength criterion should be used to determine strength, while a maximum strain criterion is best for identifying failure mode.
Use a fracture mechanics approach to predict initial damage in areas with stress singularities such as the flange tip. Initial crack length should be kept below 0.2 mm and the ratio of crack length to crack extension (a/da) should be greater than 20 for accurate results. To calculate G values use the VCCT-1 method. For VCCT-1 formulas for additional element types see references [82, 85]. Use initiation values for G_{IC} and G_{IIC} as discussed in the delamination section. The G_I / G_{II} interaction criterion in Equation (17) worked well in this study. This is the subject of an on-going study at MSU.

13. SKIN STIFFENER T - SECTIONS: FATIGUE CRACK GROWTH AND LIFETIME

13.1. Summary

As described in the preceding section, the skin-stiffener T-section specimen has been developed as an example of a structural detail where failure occurs by matrix cracking and delamination. This section describes a study intended to explore the damage development and failure of T-sections under fatigue loading. Experiments have been run to measure damage initiation conditions and geometries as well as delamination or growth rates in T-sections. Using finite element analysis and data for strength, delamination resistance, and delamination fatigue crack growth, damage initiation and growth under static and fatigue loading is predicted following a prescribed methodology and compared to experimental data. Delamination growth is by a mixture of Modes I and II, and a mixed-mode criterion has been assumed in the absence of definitive data. Overall T-section fatigue lifetime trends with varying maximum load are also established, and the sensitivity to matrix variations is explored.

The results in this section serve to define and validate a methodology for predicting delamination failures at structural details using finite element analysis and database delamination fatigue crack growth and fracture data. While the correlations of predictions with experimental data are generally good, they indicate a need for a definitive fracture mode interaction criterion for static and fatigue delamination for a range of reinforcing fabrics, matrices, and particular ply interfaces. A simplified method for predicting fatigue performance in the design of delamination-prone substructures is also presented.

13.2. Introduction

This study used the results generated in the preceding static study to choose a T-section geometry and materials; these choices were also guided by the materials used in the AOC 15/50 blade design described earlier. Test fixtures and methodology were required for fatigue loading, and it was necessary to develop schemes for test interruption and damage inspection.

The experimental goals of the study were to generate fatigue data for a representative T-section geometry; observe and measure damage initiation and growth; determine S-N lifetime curves for T-sections with various geometries; and generate a database for delamination crack growth and failure using these materials (described in the earlier section on delamination). The T-sections were to be analyzed using FEA for stress distribution, initial damage, and delamination growth. The outcome was to be a validated methodology for the prediction of static and fatigue failures in substructures of this type, with associated numerical procedures and database. This was the first effort of its type in this overall program, and was expected to identify areas requiring further development.

13.3. Experimental Methods

13.3.1. Materials

This study used the E-glass fabrics described earlier. The fabrics were D155 for 0° and 90° layers and DB120 for the ±45° layers. Most of the study used the CoRezyn 63-AX-051 ortho polyester with 1 to 2 percent MEKP catalyst. Other resins used for comparison were isophthalic polyester and Derakane 411C-50 and 8084 vinyl ester. All materials were resin transfer molded and post cured at 60 °C for two hours.

13.3.2. Test Methods

Delamination tests were conducted as described in the earlier delamination section. Fiber orientations and crack interfaces were chosen to coincide with the crack positions observed in the skin-stiffener tests. Table 36 gives a list of Mode I and II static and fatigue crack growth tests used to generate data for modeling of the T-sections.

The skin-stiffener T-section tests were based on the study in the previous section. The final geometry tested is shown in Figure 158, which is close to the "thin flange" geometry in the previous section. A variety of resin systems were used in the skin-stiffeners. A summary of the stiffener test matrix and motivations is presented in Table 37. The edges of the skin-stiffeners were polished to enhance the detectability of damage and crack growth.

Both static and fatigue tests were conducted using a high response, low force servo-hydraulic system (Instron model 8511). Slight modifications of the apparatus described in the previous section were required. A fatigue specimen under test is shown in Figure 159.

Table 36. Delamination Tests Conducted in this Section.

Series ID	Specimen Type	Layup	Crack Interface	Number of Tests	Motivation
6XX	DCB	$[\pm45/(0)_2/\pm45]_4$	(+45°/-45°)	14	static G_I test
	DCB			8	fatigue G_I test
7XX	DCB	$[(\pm45)_9/0/(\pm45)_8]$	(0°/+45°)	18	static G_I test
	DCB			8	fatigue G_I test
8XX	ENF			3	static G_{II} test
7XX - 8XX	ENF			14	fatigue G_{II} test
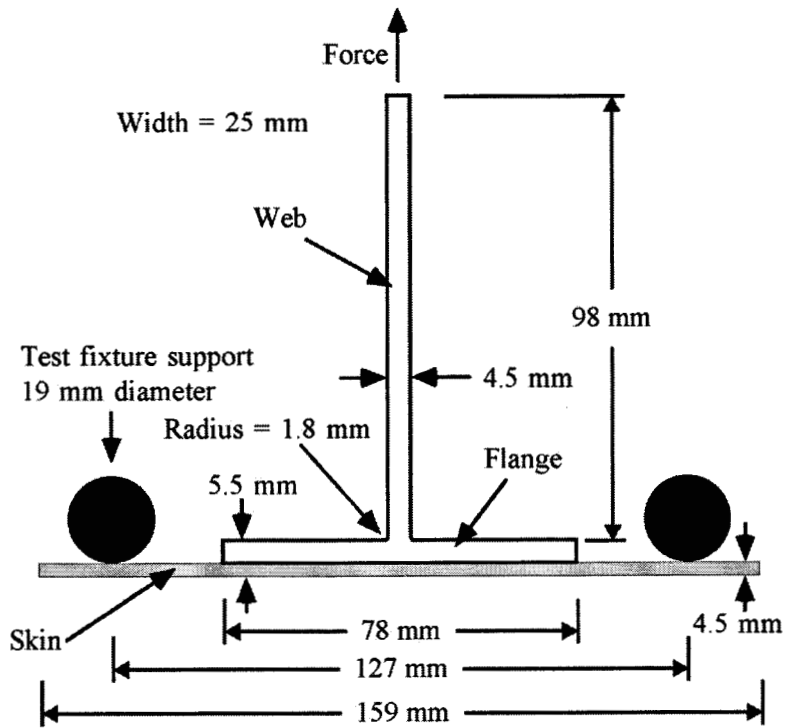
Figure 158. Skin-Stiffener Loading, Geometry and Dimensions.

Table 37. Summary of the Skin-Stiffener Tests.

Series ID	Resin	Layup (Web and Skin)	Number of Tests	Motivation
8TXX-10TXX	Ortho-polyester	$[(45/(0)_2/45]_S$	3	static test - initial damage and maximum load
8TXX-10TXX			17	fatigue
18TXX			6	static crack growth
11TXX	8084 Vinyl ester		3	static test - initial damage and maximum load
11TXX			8	fatigue
14TXX	Iso-polyester		3	static test - initial damage and maximum load
14TXX			8	fatigue
16TXX	411 Vinyl ester		3	static test - initial damage and maximum load
16TXX			9	static and fatigue

215
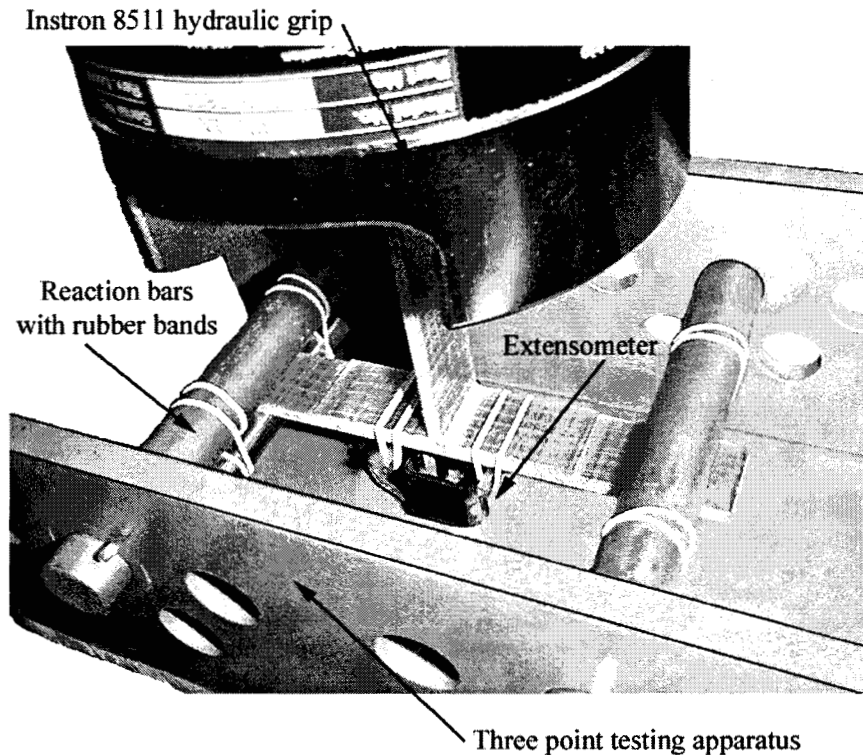
Figure 159. Typical Skin-Stiffener Fatigue Test.

Static tests were run by loading the top of the specimen at a constant displacement rate of 0.25 mm per second, yielding force-displacement curves similar to Figure 160, allowing identification of the initial damage load and the maximum load sustained. Fatigue tests were run at a low frequency of 2 to 4 Hz and an R-value of 0.1, with a sinusoidal waveform. Data for displacement, force, and strain in the skin were recorded periodically. The strain in the skin was measured with an extensometer positioned as shown in Figure 159. The specimens were inspected for damage by stopping tests after every 0.635 mm increase in the maximum displacement. Tests were continued until the maximum displacement increased by 5 mm compared with the first cycle, which corresponds to the range observed for initial damage development in static tests.

13.4. Numerical Methods and Failure Criteria

The delamination and skin-stiffener geometries were modeled using ANSYS FEA software and input elastic constants were described in the previous section. A plane strain analysis employing ANSYS plane 82 quadrilateral elements was used in the skin-stiffener models, which were also constructed using individual lamina layers and not smeared laminate properties. Half symmetry about the web of the stiffener was used to simplify the model by restricting the nodes along the mid-line to have zero X-displacement, shown in Figure 161. Three coordinate systems were constructed for the element generation of the first model. A coordinate system was developed for the web, bend region and the flange and skin regions. These coordinate systems were used to keep the orthotropic composite properties aligned with the local coordinate systems of the elements. Three material

216
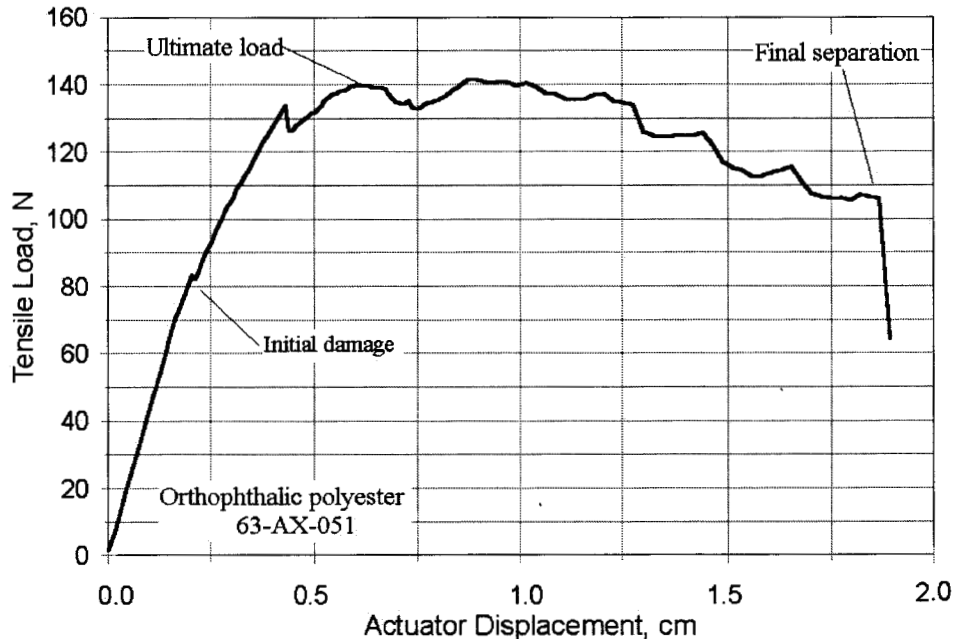
Figure 160. Typical Static Tensile Load versus Displacement Curve for a
Skin-Stiffener Specimen.

property sets were constructed from the ply properties listed in Tables 38 and 39. An orthotropic set
was constructed for each glass fabric (D155 and DB120) and one isotropic set (E=3.88 GPa, υ=0.36)
for the resin rich region between the web and stiffener, shown in Figure 162. The support from the
apparatus was modeled as a condition of no vertical y-displacement at a distance of 6.35 cm from the
web centerline. The vertical applied nodal force was normalized per unit width of the specimen and
applied to the top of the web.

Once initial damage was introduced within the FEA model, the skin-stiffener was no longer
symmetric. Thus, a full model was generated to represent the stiffener during crack propagation. Four
coordinate systems were constructed for the discretization of the full model. The three sets of
material properties that were used in the symmetric model were used in conjunction with the four
local coordinate systems. One to one element aspect ratios in the areas of high stress gradients were
implemented while low stress gradient areas had aspect ratios of three to four. Elements surrounding
the crack tip were highly refined to capture the stress gradients. A nonsymmetric mesh was used to
allow a very fine mesh only on the side where the nonsymmetric damage was present, reducing the
overall degrees of freedom by using a coarser mesh on the undamaged side.

The increase in aspect ratios in low stress gradient areas dramatically reduced the total number
of elements required for mesh generation. One disadvantage of modeling individual fabric layers is
that element heights cannot exceed the height of the fabric layers. The use of smeared properties
would eliminate this restriction. Much larger elements could then be used, which in turn would lower
the computational time. This skin-stiffener model was small enough that solving times

217

Table 38. Static Longitudinal, Transverse and Simulated Shear Properties for D155 and DB120 Ply Properties [2].
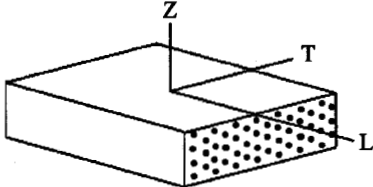
			Longitudinal Direction									Transverse Direction			
			Elastic Constants				Tension		Compression		Shear	Tension		Compression	
Fabric	layup	V_F %	E_L GPa	E_T GPa	υ_{LT}	G_{LT} GPa	UTS_L MPa	ϵ_U %	UCS_L MPa	ϵ_U %	τ_{TU} MPa	UTS_T MPa	ϵ_U %	UCS_T MPa	ϵ_U %
D155	$[0]_6$	45	35.0	8.99	0.31	4.10	987	2.83	-746	-2.02	97.7	27.2	0.32	-123	-1.67
DB120	$[0]_{16}$	44	26.6	7.52	0.39	4.12	610	2.49	-551	-2.08	84.9	24.9	0.33	-114	-2.00

Notes: E_L - Longitudinal modulus, υ_{LT} - Poisson's ratio, G_{LT} and τ_{TU} - Shear modulus and ultimate shear stress from a simulated shear (±45) ASTM D3518 test, UTS_L - Ultimate longitudinal tensile strength, ϵ_U - Ultimate tensile strain UCS_L - Ultimate longitudinal compressive strength, ϵ_U - Ultimate compressive strain. Coupons had a 13 mm gage length, DB120 fabric was separated into a $+45°$ and a $-45°$ orientation and then rotated to 0 degrees to form a unidirectional material.

were usually under five minutes on a Pentium 233 MHz machine. Smeared properties should be incorporated into larger 2-D or 3-D models with low stress gradient areas to minimize solution intervals. The final area and mesh configuration for the full model is shown in Figure 162.

The analysis of the specimens with FEA involved using the model without a crack to simulate initial behavior of the skin-stiffener in the elastic, undamaged state. High stress gradient regions were investigated at experimentally determined critical loads using the failure criteria described later. Delaminations were then inserted in the full non-symmetric stiffener model and G-values were calculated using the VCCT-1 method discussed in Chapter 9.4.

Table 39. Three-Dimensional Mechanical Properties of Material D155, $V_F = 36$ [2]

Property and test plane	Test Values	Average	Std. dev.
E_L, GPa (LT plane)	28.1, 27.0, 29.8	28.3	1.4
E_L, GPa (LZ plane)	28.0, 28.3, 27.6	28.0	0.4
E_T, GPa (TZ plane)	8.00, 7.31, 7.93	7.75	0.38
E_Z, GPa (ZX plane)	7.10, 7.65, 7.38	7.38	0.28
NU_{LT}	0.329, 0.320, 0.301	0.32	0.01
NU_{LZ}	0.305, 0.338, 0.331	0.33	0.02
NU_{TZ}	0.466, 0.395, 0.449	0.44	0.04
G_{LT}, GPa	3.31, 3.35, 3.23	3.30	0.06
G_{LZ}, GPa	3.03, 2.72, 2.70	2.82	0.19
G_{TZ}, GPa	2.78, 3.12, 1.76	2.55	0.71
UTS_L, MPa (LT plane)	891, 814, 883, 838	856	37
UTS_L, MPa (LZ plane)	679, 672, 685, 646	671	17
UTS_T, MPa (TZ plane)	26.6, 36.0, 30.4, 32.9, 29.0	31.0	3.6
UTS_Z, MPa (ZT plane)	21.7, 18.7, 20.4, 18.1	19.7	1.6
UTS_Z, MPa (ZL plane)	19.4, 17.7, 22.3, 17.1, 15.2	18.4	2.7
τ_{LT}, MPa	95.1, 82.1, 78.8	85.3	8.7
τ_{LZ}, MPa	79.6, 77.3, 77.1, 63.2	74.3	7.5
τ_{TZ}, MPa	19.9, 17.6, 12.0	16.5	4.0
Shear properties determined by V-notched beam (ASTM D5379)			

Load per unit width

Symmetric boundary
condition at web centerline

Y

Z

Web

Flange

Skin

Load pin contact
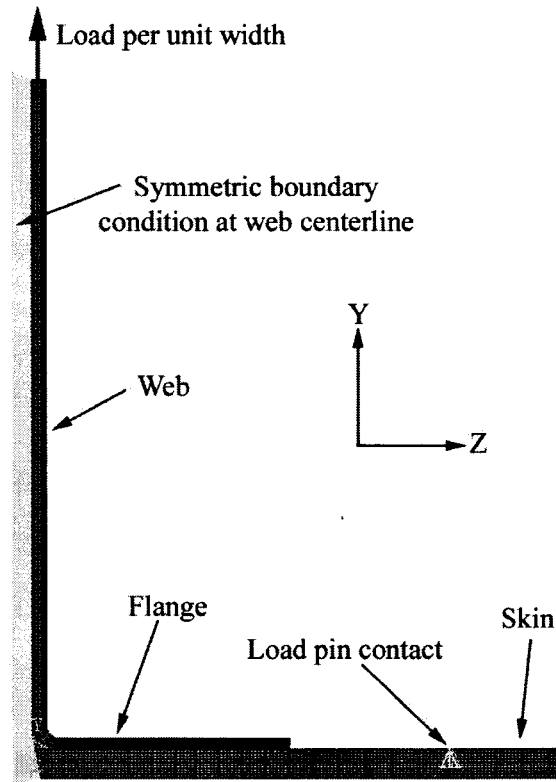
Figure 161. Symmetric Finite Element Model
for the Skin-Stiffener.

Coordinate
system #1

Coordinate
system #4

Coordinate
system #2

Resin rich
region

Coordinate system #3
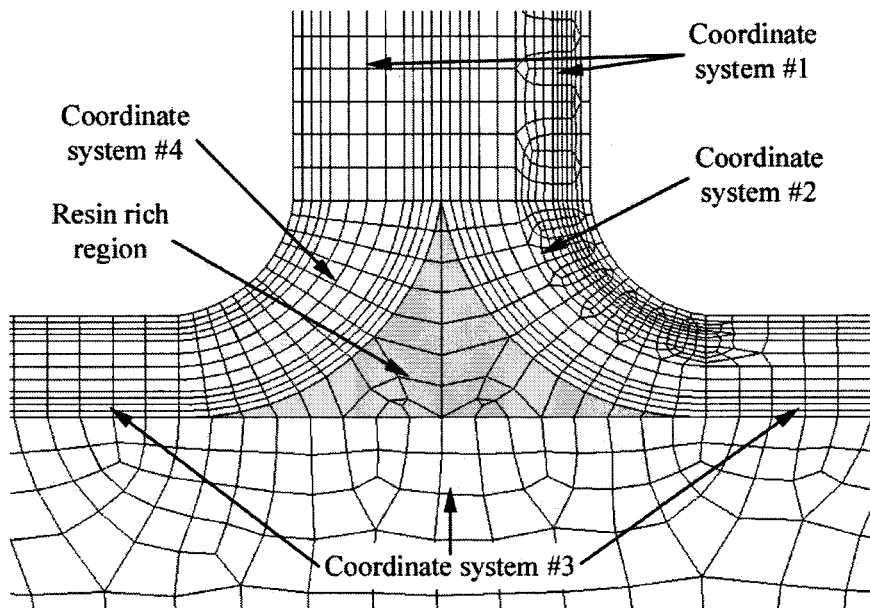
Figure 162. Coordinate System and Mesh for the Skin-Stiffener
Crack Propagation.

220

13.5. Results and Discussion

13.5.1. Static Tests

Static tests produced results similar to the previous chapter. Tests were run for all four matrices, yielding the typical load-displacement curves as described in the previous section. Tables 40 and 41 give data for the four resin systems used in this study. As noted in the environmental section, the resins with higher delamination resistance in Mode I and II tests (delamination section) give the highest loads for initial damage and maximum load. The data in Table 40 are for an entirely new set of tests fabricated and tested in this study. The data are in good agreement with those in Table 30, shown previously.

Damage in the ortho-polyester skin-stiffener is shown highlighted in Figure 163, and conditions for static damage in terms of crack initiation and delamination growth are given in Table 41.
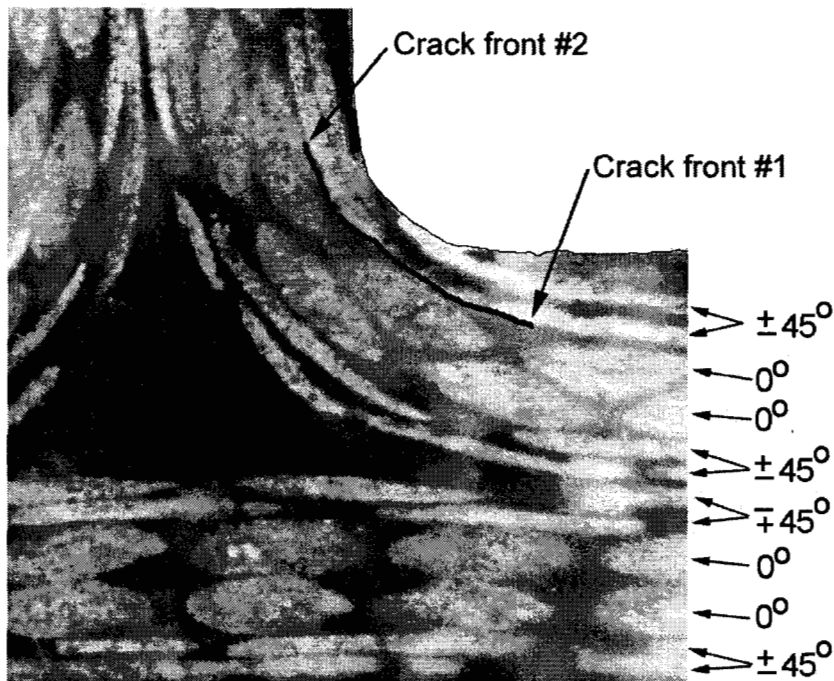
Figure 163. Location of Delamination and Nomenclature for Crack Fronts Under Static Loading (crack is in the 0° / 45° interface).

221

Table 40. Static Load and Crack Length Data for Ortho-Polyester Skin-Stiffeners; Parentheses indicate the standard deviation.

Initial Damage		Critical load for crack growth, N/cm	Number of tests
Load, N/cm	Crack length, mm		
94.9 (6.8)	2.48 (0.2)	129 (8)	6

Table 41. Average Load and Displacement Data for Different Resins in the Skin-Stiffener Geometry. Parentheses indicate the standard deviation.

Matrix	Initial damage load, N/cm	Maximum displacement at initial damage load, cm	Ultimate load, N/cm	Number of tests
Ortho-polyester	87.0 (5.9)	0.22 (0.02)	144 (2)	3
Iso-polyester	98.2 (2.2)	0.24 (0.01)	166 (1)	3
411 vinyl ester	144 (61)	0.44 (0.24)	198 (1)	3
8084 vinyl ester	189 (26)	0.48 (0.08)	221 (11)	3

As the structure was loaded for the second time, the upper crack front (crack front #2) grew toward the web in the 0°/45° interface. The lower crack front (crack front #1) grew transversely through the 0° ply and arrested. Similar delamination locations and growth for ortho-polyester skin-stiffeners were reported in the previous section. Note that the crack front #2 is in the 0°/45° interface, but growing in the 90° direction. This corresponds to an ENF or DCB test with the crack in a 90°/45° interface (see delamination section).

13.5.2. Fatigue Tests

Once a static baseline had been established for the skin-stiffeners, cyclic loading was investigated. Two series of cyclic tests were performed. The first series of tests used the ortho-polyester matrix material to determine initial damage location, rate of damage accumulation, change in structure stiffness, change in maximum bending strain and cycles to failure at specific load levels. The second series of fatigue tests were performed on skin-stiffeners with different resins to observe cycles to failure at specific load levels.

Damage propagation was determined in detail for skin-stiffeners with the ortho-polyester resin. An initial, audible, crack similar to that observed at initial damage in static tests occurred in the fillet area between the web and the flange for the fatigue specimens during the period of the cyclic test (crack #1) shown in Figure 164.

The upper crack front (step #2) grew into the web region but stayed in the 0°/45° interface. The lower crack front (step #3) grew transversely through the 0° ply and arrested. It is believed that

222

the load paths changed within the stiffener when the crack grew transversely through the 0° ply. When the transverse crack appeared, additional transverse cracks occurred at the (martix/45°) interface (crack #2). A delamination then propagated between the flange and skin ±45° interface causing a significant increase in compliance which resulted in stiffener/flange pull-off.

As damage accumulated within the bend region, a reduction in specimen stiffness occurred. This resulted in an increase in the maximum actuator displacement as shown in Figure 165. As the compliance of the stiffener increased, the maximum bending strain in the skin showed a similar trend. The fatigue crack growth rate, da/dN, was obtained from crack growth observations during testing using a scaled magnifier. G values were determined using FEA VCCT stiffener models. Crack growth per cycle (da/dN) versus G_{max} is shown in Figure 166, where G_{max} was determined by FEA.
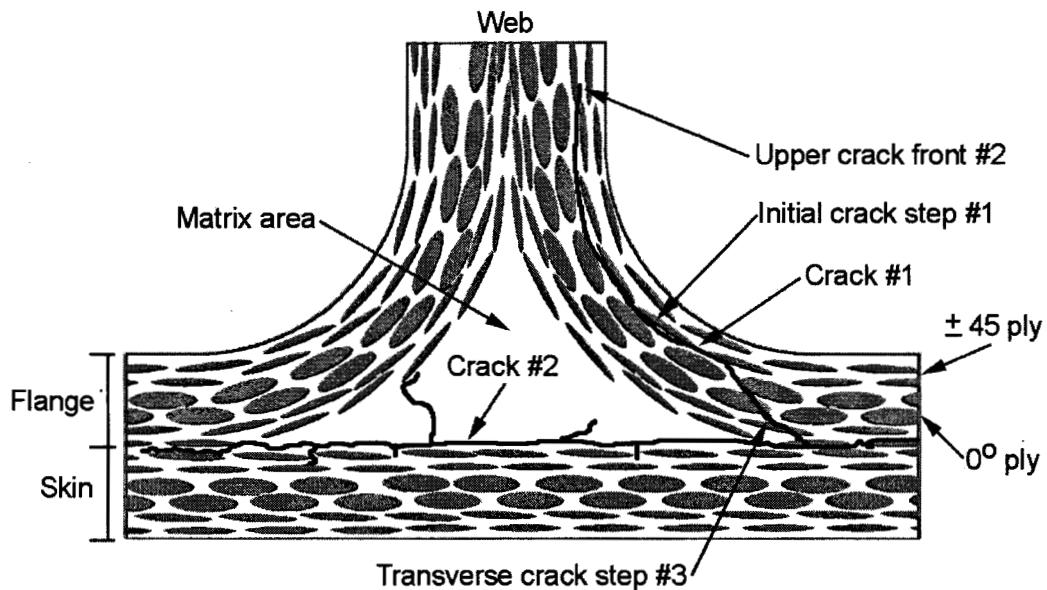
Figure 164. Skin-Stiffener Crack Sequence During Fatigue Loading.

223
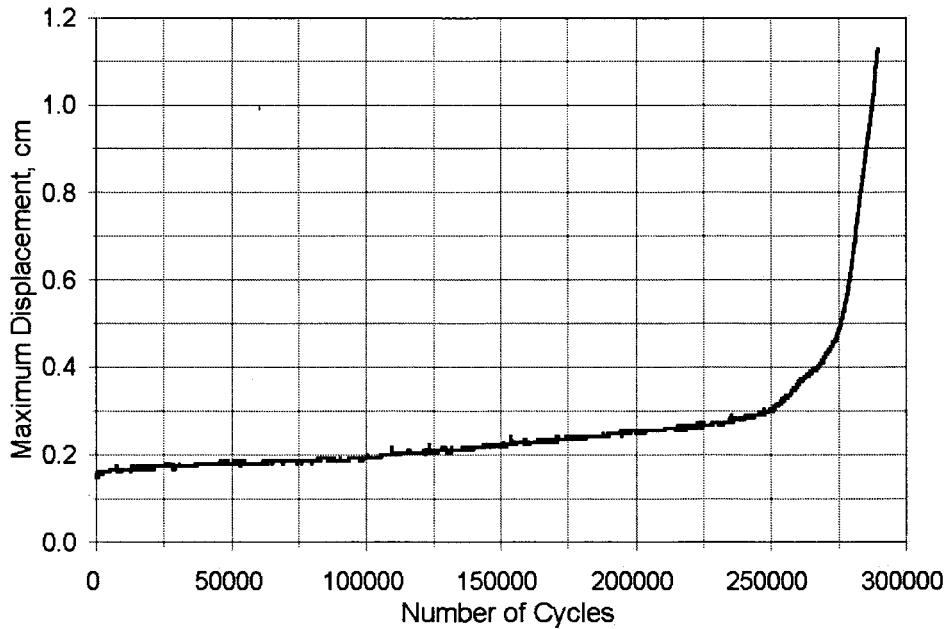
Figure 165. Skin-Stiffener Maximum Cyclic Displacement versus Number of Cycles.
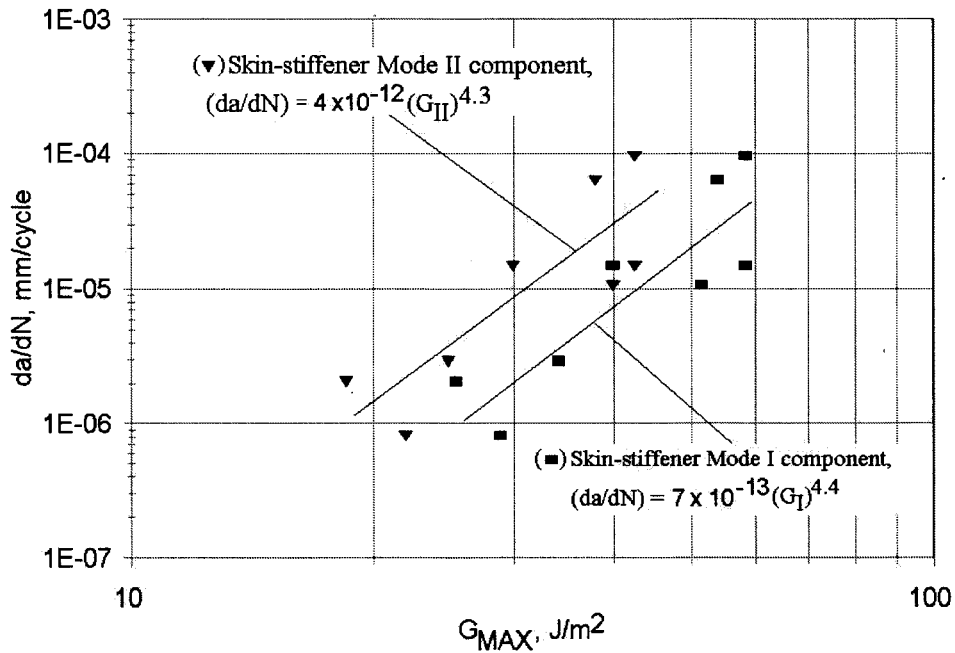
Figure 166. Fatigue Crack Growth Rate versus G_{max} in the $0°/45°$ Interface of Ortho-Polyester Skin-Stiffeners.

224

13.6. Correlation of Predicted and Experimental Results

Finite element analysis was conducted on the relevant geometries as described earlier. Local strength and delamination criteria based on test data were implemented with the FEA results to predict the onset of growth of damage, first in static tests and then in fatigue tests. Methodologies for damage prediction were established.

13.6.1. Delamination Modeling

To validate the FEA procedures for damage analysis, they were first applied to the simpler Mode I DCB delamination test geometry. Both 2-D and 3-D models were used with the virtual crack closure method (VCCT-1) in the ANSYS software (described earlier).

The FEA calculations were validated against the Mode I delamination test data for the $[(\pm 45)_9/0/(\pm 45)_8]$ laminate. This established the FEA mesh sizes which gave accurate results at delamination cracks. Test specimen DCB870 was used as the basis for the model, and the G_I values calculated by the VCCT-1 method. For the 3-D case, the G value was averaged across the width of the crack front, as it varies with position (see Reference 40 for details).

13.6.2. Skin-Stiffener Models

The skin-stiffener was modeled in ANSYS as described earlier. The goals of the skin-stiffener modeling were to predict static linear displacements, initial damage load and location using a maximum strain failure criterion. After the initial damage load and location were known, the determination of the critical load to propagate the "pop-in" crack was of interest. Finally, determination of fatigue life at specified loads was to be analyzed and predicted using Mode I and II input data. The bend region of the skin-stiffener was the prime area of interest. This was the damage initiation site for both the static and cyclic tests.

13.6.3. Static FEA Prediction versus Experimental Results

The symmetric half model of the skin-stiffener was incrementally loaded with no damage to confirm the stiffener experimental linear displacement and bending strains. A plot of load versus displacement for the experimental specimen and FEA model were in good agreement, as in the study reported in the previous section. Once displacements and strains were confirmed using the FEA model, initial failure analysis was performed to determine the local failure location and load to initiate damage. Experimental observations showed that delaminations occurred at the 0°/45° interface, with the crack growing in the 90° direction. The strains in the bend region were calculated using a load of 1 N per cm of width. Since the model was a linear elastic analysis, the strains were scaled until failure occurred using the maximum strain criterion for the data in Table 42. Before strain results could be extracted from the model, the output was viewed in the cylindrical coordinate system used to create the stiffener bend region. Typical contour plots in the bend region for the tangential and radial strains are presented in Figures 167 and 168 respectively. The strains were rotated from the global coordinate system to the local cylindrical coordinate system so strains were tangent and normal to the bend radius.

Table 42. Comparison of Predicted Initial Damage Load Using
the Maximum Strain Criterion with Experimental data.

Ply	Maximum strain criterion initial damage load, N/cm	Average experimental initial damage load, N/cm	Percent difference
45°	82.6	94.9	13
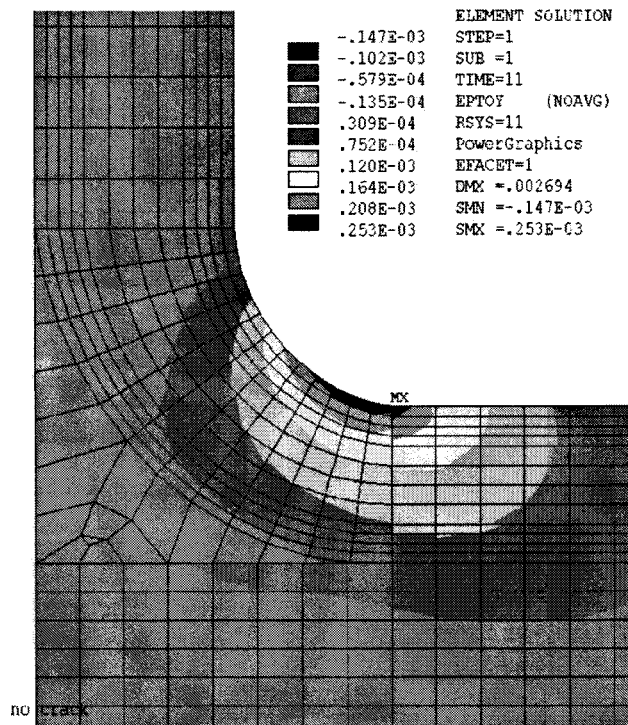
Figure 167. Skin-Stiffener Tangential Strain Plot at
the Bend Region (no crack).

226
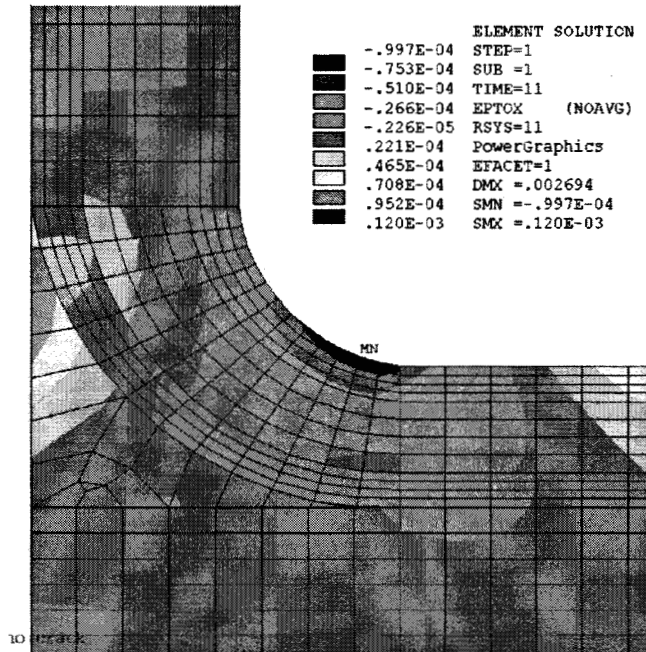
Figure 168. Skin-Stiffener Radial Strain Plot at the Bend Region (no crack).

In the bend region local coordinate system, the (x) direction was the radial direction, the (y) direction was tangent to the bend radius and the (z) direction was orthogonal to (x) and (y). The maximum strain criterion predicted an initial damage load of 82.6 N/cm. The transverse tensile failure occurred in the bend region 45° ply due to interlaminar radial stresses. The predicted damage load was 13 percent lower than the experimental value. This is considered to be acceptable accuracy given the complicated damage state. A combined stress or strain criterion could also have been employed, but the results would have been similar.

Once the initial damage location was determined, the nonsymmetric (full) model was analyzed using a crack length of 2.48 mm inserted between the 45°/0° plies and an applied load of 129 N/cm. The crack used in the model was the observed experimental static "pop-in" crack length. A typical plot of the tangential stress field in the bend region is shown in Figure 169. In reference to all cracks in the skin-stiffener model, crack front #1 is the lower crack tip extending toward the stiffener flange tip. Crack front #2 is the crack tip extending toward the stiffener web section. FEA results for G_I and G_{II} at the critical load for crack growth are compared in Table 43 with experimental G_{IC} and G_{IIC} from DCB and ENF delamination tests. The G_{IC} value used is that from the R-curve in Figure 100 at a crack extension of 2.48 mm. The cracks in the skin-stiffener are mixed-mode, with both G_I and G_{II} components. The values of G_I and G_{II} calculated by FEA for the skin-stiffener delamination crack at the load which produced crack growth are far below the G_{IC} and G_{IIC} values from the DCB and ENF tests for the same ply interface. This is in contrast to the case for a similar size crack at the end of the flange in the previous section. In that case, the interface cracked was 0°/0° and 45°/-45°, with the crack growing in the 0 direction. The value of G_{IC} in that case was much lower, in the range of 140 J/m², similar to the calculated value for the skin-stiffener here. Thus, there may be some problem

227

introduced by the use of R-curve values of G_{IC}. The initial G_{IC} values for the 90°/45° interface ranged from 132 to 261 J/m^2, close to the values calculated for the skin-stiffener G_I.

Table 43. Strain Energies for a Load of 129 N/cm and a 2.48 mm Long Crack in The Bend Region of Skin-Stiffener Compared with G_{IC} and G_{IIC} Delamination Test Data.

Mode I and II delamination data (for a 90°/45° Interface Crack)		Mode I and II energies at critical load for delamination growth in skin-stiffener, by FEA	
G_{IC}, J/m^2	G_{IIC}, J/m^2	G_I, J/m^2	G_{II}, J/m^2
342*	941	143	101

* This value was determined from the curve fit of the R-curve data in Figure 101, taken at a crack extension of 2.48 mm.
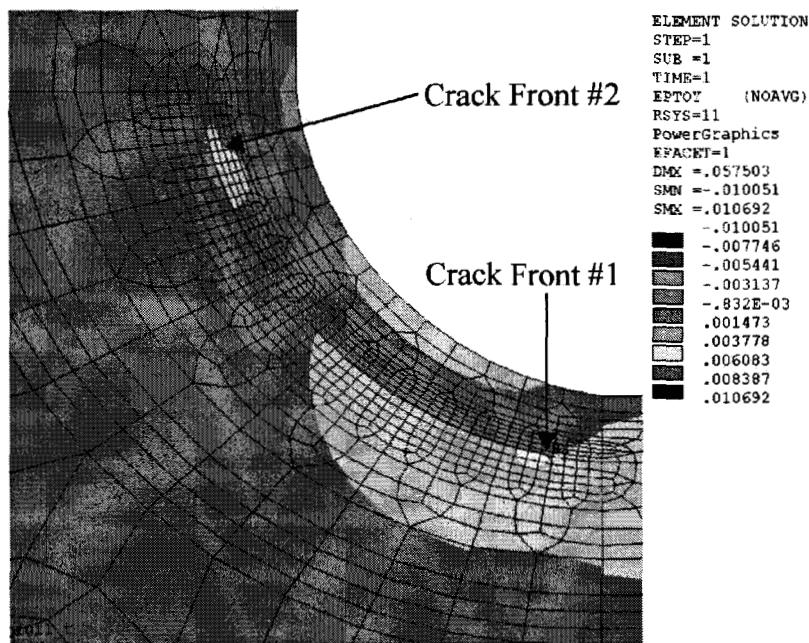
Figure 169. FEA Tangential Strain Plot with Crack Front Locations.

To explore the apparently very low G values for the skin-stiffener relative to R-curve values, the use of a mixed-mode criterion for crack growth has been investigated. The skin-stiffener G values shown in Table 43 were inserted into Equation 17 using exponents of 1 (m = n = 2) and 1/2 (m = n = 1) to determine F. For crack growth to occur, recall that the sum of the two ratios, F, must be greater than or equal to one.

The values of G_I and G_{II} in any elastic solution vary with the force squared [75]. This was

228

confirmed in the present study by running the VCCT model at different force levels; details are given in Reference 40. The assumed variation of G_I and G_{II} with P^2 for a specified crack length fit the FEA results accurately. This demonstrates that a crack model can be run with an arbitrary applied load (P_{model}), and G values can then be determined using the mode interaction criterion in Equation 17. The interaction sum F then can be used to scale the load applied to the model (P_{model}) to determine the critical load (P_{cr}) that will propagate the crack. The sequence of events used in determining the critical static load that initiates crack growth for the skin-stiffener is shown in Figure 170 (represented here in terms of a "design" sequence). Due to the uncertainty in using R-curve data for G_{IC}, a second method, termed Method B, was to calculate the mode interaction using a conservative value for G_{IC} taken from initiation results for a 0°/0° interface in the previous section.

Using m and n values of 2 and 1 in Equation 17, and the R-curve G_{IC} value (Method A), the interaction sums F were 0.56 and 0.98 respectively, shown in Table 44. This resulted in predicted crack propagation loads of 173 and 130 N/cm respectively. This analysis shows that exponents for m=n=1 seem to correlate well with the experimental data. A difference of 1.2 percent from the experimental critical propagation load of 129 N/cm was obtained with ratio exponents m = n = 1, compared to a difference of 34 percent with ratio exponents of m = n = 2. However, as noted earlier, the DCB G_{IC} of 342 J/m2 was taken from an R-curve (Figure 101) at the observed 2.48 mm crack extension. Had the initiation G_{IC} values from the DCB tests, ranging from 132 to 261 J/m^2, with an average of 191 J/m^2, been used, the prediction with m=n=2 would have been much closer, as was the case in the previous section. If, as in Table 22, crack extensions up to 2 mm were allowed for the initiation G_{IC}, the average value would increase to 273 J/m^2. Thus, the use of R-curve values to represent initial crack formulation in a substructure may not be justified. If a conservative initiation value of G_{IC} is used, taken as the G_{IC} for initiation in a 0°/0° interface (Method B), then values of m=n=2 in Equation 17 are appropriate. the choice of G_{IC} definition from DCB tests is particularly sensitive for interfaces containing a 90° ply, as noted in the delamination section. Thus, if the G_{IC} for initiation in a 0°/0° interface is used, good agreement is found for the force prediction using m=n=2 in Equation 17, the same conclusion as for delamination at the edge of a thick flange in the previous section. This also agrees with the observed crack in the T-section (Figure 163), which shows no secondary cracking, like a 0°/0° interface.

13.6.4. Fatigue FEA Prediction versus Experimental Results

The same skin-stiffener model was used to predict behavior for the fatigue loading tests. Experimental observations showed that delaminations occurred in the (0°/45°) interface. The non-symmetric model was analyzed with various crack lengths to investigate the mode interaction as crack front #2 propagated toward the web. Crack lengths in the fatigue model were varied from 1.2 mm to 9.0 mm to determine mode interactions for various crack lengths in the bend region. A plot of G versus crack length for crack front #2 is shown in Figure 171. G_I varied from 55 percent to 99 percent of the total G (G_T) for crack lengths from 1.2 mm to 9.5 mm as shown in Figure 171. The crack front becomes mode I dominated as the crack progresses around the bend region toward the web of the stiffener.

Table 44. G-Values, Interaction Sums and Predicted Critical Loads for the FEA Skin-Stiffener Model. Method A uses G_{IC} from R-curve data at a crack length of 2.48 mm; Method B uses G_{IC} initiation data for a 0°/0° Interface.

		Method A	Method B
G_{IC} and G_{IIC} from DCB and ENF Tests	G_{IC}, J/m^2	341.8	138
	G_{IIC}, J/m^2	941.3	1293
G_I and G_{II} at the critical load from FEA	G_I, J/m^2	143.1	143.1
	G_{II}, J/m^2	101.4	101.4
Experimental critical load, N/cm		128.6	128.6
F, Linear exponent ratios, m=n=2 (Equation 17)		0.56	1.12
Predicted critical load, N/cm		172.6	122
F, 1/2 exponent ratios, m=n=1 (Equation 17)		0.98	1.30
Predicted critical load, N/cm		130.2	113

A similar methodology to that used to predict critical static loads was used to determine the cyclic crack growth rate of the skin-stiffeners at a specified load level. Three specific experimental cases were investigated that were run at various load levels resulting in various crack growth rates (da/dN). The experimental skin-stiffener specimens were 9T9 and 10T3. The average crack length, DCB and ENF experimental G_I and G_{II}, and FEA G_I and G_{II} are shown in Table 45.

The DCB and ENF G values were obtained from the inverse of the power law curve-fit Equation 17 (Figures 171 and 172) relating G and (da/dN) for the DCB and ENF specimens. In Equation 17, if the sum of the two ratios F is equal to one, it is assumed that crack growth will occur at the chosen rate (da/dN). Since G is proportional to P^2, the load can be scaled by F to obtain the predicted load for the selected growth. Ratio sums F, predicted load, crack length, crack growth rate and experimental load are presented in Table 46.

When the normalized G_I and G_{II} components of the skin-stiffener are compared to the individual mode tests (DCB and ENF), the Mode II -G components (Figure 173) possess similar slopes but very different G_{II} values. The Mode I - G component (Figure 174) of the stiffener gives approximately half the exponent of the DCB Mode I test, but the G_I values are closer together than are the G_{II} values. These discrepancies may be due to geometric effects since the stiffener crack is in the bend region. The interaction term (F) which correlates the data best is 0.5 (m = n = 1), the same as for the static case using R-curve values (Method A).
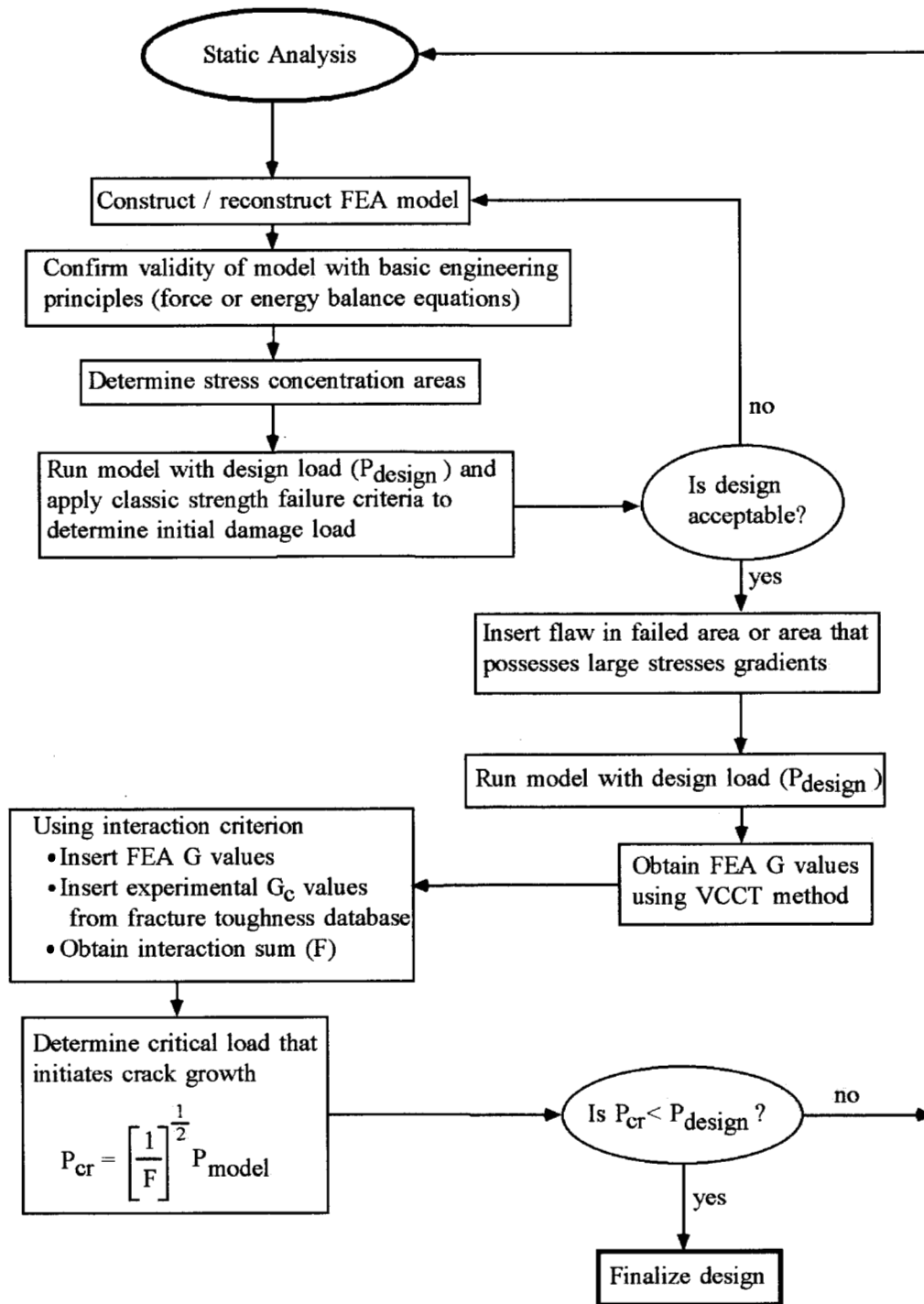
Figure 170. Sequence of Events for Static Analysis of Skin-Stiffener.

Within the figure, the following text appears:

Static Analysis

Construct / reconstruct FEA model

Confirm validity of model with basic engineering principles (force or energy balance equations)

Determine stress concentration areas

Run model with design load (P_{design}) and apply classic strength failure criteria to determine initial damage load

Is design acceptable?

no

yes

Insert flaw in failed area or area that possesses large stresses gradients

Run model with design load (P_{design})

Obtain FEA G values using VCCT method

Using interaction criterion
• Insert FEA G values
• Insert experimental G_c values from fracture toughness database
• Obtain interaction sum (F)

Determine critical load that initiates crack growth

$$P_{cr} = \left[\frac{1}{F}\right]^{\frac{1}{2}} P_{model}$$

Is $P_{cr} < P_{design}$?

no

yes

Finalize design

The sequence used in determining the critical fatigue load that produces a particular value of crack growth rate in the skin-stiffener is shown in Figure 175, again cast in terms of design. The overall lifetime would then require integration of the crack growth rate as the crack extends to failure in a particular geometry. For example, a growth rate of 10^{-6} mm/cycle would produce a 2 mm long delamination in 2×10^6 cycles if the G values remained constant as the crack grew, which is in approximate agreement with Figure 175. For design, it may be significant to identify force levels which produce crack growth at a significant rate, like 10^{-6} mm/cycle, rather than to integrate the rate for complex, changing geometries, to predict total failure.
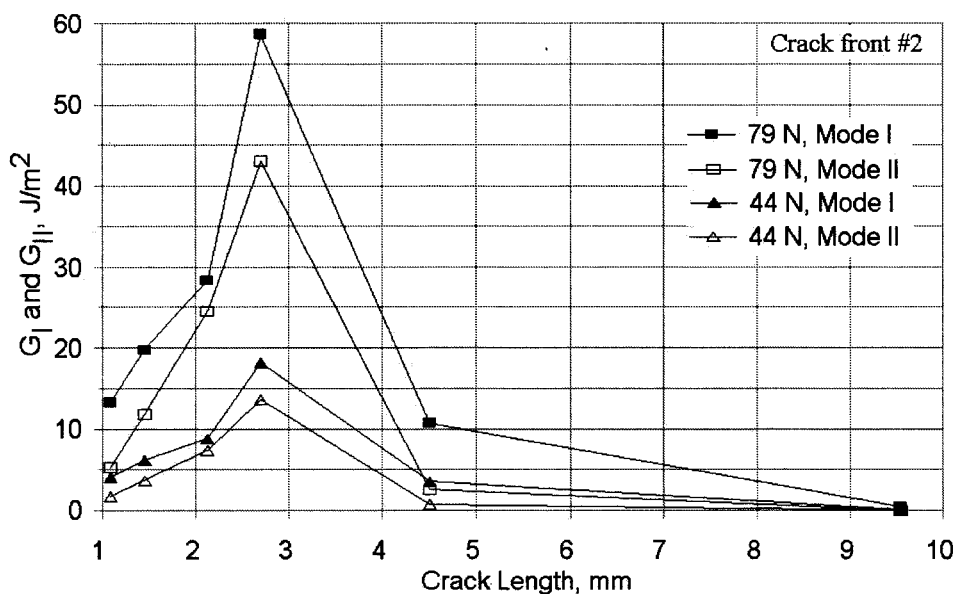
Figure 171. G_I and G_{II} versus Crack Length for Crack Front #2, at two loads.
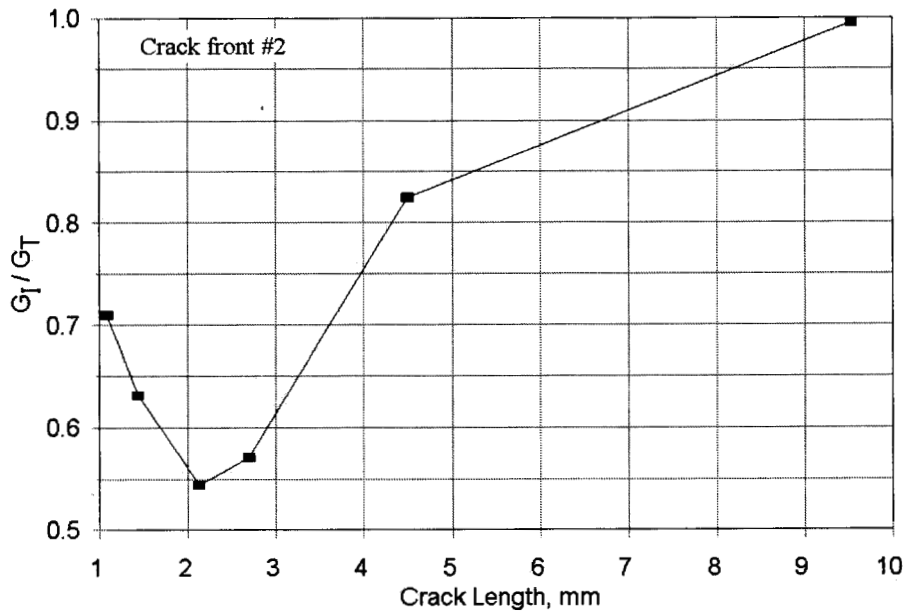
Figure 172. Normalized G_I/G_T versus Crack Length for Crack Front #2 in the Bend Region.

Table 45. Strain Energies and Crack Lengths for DCB and ENF Crack Growth Compared with Skin-Stiffener Values at the Same Crack Growth Rate.

Specimen	Crack growth rate (da/dN), mm/cycle	Crack length, mm	Corresponding G_I and G_{II} from DCB and ENF data at given (da/dN), J/m²		Skin-stiffener calculated G_I and G_{II} from FEA, J/m²	
			G_I	G_{II}	G_I	G_{II}
9T9	8.09×10^{-7}	2.4	62.9	119	25	20.3
10T3	9.47×10^{-5}	2.8	113.8	289.3	58.5	42.5
10T3	6.31×10^{-5}	2.9	107.9	268.2	54	38.3

Table 46. Experimental and Predicted Loads for Different Crack Growth Rates in the Bend Region of Cyclic Loaded Skin-Stiffeners.

Specimen	Crack length, mm	da/dN, mm/cycle	Ratio sum (F)		Experimental load, N/cm	Predicted load, N/cm (m,n = 0.5)	error, %
			m, n = 1	m, n = 0.5			
9T9	2.4	8.09×10^{-7}	0.57	1.04	61.3	60.1	2.0
10T3	2.8	9.47×10^{-5}	0.66	1.09	78.8	75.5	4.2
10T3	2.9	6.31×10^{-5}	0.64	1.10	78.8	75.1	4.6

233

The method described above is, as in the static case, complicated by use of growing cracks with secondary cracking in some cases. This is difficult to avoid with fatigue cracks, where true initiation values are difficult to establish. A more simple and conservative approach is to base substructure design on threshold values for fatigue crack growth. Figures 102 and 103 show that threshold values of $G_{IC}/10$ and $G_{IIC}/10$ would fall below the data for the slowest crack growth which could be measured. This is also consistent with threshold data in References 50, 98 and 99. As in Method B for the static case (Table 44), where G_{IC} and G_{IIC} were taken as initiation values for cracks in 0°/0° interfaces, this method, using G_{IC} and G_{IIC} values for a 0°/0° interface (Table 44) and m=n=2, using Equation 20, predicts a load of 38.6 N/cm for no fatigue crack extension (Table 47). This is well below the experimental load for the slowest cracks observed (Table 46) of 61.3 N/cm, and is about 30 percent of the experimental static crack growth load. This appears to be a practical method of fatigue design against delamination in structural details. A higher value like $G_{IC}/5$ and $G_{IIC}/5$ might be more accurate, and appears to be justified for fabric type structures [99]; this would give a critical load of 54.5 N/cm, which is less conservative.

Table 47. Results of Simplified Method for Prediction of Conservative Load for Safe Fatigue Design.

G_{IC} (DCB, 0°/0° Interface Initiation Value), J/m^2	138
G_{IIC} (ENF, 0°/0° Interface Initiation Value), J/m^2	1293
$G_{IC}/10$, J/m^2	13.8
$G_{IIC}/10$, J/m^2	129.3
Predicted Load, N/cm	38.6
$G_{IC}/5$, J/m^2	27.6
$G_{IIC}/5$, J/m^2	258.6
Predicted Load, N/cm	54.5
Lowest experimental load where fatigue crack growth is observed, N/cm	61.3

An adjustment to Equation 17 for this case is:

$$F_F = \frac{G_{IC}/(5 \, or \, 10)}{G_I \, model} + \frac{G_{IIC}/(5 \, or \, 10)}{G_{II} \, model} \qquad (20)$$

where

$$P_F = (\frac{1}{F_F})^{1/2} P_{model} \; ; \; P_{model} = 129 \; N/cm, \; G_{I \, model} = 143 J/m^2 \; ; \; G_{II \, model} = 101 \; J/m^2$$

and P_{model} is the static experimental load for delamination, G_{Imodel} and $G_{IImodel}$ are the FEA values at this

234

load. Alternately, any load applied to the model containing a crack could be used, with FEA values for G_I and G_{II}.
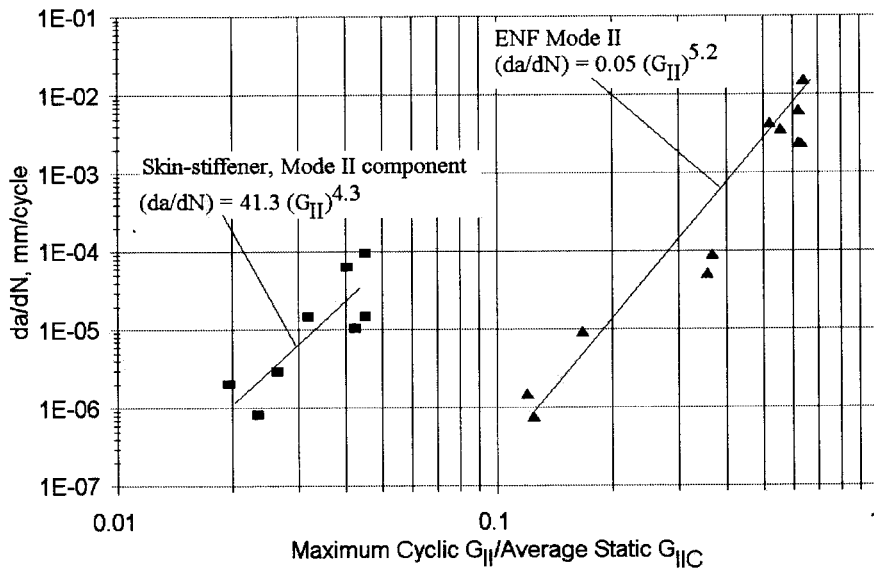
Figure 173. Crack Growth Rate versus $G_{II\ Component}$, Skin-Stiffener Specimen Compared with ENF Specimen.
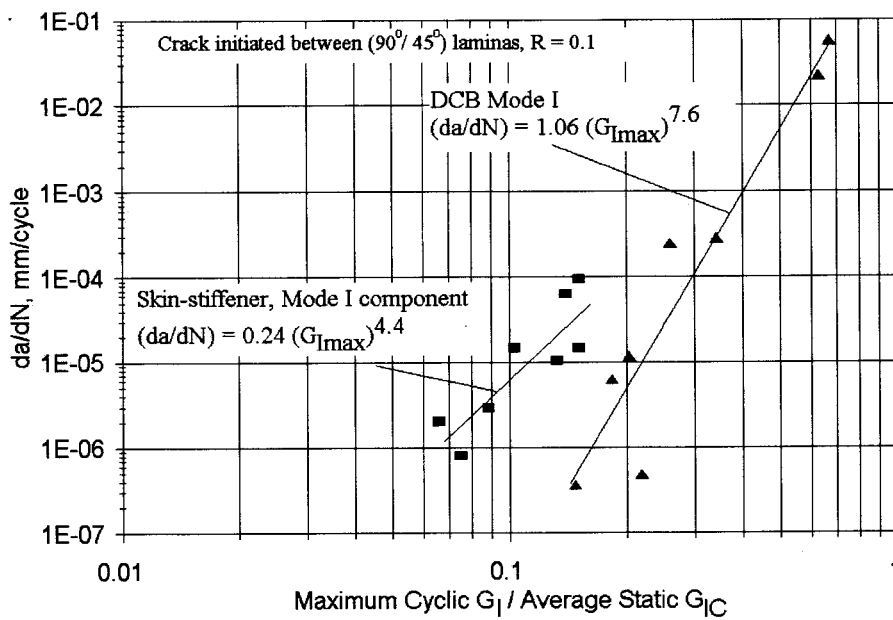
Figure 174. Crack Growth Rate versus $G_{I\ Component}$, Skin-Stiffener Specimen Compared with ENF Specimen.
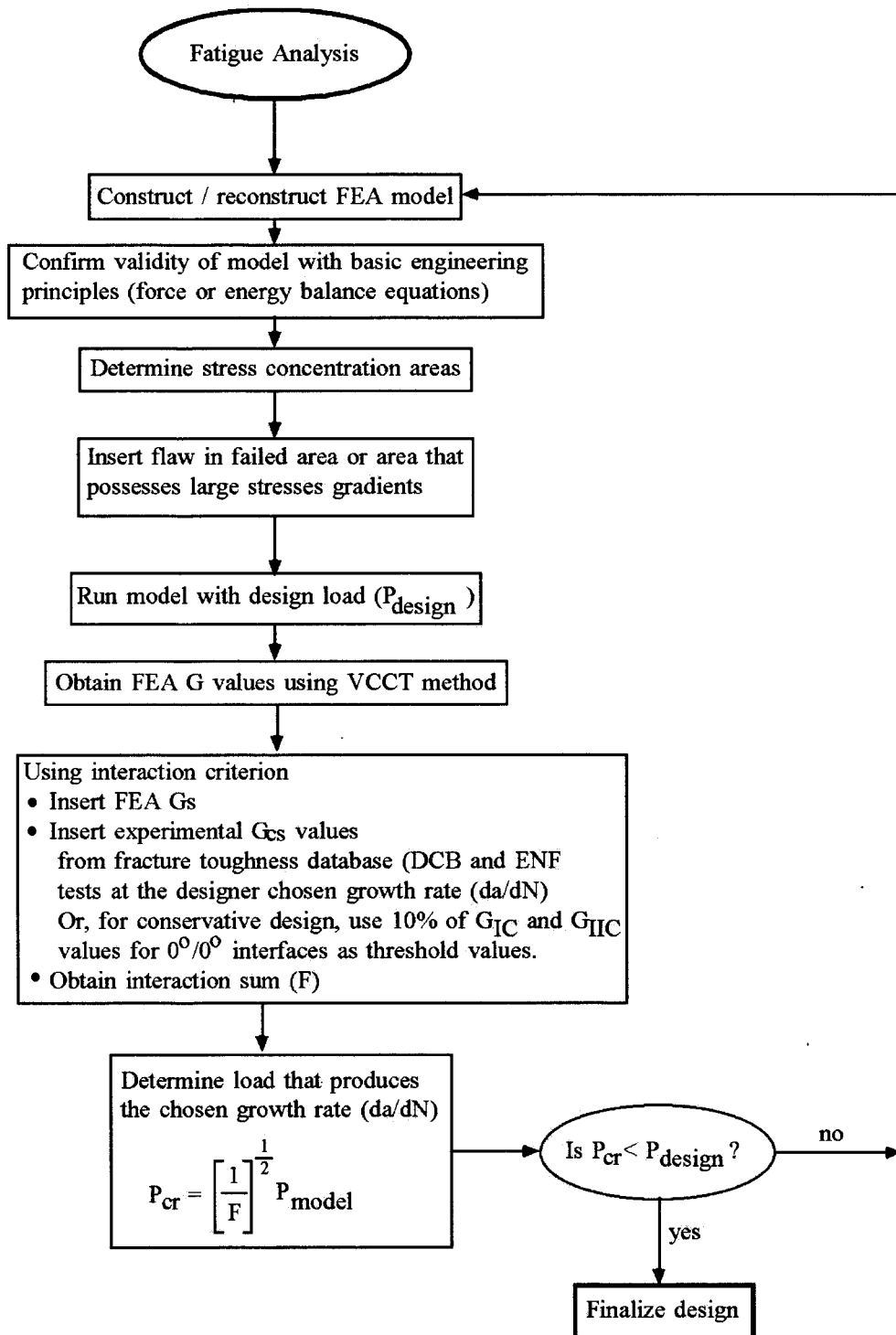
Figure 175. Sequence of Events for Fatigue Crack Growth Analysis.

The flowchart contains the following elements:

- Fatigue Analysis
- Construct / reconstruct FEA model
- Confirm validity of model with basic engineering principles (force or energy balance equations)
- Determine stress concentration areas
- Insert flaw in failed area or area that possesses large stresses gradients
- Run model with design load (P_{design})
- Obtain FEA G values using VCCT method
- Using interaction criterion
  - Insert FEA Gs
  - Insert experimental Gcs values from fracture toughness database (DCB and ENF tests at the designer chosen growth rate (da/dN) Or, for conservative design, use 10% of G_{IC} and G_{IIC} values for $0°/0°$ interfaces as threshold values.
  - Obtain interaction sum (F)
- Determine load that produces the chosen growth rate (da/dN)
  $$P_{cr} = \left[\frac{1}{F}\right]^{\frac{1}{2}} P_{model}$$
- Is $P_{cr} < P_{design}$? — no
- yes
- Finalize design

13.7. Fatigue Lifetime with Different Resins

Skin-stiffeners were tested in fatigue with the additional three resin systems (see Table 41 for static data). Damage initiation was similar in mode for all of the systems tested. All cracks formed in the 0°/45° interface and propagated in a manner similar to the fatigue crack growth in the ortho-polyester stiffeners. The criterion used for specimen failure was defined as reaching a maximum cyclic deflection of 0.43 cm. This was the displacement for initial damage for the static ortho-polyester skin-stiffener specimens. Thus, the lifetimes given are for a displacement failure criterion which correlates with damage development, as confirmed experimentally for each system.

The maximum cyclic load versus number of cycles to failure is plotted for each of the matrix materials in Figure 176. The vinyl esters operated at the highest maximum loads to equivalent cycles to failure when compared to the three other matrix materials. The 8084 vinyl ester produced the largest initial and maximum loads during the static load tests, and also performed the best on an absolute load scale during fatigue testing. However, when the fatigue sensitivity is viewed relative to the static performance by normalizing the cyclic loads by the static failure load, the order reverses. Now the 8084 system shows the most rapid loss in load carrying ability relative to its static strength (Figure 177). Also demonstrated in Figure 177, the polyester resin system can operate at higher percentages of the maximum static load when compared to the vinyl ester resin systems.
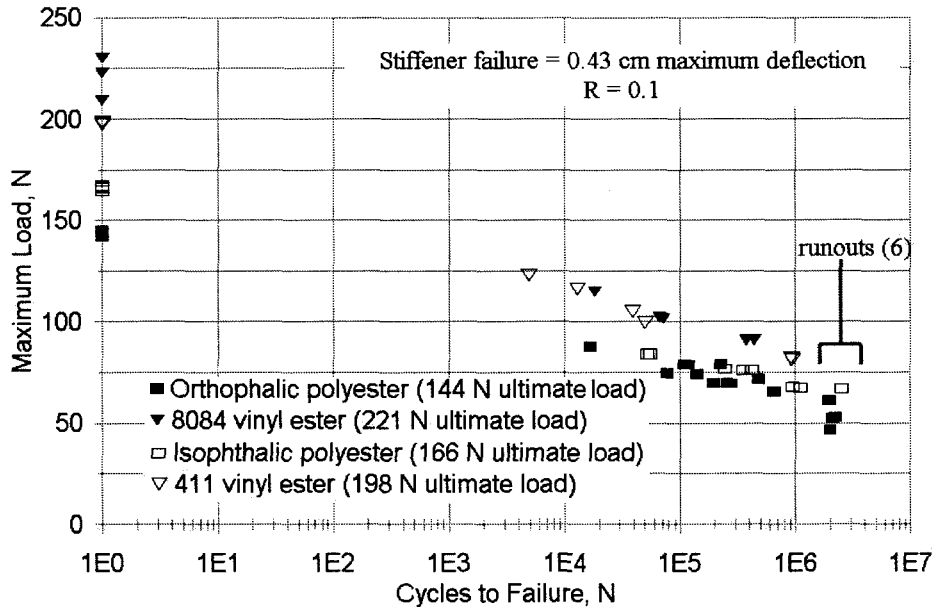
Figure 176. Comparison of Different Matrix Materials in Fatigue Life S-N Data for Skin-Stiffeners. (Maximum Cyclic Load versus Number of Cycles to Reach a Deflection of 0.43 cm).

237
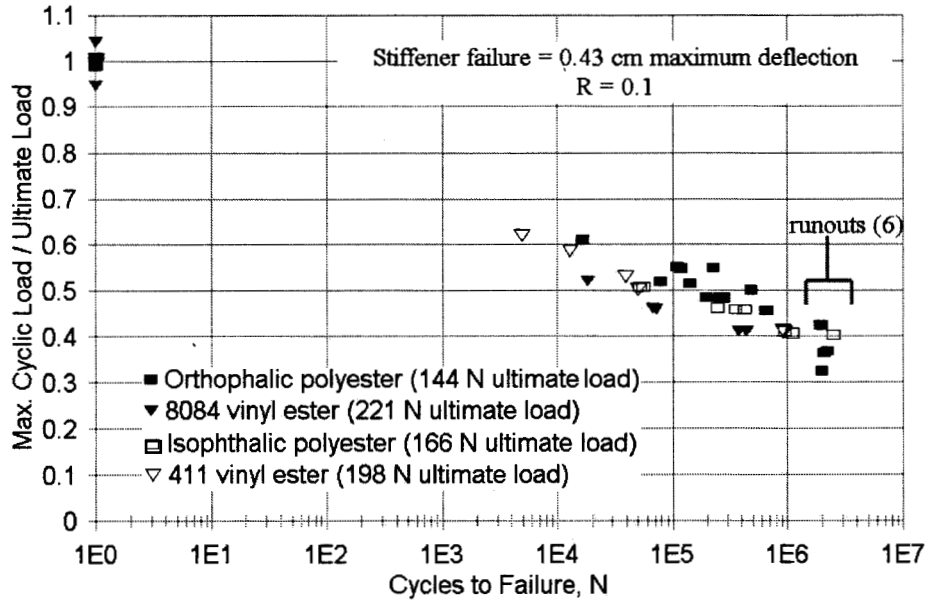
Figure 177. Maximum Cyclic Load / Ultimate Monotonic Load versus Number of Cycles to Reach a Deflection of 0.43 cm.

13.8. Conclusions

This section reports on a study which represents the first complete attempt in this program to predict initial cracking and delamination failure in a complex structural detail under both static and fatigue loading. The use of a commercial finite element code combined with basic strength data for damage initiation and fracture and fatigue crack growth data for delamination yields predictions for the load carrying capability of the structural detail which are in substantial agreement with experimental data, if a reasonable mixed mode delamination criterion is assumed. Methodologies for static and fatigue design of details are presented. Further work on mixed mode criteria and other geometries is needed to further validate this approach. A simplified, conservative approach is to use G_{IC} and G_{IIC} values for initiation in a 0°/0° interface, and threshold values of 10 percent of these for fatigue, coupled with a linear G interaction criterion, m=n=2 in Equation 17.

The results for static and fatigue testing of skin-stiffener specimens with four matrix materials lead to clear conclusions. As reported in the matrix/environmental section, resins with improved interlaminar toughness produce skin-stiffener specimens with greater resistance to damage development and failure under static loading; these results for new batches of material and more consistent material thicknesses confirm the results in the earlier section. In fatigue, the tougher resins also perform better; however, the data tend to converge at higher cycles, so the static advantages of the tougher systems is gradually lost; this is consistent with other fatigue studies using toughened resins.

238

13.9. Design Recommendations

Figures 170 and 175 provide a design sequence for predicting the static and fatigue lifetime of structural details of this type. Data required are the usual ply ultimate strength properties, as well as Mode I and Mode II fracture toughness and fatigue crack growth data for appropriate interfaces. (Many of these data are now available in the database for the most common reinforcing fabrics and resins; additional data are being developed.) An FEA model is constructed for the proposed geometry and ply layup, and areas of high stress (or high stress gradient, as in the previous section) are identified. Identify the loads to produce local failure, and insert a small crack at these locations; the crack length can be set by an iterative process, so that the sum F in Equation 17 reaches 1.0. The design loads are then compared to the load predicted to produce crack extension, and a safety factor is determined.

A similar approach is used in fatigue, inserting a crack in areas of high stress or stress gradient. A load is then applied to obtain G values, and scaled to the critical load to produce a particular crack growth rate, following the procedure in Figure 175. This load can then be compared to design loads to establish a safety factor for the design in fatigue. This process is iterated until a design is determined which produces an acceptable safety factor.

A simplified, conservative approach is recommended, where G_{IC} and G_{IIC} values are taken as initiation values for a 0°/0° interface, using the appropriate resin, fabric, and fiber content. This approach produces accurate static predictions for delamination if exponents m=n=2 are used in Equation 17, producing a linear mode interaction in terms of G (this is the equivalent to the method used in the previous section). For fatigue, a simplified, conservative approach is to design for threshold values for G to produce delamination values in fatigue. A reasonable assumption is that threshold values are 10 percent of initiation G_{IC} and G_{IIC} values.

239

14. SANDWICH PANEL CLOSEOUTS

14.1. Summary

Typically, sandwich panel construction is used in the trailing edge side of most blades to increase resistance to panel buckling of thin airfoil skins (Figures 142 and 143). Sandwich panels are composed of thin structural skins and a very lightweight core material, such as balsa, polymer foam, or honeycomb. The thickness added by the core raises the moment of inertia of thin panels, increasing the bending stiffness and buckling resistance at little expense in terms of weight or cost. Achieving the same buckling resistance with a thicker laminate would greatly add to weight and cost. Other stiffening methods such as multiple webs and "hat" shaped ribs are also effective. Studies of sandwich panel buckling resistance have been reported for basic panel parameters [37, 100] in the context of the AOC 15/50 blade design. This chapter explores the performance of closeout areas where the sandwich panel transitions into normal laminate.

The results show very poor tensile performance for the standard 30° longitudinal closeout geometry. Delamination and failure occur at much lower strains than can be withstood for the laminate or sandwich panel without terminations. Decreasing the termination angle to 10° or 5° significantly increases the structural performance, with the 5° case approaching the control laminate performance with no closeout. Finite element predictions based on point-stress failure criteria are in good agreement with the experimental data, using input material properties for the fiberglass and balsa which were developed in this study. In tensile fatigue, the sandwich panel lifetime without closeouts approached that of the baseline laminate (Chapter 10.4). Specimens with a 30° closeout showed a similar fatigue sensitivity to other delamination results, but a steeper S-N curve to failure than for the base laminate. On an absolute basis, the strain levels for delamination and failure at 10^6 cycles were low, in the range of 0.3 percent, compared with the baseline laminate value above 1.0 percent. Design recommendations are given at the end of the chapter.

14.2. Introduction

Sandwich panels in any blade design must involve transitions to normal laminate at the edges, termed closeouts or terminations. While the basic sandwich panel has tensile static and fatigue resistance close to those of the basic laminate without a core, the closeout areas contain more complex geometry which causes stress concentrations and may lead to delamination or in-plane failures. Typical closeout areas are shown in Figure 142, and cross-sections of longitudinal and transverse terminations are shown in Figure 178.

Stresses are transferred gradually in sandwich panels due to the low stiffness of the core; the complex shape of the upper surface (Figure 179) also contributes bending stresses, and core thickness-direction stresses vary from tensile to compressive (points 1 and 3) as the distance varies along the panel. Given enough length, the face sheet strains eventually equalize (point 7). One result of this stress transfer pattern is that test specimens must be sufficiently long to allow stress transfer.

240

Longitudinal Sandwich Termination (Standard 30 degree taper)

Transverse Sandwich Termination at Spar Cap (10 degree taper)

Transverse Sandwich Termination at Spar Cap (90 degree taper)
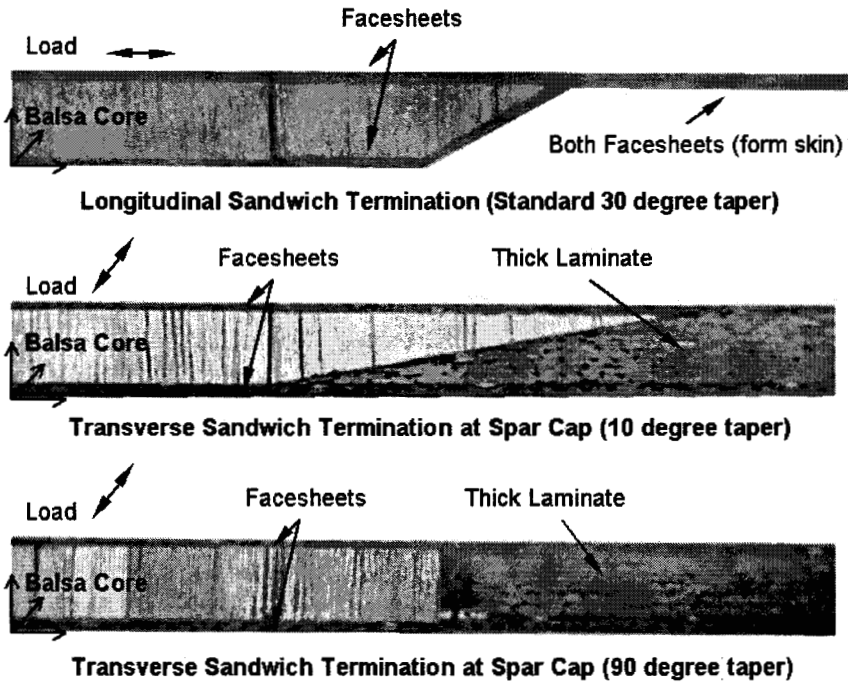
Figure 178. Local Detail Regions of Sandwich Terminations.
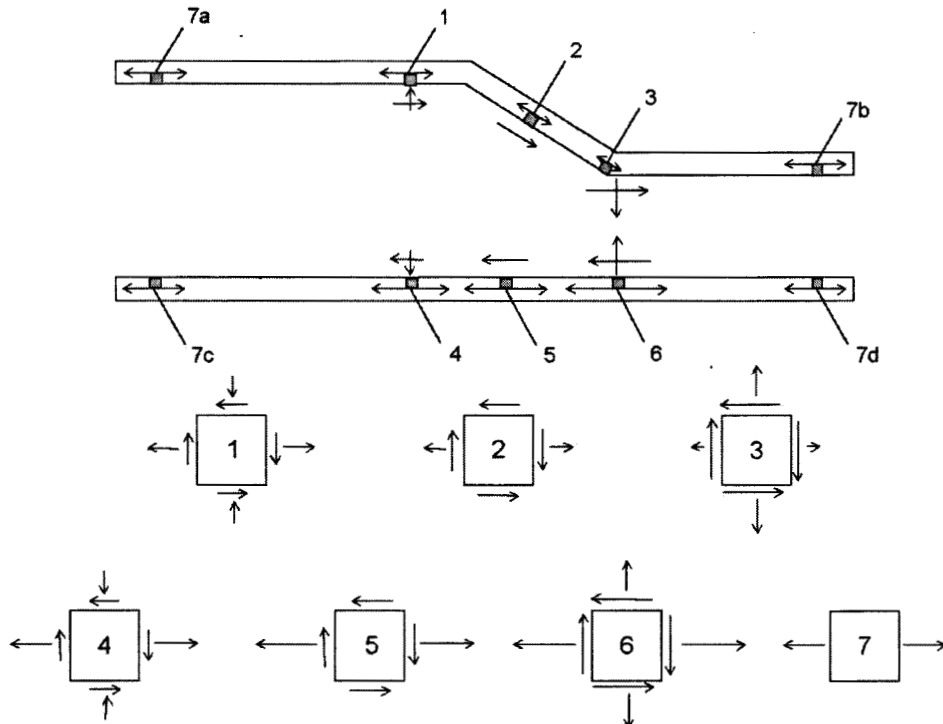
Figure 179. Illustration of Load Transfer in a Sandwich to Thin Laminate Transition Loaded in Tension, Including Stress States at Several Locations (length of arrows represent relative magnitudes).

241

This study involved tensile testing and analysis of the standard 30° longitudinal termination shown in Figure 178, as well as a parametric study of variations in this geometry. Transverse terminations to thicker laminates were studied in less detail. Significant test development was required for this research to allow meaningful testing of coupons containing terminations under static and fatigue loading. Basic material properties for the balsa were also determined using a variety of tests. The study was limited to tensile loading. This report briefly summarizes the major results of the experimental program and finite element modeling; details are available in Reference 42. It should be recognized that terminations of this type are routinely located in areas of low stress in the blade, and so their design may not be optimized structurally.

14.3. Experimental Methods

A wide range of processing and testing methods were explored in Reference 42. This report will only summarize the successful methods and materials used for the main part of the study. Test specimens were fabricated by hand layup using the same materials and configuration as in the AOC 15/50 blade design. The balsa core was commercial Contourkore material from Baltek [101] which has a light scrim on one side and is scored to allow forming to complex shapes (Figure 180). Resin filled the scored areas and was absorbed into some of the balsa as well, although the balsa surface is sealed to reduce permeability.

Tables 48 and 49 summarize the materials and their properties. Balsa core properties were obtained from tension and shear experiments conducted in this study, as well as from literature sources. The Contourkore balsa is supplied in sheets assembled from a number of slices out of various trees, and so is quite variable in properties.

Figures 181, 182 and 183 give measured variations in balsa density, tension, and shear tests, respectively. Tables 50 and 51 compare the tension and shear properties measured in this study with literature values. The low and high literature values from the Wood Handbook [102] represent the tangential and radial directions of the grain, respectively. The balsa properties used in the FEA models were an assembly from various sources, indicated in Table 52.
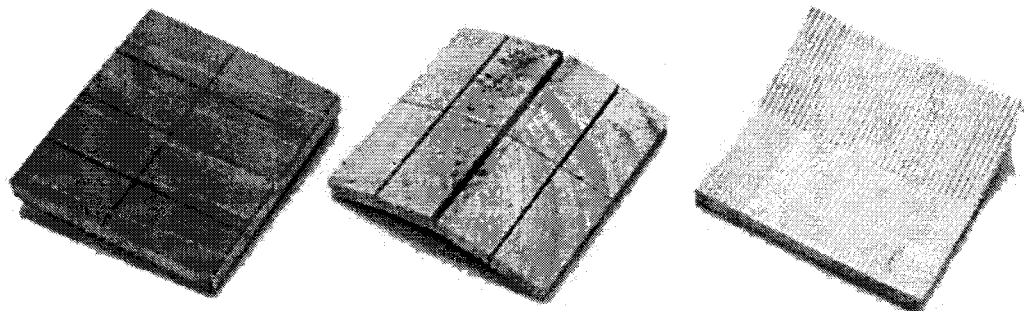
Figure 180. Sandwich Panel (right), Contourkote (scored side), and Contourkore (scrim side).

242

Test specimens were strain-gaged as shown in Figure 184, which also shows both the standard, nonsymmetric, specimen, and a symmetric specimen tested for comparison to reduce bending effects. Figure 185 shows specimens with a thin laminate transition having different fillet tapers, termed F30, F20, F10, and F5 for the different angles. Only the 30° fillet is a standard commercial product. Other angles were machined to shape as described in Reference 42. Closeouts to thick laminate differ strongly in geometry and mechanics; the three cases tested are shown in Figure 186. The thick laminate material adjacent to the balsa was built up using Owens Corning DB400 (±45°); resin rich areas near the balsa joint were unavoidable.

Table 48. Ultimate Strength and Strain Properties Used in the FEA Analysis.

	A130 (0° plies)*	DB120 (±45° plies)*	Balsa (Baltek)	Polyester resin
V_f	0.36	0.29	---	---
Ultimate Strengths				
Tension, 0°, MPa	701	89	13	54
Tension, 90°, MPa	34	89	---	---
Compression, 0°, MPa	-270	-170	4	54 x 1.5**
Compression, 90°, MPa	-93	-170	---	---
Shear	87	---	3	54**
Ultimate Strains				
Tension, 0°, %	2.53	1.06	---	2.00
Tension, 90°, %	0.39	1.06	---	---
Compression, 0°, %	-0.92	-2.03	---	---
Compression, 90°, %	-1.05	-2.03	---	---

*Calculated from classical laminate theory. ** Estimated

Table 49. Elastic Constants Used in FEA Analysis.

Material	V_F	Elastic Modulus[1], GPa			Poisson Ratios[1]			Shear Modulus[1], GPa		
		E_X	E_Y	E_Z	υ_{XY}	υ_{XZ}	υ_{YZ}[2]	G_{XY}	G_{XZ}	G_{YZ}
A130	0.36	29.96	7.10	7.43	0.35	0.33	0.44	2.43	2.86	1.65
DB120	0.29	8.35	5.96	8.35	0.37	0.44	0.27	1.99	5.03	5.03
DB120[3]	0.29	2.08	1.39	2.08	0.13	0.80	0.08	0.40	4.62	4.62
Balsa (Baltek)	---	0.053	2.51	0.053	0.11	0.34	0.36	0.16	0.16	0.16
Resin	---	3.18	3.18	3.18	0.35	0.35	0.35	1.18	1.18	1.18

[1] Properties in coordinates of finite element models shown in Figure 186.

[2] Calculated from: $\upsilon_{XY}/E_X = \upsilon_{YX}/E_Y$

[3] Estimated using laminate analysis after matrix cracked ($E_2=G_{12}=0.2$ of original values).
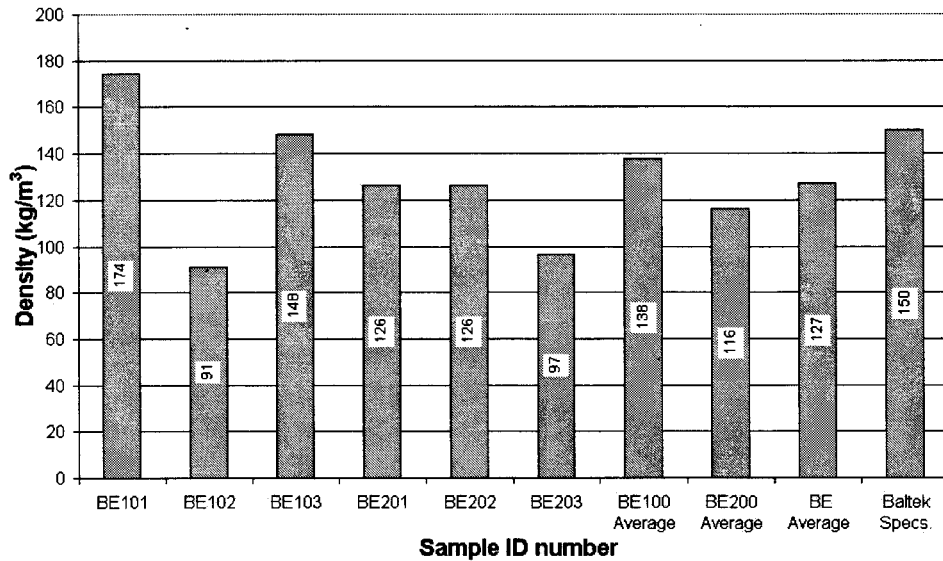
Figure 181. Density of Baltec Contourkore Material, Individual Test Results and Averages (with scrim removed).

244
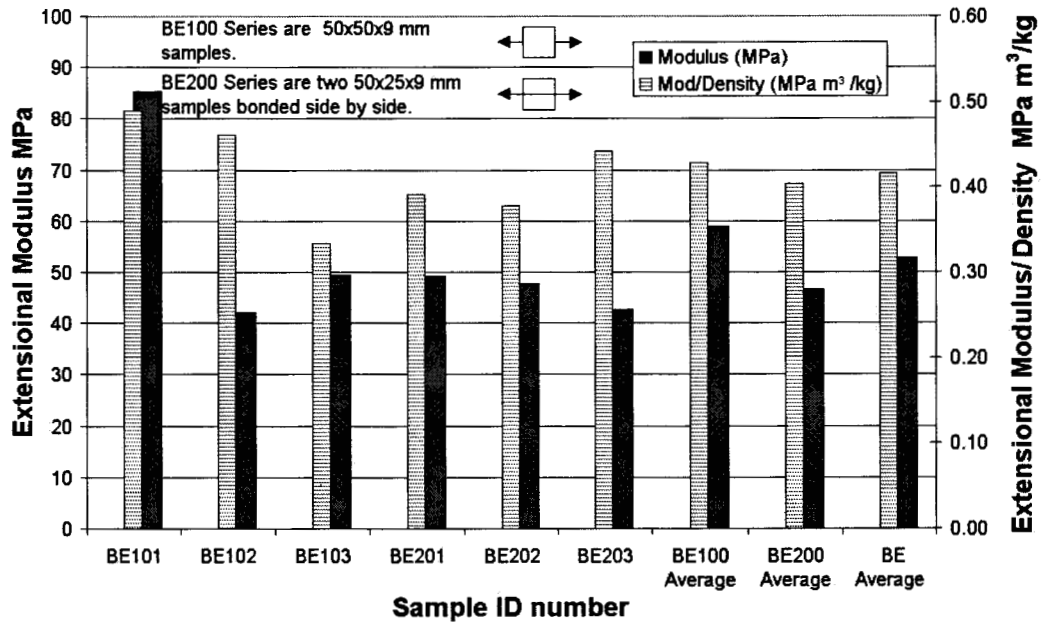
Figure 182. Extensional Modulus and Modulus/Density Ratio of Balsa Perpendicular to the Grain.
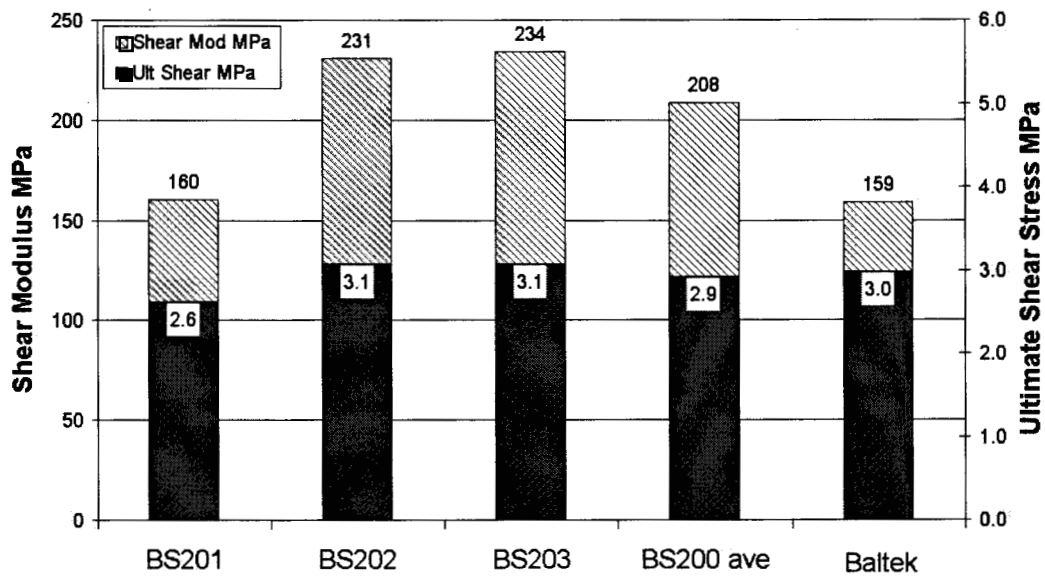
Figure 183. Shear Modulus and Ultimate Strength of Balsa (Test Method ASTM C273).

Table 50. Experimental Results of Balsa Extensional Modulus Tests.

| Experimental Result | Balsa modulus experiments | | | Supplier | Literature | |
	Average	Standard deviation	COV (%)	Baltek [101]	Wood Handbook [102]	Feichtinger [103]
Density (kg/m³)	127	31.3	24.6	150	150	150
Modulus (MPa)	52.8	16.2	30.8	---	53 - 164 [1]	1015
Modulus/density (MPa m³/kg)	0.42	0.06	14.0	---	0.35 - 1.09	6.77
Strength (MPa)	0.73	0.30	41.0	---	1.0 [2]	---
Strength/density (MPa m³/kg)	0.0056	0.0009	17.0	---	---	---

[1] Calculated using ratios presented in the Wood Handbook [104].
[2] From Science and Technology of Wood (density unknown) [107].

Table 51. Shear Modulus and Ultimate Shear Strength of Balsa.

	Experiment	Baltek [101]	Kilbourn [104]	Mil Handbook 23A [105]	Wienhold [106]	Wood Handbook
Density, (kg/m³)	150	150	155	160	152	160
Shear Modulus (MPa)	208	159	---	156 - 235 [1]	---	---
Ultimate Shear (MPa)	2.93	2.98	3.00	2.0 - 2.35 [1]	2.38	2.07

[1] Range is due to modulus parallel and perpendicular to growth rings.

Table 52. Origin of all Balsa Properties.

Material Property*	Value (MPa)	Source	Rational
E_X	52.8	Experiment	Wide range from literature
E_Y	2510	Baltek [101]	Given as specification
E_Z	52.8	Experiment	Wide range from literature
υ_{XY}	0.11	Wood Handbook Averaged tangential and radial values [102]	Source given by Baltek
υ_{XZ}	0.34		
υ_{YZ}	0.36		
G_{XY}, G_{XZ}, G_{YZ}	159	Baltek [101]	Given as specification
Utx	13	Feichtinger [103]	Source given by Baltek
τ_{XY}	3	Baltek [101] and Experiment	Given as specification

*Grain is in direction of y axis.

246

Fillet Strain Gage ⟍

Straight Strain Gage ⟍

Fillet Strain Gage ⟍

Straight Strain Gage ⟍
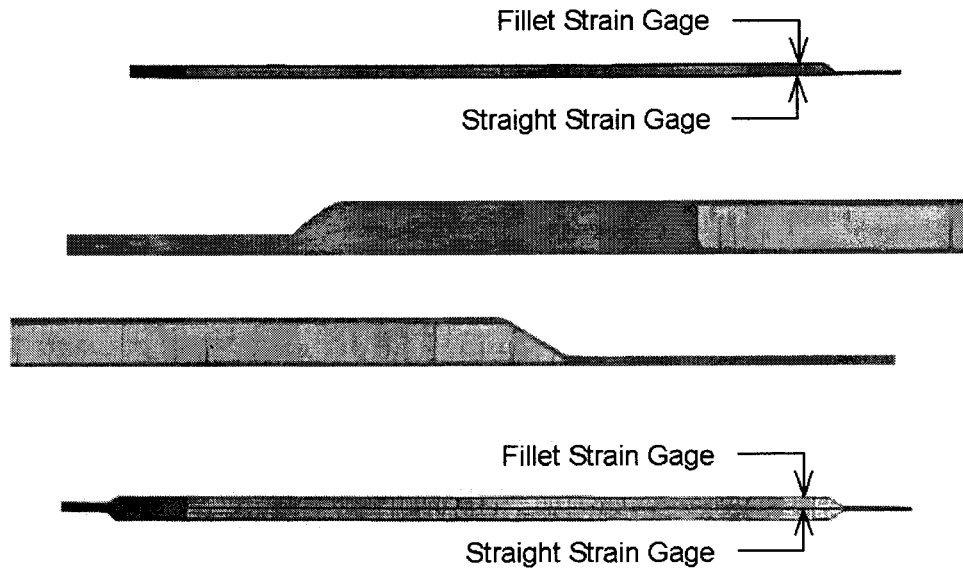
Figure 184. F30, Standard 30° Fillet Specimen (Top), Close-up of Solid Core Tapered for Gripping, Close-up of Sandwich Transition, and Two Sides Secondary Bonded Together to Form One Symmetric Specimen. ("Fillet" Refers to the Facesheet Which Covers the Balsa; "Straight" Refers to the Facesheet Which Remains Straight).

5° — F5

10° — F10

20° — F20

30° — F30
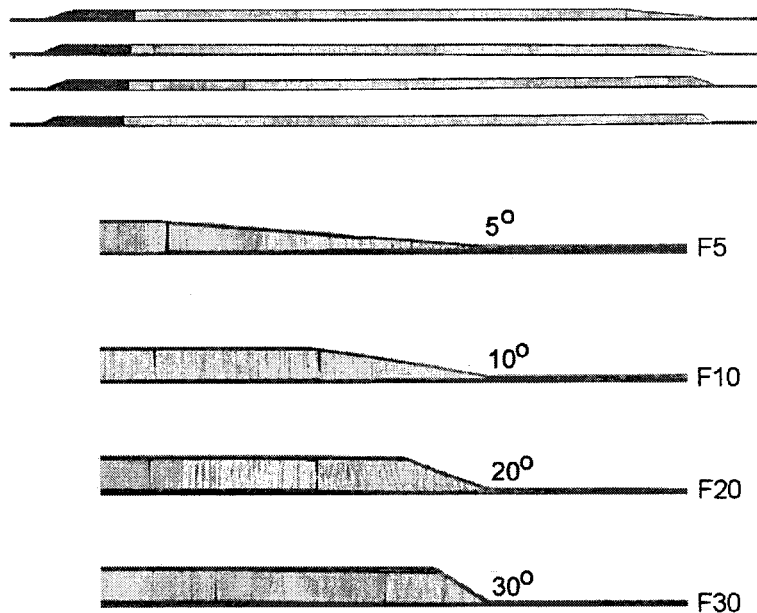
Figure 185. Thin Laminate Termination Specimens with Fillet Angles 5, 10, 20 and 30 Degrees (Top), and Close-up of Sandwich Transition End Area of Each Specimen.

247
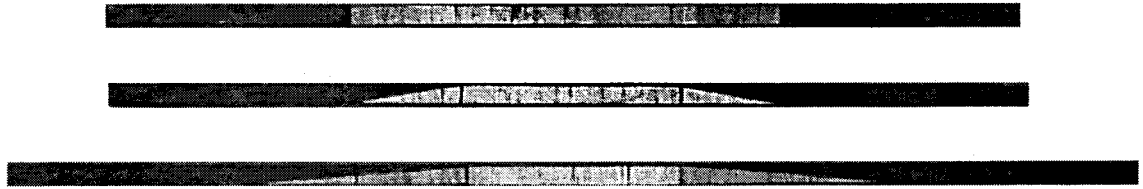
Figure 186. Thick Termination Specimens: 90 (top), 10 and 5 (bottom) Degrees.

14.4. Numerical Modeling

Each of the major test geometries was modeled using ANSYS finite element software with Plate 13 elements. The main macro was developed for the F30 geometry, then varied for the other cases. Details can be found in Reference [42]. In Figure 187 a photograph of the F30 geometry is shown along with the material boundaries and coordinates used in the FEA discretization. Care was needed to keep the material directions consistent in the various areas. A neat resin area was included at the tip of the fillet as seen in micrographs like Figure 188. A typical mesh for the F30 geometry is shown in Figure 189. Input material properties used in the FEA models are given in Tables 48 and 49.
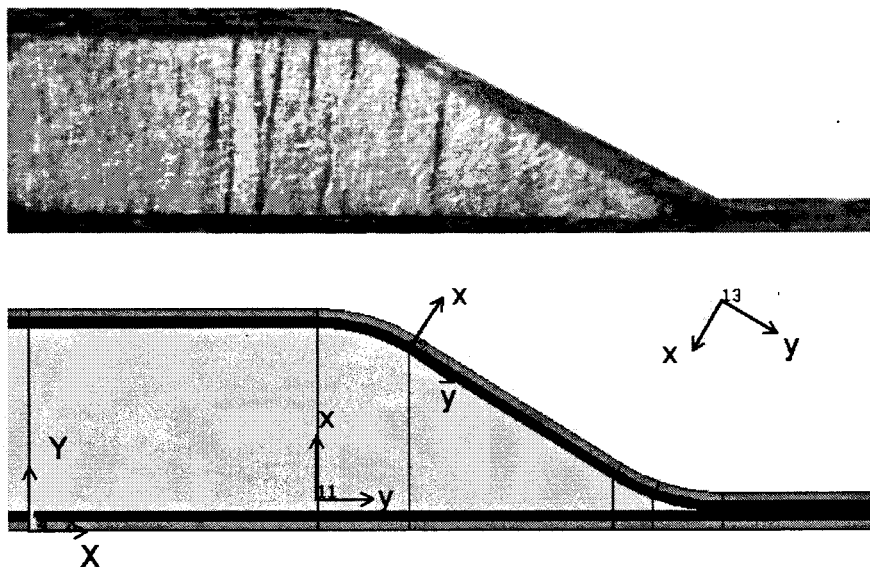
Figure 187. Close-up Photograph of F30 Specimen (Top), and Close-up of FEA Model With Areas Outlined, Material Properties Shaded and Local and Global Coordinate Systems Shown.

248
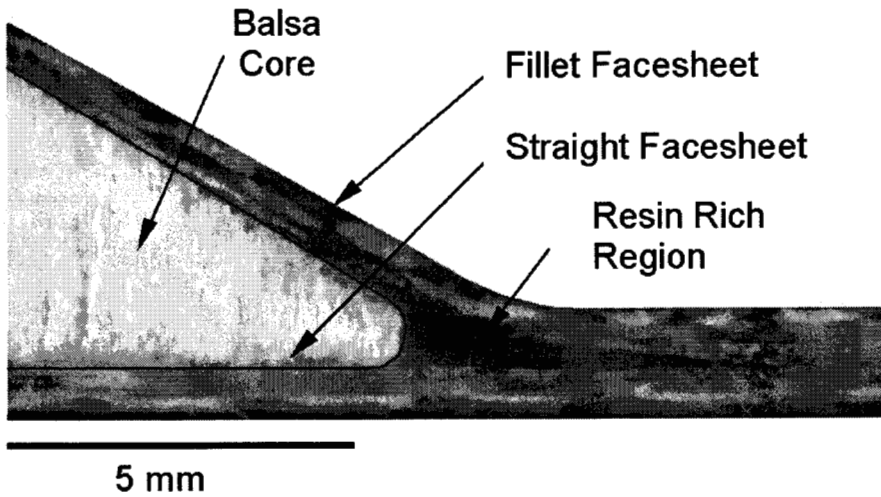
Figure 188. F30 Closeout with Balsa Highlighted, and Showing Resin Rich Region.
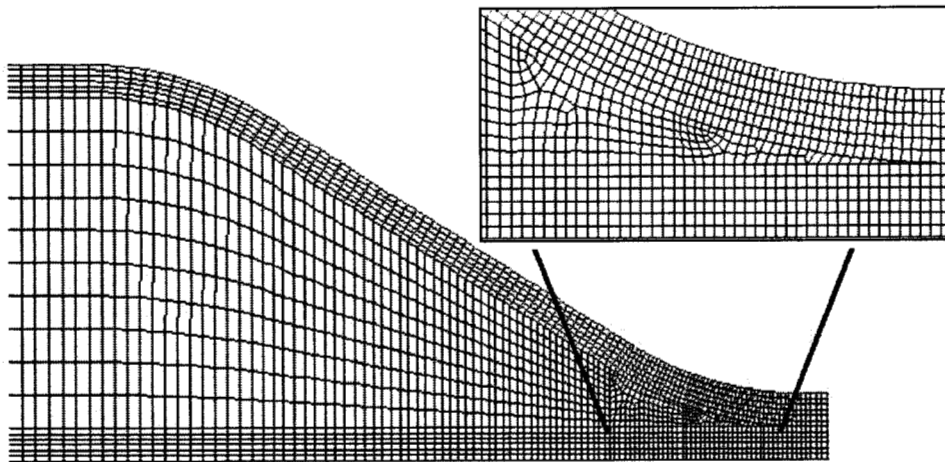
Figure 189. Mesh of F30 Model with Detail of Fillet Region.

249

14.5. Results and Discussion

14.5.1. Sandwich Termination into Thin Laminates

The main focus of this study was the termination into a thin laminate. Due to resin content variation, a nominal thickness for the laminate of 1.92 mm was assumed in calculations, representing an average fiber content of 33.8 percent by volume (following earlier discussion (Chapter 11), the local fiber contents in the 0° and ±45° layers were taken as 36.3 percent and 29.2 percent respectively, in establishing the input properties in Tables 48 and 49).

The failure mode for typical F30 specimens is shown in Figure 190. Delamination progressed gradually from a spot near mid-width or, in other cases, the entire width delaminated simultaneously. The delamination stress was taken as the stress when the delamination spread across the entire specimen width. The strain and stress to delamination and failure for various geometries are given in Table 53 and Figures 191 and 192. The stress for delamination in the F30 specimens averaged only 25 percent of the strength for the facesheet materials, and fiber failure was at a stress of 58 percent of the facesheet strength (all stresses are calculated based on the nominal thickness, ignoring the core). Thus, under static tensile loads, the standard 30° fillet configuration sustains severe damage and failure at stresses far below those for the facesheet or the sandwich panel away from the transition.
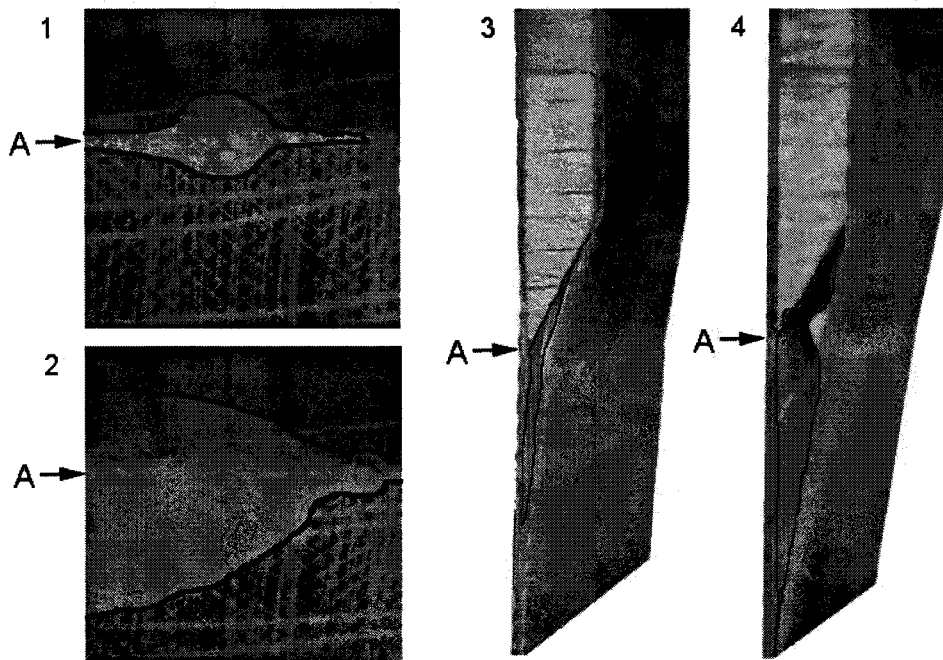
Figure 190. Steps During Delamination of F30 Specimen (Front (1 and 2) and Edge Views, Point A is Edge of Thin Laminate).

250

Table 53. Delamination and Ultimate Failure Conditions of Thin Laminate Termination Specimens and Baseline Materials.

Geometry	Number of specimens	Delamination				Ultimate Failure			
		Strain %	COV %	Stress MPa	COV %	Strain %	COV %	Stress MPa	COV %
Baseline Specimens									
Facesheet	3	--	--	--	--	2.69	3.30	383	251
Sandwich Panel	3	--	--	--	--	2.64	1.45	409	1.80
Asymmetric Specimens									
F30	3	0.44	4.63	95	4.13	1.17	9.45	222	8.06
F30R	3	0.56	18.06	99	19.99	1.36	8.07	222	3.83
F20	3	0.79	14.99	142	14.55	1.48	19.69	242	18.72
F10	3	1.27	0.23	246	17.57	1.78	6.71	276	16.15
F5	3	2.31	2.21	359	2.93	2.33	5.27	364	3.59
Symmetric Specimens									
F30	3	0.62	1.24	124	13.87	1.31	2.20	256	0.81
F30R	3	0.46	7.81	87	1.22	1.11	13.27	242	8.13
F20	3	0.58	8.40	90	13.5	1.23	12.43	286	7.70
F10	3	1.39	5.94	242	6.23	1.84	6.97	311	5.46
F5	3	2.29	5.42	360	4.98	2.29	5.42	360	4.98
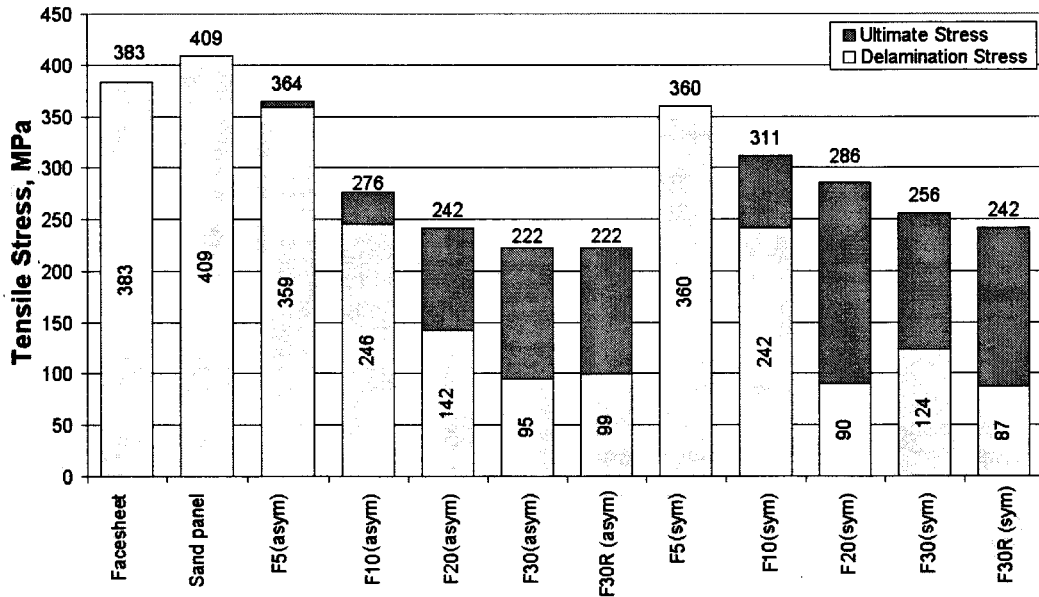
Figure 191. Stress Values for Each Type of Thin Laminate Termination, at Full
Width Delamination and Fiber Failure (Average Values).
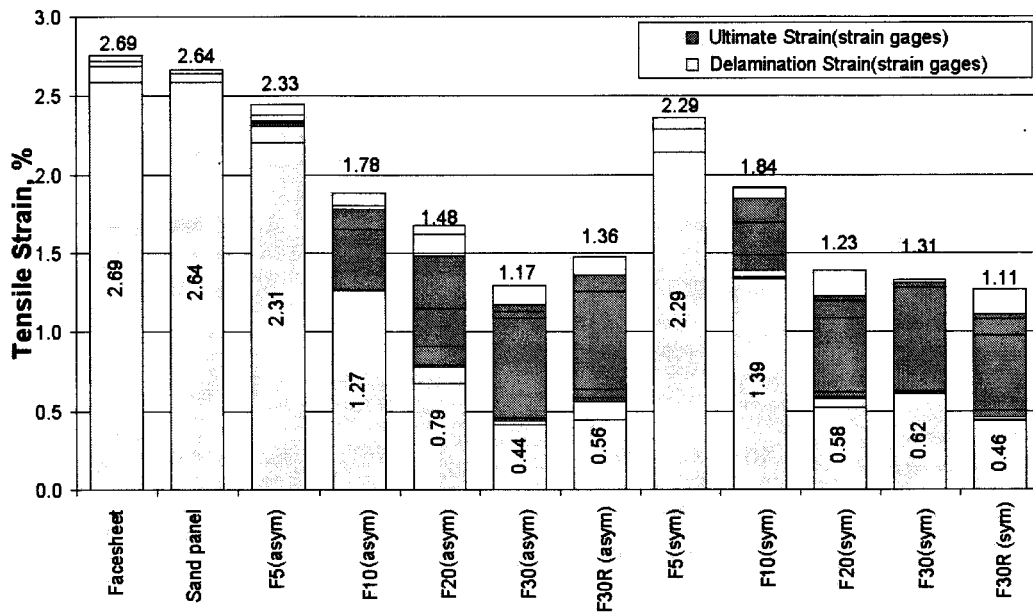
Figure 192. Strain Values for Each Type of Thin Laminate Termination at Full
Width Delamination and Fiber Failure (Strain Gages Located as Shown in Figure
181; Lines Give Values for Individual Test Specimens; Average Values Indicated
Numerically).

When the fillet transition is made more gradual by using a smaller angle at the edge, the improvement is remarkable. Table 54 shows the delamination and ultimate strengths for each case as a percent of the facesheet value. The 10° termination still delaminates at 64 percent of the facesheet strength, but the 5° case approaches the facesheet performance at 94 percent. While a 5° taper may seem extreme for an actual blade manufacturing process, it was readily prepared in the lab, and would not appear to add significantly to blade overall cost (while removing a major potential source of material safety factors). Typical fillet strips used for each case are shown in Figure 193.

Table 54. Delamination and Ultimate Strengths for Each Specimen Type, Expressed as a Percentage of the Facesheet Control Values.

Geometry	Asymmetric Delamination %	Symmetric Delamination %	Asymmetric Ultimate %	Symmetric Ultimate %
FC (baseline)	100	100	100	100
F30	24.7	32.4	58.1	66.8
F30R	25.9	23	58.1	63.1
F20	37.1	23	63.2	74.6
F10	64.1	63	72.1	81.3
F5	93.7	93.9	95.0	93.9

The symmetric, back to back specimens (Figure 184) were tested to avoid significant out-of-plane bending effects, since actual blade geometries would constrain the deformations. The results were not encouraging, as the delamination values were only slightly improved at best, and decreased in some cases (see Reference 42 for details). Thus, the specimen bending in the unsymmetrical specimens does not appear to decrease the measured properties significantly. Replacing the balsa in the transition region with solid laminate (F30R, Figure 192) did not lead to measurable improvement.

14.5.2. Sandwich Termination into Thick Laminate

The transverse terminations into thick laminates (Figure 178) were studied in less detail. Tables 55 and 56 give results for the termination cases having angles of 90°, 10° and 5°, relative to the standard laminate ultimate properties. As for the thin laminate case, the strength values are greatly reduced for the most severe, 90° termination. The more gradual transitions show more acceptable strength reductions on the order of 25 percent.

253
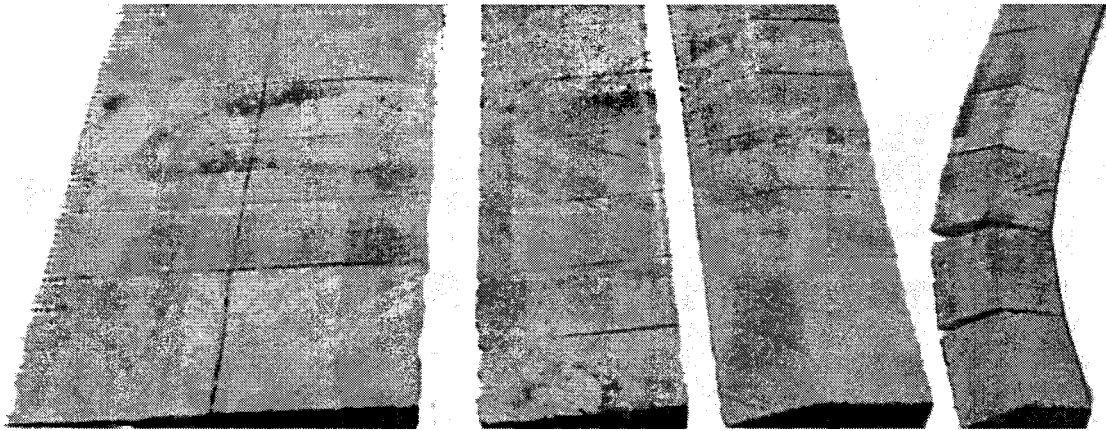
Figure 193. Balsa Fillet Strips for Various Tests (left to right): 5, 10, 20 and Baltek 30 Degrees.

Figure 194. Detail of Fillet Region Showing Solid DB400 Laminate Fillet.

Table 55. Delamination and Ultimate Failure for Thick Sandwich
Terminations and Baseline Material.

Geometry	Number of specimens	Delamination				Ultimate			
		Strain %	COV %	Stress MPa	COV %	Strain %	COV %	Stress MPa	COV %
Sandwich panel (baseline)	3	---	---	---	---	2.64	1.5	409	1.8
S90	3	1.00	35.7	176	32.2	1.31	39.2	230	28.2
S10	3	1.46	10.0	256	8.9	2.01	7.7	335	4.6
S5	3	2.11	6.6	314	3.8	2.11	6.6	314	3.8

Table 56. Delamination and Ultimate Failure for Thick Sandwich Terminations as a Percentage of the Sandwich Panel Strength.

Geometry	Delamination %	Ultimate %
Sandwich Panel (baseline)	100	100
S90	43.0	56.2
S10	62.6	81.9
S5	76.8	76.8

14.5.3. Fatigue

Tensile fatigue tests (R = 0.1, with 3 to 4 Hz frequency) were carried out on the baseline laminate, sandwich panel, and 30F termination with the thin laminate. The test specimens for the F30 termination were shortened as shown in Figure 195, due to testing machine limitations. The static delamination and ultimate values were higher for this geometry than for the standard F30 specimen, as indicated in Table 57.

Figure 195. Fatigue Specimen for F30 Fillet (asymmetric) (Showing Spacer on the Right End to Align Loading Parallel to the Center of the Sandwich).

Table 57. Static Tensile Delamination and Ultimate Failure of Fatigue F30 Specimens versus Standard F30 Specimens (Asymmetric Cases).

Geometry	Number of specimens	Delamination				Ultimate			
		Strain %	COV %	Stress MPa	COV %	Strain %	COV %	Stress MPa	COV %
Standard specimen	3	0.44	18.1	99	4.1	1.17	9.5	222	8.1
Fatigue specimen	3	0.63	13.2	116	12.5	1.45	4.8	238	5.1

The fatigue results for the baseline laminate and sandwich panel control materials were reported earlier in Chapter 10.4. The baseline laminate showed good fatigue performance as anticipated from the low fiber content. The sandwich panel showed only slightly more fatigue sensitivity than did the base laminate. Fatigue data for the F30 closeout indicating various stages of delamination are given in Figure 196. The scatter in both the static and fatigue results is great, but trend lines could be fit and discriminated. The slopes, b, are similar to those described earlier for matrix dominated fatigue. A plot of delamination fronts for various cycles for typical specimens is given in Figure 197.
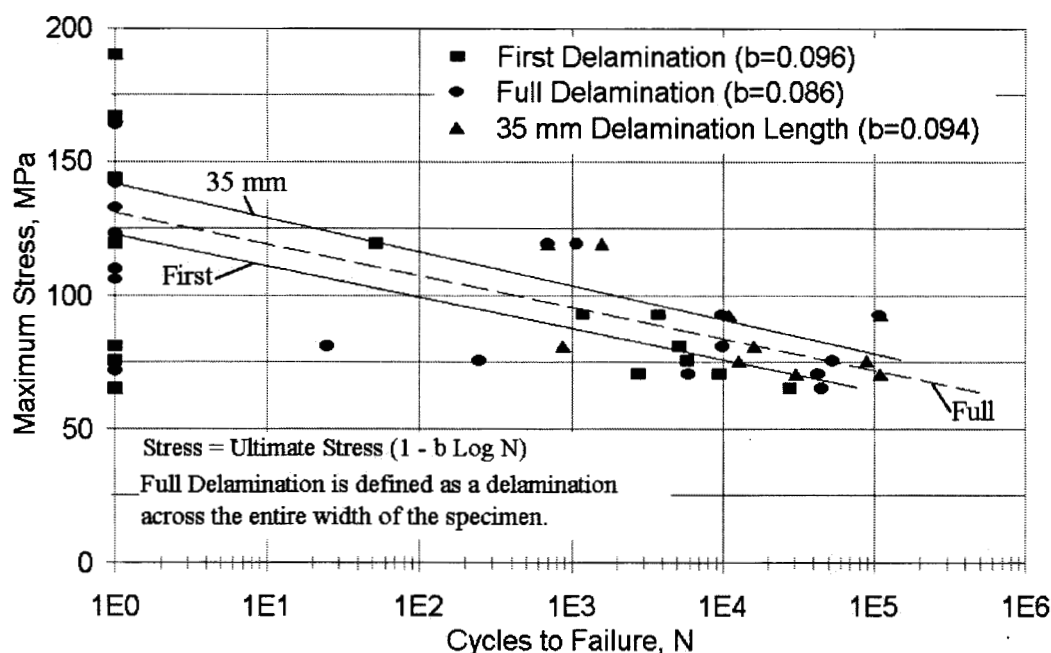
Figure 196. S-N Plot of Various Delamination Stages: Initiation, Full Width, and of 35 mm Length (F30 asymmetric, R = 0.1).

Results for total fiber failure and full width delamination are given in Figure 198. While delamination occurs at stresses far below fiber failure in static loading, the data tend to converge around 10^5 to 10^6 cycles, due to the differences in slope of the S-N trends for delamination and fiber failure. The total failure S-N trend is slightly steeper than for the baseline laminate or sandwich panel, as indicated in Figure 199. Most significant is the great decrease in static strength for the F30 termination relative to the baseline materials; the greater fatigue sensitivity exacerbates this difference.

Fiber failure happened in the straight facesheet first, as in the static tests. Fiber failure almost always followed a stitch (bead) or the fillet tip, producing very linear failures across the width of the specimen. A typical failure is shown in Figure 200.
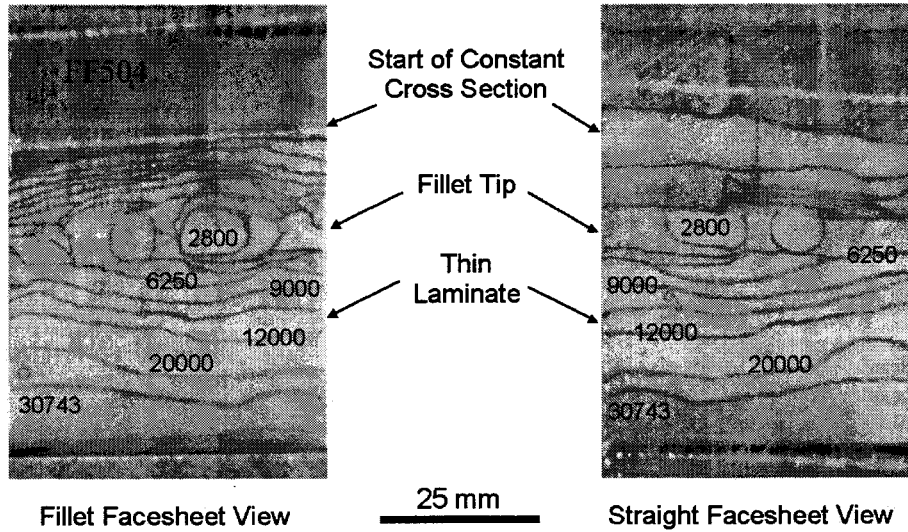
Figure 197. Delamination Boundaries at Various Numbers of Cycles During Fatigue of a Typical Fillet Fatigue Specimen.
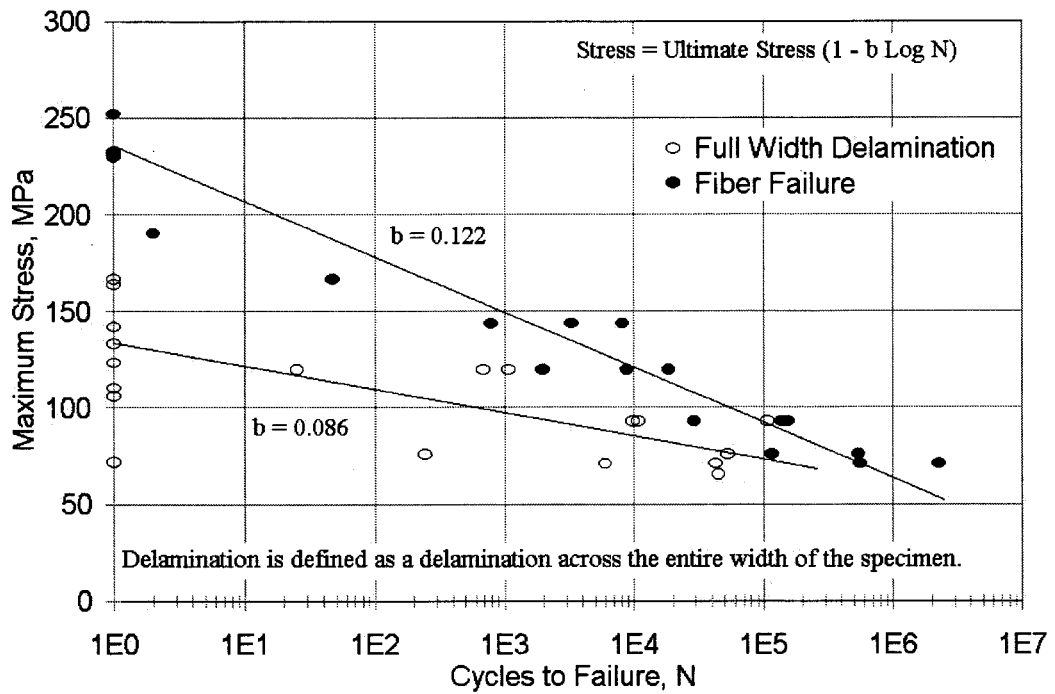
Figure 198. S-N Plot for Full Width Delamination and Tensile Failure of F30 Specimen Tested in Fatigue at R = 0.1.
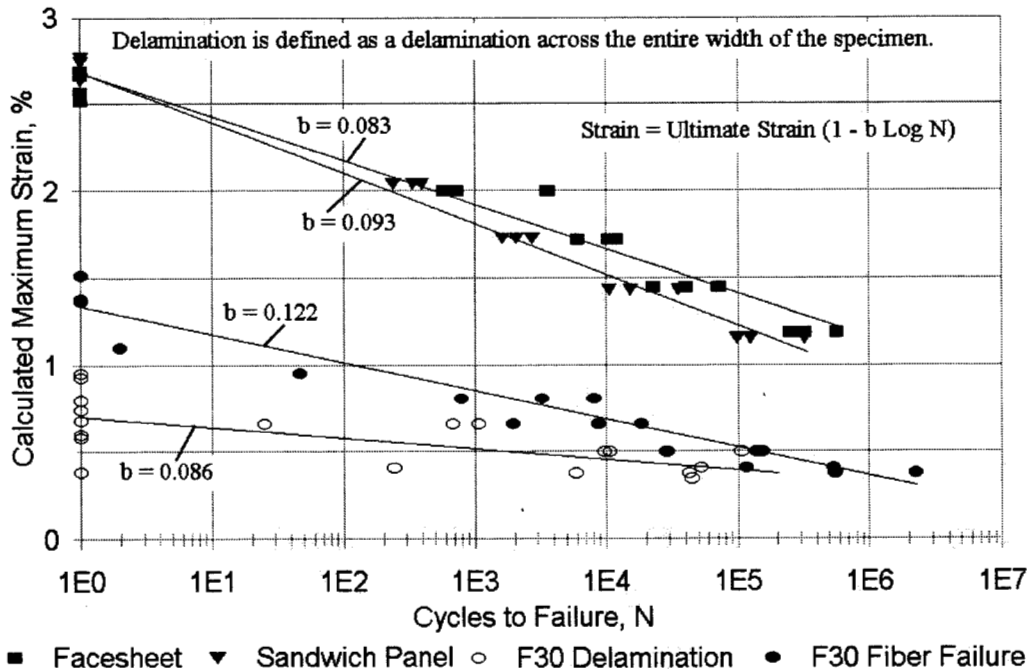
Figure 199. Comparison of F30 Fillet, Sandwich Panel, and Facesheet Control S-N Data, R = 0.1.
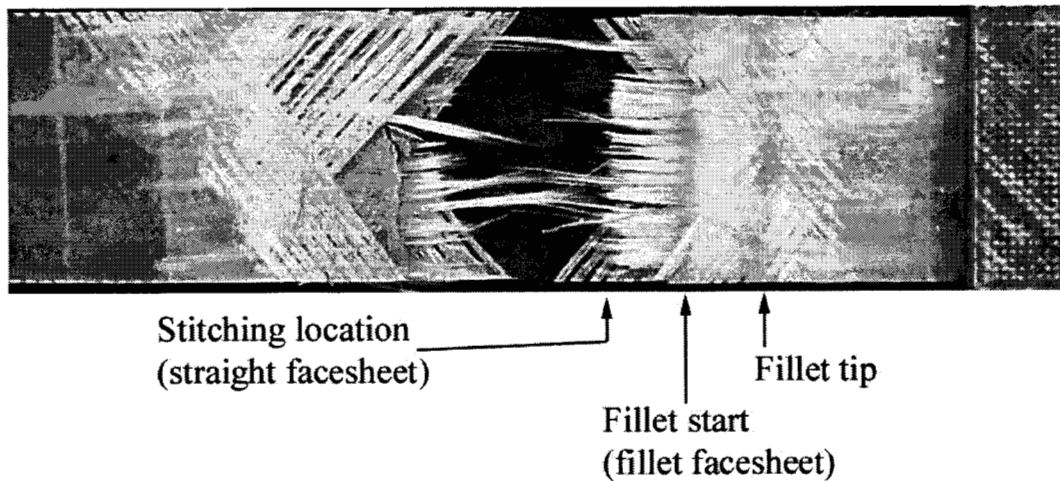
Figure 200. Detail of Typical Fatigue Failure of F30 Specimen, Showing Positions Relative to Fillet Tip. Stitching Indicates the Position of the Bead in the Woven A130 Fabric.

14.5.4. Finite Element Predictions

Finite element predictions were run for the baseline materials and various cases containing terminations under static loading. Experimental and predicted stress-strain curves for the sandwich panel specimen with no termination is shown in Figure 201. Good agreement is seen between the prediction and experiments; matrix cracking in the ±45° layers was modeled by assuming a bilinear stress-strain curve for those layers [42].

Comparisons between predicted and experimental strain distribution along an F30 specimen with increased length compared with standard specimens [42] are given in Figure 202. Experimental strains were measured with an extensometer. Agreement is again good. The standard F30 specimen predicted and experimental stress-strain curves are shown in Figure 203. Results are shown for both the straight and filet sides of the specimen (Figure 178); as noted earlier, strains are always much higher on the straight side. Whether or not delamination was included in the FEA model did not make a great difference [42]. A comparison of strain maps along the specimen length is shown in Figure 204 at a stress near the failure stress.
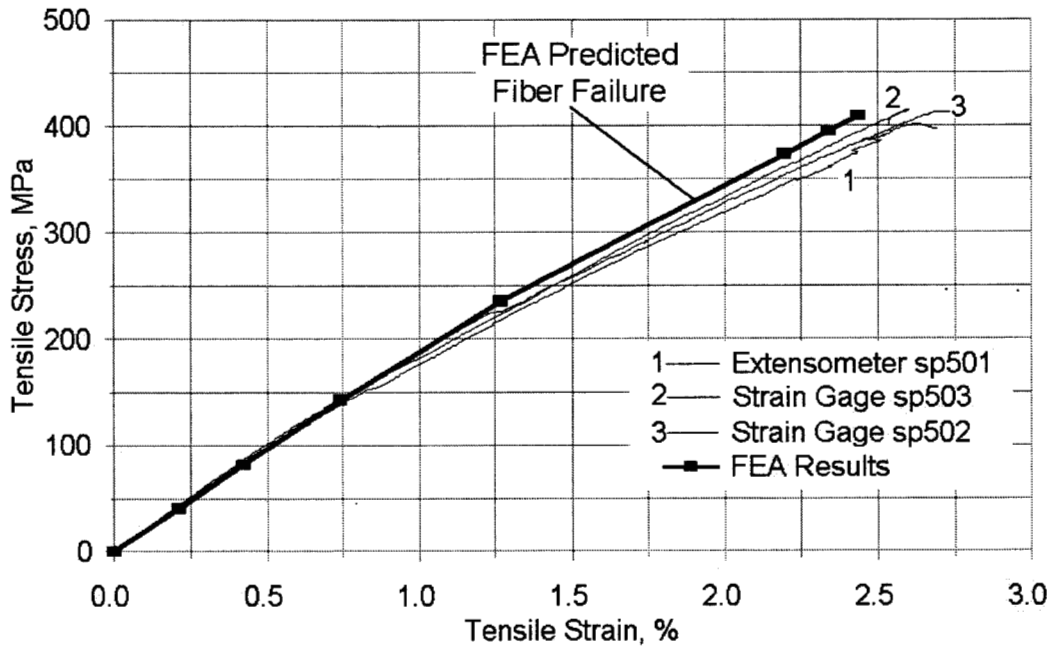
Figure 201. Stress-Strain Plot for Sandwich Panel Tests With No Terminations, Including Experimental Plots and FEA Results.
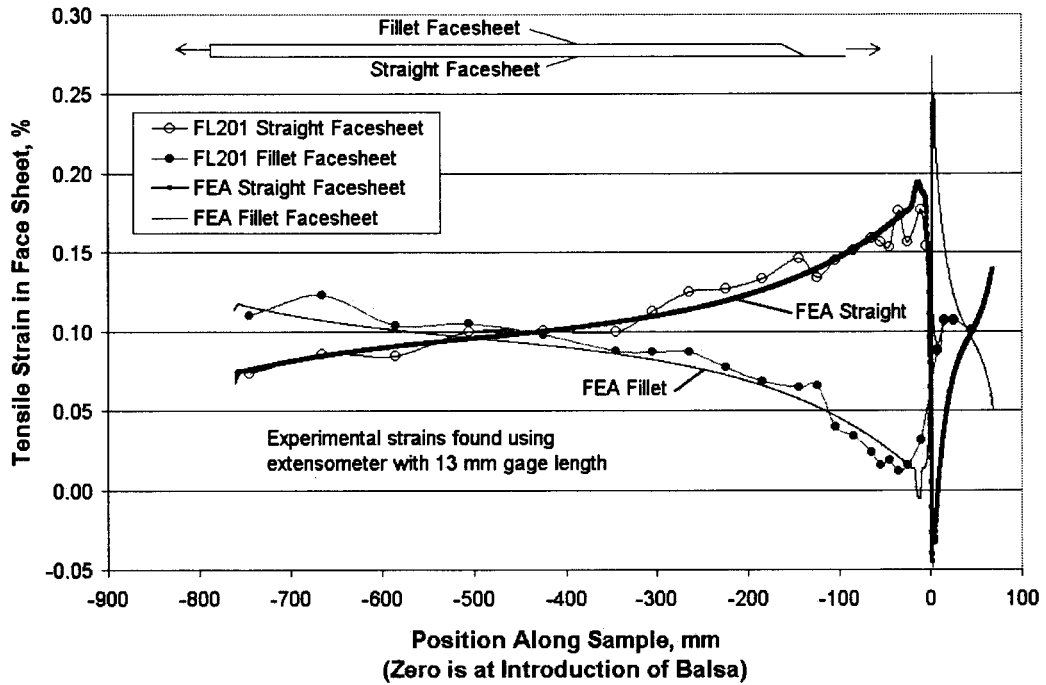
Figure 202. Strain Mapping of F30 Extra Long Specimen; Comparison of Experimental and Predicted Strains.
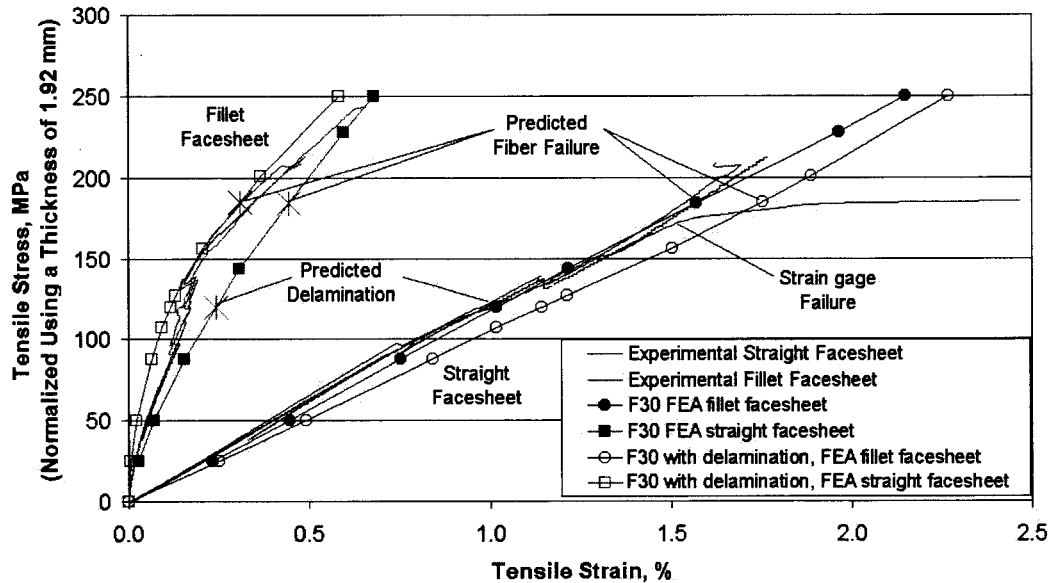
Figure 203. F30 Fillet Experimental Data Compared with FEA Results for Model With and Without Delamination Included. Strains are at the Positions of the Strain Gages in Figure 183.

260
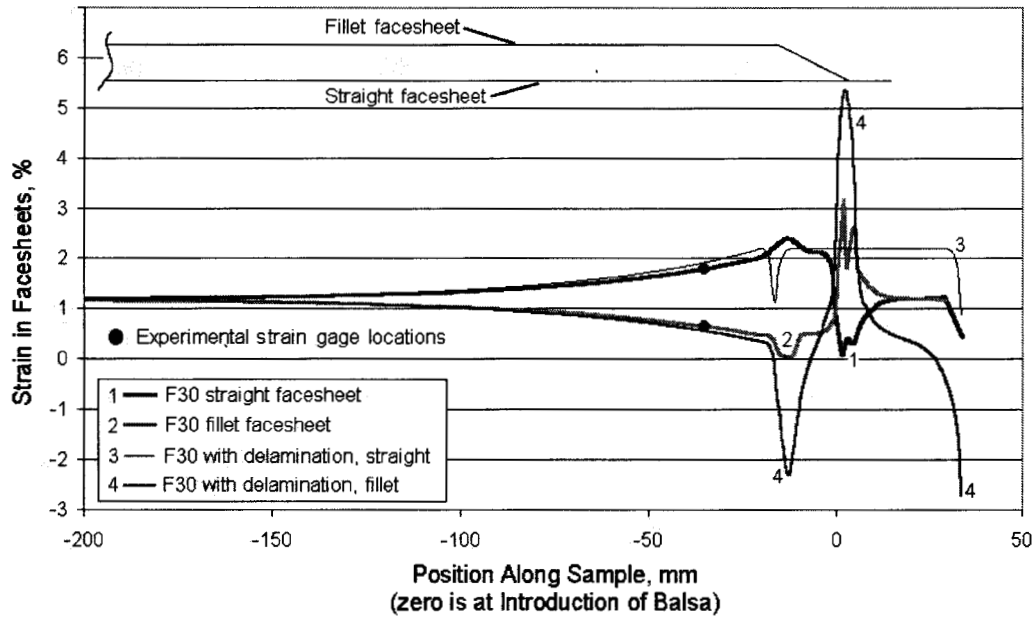
Figure 204. Predicted Surface Strains from F30 Models With and Without Delamination at a Stress of 222 MPa (F30 Fiber Failure Stress).

Comparisons between predicted and experimental stresses for delamination and failure of various thin laminate terminations are given in Table 57. Predicted stresses generally fall below experimental values, with differences ranging up to 30 percent. Predicted strain distributions for the various geometries at a stress of 95 MPa are compared in Figure 205.

The differences in predicted and experimental values in Table 58 may relate to several factors. Delamination was predicted from the von Mises stress (and neat resin strength data) in the resin region at the fillet tip, where local stress concentrations were determined and delaminations were observed to initiate. (A second, higher stress concentration area in the resin was a result of the model geometry, and was ignored [42]). Fiber failure was predicted by a point-stress criterion in the A130 fabric layer. A more realistic criterion involving characteristic distances or volumes might give a more accurate prediction in the presence of stress gradients [105]. Delamination cracks could also be inserted in the model and evaluated as in the previous two chapters, but this has not yet been done in this study.

261

Table 58. Experimental and Numerical Values for Asymmetric
Fillet Specimens, Thin Laminate Terminations.

| Specimen | Delamination | | | | Ultimate | | | |
| | Experiment | | Model | | Experiment | | Model | |
	Stress MPa	COV %	Stress MPa	Error %	Stress MPa	COV %	Stress MPa	Error %
F30	95	4.1	120	27.0	222	8.1	184	-17.2
F30R	99	20.0	109	9.7	222	3.8	193	-13.2
F20	142	14.6	123	-13.4	242	18.7	219	-9.5
F10	246	17.6	204	-16.9	276	16.2	274	-0.7
F5	359	2.9	250	-30.4	364	3.6	308	-15.4
Note: Negative errors are conservative.								
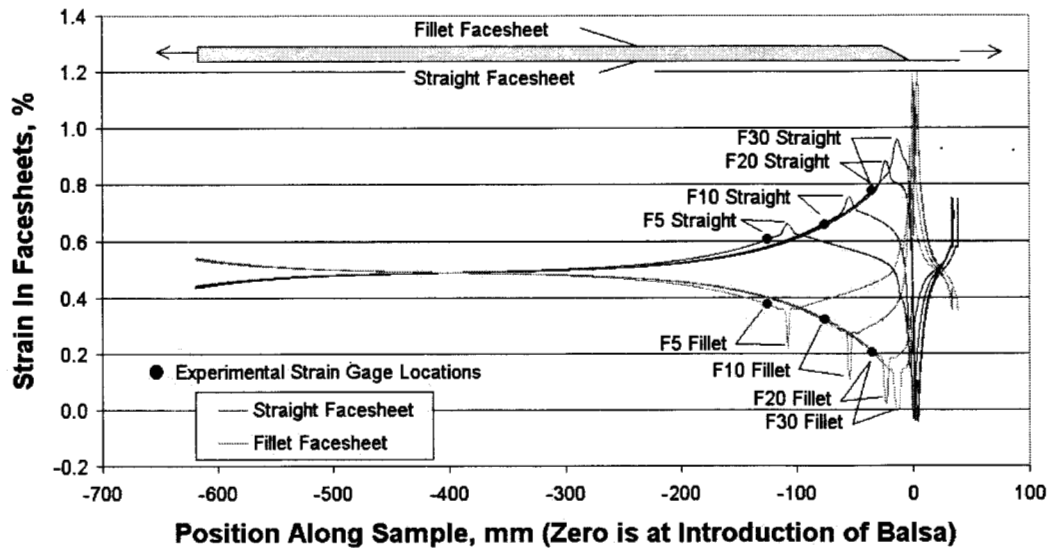
Figure 205. Predicted Strains in Each Facesheet of Fillet Specimens at a Stress of 95 MPa (F30 experimental delamination stress).

14.6. Conclusions

This study shows the importance of sandwich panel terminations in the structural response of laminates. The commercial 30° edge termination (to a thin laminate) reduced the strength to 58 percent of the facesheet strength, with major delamination at 25 percent. Similar magnitudes of reduction were observed with thick laminate transitions. The low static strength was further exacerbated by fatigue loading, which produced a steeper S-N trend at failure than for the base laminate.

These strength reductions were greatly reduced by using a shallower angle at the edge of the termination, with a 5° angle nearly eliminating the strength loss. While 5° may present manufacturing problems, it would greatly reduce required partial safety factors for these details.
Finite element predictions gave reasonable accuracy for delamination and failure. Predicted (FEA) trends with geometry also agreed approximately with experimental results.

The major deficiency of this study is that it does not include compressive loading, which could result in severe strength losses as well. Compressive tests and geometries of this type are very difficult to conduct without extreme bending and buckling problems. However, the compressive strength aspect would be predicted by FEA to follow similar trends to those predicted in this study for both delamination and failure (only the signs of the stresses would be changed). Modeling delaminations with fracture mechanics might produce greater accuracy and reduce complications from local extraneous stress concentrations in the resin rich areas. Tougher resin systems could improve performance with terminations like the 30° case.

14.7. Design Recommendation

The knockdown or safety factor required for sandwich panel terminations could be greatly reduced by using a shallower angle in the termination. An angle of 5° would greatly improve performance, and would seem to be practical. This could be important in cases where terminations occur in high-stress parts of a blade.

15. CONCLUDING REMARKS

Most of the foregoing, as well as previous reports, has dealt with static and fatigue strength problems associated with typical low cost composite materials used in most blades. Many of the materials problems addressed in Part A occur due to the use of heterogeneous, stranded glass fabrics and brittle, environmentally-sensitive resins, and wet hand lay-up or RTM-type processes. Many of these problems would be greatly reduced or eliminated by the use of well dispersed, straight fibers in a tough, environmentally resistant resin. Typical aerospace prepreg manufacturing approximates this condition, but at great cost. Current prepreg blade manufacturing might also closely approximate this condition, with the possible exception of the resin toughness (improving resin toughness is usually expensive). The extent to which a large blade can be consistently manufactured with straight fibers using prepreg is not known, but chances would seem to be greater as compared with some variation of RTM with a fabric like the bonded fabrics described in Chapter 3, or the stitched large tow carbon fabric in Figure 105.

If the fibers were straight and well dispersed, the general laminate static and fatigue properties away from detail areas should consistently achieve the best possible levels obtainable with the glass or carbon reinforcement. Much more testing is still required for the large tow carbon materials, such as characterization under different loading conditions to obtain complete Goodman diagrams for laminate configurations of interest, including high cycles. Spectrum loading and cumulative damage testing is also needed for these materials. Materials of this type would still require considerable study in the structural detail and delamination area, to provide efficient but reliable structural detail design methodologies.

With regard to conventional hand layup, RTM, and resin infusion processes which use stranded fabrics of various types, the findings presented in this report lead to a basic question of how to approach research and development efforts on blade materials: should efforts continue to find the combinations of fabric architecture, resin and process which provide the best static and fatigue performance, or is there now ample evidence that improved materials are subject to greater knockdowns at flaws and structural details, so that a design using rational safety factors would arrive at similar design allowables for both ends of the materials spectrum? For example, the Ahlstrom 0° fabric (42024L/M50, Figure 30) appeared to have an optimum architecture, with large, straight strands in the warp direction, but with adequate resin paths to provide high permeability. However, in practice, laminates constructed with this fabric showed poor compressive strength in the same range as woven fabrics like A130, due to waviness in the strands when molded. Furthermore, the tensile fatigue resistance was low, even at low fiber contents, due to stitching to the mat which carries the strands, locally raising the fiber content near the stitching to levels where tensile fatigue resistance is poor. If the waviness and stitching had not occurred in the flat laminates used for test specimens, then high knockdowns would probably have been introduced around areas such as ply drops, which are impossible to avoid in a realistic, low cost design. This line of reasoning leads to the conclusion that material systems which are least expensive and easiest to process would ultimately have design allowables which would be close to those of optimal materials. Perhaps even economical woven roving type of fabrics would provide similar designs if most of the strands were in the 0° direction. Database values for balanced 0/90 woven roving laminates (Material ROV) are similar to those for

the Ahlstrom fabric laminates if adjusted to the same 0° material content.

The use of processes like hand layup, RTM, and resin infusion with fabrics like UC1018V might provide properties close to prepregs, without the major knockdowns associated with strand crowding. Resin would need to flow in the thickness direction due to the low permeability. However, the waviness knockdown on compression strength would be difficult to avoid in complex blade structures. Tensile fatigue resistance should be improved relative to stranded fabrics at higher fiber contents, and there should be little sensitivity to flaws and details as long as the overall fiber content remained in the 50 percent volume range.

The alternative of using stranded fabrics and keeping the fiber content below 40 percent by volume would provide relatively poor stiffness and ultimate tensile strength, but the tensile fatigue resistance would be good as long as the strands were not tightly stitched to a backing. However, it appears doubtful that knockdowns for strand packing, which raises the fiber content locally around flaws and details, could be avoided. Thus, there is little benefit to the good fatigue resistance in simple test specimens if it is lost in unavoidable details.

The design of structural detail areas against delamination is essential, regardless of the material system or processing method. Away from singularity areas (see Figure 90) it is necessary to model the area with finite elements, and to apply a point-stress based failure criterion (maximum strain or quadratic) to high stress areas. The mode of failure should be identified from a maximum strain criterion. If, as is often the case, the failure mode is by matrix failure in the through-thickness direction, then a second-stage analysis should include the insertion of a delamination crack several millimeters long in the high stress area (see Chapters 13 and 14). The VCCT-1 method will then provide values for G_I and G_{II}, from which static and delamination failure can be predicted following the simplified methods presented in Chapter 14. In singular areas, a crack of several millimeters should be inserted without first applying a point-stress criterion, and the preceding prediction method followed for delamination. Further research is underway to validate this procedure for other geometries, and to provide basic delamination data for other materials systems (including mixed-mode delamination testing). An additional application of fracture mechanics is currently being explored for splitting parallel to the 0° fibers in the primary structure. The purpose of this study is to establish the off-axis ply content, and frequency of interruption of the 0° plies, necessary to resist the growth of major cracks parallel to the main load-bearing 0° plies.

REFERENCES

1. Mandell, J.F., Reed, R.M. Jr. and Samborsky, D.D., "Fatigue of Fiberglass Wind Turbine Blade Materials," Contractor Report SAND92-7005, Sandia National Laboratories, Albuquerque, NM (1992). [http://infoserve.library.sandia.gov/sand_doc/1992/927005.pdf]

2. Mandell, J.F. and Samborsky, "DOE/MSU Composite Material Fatigue Database: Test Methods, Materials, and Analysis," Contractor Report SAND97-3002, Sandia National Laboratories, Albuquerque, NM (1997). [http://infoserve.library.sandia.gov/sand_doc/1997/973002.pdf]

3. Mandell, J. F., Samborsky, D. D., Combs, D.W., Scott, M.E., and Cairns, D. S, "Fatigue of Composite Material Beam Elements Representative of Wind Turbine Blade Substructure," NREL Contractor Report SR-500-24379, November 1998. [http://www.nrel.gov/docs/fy99osti/24379.pdf]

4. Mandell, J.F., Reed, R.M., and Samborsky, D.D., "High Cycle Fatigue of Wind Turbine Blade Materials," in SED-Vol 12, *Wind Energy 92*, P.S. Veers, S.M. Hock, eds., ASME, New York, p. 105 (1992).

5. Mandell, J.F., Reed, R.M. Jr., Samborsky, D.D., and Pan, Q., "Fatigue Performance of Wind Turbine Blade Materials," in SED-Vol 14, *Wind Energy 93*, S. Hock, ed., ASME, New York, pp. 191-198. (1993).

6. Mandell, J.F., Creed, R.M. Jr., Pan, Q., Combs, D.W., and Shrinivas, M., "Fatigue of Fiberglass Generic Materials and Substructures" in SED-Vol 15, *Wind Energy 94*, W.D. Musial, S.M. Hock and D.E. Berg, eds., ASME, New York, pp. 207-213 (1994).

7. Mandell, J.F., Combs, D.E., and Samborsky, D.D., "Fatigue of Fiberglass Beam Substructures," *Wind Energy 1995*, W.D. Musial, S.M. Hock, and D.E. Berg, Eds., SED-Vol. 16, ASME, pp. 99 - 106 (1995).

8. Samborsky, D. and Mandell, J.F., "Fatigue Resistant Fiberglass Laminates for Wind Turbine Blades," *Wind Energy 1996*, ASME, pp. 46-51 (1996).

9. Mandell, J.F.and Samborsky, D.D., "MSU/DOE Wind Turbine Blade Composite Material Fatigue Database," November 1995, Sandia National Laboratories, Albuquerque, NM, 87185. Updates available at www.sandia.gov/Renewable_Energy/wind_energy/other/973002upd02.pdf

10. Sutherland, H.J. and Mandell, J.F., "Application of the U.S. High Cycle Fatigue Data Base to Wind Turbine Blade Lifetime Predictions.," *Wind Energy 1996*, ASME, pp. 85-92. (1996). [www.sandia.gov/Renewable_Energy/wind_energy/asme/ASME1-96p85.pdf]

11. Mandell, J.F., Samborsky, D.D., and Cairns, D.S., "Advanced Wind Turbine Blade Structure Development Program at Montana State University," *Wind Energy 1997*, ASME/AIAA, 189-196 (1997).

12. Cairns, D.S., Mandell, J.F., Scott, M.E., Maccagnano, J.Z.,"Design Considerations for Ply Drops in Composite Wind Turbine Blades," *Wind Energy 1997*, ASME/AIAA, pp. 197 - 208. (1997).

13. Cairns, D. S., Haugen, D. J., Mandell, J. F., and Samborsky, D. D., "Fracture of Skin/Stiffener Intersections in Composite Wind Turbine Structures," *Wind Energy 1998*, ASME/AIAA, pp. 334 - 343. (1998).

14. Mandell, J. F., Samborsky, D. D., Scott, M.E., and Cairns, D. S, "Effects of Structural Details on Delamination and Fatigue Life of Fiberglass Laminates," *Wind Energy 1998*, ASME/AIAA, pp. 323 - 327. (1998).

15. Samborsky, D. D., Mandell, J. F., and Cairns, D. S, "Selection of Reinforcing Fabrics for Wind Turbine Blades," *Wind Energy 1999*, AIAA-99-0024, ASME/AIAA, pp. 32-42. (1999).

16. Mandell, J. F., Samborsky, D. D., Sutherland, H. J., "Effects of Materials Parameters and Design Details on the Fatigue of Composite Materials for Wind Turbine Blades," *1999 European Wind Energy Conference*, 1-5 March 1999, Nice, France, pp. 628-633. [www.sandia.gov/Renewable_Energy/wind_energy/other/EWEC99-1.pdf]

17. Cairns, D.S., Mandell, J.F., Scott, M.E., Maccagnano, J.Z.,"Design and Manufacturing Considerations for Ply Drops in Composite Structures," *Composites: Part B* 30 (1999) pp. 523-534.

18. Mandell, J.F., Samborsky, D.D., Li. M., Orozco, R., and Cairns, D.S., "Selection of Fiberglass Matrix Resins for Increased Toughness and Environmental Resistance in Wind Turbine Blades," *Wind Energy 2000*, AIAA-2000-0057, ASME/AIAA, pp. 354-366. (2000)

19. Wahl, N, Samborsky, D.D., Mandell, J.F., and Cairns, D.S., "Spectrum Fatigue Lifetime and Residual Strength for Fiberglass Laminates in Tension,"*Wind Energy 2001*, AIAA-2001-0025, ASME/AIAA. (2001)

20. Wahl, N, Samborsky, D.D., Mandell, J.F., and Cairns, D.S., "Effects of Modeling Parameters on the Accuracy of Spectrum Fatigue Lifetime Predictions for a Fiberglass Laminate,"*Wind Energy 2002*, ASME/AIAA.

21. Wahl, N.K, Mandell, J.F., Samborsky, D.D., "Spectrum Fatigue Lifetime and Residual Strength for Fiberglass Laminates," Sandia Contractor Report (to be published).

22. Samborsky, D.D., Mandell, J.F., "Very High Cycle Tension Fatigue of Polyester Impregnated E-glass Strands," Journal of Composites Technology and Research, ASTM, to be published.

23. Mandell, J.F., Samborsky, D.D., Wahl, N.K., Sutherland, H.J., "Testing and Analysis of Low Cost Composite Materials Under Spectrum Loading and High Cycle Conditions," ASTM Symposium: May 29-31, 2002, Tours, France (to be published).

24. Reed, Robert, "Long Term Fatigue of Glass Fiber Reinforced Composite Materials for Wind Turbine Blades," M.S. Thesis, Department of Chemical Engineering, Montana State University, 1991.

25. Creed, Richard, "High Cycle Tensile Fatigue of Unidirectional Fiberglass Composite Tested at High Frequency," M.S. Thesis, Department of Chemical Engineering, Montana State University, 1993.

26. Shrinivas, Modayur, "Three Dimensional Finite Element Analysis of Matrix Cracks in Multidirectional Composite Laminates," M.S. Thesis, Department of Mechanical Engineering, Montana State University, 1993.

27. Pan, Rena, "Fatigue Behavior of Glass Fiber Reinforced Composite Materials for Wind Turbine Blades," M.S. Thesis, Department of Chemical Engineering, Montana State University, 1994.

28. Hedley, Chuck, "Mold Filling Parameters in Resin Transfer Molding," M.S. Thesis, Department of Chemical Engineering, Montana State University, 1994.

29. Belinky, Andrew, "High Cycle Compressive Fatigue of Unidirectional Glass/Polyester Performed at High Frequency," M.S. Thesis, Department of Chemical Engineering, Montana State University, 1994.

30. Wei, Guangxi, "High Cycle Longitudinal and Transverse Fatigue of Unidirectional Glass/Polyester Composites," M.S. Thesis, Department of Chemical Engineering, Montana State University, 1995.

31. Combs, David, "Design, Analysis and Testing of a Wind Turbine Blade Substructure," M.S. Thesis, Department of Mechanical Engineering, Montana State University, 1995.

32. Bian, Jinhua, "Fiberglass Composite Tensile Fatigue Resistance: Fiber Surface Damage Analysis and Fatigue Resistant Fiber Coating," M.S. Thesis, Department of Chemical Engineering, Montana State University, 1996.

33. Humbert, Dell, "Modeling of Resin Transfer Molding of Composite Materials With Orientated Unidirectional Plies," M.S. Thesis, Department of Chemical Engineering, Montana State University, 1996.

34. Scott, Ethan, "Effects of Ply Drops on the Fatigue Resistance of Composite Materials and Structures," M.S. Thesis, Department of Chemical Engineering, Montana State University, 1997.

35. Haugen, Darrin, "Fracture of Skin-Stiffener intersections in Composite Wind Turbine Blade Structures," M.S. Thesis, Department of Mechanical Engineering, Montana State University, 1999.

36. Orozco, Ricardo, "Effects of Toughened Matrix Resins on Composite Materials for Wind Turbine Blades," M.S. Thesis, Department of Chemical Engineering, Montana State University, 1999.

37. Sears, Aaron, "Experimental Validation of Finite Element Techniques for Buckling and Postbuckling of Composite Sandwich Shells," M.S. Thesis, Department of Chemical Engineering, Montana State University, 1999.

38. Samborsky, Daniel, D. "Fatigue of E-glass Fiber Reinforced Composite Materials and Substructures," M.S. Thesis, Department of Civil Engineering, Montana State University, 1999.

39. Li, Mei, "Temperature and Moisture Effects on Composite Materials for Wind Turbine Blades," M.S. Thesis, Department of Chemical Engineering, Montana State University, 2000.

40. Morehead, Robert, "Fatigue of Skin-Stiffener Intersections in Composite Wind Turbine Blade Substructures," M.S. Thesis, Department of Mechanical Engineering, Montana State University, 2000.

41. Rossell, Scott, "Fluid Flow Modeling of Resin Transfer Molding for Composite Material Wind Turbine Blade Structures," M.S. Thesis, Department of Chemical Engineering, Montana State University, 2000.

42. Evertz, Russell, "Investigation of Core Closeouts in Fiber-Reinforced Sandwich Laminates," M.S. Thesis, Department of Mechanical Engineering, Montana State University, 2001.

43. Wahl, Neil, "Spectrum Fatigue Lifetime and Residual Strength for Fiberglass Laminates," Ph.D. Thesis, Department of Mechanical Engineering, Montana State University, 2001.

44.	Wang, Lei, "Effects of In-plane Fiber Waviness on the Properties of Composite Materials," M.S. Thesis, Department of Chemical Engineering, Montana State University, 2001.

45.	Sutherland, H.J., "On the Fatigue Analysis of Wind Turbines," Report SAND99-0089, Sandia National Laboratories, Albuquerque, NM (1999).

46.	McKittrick, L., Cairns, D., Mandell, J.,Combs, D., Rabern, D., and Van Luchene, D., "Analysis of a Composite Blade Design for the AOC 15/50 Wind Turbine Using a Finite Element Model," Report SAND2001-1441, Sandia National Laboratories, Albuquerque, NM (2001).

47.	Mayer, R.M.,ed.,"Design of Composites Structures Against Fatigue, Applications to Wind Turbine Blades, Antony Rowe Ltd., Chippenham, Wiltshine, GB (1996).

48.	Hunston, D.L., Moulton, R.J., Johnston, and Bascom, W.D., in Toughened Composites, ASTM STP 937, N.J. Johnston, Ed., American Society for Testing and Materials, Phil., 1987, pp. 74-94.

49.	Russell, A.J., and Street, K.N., in Delamination and Debonding, ASTM STP 876, W.S. Johnston, Ed., American Society for Testing and Materials, Phil., 1986, pp. 349-370.

50.	Mandell, J.F, and Tsai, J.Y., "Effects of Porosity on Delamination of Resin Matrix Composites," Report WRTC-TR-89-3032, Flight Dynamics Laboratory, Wright Patterson Air Force Base, Ohio (1990).

51.	Solin, J., "Methods for Comparing Fatigue Lives for Spectrum Loading," *International Journal of Fatigue*, Vol. 12, No. 1, 1990.

52.	Hwang, W. and Han, K. S., "Cumulative Damage Models and Multi-Stress Fatigue Prediction," *Journal of Composite Materials,* Vol. 20, 1986.

53.	Schaff, Jeffery R. and Davidson, Barry D., "Life Prediction Methodology for Composite Structures. Part I - Constant Amplitude and Two-Stress Level Fatigue," *Journal of Composite Materials,* Vol. 31, No. 2., 1997.

54.	Schaff, Jeffery R. and Davidson, Barry D., "Life Prediction Methodology for Composite Structures. Part II - Spectrum Fatigue," *Journal of Composite Materials*, Vol. 31, No. 2, 1997.

55.	Bond, I. P., "Fatigue Life Prediction for GRP Subjected to Variable Amplitude Loading," *Composites, Part A: Applied Science and Manufacturing*, 1999.

56. van Delft, D. R. V., de Winkel, G. D., and Joossee, P. A., "Fatigue Behaviour of Fibreglass Wind Turbine Blade Material Under Variable Amplitude Loading," *Proceedings of 35th Aerospace Sciences Meeting & Exhibit, 1997,* American Institute of Aeronautics and Astronautics.

57. Echtermeyer, A. T., Kensche, C., Bach, P., Poppen, M., Lilholt, H., Andersen, S. I., and Brøndsted, P., "Method to Predict Fatigue Lifetimes of GRP Wind Turbine Blades and Comparison With Experiment," *Proceedings of 1996 European Union Wind Energy Conference,* 1996.

58. Hashin, A. And Rotem, Z., "Cumulative Damage Theory of Fatigue Failure," *Materials Science and Engineering, 34,* 1978.

59. Broutman, L. J. and Sahu, S., "A New Theory to Predict Cumulative Fatigue Damage in Fiberglass Reinforced Plastics," *Composite Materials: Testing and Design, ASTM STP 497,* American Society for Testing and Materials, 1972.

60. Yang, J. N. and Jones, D. L., "Effect of Load Sequence on the Statistical Fatigue of Composites," *AIAA Journal,* Vol. 18, No. 12, 1980.

61. ten Have, A. A., "WISPER and WISPERX, Final Definition of Two Standardized Fatigue Loading Sequences for Wind Turbine Blades," NLR TP 91476 U, National Aerospace Laboratory NLR, the Netherlands.

62. ten Have, A. A., " WISPER and WISPERX, A Summary Paper Describing Their Background, Derivation and Statistics," NLR TP 92410 U, National Aerospace Laboratory NLR, the Netherlands.

63. Miner, M. A., "Cumulative Damage in Fatigue," *Journal of Applied Mechanics,* Sept., 1945.

64. Mandell, J. A. and Meier, Urs, "Effects of Stress Ratio, Frequency, and Loading Time on the Tensile Fatigue of Glass-Reinforced Epoxy," *Long Term Behavior of Composites.*

65. LI, Chia-Geng, "Fatigue of Fiber Reinforced Plastics," Masters Thesis, Massachusetts Institute of Technology, February 1983.

66. Mandell, J.F., Huang, D.D., McGarry, F.J., "Tensile Fatigue Performance of Glass Fiber Dominated Composites," *Composites Technology Review,* Vol. 3, No. 3, 1981, pp. 96-102.

67. Mandell, J.F., McGarry, F.J., Hsieh, A.J.-Y and LI, C.G., "Tensile Fatigue of Glass and Composites with Conventional and Surface Compressed Fibers," Reinforced Plastics Composites Institute, SPI, Paper 7-G, 1985.

68. Lifshitz, J.M, "Composite Materials, Volume 5, Fracture and Fatigue," L.J. Broutman, ED., Academic Press, New York, 1974, p. 249.

69. Charles, R.J., "Fracture," B.L. Averbach, D.K Felbeck, G.T.Hahn, and D.A. Thomas, Eds., Technology Press (M.I.T.), Cambridge, and Wiley, New York, 1959, p. 225.

70. Owen, M.J., "Static and Fatigue Strength of Glass Chopped Mat/Polyester Resin Laminates," Proceedings of ASTM Symposium on Short Fiber Reinforced Composite Laminates, Minneapolis, April 1980.

71. Mandell, J.F., "Fatigue Behavior of Short Fiber Composite Materials (Ch. 7)," The Fatigue Behavior of Composite Materials, K.L. Reifsnider, Ed., Elsevier (1990).

72. ASM International, "Composites, Volume 1, Engineered Materials Handbook," ASM International, Materials Park, Ohio, 1987.

73. U. S. Department of Defense, "The Composite Materials Handbook," MIL-17 Mil-HDBK-17-1F, January, 1997. (www.mil17.org)

74. de Charentenay, F.X., "Concluding Remarks on the Application of Fracture Mechanics to Composite Materials", Application of Fracture Mechanics to Composite Materials, K. Friedrich Ed., Elsevier (1989).

75. Broek, D., "Elementary Engineering Fracture Mechanics," 4th Edition, Kluwer Academic Publishers, 1986.

76. Friedrich, K., ed., "Composite Materials Series, Vol. 6, Application of Fracture Mechanics to Composite Materials," R.B. Pipes, Series ed., Elsevier, New York (1989).

77. Cairns, D.S., "Static and Dynamic Mode II Strain Energy Release Rates in Toughened Thermosetting Composite Laminates," *ASTM Journal of Composites Technology and Research*, Vol. 14, No. 1, Spring 1992, pp. 37-42.

78. Russell, A.J., Street, K.N., "Moisture and Temperature Effects on the Mixed -Mode Delamination Fracture of Unidirectional Graphite/Epoxy," Delamination and Debonding of Materials, ASTM STP 876, W. S. Johnson, Ed., American Society for Testing and Materials, Philadelphia, 1985, pp. 349-370.

79. Mignery, L.A., Tan, T.M., Sun, C.T., "The Use of Stitching to Suppress Delamination in Laminated Composites," Delamination and Debonding, ASTM STP 876, W. S. Johnson, Ed., American Society for Testing and Materials, Philadelphia, 1985, pp. 371-385.

80. Hyer, M.W., Cohen, D., "Calculation of Stresses and Forces Between the Skin and Stiffener in Composite Panels," Proceedings of the 28th AIAA/ASME/ASCE/AHS Structures, Structural Dynamics, and Materials conference, AIAA, Washington, DC, April 1987.

81. Hyer, M.W., Cohen, D., "Calculation of Stresses and Forces Between the Skin and Stiffener in Composite Panels," *AIAA Journal*, Vol. 26, No. 7, 1988, pp. 852-858.

82. Cohen, D., Hyer, M.W., "Influence of Geometric Nonlinearities on Skin-Stiffener Interface Stresses," 29th AIAA/ASME/ASCE/AHS Structures, Structural Dynamics, and Materials Conference, Paper 88-2217, Williamsburg, VA, April 18-20, 1988, pp. 1055-1061.

83. Rybicki, E.F., Kanninen, M.F., "A Finite Element Calculation of Stress Intensity Factors by a Modified Crack Closure Integral," *Engineering Fracture Mechanics*, Vol. 9, 1977, pp. 931-938.

84. Wang, J.T., Raju, I.S., "Strain Energy Release Rate Formulae for Skin-Stiffener Debond Modeled with Plate Elements," *Engineering Fracture Mechanics*, Vol. 54, No. 2, 1996, pp. 211-228.

85. Kassapoglou, C., "Stress Determination at Skin-Stiffener Interfaces of Composite Stiffened Panels Under Generalized Loading," *Journal of Reinforced Plastics and Composites*, Vol. 13, June 1994, pp. 555-572.

86. Minguet, P.J., Fedro, M.J., O'Brien, T.K., Martin, R.H., Ilcewics, L.B., "Development of Structural Test Simulating Pressure Pillowing Effects in a Bonded Skin/Stringer/Frame Configuration," Proceedings of the Fourth NASA/DoD Advanced Composites Technology Conference, Salt Lake City, Utah, June 1993, pp. 863-880.

87. "Volume I, Procedures, Chapter 3 Structural Analysis, Section 3.9 Fracture Mechanics," ANSYS User's Manual, pp. 3-163.

88. Jerram, K., Discussion on Stress Intensity Factors for a Part-Circular Surface Flow, by F. W. Smith and M. J. Alavi, Discussion 11-62, 1st International Conference on Pressure Vessel Technology, Delft, Netherlands, 29 Sept. - 2 Oct. 1969, PVPD of ASME Discussion 11-62, p.160.

89. Hellen, T.K., Blackburn, W.S., "The Calculation of Stress Intensity Factors in Two and Three-Dimensions Using Finite Elements," Second National Congress on Pressure Vessels and Piping, June 23-27, 1975, San Francisco, California.

90.   Reeder, J.R., "A Bilinear Failure Criterion for Mixed-Mode Delamination," Composite Materials: Testing and Design (Eleventh Volume), ASTM STP 1206, E. T. Camponeschi, Jr., Ed., American Society for Testing and Materials, Philadelphia, 1993, pp. 303-322.

91.   Grimes, G.C., "Test Methods and Design Allowables for Fibrous Composites," ASTM 734, C.C. Chamis, ed., ASTM, Phil., 1981, pp.281-337.

92.   Personal Communication, R. Yamamoto, Toray Industries, Inc.

93.   Folkes, M.J., "Short Fibre Reinforced Thermoplastics," Research Studies Press, Wiley, New York, (1982).

94.   Chawla, K.K., *Composite Materials, Science and Engineering*, Springer-Verlag publishers, 1987, p. 186.

95.   Adams, D.F., Doner, D.R., "Transverse Normal Loading of a Unidirectional Composite", *Journal of Composite Materials*, Vol. 1, 1967, p. 152.

96.   Cairns, D., Skramstad, J., "Evaluation of Hand Lay-up and Resin Transfer Molding in Composite Wind Turbine Blade Manufacturing," Report SAND00-1425, Sandia National Laboratories, Albuquerque, NM (2000).

97.   Mandell, J.F, and Tsai, J.Y., "Effects of Porosity on Delamination of Resin Matrix Composites," Report WRTC-TR-89-3032, Flight Dynamics Laboratory, Wright Patterson Air Force Base, Ohio (1990).

98.   Kussmaul, K., Alberti, M., Eisele, U. and Schneider, T., "Composite Materials Fatigue and Fracture, Fifth Volume," STP 1230, R.H. Martin, Ed., ASTM, Phil., (1995), pp. 61-84.

99.   Bathias, C. and Laksimi, A., "Delamination and Debonding of Materials," ASTM STP 876, W.S. Johnson, Ed., ASTM, Phil. (1985), pp. 217-237.

100.   C. Lindenburg, T. Bax, U. Hindenlang, P.A. Joosse, C. Kensche, J. Korsgaard, A. Roehm, "Buckling Load Analysis Methods for Rotor Blade Design," *1999 European Wind Energy Conference*, 1-5 March 1999, Nice, France, pp. 634-637.

101.   Baltek Corporation (1999), Baltek Corporation Product Data, Northvale, NJ.

102.   Forest Products Laboratory (1987) Wood Handbook: Wood as an Engineering Material, Handbook 72, U. S. Department of Agriculture, Washington, DC.

103.   Feichtinger, K. (1986), Properties of End-Grain Balsa Core Material as a Function of Density, March, 1986.

104. Kilbourn, C. (2000), "Balsa Wood Core Material Design Values," 1331-1340, Proceedings of the 45th International SAMPE Symposium and Exhibition, Covina, CA.

105. U. S. Department of Defense, Mil-Handbook-23A (1968) Structural Sandwich Composites.

106. Wienhold, P., Lennon, A., Roberts, J., Rooney, M., Kercher, A., Nagle, D., Sorathia, U. (2000), "Characterization of Carbonized Wood Core for Use in FRP Sandwich Ship Structures," 1700-1712, Proceedings of the 45th International SAMPE Symposium and Exhibition, Covina, CA.

107. Tsoumis, G. (1991) Science and Technology of Wood-Structure, Properties, Utilization, Van Nostrand Reinhold, New York, NY.

108. Nuismer, R.J., and Whitney, J.M., "Fracture Mechanics of Composites," ASTM STP 593, ASTM, Phil, (1975), pp. 117-142.

DISTRIBUTION

T. Almeida
TPI Composites Inc.
373 Market Street
Warren, RI 02885

H. Ashley
Dept. of Aeronautics and
  Astronautics Mechanical Engr.
Stanford University
Stanford, CA 94305

K. Bergey
University of Oklahoma
Aero Engineering Department
Norman, OK 73069

R. Blakemore
Enron Wind Corp.
13681 Chantico Road
Tehachapi, CA 93561

C. P. Butterfield
NREL
1617 Cole Boulevard
Golden, CO 80401

G. Bywaters
Northern Power Systems
Box 999
Waitsfield,VT 05673

J. Cadogan
Office of Geothermal & Wind
  Technology
EE-12
U.S. Department of Energy
1000 Independence Avenue SW
Washington, DC 20585

D. Cairns
Montana State University
Mechanical & Industrial Engineering Dept.
220 Roberts Hall
Bozeman, MT 59717

S. Calvert
Office of Geothermal & Wind
  Technology
EE-12
U.S. Department of Energy
1000 Independence Avenue SW
Washington, DC 20585

J. Chapman
OEM Development Corp.
840 Summer St.
Boston, MA 02127-1533

C. Christensen
Enron Wind Corp.
13681 Chantico Road
Tehachapi, CA 93561

R. N. Clark
USDA
Agricultural Research Service
P.O. Drawer 10
Bushland, TX 79012

J. Cohen
Princeton Economic Research, Inc.
1700 Rockville Pike
Suite 550
Rockville, MD 20852

C. Coleman
Northern Power Systems
Box 999
Waitsfield, VT 05673

C. A. Cornell
Civil Engineering Department
Stanford University
Stanford, CA 94305

K. J. Deering
The Wind Turbine Company
515 116th Avenue NE
No. 263
Bellevue, WA 98004

A. J. Eggers, Jr.
RANN, Inc.
744 San Antonio Road, Ste. 26
Palo Alto, CA 94303

D. M. Eggleston
DME Engineering
1605 W. Tennessee Ave.
Midland, TX 79701-6083

P. R. Goldman
Director
Office of Geothermal & Wind
  Technology
EE-12
U.S. Department of Energy
1000 Independence Avenue SW
Washington, DC 20585

G. Gregorek
Aeronautical & Astronautical Dept.
Ohio State University
2300 West Case Road
Columbus, OH 43220

D. Griffin
Global Energy Concepts
5729 Lakeview Drive NE, Ste. 100
Kirkland, WA 98033

C. Hansen
Windward Engineering
4661 Holly Lane
Salt Lake City, UT 84117

C. Hedley
Headwaters Composites
105 E. Adams St.
Three Forks, MT 59752

S. Hock
Wind Energy Program
NREL
1617 Cole Boulevard
Golden, CO 80401

Bill Holley
3731 Oakbrook Court
Pleasanton, CA 94588

K. Jackson
Dynamic Design
123 C Street
Davis, CA 95616

E. Jacobsen
Enron Wind
13000 Jameson Rd.
Tehachapi, CA 93561

D. Malcolm
Global Energy Concepts
5729 Lakeview Drive NE, Ste. 100
Kirkland, WA 98033

J. F. Mandell   (20)
Montana State University
302 Cableigh Hall
Bozeman, MT 59717

T. McCoy
Global Energy Concepts
5729 Lakeview Drive NE, Ste. 100
Kirkland, WA 98033

L. McKittrick
Montana State University
Mechanical & Industrial Engineering Dept.
220 Roberts Hall
Bozeman, MT 59717

P. Migliore
NREL
1617 Cole Boulevard
Golden, CO 80401

W. Musial
NREL
1617 Cole Boulevard
Golden, CO 80401

NWTC Library (5)
NREL
1617 Cole Boulevard
Golden, CO 80401

B. Neal
USDA
Agricultural Research Service
P.O. Drawer 10
Bushland, TX 79012

V. Nelson
Department of Physics
West Texas State University
P.O. Box 248
Canyon, TX 79016

J. W. Oler
Mechanical Engineering Dept.
Texas Tech University
P.O. Box 4289
Lubbock, TX 79409

T. Olsen
Tim Olsen Consulting
1428 S. Humboldt St.
Denver, CO 80210

R. G. Rajagopalan
Aerospace Engineering Department
Iowa State University
404 Town Engineering Building
Ames, IA 50011

J. Richmond
MDEC
3368 Mountain Trail Ave.
Newbury Park, CA 91320

Michael Robinson
NREL
1617 Cole Boulevard
Golden, CO 80401

D. D. Samborsky
Dept. of Chemical Engineering
Montana State University
Cableigh Hall
Bozeman, MT 59717

D. Sanchez
U.S. Dept. of Energy
Albuquerque Operations Office
P.O. Box 5400
Albuquerque, NM 87185

L. Schienbein
Sustainable Energy Technologies
350 Hills Street, #108
Richland, WA 99352

R. Sherwin
Atlantic Orient
PO Box 1097
Norwich, VT 05055

Brian Smith
NREL
1617 Cole Boulevard
Golden, CO 80401

K. Starcher
AEI
West Texas State University
P.O. Box 248
Canyon, TX 79016

F. S. Stoddard
79 S. Pleasant St. #2A
Amherst, MA 01002

A. Swift
University of Texas at El Paso
320 Kent Ave.
El Paso, TX 79922

R. W. Thresher
NREL
1617 Cole Boulevard
Golden, CO 80401

S. Tsai
Stanford University
Aeronautics & Astronautics
Durand Bldg. Room 381
Stanford, CA 94305-4035

W. A. Vachon
W. A. Vachon & Associates
P.O. Box 149
Manchester, MA 01944

C. P. van Dam
Dept. of Mech. and Aero. Eng.
Univ. of California, Davis
One Shields Avenue
Davis, CA 95616-5294

B. Vick
USDA, Agricultural Research Service
P.O. Drawer 10
Bushland, TX 79012

N. K. Wahl
Engineering Department
Montana Tech of The Univ. of Montana
1300 West Park Street
Butte, MT 59701

R. E. Wilson
Mechanical Engineering Dept.
Oregon State University
Corvallis, OR 97331

M. Zuteck
601 Clear Lake Road
Clear Lake Shores, TX 77565

M.S. 0557	T. J. Baca, 9125
M.S. 0557	T. G. Carne, 9124
M.S. 0615	R.L. Perry, 6252
M.S. 0708	T. D. Ashwill, 6214
M.S. 0708	D. E. Berg, 6214
M.S. 0708	H. M. Dodd, 6214 (25)
M.S. 0708	R. R. Hill, 6214
M.S. 0708	P. L. Jones 6214
M.S. 0708	D. L. Laird, 6214
M.S. 0708	D. W. Lobitz, 6214
M.S. 0708	J. Ortiz, 6214
M.S. 0708	M. A. Rumsey, 6214
M.S. 0708	H. J. Sutherland, 6214
M.S. 0708	P. S. Veers, 6214
M.S. 0708	J. Zayas, 6214
M.S. 0847	K. E. Metzinger, 9126
M.S. 1490	A. M. Lucero, 12660
M.S. 0958	M. Donnelly, 14172
M.S. 0612	Review & Approval Desk, 9612
	For DOE/OSTI
M.S. 0899	Technical Library, 9616 (2)
M.S. 9018	Central Technical Files, 8945-1